Transcriptional changes linked with extracellular matrix remodeling underlie right ventricular failure and its reversibility in chronic thromboembolic pulmonary hypertension

Inaugural Dissertation

submitted to the

Faculty of Medicine

in partial fulfillment of the requirements

for the PhD-Degree

of the Faculties of Veterinary Medicine and Medicine

of the Justus Liebig University Giessen

by Leili Jafari

from Tehran, Iran

Giessen 2023

From

Kerckhoff Clinic, Department of Cardiology
Department of Internal Medical, Medial Clinic I - Cardiology/Angiology
Faculty of Medicine of the Justus Liebig University Giessen

Director: Prof. Dr. med. Christian Hamm

and

Max-Planck-Institute for Heart and Lung Research
Department of Internal Medicine, Medical Clinic II
Faculty of Medicine of the Justus Liebig University Giessen

Director: Prof. Dr. med. Werner Seeger

Chair: **Prof. Dr. Ralph Schermuly**

Vice-chair /Co-supervisor: **Prof. Dr. Richard Göttlich**

First reviewer/ Supervisor: **PD Dr. Christian Troidl**

Second reviewer: **Prof. Dr. Irene Lang**

Date of Doctoral Defense:14th October 2024

Declaration

I declare that I have completed this dissertation single-handedly without the unauthorized help of a second party and only with the assistance acknowledged therein. I have appropriately acknowledged and referenced all text passages that are derived literally from or are based on the content of published or unpublished work of others, and all information that relates to verbal communications. I have abided by the principles of good scientific conduct laid down in the charter of the Justus Liebig University of Giessen in carrying out the investigations described in the dissertation."

_____

Dedicated to:

All the patients whose samples I was honored and privileged to work with

Table of Contents*

List of Tables ……VIII

List of Figures ……IX

List of Abbreviations ……XII

1. Introduction ……1

1.1. Pulmonary vascular system and right ventricle ……1

1.1.1. RV and interventricular septum: physiology and function ……1

1.1.2. Cell types in the adult heart ……2

1.1.3. Chamber-specific gene expression pattern in the human heart ……3

1.2. Pulmonary hypertension ……3

1.2.1. PH classification ……4

1.3. Chronic thromboembolic pulmonary hypertension ……4

1.4. CTEPH pathophysiology ……6

1.5. CTEPH diagnosis ……7

1.6. Features of the RV and IVS in CTEPH ……8

1.7. Treatment approaches for CTEPH ……11

1.7.1. Pulmonary endarterectomy ……11

1.7.1.1. The effect of PEA on right heart function ……12

1.7.2. Balloon pulmonary angioplasty ……12

1.7.3. Medial therapy ……13

1.8. Role of transcription factors in CTEPH and RV remodeling ……13

1.9. Biomarker in CTEPH ……14

1.10. Animal models of CTEPH ……16

1.11. Animal models of RV remodeling ……16

1.12. Available transcriptomic datasets for the human RV ……17

1.13. Ankyrin Repeat Domain 1 (ANKRD1) ……18

1.13.1. Role of ANKRD1 in cardiovascular disease ……19

1.13.2. Role of ANKRD1 in pulmonary hypertension ……20

1.14. Activating Transcription Factor 3 (ATF3) ……20

1.14.1. Role of ATF3 in cardiovascular disease ……21

1.14.2. Role of ATF3 in pulmonary hypertension ……22

1.15. Interleukin 7 Receptor (IL7R) ……23

1.15.1. Role of IL7R in cardiovascular disease ……23

1.15.2. Role of IL7R in pulmonary hypertension ……24

1.16. Inhibin Subunit Beta B (INHBB) 25
1.16.1. Role of INHBB in cardiovascular disease ...26
1.16.2. Role of INHBB in pulmonary hypertension ...26
1.17. Serpin Family E Member 1 (SERPINE1) 27
1.17.1. Role of SERPINE1 in cardiovascular disease 27
1.17.2. Role of SERPINE1 in pulmonary hypertension 28
2. Amis and Objectives ...30
3. Materials and Methods 32
3.1. Materials 32
3.1.1. Reagents and chemicals 32
3.1.2. Kits 33
3.1.3. Cell culture medium and reagents 33
3.1.4. Other materials 34
3.1.5. Equipments 34
3.2. Methods 35
3.2.1. Human heart tissue from the CTEPH cohort 35
3.2.2. RNA isolation from the human right ventricle free wall and IVS of patients with CTEPH 36
3.2.2.1. Tissue homogenization using the bead beating method 36
3.2.2.2. Dry cryo-pulverization method 37
3.2.3. Quality and Quantity of the isolated RAN from the samples 37
3.2.4. RNA sequencing 37
3.2.5. RNA-seq analysis 38
3.2.5.1. Dwonstream analysis of RNA-seq data 38
3.2.5.2. Pathway enrichment anaylsis 39
3.2.6. Cell culture 39
3.2.6.1. Treatment of human cardiac cells 40
3.2.6.2. Hypoxia treatment 40
3.2.6.3. Enzyme-linked immunosorbent assay (ELISA) 40
3.2.6.3.1. DuoSet ELISA Development System 41
3.2.6.3.2. ANKRD1 (Novus Biologicals) 41
3.2.6.3.3. IL7R (Invitrogen) 41
3.2.7. Animal experiments 41
3.2.7.1. Experimental groups 42

3.2.7.2. Pulmonary artery banding model (PAB) ……..……....42
3.2.7.3. Monocrotaline (MCT)-induced PH rat model …….……...…..43
3.2.7.4. Hemodynamic, MRI, and RV hypertrophy measurements ……..……..43
3.2.8. RNA isolation from the cells ……...…….……43
3.2.9. RNA isolation from the tissue ……...…….....….44
3.2.10. Reverse transcription of RNA ……...……....…….....44
3.2.11. Quantitative real-time PCR ……...……...…….…...44
3.2.12. Protein isolation from tissue ……...……..…….....46
3.2.13. Protein quantification …...……...…….……...…….…46
3.2.14. Western blotting ……...……...…….…46
3.2.15. RNA interference and treatment of the cells …….....…48
3.2.16. Cell proliferation assay ……...…….....49
3.2.17. Wound healing assay ……...……...……..49
3.2.18. Tube formation assay ……...…….……....…….....49
3.2.19. Matrix stiffness-dependent cell culture experiments …...……...…....50
3.2.20. Statistical analysis ……...…….....50
4. Results ……..……..……...…….…….....51
4.1. Classification of the patients with CTEPH based on ECS/ERS guidelines ...….....51
4.2. Effect of PEA on the clinical parameters in the confirmatory cohort: B-prePEA versus B-postPEA …...…...…….…..…..…..……..….56
4.3. RNA quality and quantity of human heart tissue ……..…….…….....57
4.4. Transcriptomic profiling of the RV and septum in patients with CTEPH before and after PEA ……..……..…….....…….....58
4.5. Principal component analysis of RNA-seq ……....….....…...…59
4.6. Volcano plots of the differentially expressed genes in the exploratory and confirmatory cohort …….……...……...…...…...59
4.7. Heatmaps of the differentially expressed genes in the exploratory and confirmatory cohort …….…….……...…….....…….…...60
4.8. Tree plots showing the hierarchical clustering of enriched terms in the exploratory and the confirmatory cohort ……...…..……..…….……...…….61
4.9. Gene set enrichment analysis in the exploratory and confirmatory cohort ……..……....……...…….…...…61
4.10. DEGs between the B-prePEA and B-postPEA groups in the confirmatory cohort …….……...…….……...…….....…68

4.11. Pathway analysis in the confirmatory cohort of B-postPEA versus B-prePEA ……70
4.12. Analysis of the transcriptomic profile of the right ventricle and septum at prePEA and comparing it to the septum at postPEA in patient-paired samples……74
4.13. Pathway enrichment analysis ……76
4.14. Pathway analysis for target selection ……78
4.15. Correlation between *ANKRD1*, *ATF3*, *IL7R*, *INHBB*, and *SERPINE1* expression and clinical parameters in the confirmatory cohort 81
4.15.1. Correlation between *SERPINE1* expression and clinical parameters of B-prePEAm and B-prePEAs groups ……..81
4.15.2. Correlation between *IL7R* expression and clinical parameters in the B-prePEAm and B-prePEAs groups ……..82
4.15.3. Correlation between *INHBB* expression and clinical parameters in the B-prePEAm and B-prePEAs groups ..……82
4.15.4. Correlation between *ANKRD1* expression and clinical parameters in the B-prePEA and B-postPEA groups ……83
4.15.5. Correlation between *IL7R* expression and clinical parameters in the B-prePEA and B-postPEA groups……83
4.15.6. Correlation between *INHBB* expression and clinical parameters in the B-prePEA and B-postPEA groups ……84
4.15.7. Correlation between *SERPINE1* expression and clinical parameters in the B-prePEA and B-postPEA groups ……84
4.16. The effect of different growth factors on *ANKRD1*, *ATF3*, *CILP1*, *IL7R*, *INHBB*, and *SERPINE1* expression in human cardiac cells ..……..85
4.16.1. The effect of TGF-β1 and TNF-α stimulation on CILP1 expression of in HCFs ……85
4.16.2. The effect of TGF-β1 and TNF-α stimulation on *ANKRD1*, *ATF3*, *IL7R*, *INHBB*, and *SERPINE1* in HCFs ……86
4.16.3. The effect of TNF-α stimulation on *ANKRD1*, *ATF3*, *IL7R*, *INHBB* and *SERPINE1* expression in HCMECs……..88
4.17. Screening of *ANKRD1*, *ATF3*, *IL7R*, *INHBB*, and *SERPINE1* expression in hypoxia-exposed HCFs and HCMEC ……90
4.18. Detection of SERPINE1 and POSTN secretion in the cell culture supernatant

by enzyme-linked immunosorbent assay ..……...…...……92
4.18.1. SERPINE1 secretion from HCFs and HCMECs ……...……...…...……..92
4.18.2. POSTN secretion from HCFs and HCMECs …..…….…...…..….....……94
4.18.3. IL7R secretion from HCFs ....……..…....…....……...……..95
4.18.4. ANKRD1 secretion from HCFs ……..……..……..……..……95
4.19. Transient knockdown of ANKRD1, ATF3, IL7R, INHBB, and SERPINE1 by siRNA AMARTpool in HCFs …..…….……..……95
4.20. Transient knockdown of ANKRD1, ATF3, IL7R, INHBB, and SERPINE1 by siRNA SMARTpool in HCMECs ..……...……...…….…….……..…98
4.21. Inhibition of both ANKRD1 and SERPINE1 attenuate the expression in HCFs and HCMECs ……..…..…..……...……..…..99
4.22. Effects of ANKRD1, SERPINE1, ATF3, IL7R, and INHBB knockdown on HCFs and HCMECs proliferation ……..……..……..…….101
4.23. The effect of mechanical cues by the extracellular matrix stiffness on *ANKRD1, ATF3*, *IL7R*, *INHBB*, and *SERPINE1* expression .....…..103
4.24. siRNA knockdown of ANKRD1, SERPINE1, ANKRD1/SERPINE1, ATF3, IL7R, and INHBB induce tube structure formation in HCMECs ……..…..……..104
4.25. siRNA knockdown of ANKRD1, SERPINE1, ANKRD1/SERPINE1, ATF3, *IL7R, and INHBB* induced the migration of HCFs ....…….....……..107
4.26. Evaluation of right ventricle function by the invasive and noninvasive method in MCT-induced PH rats …...…….……...…...……..…….108
4.26.1. mRNA expression of *Ankrd1*, *Atf3*, *Il7r*, *Inhbb*, and *Serpine1* in MCT-induced PH rats ……..……..……..…..……109
4.26.2. Protein levels of ANKRD1 and SERPINE1 in the RV of MCT-induced PH rats …….……...……..……..…..……110
4.26.3. Correlation between *Ankrd1*, *Atf3*, *Il7r*, *Inhbb*, and *Serpine1* mRNA levels and the hemodynamic parameters of the RV in MCT-induced PH rats …….111
4.27. Evaluation of right ventricle function by invasive and noninvasive methods in PAB models ……..…….112
4.27.1. *Ankrd1*, *Atf3*, *Il7r, Inhbb*, and *Serpine1* mRNA levels in the RV of rats PAB model ….....……...…….……..……113
4.27.2. Protein levels of ANKRD1 and SERPINE1 in the RV of rats PAB model …….…….....114
4.27.3. Correlation between *Ankrd1*, *Atf3*, *Il7r*, *Inhbb*, and *Serpine1* mRNA levels and

the hemodynamic parameters of the RV in the rats PAB model ……115
5. Discussion ……117
5.1. Significance of living- CTEPH human cohort ……117
5.2. Influence of RNA isolation method on gene expression profile ……118
5.3. Importance of gene expression profile in RV and septum of living patients with CTEPH cohort ……118
5.4. Activation of main KEGG Pathways in CTEPH cohort ……118
5.5. Role of ANKRD1 and SERPINE1 in Hippo signaling pathway ……119
5.6. TGF-beta signaling pathway……119
5.7. Pathway enrichment analysis in prePEAm versus prePEAs in the exploratory and confirmatory cohort ……120
5.8. Expression of selected targets in postPEA vs. prePEA in the confirmatory cohort ……120
5.9. Pro-PH stimuli induce *ANKRD1*, *ATF3*, *IL7R*, *INHBB* and *SERPINE1* expression in cardiac cells ……121
5.10. *Ankrd1*, *Serpine1*, *Atf3*, *Il7r* and *Inhbbb* expression in an experimental animal model of PH ……122
5.11. Hypoxia induces *ANKRD1*, *SERPINE1*, *ATF3*, *IL7R* and *INHBB* expression in cardiac cells ……123
5.12. ANKRD1 regulates diverse cellular processes ……124
5.13. ATF3 regulates diverse cellular processes ……124
5.14. IL7R regulates diverse cellular processes ……125
5.15. INHBB regulates diverse cellular processes ……125
5.16. SERPINE1 regulates diverse cellular processes ……126
5.17. Circulation of ANKRD1, SERPINE1, ATF3, IL7R, and INHBB in plasma ...126
6. Limitations ……127
7. Outlook ……129
Summary ……131
Zusammenfassung ……133
References ……XVI
Appendix ……XXXIV
Acknowledgments ……XXXVIII

* Formating guidelines:

Page numbering: The Roman numerals were used for the Table of Contents, List of Figures, List of Abbreviations, References, Appendix, Acknowledgments, and Curriculum Vitae. The main body of the thesis includes the Introduction, Aims and Objectives, Material and Methods, Results, Discussion, Limitations, Outlook, Summary, and Zusammenfassung follows normal numbering conventions.

The human genes are written in upper-case and when the genes refer to the mRNA expression they are written in italics. The protein symbols are similar to their corresponding gene symbols and they are written in upper-case.

The animal genes are written in italics, with only the first letter in upper-case and protein symbols are also written in upper-case.

List of Tables

Table 1: Comprehensive classification of PH ……..……...……..….5
Table 2: CTEPH prediction score ……..……7
Table 3: List of reagents and chemicals ……...……...…32
Table 4: List of used kits ……...……..….33
Table 5: List of cell culture medium and reagents ……...…….....33
Table 6: List of additionally used materials ……...……..…...….34
Table 7: List of the equipments ……...……....…34
Table 8: The number of heart tissue samples in patients with CTEPH for RNA isolation ……..…….……..37
Table 9: Composition of reverse transcription master mix ……...……..…….44
Table 10: qRT-PCR reaction mix components ……...…….…….45
Table 11: Thermocycler steps for qRT-PCR ……...…….……...…45
Table 12: Composition of 5X gel loading buffer ……..…..……...……..46
Table 13: Composition of polyacrylamide gels ……...……47
Table 14: Composition of 1XSDS Running buffer ……...……..….47
Table 15: Composition of 1X blotting buffer ……...…….……..47
Table 16: Composition of TBST buffer ……..…….48
Table 17: List of antibodies ……..……...…….…….…....48
Table 18: Risk factors and comorbidities of the patients with CTEPH before PEA …..…..…53
Table 19: Clinical characteristics of the patients with CTEPH in the exploratory Cohort …….....54
Table 20: Clinical characteristics of the patients with CTEPH in the confirmatory Cohort …….....55
Table 21: The effect of PEA on the clinical parameters of CTEPH patients in the confirmatory cohort of B-PrePEA versus B-postPEA ……..……...…56
Table 22: The effect of PEA on the clinical parameters of patients with CTEPH in the confirmatory cohort comparing B-PrePEA and B-postPEA (three paired patients) ……...……..…57

List of Figures

Figure 1: Potential role of impaired endothelium in CTEPH microvasculopathy ……..……..6
Figure 2: The pathophysiology of RV remodeling in CTEPH ……..…….…....…….....10
Figure 3: Schematic representation of therapeutic approaches in CTEPH …….....11
Figure 4: Circulating biomarkers for CTEPH ……..……..….....15
Figure 5: The location of RV (prePEA) and Septum (postPEA) biopsies in CTEPH Cohort ...……..……..……..…....….35
Figure 6: Biopsy procedure for the RV and septum of patients with CTEPH …...…..……....…...36
Figure 7: Study population in CTEPH cohort ……..……..……..…….....…...51
Figure 8: A flowchart of the classification of the patients with CTEPH ……..……..……..…..…...52
Figure 9: An electropherogram showing the regions that indicate the quality of RNA from the heart tissue of the patients with CTEPH ……..……...……..…....…57
Figure 10: Segments of the electropherogram showing the peak distribution of RNA from the prePEA sample ……...…….....….....58
Figure 11: Schematic of the approach used to examine CTEPH heart tissue ……..…...…….58
Figure 12: PCA of the RNA-seq data ……....……...…59
Figure 13: Volcano plots of differentially expressed genes ……..….....….....…..60
Figure 14: Heatmap of DEGs in the RNA-Seq data ……..……..…..…….…..61
Figure 15: Top 20 and 100 enrichment terms and pathways in moderate and severe risk group ……..……..…….....…64
Figure 16: Top 20 and 100 enriched terms and pathways in B-prePEA patients of confirmatory cohort …….....……..……...…...66
Figure 17: Top 20 and 100 enrichment terms and pathways in the exploratory and confirmatory of CTEPH patients before PEA …….....……68
Figure 18: PCA of the RNA-seq data ……..…..….....…..68
Figure 19: Volcano plots of differentially expressed genes ……..……..……...…...69
Figure 20: Heatmaps of DEGs in the RNA-seq data …...……...70
Figure 21: Top 20 and 100 enriched terms and pathways of pre and post PEA…….……..74
Figure 22: PCA of the RNA-seq data ……..……...….…….74
Figure 23: Volcano plots of differentially expressed genes ……..…….……75
Figure 24: Heatmaps of DEGs in the RNA-seq data ……..……....…….…….75
Figure 25: Top 20 and 100 enriched terms and pathways …….…….....…….77
Figure 26: Comparison of clusters for target selection ……..…….…..78
Figure 27: Pathway analysis for target selection in CTEPH cohort ……..…....……80
Figure 28: Correlation between *SERPINE1* expression and clinical parameters in the B-prePEAm and B-prePEAs groups ……..……...…….82

Figure 29: Correlation between *IL7R* expression and clinical parameters in B-prePEAm and prePEAs ……..…….....82
Figure 30: Correlation between *INHBB* expression and clinical parameters in the B-prePEAm and prePEAs groups ……...…...….....83
Figure 31: Correlation between *ANKRD1* expression and clinical parameters in the B- prePEA and B-postPEA groups ……..……..…….....83
Figure 32: Correlations between *IL7R* expression and clinical parameters in the B-prePEA and B-postPEA groups ……...……..….....……...84
Figure 33: Correlations between *INHBB* expression and clinical parameters in the B-prePEA and B-postPEA groups ……...……..…...…84
Figure 34: Correlations between *SERPINE1* expression and clinical parameters in the B-prePEA and B-postPEA groups ……..…….....….…85
Figure 35: Stimulation of primary HCFs with profibrotic and proinflammatory stimuli induced *CILP1* expression ……..……..…….....….....…86
Figure 36: Stimulation of primary HCFs with profibrotic and proinflammatory stimuli induced *ANKRD1*, *ATF3*, *IL7R*, *INHBB*, and *SERPINE1* expression ..……..……...….....…… 88
Figure 37: Stimulation of primary human HCMECs with proinflammatory stimuli induced *ANKRD1*, *ATF3*, *IL7R*, *INHBB*, and *SERPINE1* expression …….……..…….....…….…90
Figure 38: Hypoxia exposure in primary HCFs and HCMECs changed the mRNA expression levels of *ANKRD1*, *ATF3*, *IL7R*, *INHBB*, and *SERPINE1* ..….....….....…...92
Figure 39: Detection of SERPINE1 levels in conditioned media of cultured HCFs and HCMECs 94
Figure 40: Detection of POSTN concentrations in the conditioned media of cultured HCFs and HCMECs ……...…….…….....….95
Figure 41: Detection of IL7R concentrations in the conditioned media of cultured HCFs …….....95
Figure 42: Knockdown of ANKRD1, ATF3, IL7R, INHBB, and SERPINE1 in HCFs …….…….....….98
Figure 43: Knockdown of ANKRD1, ATF3, IL7R, INHBB, and SERPINE1 in HCMECs …..…...….....99
Figure 44: Single and double knockdown of ANKRD1 and SERPINE1 in HCFs and HCMECs 101
Figure 45: Effect of siRNA knockdown of ANKRD1, SERPINE1, SERPINE1/ANKRD1, ATF3, IL7R, and INHBB on HCFs and HCMECs proliferation ……..…...….....102
Figure 46: Schematic representation of the experimental design ……..……...….....…...103
Figure 47: HCFs were cultured on 1kPa (soft matrix) and 50 kPa (stiff matrix) harvested after 12-, 24-and 48 hours …….…….....104
Figure 48: siRNA knockdown of ANKRD1, SERPINE1, SERPINE1/ANKRD1, ATF3, IL7R, and INHBB affected tube formation in HCMECs ……..…...….....….106
Figure 49: siRNA knockdown of ANKRD1, SERPINE1, SERPINE1/ANKRD1, ATF3, IL7R, and INHBB induced migration in HCFs by the effecting wound closure …….....…..108
Figure 50: Schematic representation of the experimental design ……..…...…...…...…….....…..108

Figure 51: Cardiac function measured by noninvasive MRI or invasive hemodynamics via right heart catheterizations in MCT-induced PH rats …….....109
Figure 52: mRNA levels of *Ankrd1*, *Atf3*, *Il7r*, *Inhbb*, and *Serpine1* in the right ventricle of MCT-induced PH rats ……...…....….110
Figure 53: Protein levels of ANKRD1 and SERPINE1 in the RV of MCT-induced PH rats ……...111
Figure 54: Correlation between *Ankrd1*, *Atf3*, *Il7r*, *Inhbb*, and *Serpine1* levels and the RV hemodynamics parameters of MCT-induced PH rats …….…..…....112
Figure 55: Schematic representation of the experimental design ……..…….……..…113
Figure 56: Measurements of cardiac function by noninvasive MRI or invasive hemodynamics via right heart catheterizations in rats PAB model of rat RV hypertrophy ……..…….....113
Figure 57: *Ankrd1*, *Atf3*, *Il7r*, *Inhbb*, and *Serpine1* mRNA levels in the RV of the rats PAB model ..…….…….……..……114
Figure 58: Protein levels of ANKRD1 and SERPINE1 in the RV of the rats PAB model ….……...115
Figure 59: Correlation between *Ankrd1*, *Atf3*, *Il7r*, *Inhbb*, and *Serpine1* mRNA levels and the hemodynamics parameters of the RV in the rats PAB model ……..….....……....116

List of Abbreviations

ΔCt	Threshold-cycle difference (HPRT-GOI)
6MWD	Six-minute walk distance
ADAMTS13	A disintegrin and metalloproteinase with thrombospondin type 1 motif member 13
ADHIB	Alcohol dehydrogenase 1B beta polypeptide
AGEs	Advanced glycation end products
AHSP	Alpha hemoglobin stabilizing protein
AKR1C1	Aldo-keto reductase family 1 member C1
ALAS2	5'-aminolevulinate synthase 2
ANKRD1	Ankyrin Repeat Domain 1
ANKRD2/ARPP	Ankyrin Repeat Domain 2
ANKRD23	Ankyrin Repeat Domain 23
AP-1	Activator protein 1
APA	Antiphospholipid antibody
APS	Antiphospholipid syndrome
ATF3	Activating Transcription Factor 3
BL	Baseline
BPA	Balloon pulmonary angioplasty
BrdU	Bromodeoxyuridine
BSA	Bovine serum albumin
bZIP	basic leucine zipper
Ca	Pulmonary artery compliance
CAD	Coronary artery disease
CARP	Cardiac ankyrin repeat protein
CCL3	C-C motif chemokine ligand 3
CCL4	C-C motif chemokine ligand 4
CCND1	Cyclin D1
CI	Cardiac index
CILP1	Cartilage intermediate layer protein 1
CO	Cardiac output
COPD	Chronic obstructive pulmonary disease
CRE	cAMP responsive element
CREB	cAMP responsive element-binding
cRV	compensated right ventricle
Cryo-SFM	Cryopreservation- Serum Free Medium
Ct	Cycle threshold
CTEPD	Chronic thromboembolic pulmonary disease
CTEPH	Chronic thromboembolic pulmonary hypertension
CTPA	Computed tomography pulmonary angiography
CXCL9	C-X-C motif chemokine ligand 9
DCM	Dilated cardiomyopathy
DEGs	Differentially expressed genes
DPBS	Dulbecco’s Phosphate Buffered Saline
dRV	decompensated right ventricle
ECs	Endothelial cells
ECM	Extracellular matrix
EDAT	Ethylenediaminetetraacetic acid

EDVI	End-diastolic volume index
EGR1	Early growth response factor 1
EIF2AK4/GCN2	Eukaryotic translation initiation factor 2 alpha kinase 4
ELISA	Enzyme-linked immunosorbent assay
EndMT	Endothelial-to-mesenchymal transition
ERS	European Respiratory Society
ECs	Endothelial cells
ESC	European Society of Cardiology
ESVI	End-systolic volume index
FBs	Fibroblasts
FBS	Fetal bovine serum
FCS	Fetal Calf Serum
FDR	False discovery rate
FGS	Fibroblast growth supplement
FM	Fibroblast medium
FU	Follow up
GADD153	DNA damage 153
GO	Gene ontology
GSE	Gene set enrichment
HBD	Hemoglobin subunit delta
HCFs	Human cardiac fibroblasts
HCl	Hydrochloric acid
HCMECs	Human cardiac microvascular endothelial cells
HF	Heart failure
Hox	Hypoxia
HPRT	Hypoxanthine phosphoribosyltransferase
HPRT1	Hypoxanthine Phosphoribosyltransferase 1
ICM	Ischemic cardiomyopathy
IL7R	Interleukin 7 Receptor
INHBB	Inhibin Subunit Beta B
IPAH	Idiopathic pulmonary arterial hypertension
ITGA2B	Integrin subunit alpha 2b
IVS	Interventricular septum
JDP2	c-Jun dimerization protein
JUN	Jun proto-oncogene
KEGG	Kyoto encyclopedia of genes and genomics
LA	Left atrium
LCN6	Lipocalin 6
LV	Left ventricle
LVEDD	Left ventricular end-diastolic diameter
LVEF	Left ventricle ejection fraction
MAOB	Monoamine oxidase B
MAPK	Mitogen-activated protein kinase
MARP	Muscle ankyrin repeat protein family
MCT	Monocrotaline
MI	Myocardial infarction
MMP	Matrix metalloproteinase
mPAP	mean pulmonary arterial pressure

MRI	Magnetic resonance imaging
mRNA	messenger ribonucleic acid
NCBI	National Center for Biotechnology Information
NETs	Neutrophil extracellular traps
NFkB	Nuclear factor-kB
Nox	Normoxia
NT-proBNP	N-terminal-pro-brain-type natriuretic peptide
P/S	Penicillin/streptomycin
PA	Pulmonary artery
PAB	Pulmonary arterial banding
PAH	Pulmonary arterial hypertension
PAI-1	Plasminogen activator inhibitor-1
PAPP-A	Pregnancy-associated plasma protein-A
PASMCs	Pulmonary arterial SMCs
PCR	Polymerase chain reaction
PE	Pulmonary embolism
PEA	Pulmonary endarterectomy
PAECs	Pulmonary arterial ECs
Pen Strep	Penicillin Streptomycin
PH	Pulmonary hypertension
PI3K/AKT	Phosphatidylinositol 3-kinase/protein kinase B
PPAR	Peroxisome proliferator-activated receptor
PPARG	PPAR gamma
PTE	Pulmonary thromboendarterectomy
PTGS2	Prostaglandin-endoperoxide synthase 2
qRT-PCR	quantitative reverse transcription-polymerase chain reactions
RA	Right atrium
RHC	Right heart catheterization
RAGE	Receptor for advanced glycation end products
RV	Right ventricle
RVEF	Right ventricular ejection fraction
RVH	Right ventricle hypertrophy
PVR	Pulmonary vascular resistance
RVSP	Right ventricular systolic pressure
RV/LV+S	Right ventricle/ (left ventricle+ septum)
RV-RWT	RV relative wall thickness
qRT-PCR	Quantitative real time-PCR
RIPA	Radioimmunoprecipitation Assay
SDS	Sodium dodecyl sulfate
SELENBP1	Selenium binding protein 1
SERPIN	Serine protease inhibitor
SERPINA3	Serpin family A member 3
SERPINA5	Serpin family A member 5
SERPINE1	Serpin Family E Member 1
siRNA	small-interfeing RNA
SLC4A1	Solute carrier family 4 member 1
SMCs	Smooth muscle cells
SNCA	Synuclein alpha

SOCS3	Suppressor of cytokine signaling 3
SOD3	Superoxide dismutase 3
sPAP	systolic pulmonary artery pressure
SPARCL1	SPARC like 1
TAPSE	Tricuspid annular plane systolic excursion
STAC2	SH3 and cysteine-rich domain 2
STEPA4	Six-Transmembrane Epithelial Antigen Of Prostate 4
TAPSE/sPAP	The ratio of tricuspid annular plane systolic excursion to systolic pulmonary artery pressure
TAZ	Transcriptional coactivator with PDZ-binding motif
TAC	Transverse aortic constriction
TEMED	N, N, N', N'-tetramethylethylenediamine
TF	Tissue factor
TGF-β1	Transforming growth factor beta 1
TNF-α	Tumor necrosis factor-alpha
TNS	Trypsin Neutralization Solution
tPA	Activity of tissue-type plasminogen activator
Trypsin/EDTA	Trypsin/Ethylenediaminetetraacetic Acid
uPA	urokinase-type plasminogen activator
VEGF	Vascular endothelial growth factor
VET	Venous thromboembolism
VSIG4	V-set and immunoglobulin domain containing 4
vWF	von willebrand factor
YAP	Yes-associated protein
β-ME	β-mercaptoethanol

1. Introduction

1.1. Pulmonary vascular system and right ventricle

The pulmonary vasculature has a distinctive function, structure, and volume. The main function of pulmonary circulation is transferring blood between the heart and the bronchial circulation for the gas exchange to supply the oxygenated blood to the conducting airways, pulmonary arteries, and veins. The developmental changes in prenatal to postnatal life are associated with significant changes in the pulmonary vasculature. The expansion of the pulmonary vasculature leads to the adjustment of cardiac output (CO) and maintains high blood flow with low pressure in intravascular arteries. Pulmonary vascular resistance (PVR) is about one-tenth of the resistance of the systemic circulation. This difference is attributed to the increase in endogenous vasodilators and the decrease in vasoconstrictor production (Suresh et al., 2016). The pulmonary vascular system is linked to the right-sided circulation providing a distinctive hemodynamic characteristic that adapts to various circumstances (Chamarthy et al., 2018). Studying the interaction between the right ventricle (RV) and pulmonary vasculature is crucial to reveal cardiopulmonary function, dysfunction, and failure. Therefore, the RV and pulmonary vasculature have a supply-and-demand relationship. The RV's cardiac myocytes, dimensions, and geometry are considered a supply part, whereas the pulmonary vasculature's compliance and resistance are regarded as a demand part. Assessing the hemodynamics interaction between the RV and pulmonary vasculature via ventricular-vascular coupling is an excellent tool for understanding the pathology of pulmonary hypertension (Tabima et al., 2017).

1.1.1. RV and interventricular septum: Physiology and function

The development of the mammalian heart begins from the tubular structures and ends with the four-chambered organ that directs systemic and pulmonary circulation distinctively (Lamers et al., 2002). The RV and left ventricle (LV) differ functionally, anatomically, and electrophysiologically. The RV has a larger volume and thinner free wall than the LV. RV appears triangular when viewed from the front, and the heart has a sharp right edge when viewed from the apex. In the cross-sectional view, the RV looks like a crescent. The curvature of the interventricular septum (IVS) positions the RV outflow track to that of the LV, resulting in a crossover relationship between the RV and LV outflows. The absence of this crossover relationship is a sign of cardiac malformation. Due to the unique shape and position of the RV, it is necessary to monitor the heart with different echocardiographic windows (Ho et al., 2006; Molina et al., 2016). Interestingly, LV hypertrophy thickness the IVS, whereas RV hypertrophy

(RVH) only slightly affects the IVS. Therefore, the IVS behaves like LV (LekanneDeprez et al., 1998; Franco et al., 2006). Anatomically, the RV is divided into three components: the inlet, apical trabecular, and infundibulum (Geva et al., 1998). With its distinct mesenchymal and muscular parts, the IVS is responsible for separating the RV and LV. The muscular part originates from the ventricular wall as a myocardial outgrowth, and the mesenchymal part arises from the merging of the endocardial and atrioventricular cushions. Both RV and LV myocardial cells are involved in IVS formation, which is not fully understood and remains unexplored (Eisenberg et al., 1955; Franco et al., 2006).

1.1.2. Cell types in the adult heart

The adult human heart consists of 11 cell types including ventricular cardiomyocytes, atrial cardiomyocytes, fibroblasts (FBs), pericytes, endothelial cells (ECs), smooth muscle cells (SMCs), immune cells, mesothelial cells, neuronal cells, and immune cells (lymphoid and myeloid) (Litviňuková et al., 2020). Cardiomyocytes are the primary cell type that plays a crucial role in healthy and diseased heart conditions. Apart from the cardiomyocytes, FBs, ECs, and SMCs are the most prominent cell populations in the heart. FBs comprise up to two-thirds of the adult heart and play extensive roles in the biochemical, structural, electrical, and mechanical properties of the myocardium. They also play a significant role in both cardiac disease and repair. FBs are considered a source for targets in biochemical, mechanical, and electrical signaling pathways (Camelliti et al., 2005). ECs are associated with regeneration, post-myocardial infarction (MI) remodeling, regulation of vasomotor tone, and angiogenesis. Around 95% of ECs are blood-vascular and the rest are lymphatic. SMCs and pericytes control the blood flow in heart vasculature (Talman et al., 2018). The exact cellular composition of the RV remains unstudied. However, based on its particular embryologic, functional, and morphological characteristics, and the unique response to the disease condition various cell types are assumed to contribute to the RV. It is reported that the RV interstitium has a collagen-based matrix, and the cells, including FBs, vascular cells, and immune cells are enmeshed in this matrix. RV pressure overload is related to the expansion of FBs, activation of myofibroblast, secretion of extracellular matrix (ECM) proteins, and ECs as a source of endothelin 1(Frangogiannis 2017). The role of FBs originating from embryonic mesenchymal cells in the pathogenesis of fibrosis has been studied. However, several studies showed that FBs are derived from ECs and epithelial cells in fibrosis which is linked to endothelial-to-mesenchymal transition (EndMT) and epithelial-to-mesenchymal transition (EMT). Aberrant EndMT and EMT activation leads to collagen production in myofibroblasts and the progression

of tissue fibrosis (Yano et al., 2005; Horowitz et al., 2006; Krenning et al., 2010; Cufi et al., 2010; Senoo et al., 2010).

1.1.3. Chamber-specific gene expression pattern in the human heart

Transcriptional profiling of murine heart tissue using microarray technology identified a chamber-specific gene expression pattern for genes known to have a specific functional role in the heart, such as structural proteins, proteins in the Wnt pathway, and homeobox proteins. These data showed that fewer genes are differentially expressed between the LV and RV than between the atria and ventricles. Hierarchical clustering revealed a higher correlation in gene expression between the IVS and LV than between the LV and RV. Distinct hemodynamic forces in different heart chambers require transcriptional networks that preserve the heart chambers in the adult heart (Tabibiazar et al., 2003).

Human studies also confirmed the chamber-specific gene expression patterns in the heart. Human heart tissue (n = 8) obtained from the right atrium (RA), left atrium (LA), RV, LV, and IVS of non-failing human hearts, and analysis of paired ventricular and atrial samples (n = 40) identified 5,747 differentially expressed mRNA (>1.5 fold; with a false discovery rate [FDR] of < 0.05). In addition, 435 and 82 genes were differentially expressed between the RV and LV, respectively, and 201 were differentially expressed between the RV versus LV. Furthermore, the gene expression profiles were identical between the LA and RA, and similar between the LV, RV, and IVS. RA/LA grouping and LV/RV and IVS grouping by donor highlighted the heterogeneity between human heart samples (Johnson et al., 2018).

1.2. Pulmonary hypertension

Pulmonary hypertension (PH) is a cardiopulmonary disorder with multifactorial pathological mechanisms and clinical conditions. PH management requires a multidisciplinary team and an active interaction between patients and clinicians (Humbert et al., 2022). PH is a severe and progressive disease with increased mortality. PH affects about 1% of the global population, and its incidence increases with age, with more than 10% of older adults aged >65 years affected by PH. Additionally, at least 50% of patients with heart failure (HF) are affected by PH (Mandras et al., 2020). Chronic pressure overload, particularly due to increased afterload, leads to RV remodeling and hypertrophy. In PH pathogenesis, the progression of pulmonary vascular remodeling leads to the transition of the RV from adaptive to maladaptive remodeling and,

ultimately, RV failure, which is the leading cause of mortality in patients with PH (Simonneau et al., 2019).

1.2.1. PH classification

PH is categorized into five clinical subgroups and it is identified as a mean pulmonary arterial pressure (mPAP) of ≥20 mmHg at rest. The European Society of Cardiology (ESC) and the European Respiratory Society (ERS) recently updated the classification for diagnosing and treating PH (Table 1). The main reason for classifying PH is to ease the assessment of clinical conditions with identical pathophysiological mechanisms, hemodynamics, clinical specification, and therapeutic approaches (Humbert et al., 2022).

1.3. Chronic thromboembolic pulmonary hypertension

Chronic thromboembolic pulmonary hypertension (CTEPH) is classified as a group 4 PH (Humbert et al., 2022), and it is considered a unique form of pulmonary vascular disease arising from chronic obstruction of the pulmonary arteries (Lang et al., 2014). CTEPH is a life-threatening disease with high morbidity and mortality and leads to progressive right-sided HF. (Kim et al., 2019). The incidence of CTEPH is about 3 to 5 cases per 100,000 individuals per year. However, epidemiological studies have reported that the incidence of CTEPH will continue to increase its burden (Gall et al., 2017). Despite numerous studies on CTEPH, its pathogenesis and risk factors remain ambiguous (Lang et al., 2006). Several risk factors associated with CTEPH have been reported. A prior history of pulmonary embolism (PE), non-O blood group, thyroid disease, and thyroid dysfunction are considered as risk factors for CTEPH (Krieg et al., 2020). Another study identified, that age >70 years, a family history of venous thromboembolism (VET), chronic obstructive pulmonary disease (COPD), HF, and atrial fibrillation are risk factors for CTEPH (Martinez et al., 2018). Splenectomy (Zhang et al., 2021) and antiphospholipid syndrome (APS) (Rosen et al., 2022) are also considered risk factors for CTEPH.

Risk factors related to plasma proteins include the von Willebrand factor (vWF) which plays an important role in platelet adhesion (Manz et al., 2022), and the coagulation factor VIII, which was significantly elevated in patients with CTEPH compared to healthy controls (Bonderman et al., 2003). Patients with CTEPH were reported to have decreased ADAMTS13 levels and increased vWF levels (Newnham et al., 2019).

Table 1. Comprehensive classification of PH *[(Humbert et al., 2022) Reuse permission: License Number: 5658710171093]*

Group1: Pulmonary arterial hypertension (PAH)
1.1 Idiopathic
1.1.1 Non-responders at vasoreactivity testing
1.1.2 Acute responders at vasoreactivity testing
1.2 Heritable
1.3 Associated with drugs and toxins
1.4 Associated with:
1.4.1 Connective tissue disease
1.4.2 HIV infection
1.4.3 Portal hypertension
1.4.4 Congenital heart disease
1.4.5 Schistosomiasis
1.5 PAH with features of venous/capillary (PVOD/PCH) involvement
1.6 Persistent PH of the newborn
Group 2: PH associated with left heart disease
2.1 Heart failure (HF):
2.1.1 with preserved ejection fraction
2.1.2 with reduced or mildly reduced ejection fraction
2.2 Valvular heart disease
2.3 Congenital/acquired cardiovascular conditions leading to post-capillary PH
Group 3: PH associated with lung diseases and /or hypoxia
3.1 Obstructive lung disease or emphysema
3.2 Restrictive lung disease
3.3 Lung disease with mixed restrictive/ obstructive pattern
3.4 Hypoventilation syndromes
3.5 Hypoxia without lung disease (e.g. high altitude)
3.6 Developmental lung disorders
Group 4: PH associated with pulmonary artery obstructions
4.1 Chronic thrombo-embolic PH
4.2 Other pulmonary artery obstructions
Group 5: PH with unclear and/or multifactorial mechanisms
5.1 Haematological disorders
5.2 Systemic disorders
5.3 Metabolic disorders
5.4 Chronic renal failure with or without haemodialysis
5.5 Pulmonary tumour thrombotic microangiopathy
5.6 Fibrosing mediastinitis
PAH: pulmonary arterial hypertension; HIV: human immunodeficiency virus; PVOD: pulmonary veno-occlusive disease; PCH: pulmonary capillary haemangiomatosis; HF: heart failure.

1.4. CTEPH pathophysiology

In CTEPH pathophysiology, occlusions due to organized fibrotic clots in the pulmonary artery (PA) and secondary microvasculopathy are associated with increased PVR and a progressive increase in RV failure (Liu et al., 2022). In CTEPH, since the RV is mainly affected when the occlusion is in the central part of the PA, more than one-half of the pulmonary vascular bed is deprived of circulation (Lang et al., 2016). The yellowish fibrotic clots are attached to the pulmonary vessels and contain elastin, collagen, and inflammatory cells. Pulmonary vascular remodeling is important in CTEPH microvasculopathy, and the lesions induce small muscular pulmonary arteries <500 µm, capillaries, and veins. The severity of CTEPH microvasculopathy differs among patients with CTEPH and results in increased PVR in some patients and increased risk of poor outcomes after pulmonary endarterectomy (PEA). In addition, pulmonary reperfusion edema after PEA or balloon pulmonary angioplasty (BPA) is due to improved blood flow in some parts of the lung region with changes in microvascular (Simonneau et al., 2022). Inflammation and EC dysfunction are associated with CTEPH pathogenesis (Figure 1). Treating of ECs obtained from patients with CTEPH via PEA with the nuclear factor kappa B (NF-κB) signaling inhibitor Bay 11-7085 reduced pro-inflammatory factors in ECs (Smolders et al., 2021).

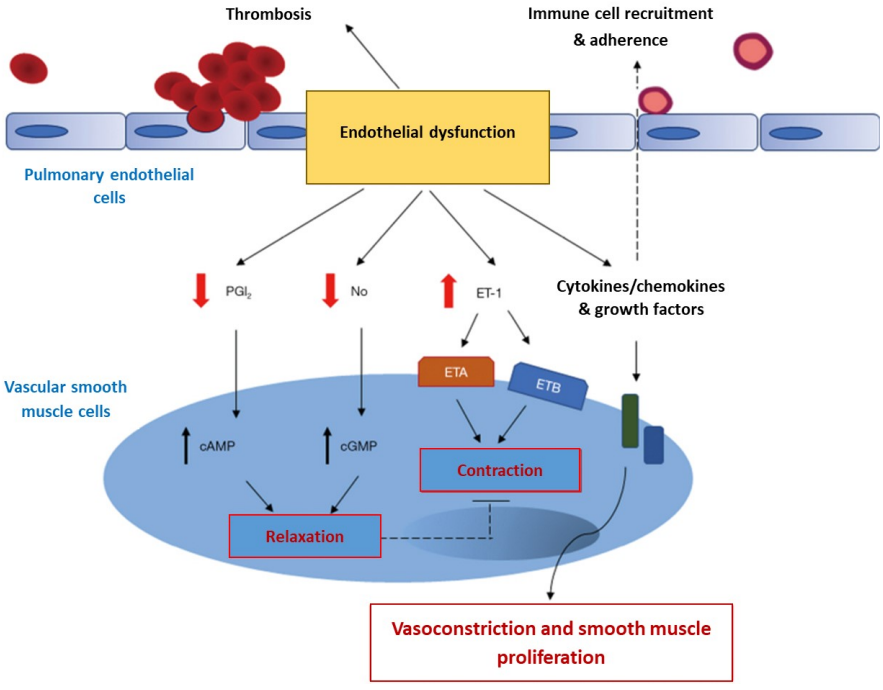

Figure 1. Potential role of impaired endothelium in CTEPH microvasculopathy. Impaired pulmonary endothelium results in altered equilibrium of vasoactive mediators such as NO, ET-1, and PGI_2 as well as cytokines, chemokines, and growth factors related to CTEPH microvasculopathy. CTEPH, chronic thromboembolic pulmonary hypertension; NO, nitric oxide; ET-1, endothelin-1; PGI2, prostacyclin. *[(Simonneau et al., 2022) Reuse permission: Distributed under the terms of the Creative Commons Attribution-NonCommercial-NoDerivatives 4.0 International License (CC BY-NC-ND 4.0)]*

Neutrophil extracellular traps (NETs) were found to be more common in patients with CTEPH. The NETs involved in monocyte differentiation and FB activation were used to resemble the cellular phenotype of FBs in PEA biospecimens from patients with CTEPH. RNA sequencing performed on FB isolated from the PA and PEA biospecimens from patients with CTEPH highlighted the role of neutrophils-mediated inflammation in enhancing transforming growth factor-beta (TGF-β) signaling pathways (Sharma et al., 2021). The contribution of both pulmonary arterial SMCs (PASMCs) and pulmonary arterial ECs (PAECs) in the remodeling of the proximal pulmonary vascular wall is based on the in vivo proliferation and migration responses of PASMCs and PAECs related to the PASMC proliferative phenotype (Quarck et al., 2012).

1.5. CTEPH diagnosis

CTEPH screening strategies are applied to patients with acute pulmonary embolism (PE), or those with or without a PE history. It is also recommended that the patient's susceptibility to CTEPH be assessed using the "CTEPH prediction score" (Table 2).

Table 2. CTEPH prediction score. *[(Ende-Verhaar et al., 2017) Reuse permission: License Number 5638200220913)]*

CTEPH prediction score	Score
Unprovoked PE	+6 points
Known hypothyroidism	+3 points
Symptom onset <2 weeks before PE diagnosis	+3 points
Right ventricular dysfunction on CT or TTE	+2 points
Known diabetes mellitus	-3 points
Thrombolytic therapy or embolectomy for the acute PE event	-3 points
Low risk: ≤6 points. High risk: >6 points. PE: pulmonary embolism; CT: computed tomography; TTE: transthoracic echocardiography.	

Based on the CTEPH prediction score, patients with >6 points are considered to have a high probability of developing CTEPH. In addition, if a patient presents with electrocardiographic criteria (right bundle branch block, R:S >1 in lead V1 with R>0.5 mV, and right QRS axis deviation >90°) and high N-terminal pro-B-type natriuretic peptide (NT-proBNP) levels, indicating RV pressure overload, they should be referred for transthoracic echocardiography (Boon et al., 2021; Verbelen et al., 2022). While the ventilation/perfusion scan is another screening method, it has high sensitivity and non-specificity, making additional diagnostic

modalities necessary (Tunariu et al., 2007). The gold standard method for diagnosing CTEPH is catheter-based pulmonary angiography, especially in combination with a right heart catheterization (RHC). Combining these two diagnostic modalities confirms the CTEPH to the sub-segmental vessels, precisely locating the lesions, and appraises RV function and pulmonary hemodynamics. Computed tomography pulmonary angiography (CTPA) in CTEPH diagnosis can provide detailed information regarding vascular wall thickness, intraluminal fibrosis, and most importantly, the patients's operability (Mahmud et al., 2018; Verbelen et al., 2022; Kiely et al., 2019).

1.6. Features of the RV and IVS in CTEPH

The main characteristic differentiating CTEPH from PE is the progressive increase in RV afterload as remodeling of small arteries results in an adaptive or maladaptive RV myocardium (McCabe et al., 2014). The pathophysiology of RV remodeling in CTEPH is illustrated in Figure 2. Three-dimensional hemodynamics were used to compare the RV and LV in subjects without a history of cardiovascular disease. It revealed an end-systolic volume of 82.1 vs 52.6 mL, an end-diastolic volume of 174.9 vs 143.6 mL, an end-systolic volume index (ESVI) of 93.3 vs. 75.8 mL/m^2, and an RV ejection fraction (RVEF) of 57.9 % vs. 63.8%, respectively (Lin et al., 2008). In healthy subjects, the IVS has a right-sided convexity. Increased RV strain either flattens the right-sided convexity or converts to left-sided convexity, leading to an alteration in CO. Patients with an mPAP ≥ 30 mmHg had a bowing IVS (An et al., 2022). RV adaptation is heterogeneous in patients with CTEPH, underscoring the importance of personalized medicine. The lower PAP observed in patients with CTEPH (45±11mmHg) than in those with pulmonary arterial hypertension (PAH; 50 ± 13 mmHg) might be important in driving RV adaptation (Quarck et al., 2009). Another study showed that both the PVR and mPAP are higher in patients with CTEPH (547 ± 242 dyn.s^{-1}.cm^{-5} and 43 ± 10 mmHg) than those with chronic thromboembolic pulmonary disease (CTEPD) (124 ± 39, dyn.s^{-1}.cm^{-5} and 17 ± 5 mmHg), highlighting the heterogeneity in terms of RV dysfunction in patients with CTEPH (McCabe et al., 2014). Another study compared patients with CTEPH with those with idiopathic PAH (IPAH) revealing that those with CTEPH had a higher RV end-diastolic volume index (EDVI) (87 ± 27 vs. 82 ± 25 mL), mean-right atrial pressure (8 vs. 7 mmHg), and lower RV relative wall thickness (0.6 ± 0.1 vs. 0.7 ± 0.2 g/mL). It also found that, the LV ejection fraction (60 % ± 10 % vs. 61% ± 10 %) and cardiac index (CI; 2.5 ± 0.8 vs. 2.5 ± 0.8 L/min/m^2) were identical in patients with CTEPH and IPAH. Additionally, it found that the RV was more dilated in patients with CTEPH than those with IPAH. Moreover, different RV afterload responses

occur in patients with CTEPH and IPAH due to RV diastolic stiffness, indicationg that other factors might contribute to RV pathophysiology in CTEPH compared to IPAH. Furthermore, this study suggested that the instantaneous increase in RV afterload in patients with CTEPH leads to various responses. However, the increased pulmonary pressure at diagnosis in patients with IPAH, explains the deliberated progression of RV remodeling compared to the abrupt RV remodeling and failure in patients with CTEPH (Braams et al., 2021).

The consistent relationship between PVR and pulmonary artery compliance is investigated through the pulmonary circulation time constant (RC). Therefore, RC is the product of PVR by pulmonary artery compliance, which represents the exponential pressure decay in the pulmonary artery during diastole. The significantly lower RC in patients with CTEPH than those with IPAH corresponds to a quicker pressure decay in diastole, followed by a broader pulse pressure and greater RV workload for a given mPAP (MacKenzie Ross et al., 2013).
The naive RV adaptation in patients with CTEPH could be explained by the late and prolonged appearance of RV dysfunction and the specific changes related to pulmonary circulation in CTEPH (Fukumitsu et al., 2020). RV adaptation and high contractility are necessary for RV outflow. Moreover, RV adaptation requires greater vascular bed space, higher oxygen demand, and lower mechanical output from the RV. RV dilatation leads to the bowing of the IVS in the LV direction. IVS bowing reduces LV preload, LV output, and systemic arterial pressure (An et al., 2022).
The importance of investigating the IVS in patients with CTEPH was highlighted in different studies because the IVS configuration was crucial for predicting PH severity. Echocardiography of IVS curvature was used to investigate the systolic PAP via RHC (sPAP $_{RHC}$). One study compared $sPAP_{RHC}$ estimated based on echocardiographic IVS curvature ($esPAP_{CURV}$) and left ventricular eccentricity index ($esPAP_{LVEI}$) to $sPAP_{RHC}$ estimated, using tricuspid regurgitant pressure gradient ($esPAP_{TRPG}$). It found that $esPAP_{CURV}$ is helpful in assessing the $sPAP_{RHC}$ for patients with CTEPH, especially in those with difficulties using TRPG (Matsumura et al., 2021).

The IVS is crucial in cardiac function and is associated with both RV and LV structure and function. Conditions that affect the IVS result in serious problems with ventricular arrhythmias and pump failure. Several non-invasive methods can be used to evaluate the IVS. However, it is challenging to identify the main causes of IVS pathology, especially hypertrophy, in older adults since they overlap with genetics (Triposkiadis et al., 2022). Measuring the septal angle

using CTPA is beneficial for assessing PVR in patients with CTEPH since it is an independent variable that correlates positively with the PVR (Liu et al, 2012).

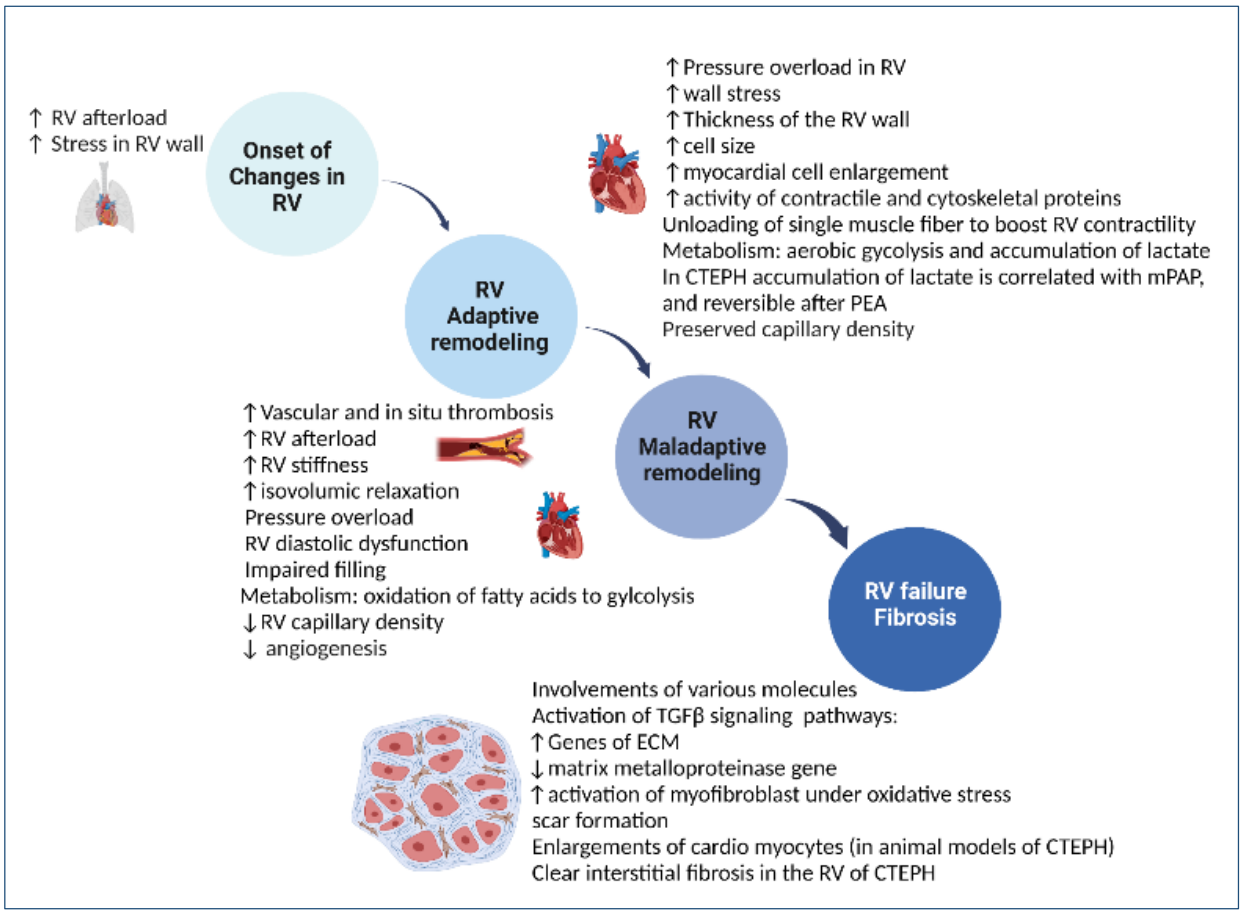

Figure 2. The pathophysiology of RV remodeling in CTEPH. The transition of the RV from the onset of the changes, remodeling (adaptive and maladaptive), and end-stage of HF (fibrosis). Abbreviations: RV, right ventricle; mPAP, mean pulmonary arterial pressure; PEA, pulmonary endarterectomy; CTEPH, chronic thromboembolic pulmonary hypertension; TGF-β, transforming growth factor-beta; ECM, extracellular matrix. The figure created with BioRender.com based on data from Simonneau et al., 2017; van de Veerdonk et al., 2016; McCabe et al., 2014; Gerges et al., 2020; Delcroix et al., 2013; Leask et al., 2015; Asona et al., 2019; Lopez et al., 2021; Noly et al., 2015; Arias-Loza et al., 2016; Sakao et al., 2015; Sutendra et al., 2013; Ryan et al., 2015.

1.7. Treatment approaches for CTEPH

A multidisciplinary team is required to treat CTEPH, which consists of a combination of PEA, BPA, and medical therapies based on occlusions in the proximal or distal area of the pulmonary arteries and the microvasculopathy, respectively (Humbert et al., 2022). Figure 3 illustrates various treatment modalities in CTEPH (Guth et al., 2022). All patients with CTEPH should receive systemic anticoagulation such as warfarin and direct oral anticoagulants, to prevent thromboembolic events (Kim et al., 2019; Delcroix et al., 2016; Matusov et al., 2021).

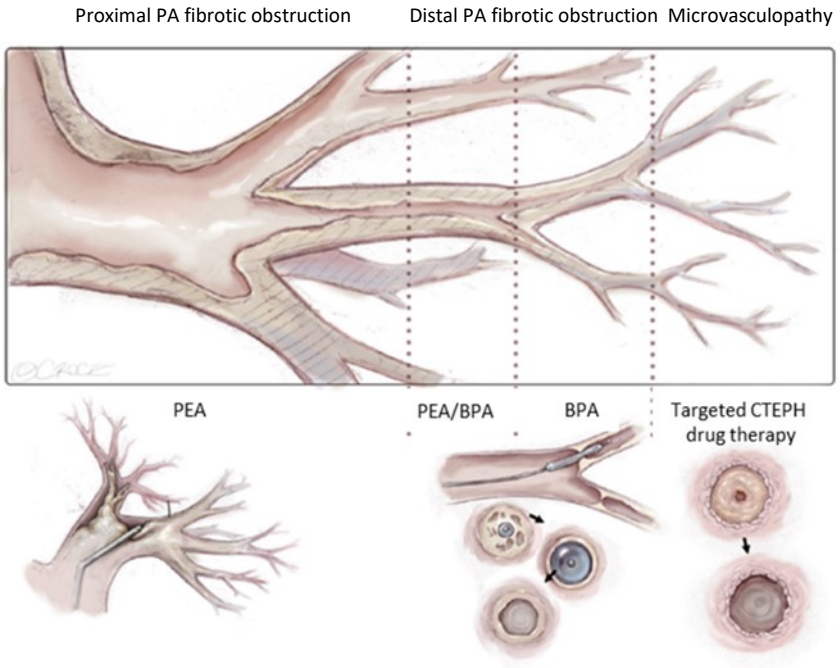

Figure 3. Schematic representation of therapeutic approaches for CTEPH. PEA is the treatment of choice for removing occlusions in the proximal area of pulmonary arteries, while, BPA is used to remove occlusions in the distal part of pulmonary arteries. Targeted medical therapy is used to treat inaccessible occlusions in the microvasculature. Abbreviations: PA, pulmonary artery; PEA, pulmonary endarterectomy; BPA, balloon pulmonary angioplasty [(Guth et al., 2022) Reuse permission: Beth Croce / Bioprespective kindly granted to reuse the image for the thesis. Credit: ©Beth Croce]

1.7.1. Pulmonary endarterectomy

Pulmonary endarterectomy (PEA), also known as pulmonary thromboendarterectomy, is a potentially curative treatment for operable CTEPH patients. A multidisciplinary CTEPH team selects the patients for surgery based on an evaluation of their operability and the risks and rewards of surgery (Verbelen et al., 2022). Thrombotic occlusions in the proximal segment of the PA are removed by PEA (Matusov et al., 2021). The operability of CTEPH patients mostly

depends on the accessibility of PA lesions and is associated with a correlation between PH severity, degree of occlusion, and multiple chronic conditions (Madani et al., 2012).

1.7.1.1. The effect of PEA on right heart function

Magnetic resonance imaging (MRI) data for patients with CTEPH before and after PEA revealed significant decreases in mPAP and a significant increase in six-minute walk distance (6MWD) was achieved at the 5-month follow-up (Czerner et al., 2020). After PEA, there is significant attenuation in both mean PAP (by about 21 mmHg) and PVR (by about 561 $dyn.s^{-1}.cm^{-5}$) compared to pre-PEA values. Inversely, the 6MWD increased significantly after PEA (Hsieh et al., 2018). Additionally, reductions in RV afterload, the rescue of IVS asynchrony, and improvements in RV systolic wall stress have been reported after PEA. The mass of the RV was improved two weeks after PEA. Tricuspid annular plane systolic excursion (TAPSE), and ESVI can be rectified after one year but cannot return to normal and healthy conditions. These parameters are not fully restored after PEA because of a possible persistent increase in RV afterload that reverses RV function and reduces PA compliance. Therefore, different treatment strategies should be applied in cases with persistent RV afterload (Liu et al., 2022; Ghio et al., 2020; Czerner et al., 2020).

1.7.2. Balloon pulmonary angioplasty

Balloon pulmonary angioplasty (BPA) is considered a treatment option for patients with CTEPH who are inoperable or have persistent PH after PEA. The guidelines recommend BPA for those who are unable to undergo PEA and/or have persistent PH after optimal medical therapy (Mahmud et al., 2018). BPA is used to re-open PA obstructions to correct the blood flow and mainly to decrease the RV afterload. The main reasons for inoperability are the location of occlusions, especially in the distal part of pulmonary arteries, and persistent PH in patients after PEA. The occlusions are mainly located in the segmental and subsegmental parts of the PA, which are accessible with a 1.5 -2.0 mm balloon. The lesion morphology in patients with CTEPH undergoing BPA has yet to be comprehensively studied. The current assessment of these lesions is conducted by cone-beam computed tomography (CT). Among the different lesion forms, webs and slits are considered the main form in patients with CTEPH undergoing BPA. Complete obstruction by web lesions can be treated if the distal run-off is confirmed (Ogo, 2015).

1.7.3. Medical therapy

Optimal medical therapy is one option for inoperable patients with CTEPH. However, its results before PEA are controversial, and it appears that the delay in surgery does not benefit these patients (Castro et al., 2020; Matusov et al., 2021). Various randomized clinical trials have examined current medical therapy for CTEPH. The most common are the CHEST-1 and CHEST-2 studies on Riociguat, the MERIT-1 study on using Macitentan to treat inoperable CTEPH patients, the BENEFIT study on using Bosentan to treat hemodynamics, the AMBER-1 study on using Ambrisentan to treat inoperable CTEPH patients, and the clinical trials on Sildenafil, and subcutaneous treprostinil to improve the exercise capacity (Ghofrani et al., 2013; et al., 2015; Jais et al., 2008; Ghofrani et al., 2017; Suntharalingam et al., 2008; Sadushi-Kolici et al., 2019).

1.8. Role of transcription factors in CTEPH and RV remodeling

Many studies have examined the role of transcription factors in heart remodeling. Abnormal physiological conditions and various stimuli can activate a cascade of signaling pathways and transcription factors with sequence-specific DNA-binding domains that are involved in transcriptionally regulating genes and diverse cellular processes (Pullamsetti et al., 2016). Critical transcription factors related to myocardial hypertrophy include members of myocyte enhancer factor 2 (MEF2), nuclear factor of activated T-cells (NFAT), signal transducers and activators of transcription (STAT), small mothers against decapentaplegic (SMAD), serum response factor (SRF), natriuretic peptide A (NPPA/ANP), fatty acid oxidation (FAO), natriuretic peptide B (NPPB/BNP), forkhead box O (FOXO), myocardin related transcription factor (MRTF), and NK-2 transcription factor related locus 5 (NKX2-5/CSX). In addition, transcription factors related to heart fibrosis, including epithelial-to-mesenchymal transition (EMT) are the NFAT and SMAD families, SRF, transcription factor 21 (TCF21), and MRTF. Moreover, peroxisome proliferator activator receptor alpha (PPARA) is associated with energy metabolism during myocardial remodeling (Hong et al., 2022; Shimizu et al., 2016; Clapham et al., 2019).

1.9. Biomarker in CTEPH

Diagnostic and prognostic biomarkers for CTEPH are in high demand. The operable form of CTEPH is the only form of PH that is curable. However, finding biomarkers is crucial for inoperable CTEPH, which is associated with poor prognosis. The circulating biomarkers in CTEPH are summarized in Figure 4 (Zhang et al., 2019). The plasma levels of neutrophils, and neutrophil components- myeloperoxidase (MPO), matrix metallopeptidase 9 (MMP-9), activated MMP-9, and double-stranded DNA were significantly higher in patients with CTEPH than in healthy controls. Plasma DNase activity was significantly lower in patients with CTEPH than in healthy controls. However, plasma levels of citrullinated histone H3 did not significantly change between patients with CTEPH and healthy controls (Sharma et al., 2021). CXCL9 plasma levels were significantly higher in CTEPH patients than in controls. In contrast, the plasma levels of other inflammatory markers, such as interleukins 1 beta (IL-1B),6 (IL-6), 8 (IL-8), and 10 (IL-10), as well as TGF-β and vascular endothelial growth factor (VEGF) did not differ significantly between patients with CTEPH and controls (Koudstaal et al., 2021). Correspondingly, plasma levels of C-reactive protein (CRP) were higher in patients with CTEPH than in controls (Quarck et al., 2009). In patients with CTEPH, high plasma levels of thrombin-activatable fibrinolysis inhibitor (TAFI) correlated with clot resistance to lysis (Yaoita et al., 2016). Another study found that serum levels of PAPP-A were significantly lower in patients with CTEPH after PEA and BPA surgery and PAPP-A plasma concentration did not correlate with patients' hemodynamic parameters (Kriechbaum et al., 2020). Another study used image-derived markers to differentiate between protein-based markers and images. They used CT images to identify biomarkers that predicted the development of CTEPH. They found that obstructive clots on the preliminary image were related to a higher risk of developing CTEPH (Lorenz et al., 2020). A retrospective study using a machine learning algorithm revealed that the RV to LV diameter ratio on CTPA was related to CTEPH severity and independently related to the post-PEA outcome (Shikhare et al., 2022). Our group identified cartilage intermediate layer protein 1(CILP1) as a biomarker of maladaptive RV in PH. CILP1 plasma levels were significantly higher in patients with PH and maladaptive RV than those with adaptive RV, dilated cardiomyopathy (DCM), and LV pressure overload (Keranov et al., 2021). Moreover, CILP1 plasma levels were significantly higher in patients with ischemic cardiomyopathy (ICM) than in the control group. High CILP1 levels in patients with ICM were related to high RV ESVI and NT-proBNP levels and low RVEF (Keranov et al., 2022).

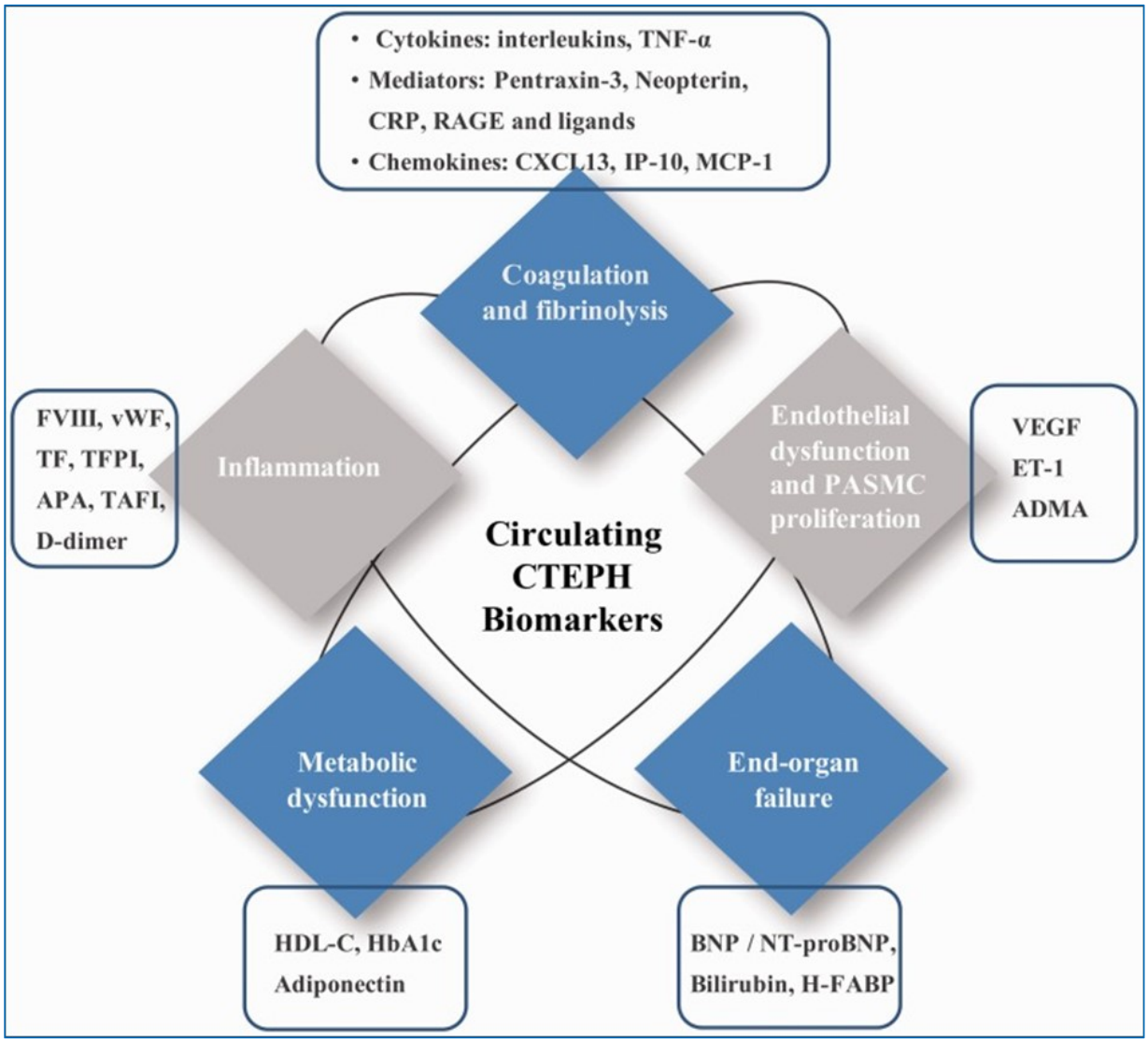

Figure 4. Circulating biomarkers for CTEPH. CTEPH, chronic thromboembolic pulmonary hypertension; PASMCs, pulmonary arterial smooth muscle cells; TNFα, tumor necrosis factor-alpha; CRP, C-reactive protein; RAGE, the receptor for advanced glycation end products; CXCL13, chemokine CXC ligand 13; IP-10, interferon-γ-induced protein-10; MCP-1, monocyte chemoattractant protein-1; FVIII, factor VIII; vWF, von Willebrand factor; TF, tissue factor;TFPI, tissue factor pathway inhibitor; APA, antiphospholipid antibody; TAFI, thrombin-activable fibrinolysis inhibitor; VEGF, vascular endothelial growth factor; ET-1, endothelin-1; ADMA, asymmetric dimethylarginine; HDL-C, high-density lipoprotein cholesterol; HbA1c, glycosylated hemoglobin A1c; BNP/NT-proBNP, brain natriuretic peptide/N-terminal-pro-brain-type natriuretic peptide Bilirubin; H-FABP, heart-type fatty acid-binding protein *[(Zhang et al., 2019) Reused permission: License Number 5638170400545]*.

1.10. Animal models of CTEPH

Since CTPEH pathogenesis is very complex, it cannot be studied using a specific animal model. Currently, rats, mice, rabbits, and hamsters are used to reproduce PE due to their accessibility and feasibility, but they have high fibrinolytic activity in plasma (Karpov et al., 2022). However, the lack of small or large animal models that mimic the clinical features of CTEPH hinders the progress in medical modalities for diagnostics and therapeutic approaches. Large animal models that mimic a successful clinical endpoint (RV failure) are rare, and most research groups failed before successfully reaching the endpoint (RV failure). In the canine model; RV remodeling and failure were reported when microspheres were injected into the pulmonary artery (Mulchrone et al., 2019). In another study, administering Alginate microspheres to rats induced CTEPH development through decreased exercise tolerance, increased RV systolic pressure (RVSP), and vascular remodeling (Karpov et al., 2021). A recent literature review comparing rodent models of CTEPH showed that rabbit models are more appropriate than other animal models due to their larger size and better resolution for magnetic resonance and X-ray techniques (Karpov et al., 2022).

1.11. Animal models of RV remodeling

Since PH is a heterogeneous and complex disease, diverse animal models are used to study its complexities. Various animal models include single-pathological-insult (SPI), multiple-pathological- insult (MPI), overexpression, and knockout are used. In SPI models one factor is used, such as monocrotaline (MCT) to simulate PH, while in MPI models, such as MCT plus, pneumonectomy, multiple factors are used to simulate more severe PH. For example, the pulmonary neointimal lesions in chronic hypoxia rat models are nearly identical to human plexiform lesions (Maarman et al., 2013; Abe et al., 2010). Pulmonary artery banding (PAB) models are used as RV pressure overload models without having any injury in pulmonary vascular. RV Maladaptive or failure occurs less frequently in PAB models than in hypoxia and MCT models. Comparing the differences in RV remodeling between chronic hypoxia and PAB models revealed that persistent and continuous pressure overload cannot lead to RV failure. Whereas in patients with PAH, excessive RVH and maladaptive RV lead to RV failure (Akazawa et al., 2020).

1.12. Available transcriptomic datasets for the human RV

The RNA-seq data for the RV of patients with HF and donors were compared to similar data for the human LV from another study. The bioinformatics analysis identified 130,790 transcripts and 800 -1000 differentially expressed genes (DEGs). The top 10 DEGs expressed explicitly in the RVs of patients with HF compared to donors were *SERPINA3*, *SERPINA5*, *LCN6*, *LCN10*, *STEAP4*, *AKR1C1*, *STAC2*, *SPARCL1*, *VSIG4*, and coagulation factor VIII (F8). Furthermore, *STEAP4*, *SPARCL1*, and *VSIG4* were identified as RV-specific biomarkers compared to LVs (di Salvo et al., 2015; Yang et al., 2014).

Another transcriptomic data set was created with adult patients with RV impairments (RVI) undergoing conduit surgery and infants with complex congenital heart disease (CCHD) undergoing tetralogy of Fallot (TOF) correction. The transcriptome profiling identified that the PPAR signaling pathway and retinol metabolism were significantly upregulated in patients with CCHD and RVI. Genes involved in retinol and PPAR signaling pathways were also upregulated, including *ADH1B*, *PPARG*, *MAOB*, and *SOD3* (Pollmann et al., 2021).

A recent study used an approach combining RNA-seq, tissue, and plasma proteomics to identify the biomarkers for RV remodeling. RNA-seq and tissue proteomics were carried out on the RV samples of patients with PH. The patients were classified as compensated RV (cRV), decompensated RV (dRV), and control (CTRL) based on their clinical parameters. The RNA-seq results showed 1226 transcripts differentially upregulated in dRV vs. CTRL, 766 in dRV vs. cRV, and 17 in cRV vs. CTRL. 1317 transcripts were differentially downregulated in dRV vs. CTRL, 905 in dRV vs. cRV, and 44 in cRV vs. CTRL. The top upregulated genes in cRV vs. CTRL were natriuretic peptide B (*NPPB*), natriuretic peptide A (*NPPA*), fibroblast growth factor 23 (*FGF23*), serpin family E member 1 (*SERPINE1*), C-C motif chemokine ligand 21 (*CCL21*), interleukin 6 (*IL-6*), cartilage oligomeric matrix protein (*COMP*), tenascin C (*TNC*), cellular communication network factor 2 (*CCN2*), and periostin (*POSTN*) which were mainly involved in inflammation and the ECM. The Proteome profiling of human RV tissue revealed 92 of proteins differentially upregulated in dRV vs. CTRL, 48 in dRV vs. cRV and, 1 in cRV vs. CTRL. In addition, 53 proteins were differentially downregulated in dRV vs. CTRL, 53 in dRV vs. cRV, and 3 in cRV vs. CTRL. The upregulated proteins dRV versus CTRL were POSTN, C-reactive protein (CRP), lactate dehydrogenase A (LDHA), latent transforming growth factor beta binding protein 2 (LTBP2), COL6A3, COL18A1, and TNC. Plasma samples from patients in the cRV PAH, dRV PAH, and CTRL groups were examined using the high-throughput multiplex Olink platform based on the proximity extension assay. The joint analysis

of these three data sets (RNA-seq and tissue, and plasma proteomics) revealed five shared genes: *COL18A1*, *LTBP-2*, *TNC*, *COL6A3*, and carbonic anhydrase 1 *(CA1*). Validation of *LTBP-2* in human RV failure and PAB and MCT animal models confirmed that its expression was significantly upregulated in dRV compared to CTRL (Boucherat et al., 2022).

1.13. Ankyrin Repeat Domain 1 (ANKRD1)

Muscle ankyrin repeat protein family (MARP) consists of three members: cardiac ankyrin repeat protein (CARP/ANKRD1), ankyrin repeat domain-containing protein 2 (ANKRD2/ARPP), and diabetes-associated ankyrin repeat protein (DARP/ANKRD23). They are expressed in the cytoplasm and the nucleus of cardiomyocytes and skeletal muscle cells and they play an important role in signal transduction. The expression of ANKRD1 is modulated under different pathological conditions. ANKRD1 interaction with tumor protein p53 (TP53) leads to its upregulation both in vitro and in vivo (Kojic et al., 2010). ANKRD1 has a special role in the development of heart chambers, and it regulates the cardiac homeobox gene *NKX 2-5*, which is downstream of cardiac gene expression and the cardiac muscle cell lineage marker. Experiments using three transgenic mice with various ANKRD1 promoter/lacZ constructs (p2.5 kb/lacZ, p0.295 kb/21 lacZ, and p2x 0.128 kb TATA/lacZ) and a lacZ/knock-in mouse revealed that ANKRD1 has a segregated 5' cis-regulatory elements that manage its chamber specific gene expression. The transgene was expressed in the whole heart, in both knock-in and p2.5 kb/lacZ mice, but only in the RV, in the p0.295 kb/21 lacZ mice, revealing the involvement of cis-regulatory elements in heart chambers (Kuo et al., 1999).

ANKRD1 is a transcriptional regulator that regulates phenylephrine, a hypertrophic regulator. ANKRD1 localizes with extracellular signal-regulated kinases 1/2 (ERK1/2) and GATA binding protein 4 (GATA4) in the sarcomeric complex region to increase the phosphorylation of GATA4 and the subsequent translocation of ANKRD1 to the nucleolus to activate hypertrophic gene expression (Zhong et al., 2015). ANKRD1 contributes to various signaling pathways such as TGF-β/SMAD and Hippo signaling pathways. It plays an important role in wound healing and stiffness. *ANKRD1* deletion causes wound contraction phenotype (Samaras et al., 2015; Bogomolovas et al., 2015).

The role of ANKRD1 in cell proliferation has been studied. Small-interfering RNA (siRNA) knockdown of *ANKRD1* in muscle satellite cells leads to larger cell clusters and increased proliferation than the control (Beyer et al., 2016). ANKRD1 is a downstream target of the TGF-β/SMAD signaling pathway (Kanai et al., 2001). It was recently reported that *ANKRD1* and *SERPINE1* are the target genes of yes-associated protein (YAP)/transcriptional coactivator with

PDZ-binding motif (TAZ) and siRNA knockdown of YAP/TAZ downregulated ANKRD1 and SERPINE1. Furthermore, YAP/TAZ siRNA knockdown with TGF-β1 inhibition resulted in the inhibition of *SERPINE1*, but not *ANKRD1*, and its expression depended on YAP/TAZ activity (Strippoli et al., 2020; Tang et al., 2022). While the role of ANKRD1 in tumor angiogenesis has not been fully elucidated, ANKRD1 has been associated with its role in angiogenesis via matrix metalloproteinase (MMP)-mediated ECM remodeling (Hooglugt et al., 2021; Shi et al., 2005).

1.13.1. Role of ANKRD1 in cardiovascular disease

ANKRD1 is a gene with various functions ranging from cardiac development to disease conditions including inflammation, wound healing, fibrosis, apoptosis, and adaptive and maladaptive remodeling (Murphy et al., 2020). The role of ANKRD1 in hypoxia is not fully understood. The expression pattern of *ANKRD1* in animal models was related to the degree of hypoxia and the species (Bank et al., 2010). Another study reported the correlated expression of hypoxia-inducible factor 1 alpha subunit (*HIF1A*) and *ANKRD1* ($r = 0.703$, $p = 0.001$; Shinjo et al., 2017). *ANKRD1* expression is elevated in HF and myocardial hypertrophy. Both cytosolic and sarcomeric translocation of ANKRD1 increases its role in the pathogenesis of hypertrophy. Mutations in *ANKRD1* are associated with hypertrophic cardiomyopathy with enhanced ANKRD1 stability, while the interaction between ANKRD1 and four-and-a-half LIM domains 2 (FHL2) was interrupted in DCM (Zhong et al., 2015). Furthermore, the identification of a heterozygous missense mutation in ANKRD, which is involved in the stretch-based signaling machinery, makes it a specific gene in patients with DCM (Moulik et al., 2009). Elevated ANKRD1 expression appears to indicate adverse clinical outcomes whereas it is unclear whether *ANKRD1* overexpression in hypertrophy is related to the maladaptive or adaptive response of the heart. While *ANKRD1* overexpression of is involved in hypertrophy, ANKRD1 cytosolic translocation is associated with the maladaptive response of the heart (Chen et al., 2014).

RNA-seq data for LV specimens from patients with DCM or ICM and controls showed that cytoskeletal genes exhibited consistent behavior in both DCM and ICM. Further analysis showed *ANKRD1* was upregulated in both the ICM (2.3-fold, $P<0.01$) and DCM (2.5-fold, $P<0.05$) compared to the control group. Furthermore, *ANKRD1* mRNA expression levels correlated with LV function and altered systolic and/or diastolic function, confirming the high levels of ANKRD1 in HF (Herrer et al., 2014).

1.13.2. Role of ANKRD1 in pulmonary hypertension

Affymetrix gene expression analysis was performed on the explanted lungs of patients with pulmonary fibrosis (PF) and IPAH. Pulmonary arterial pressure (PAP) was measured before lung transplantation and the patients were classified into three groups based on their mPAP including severe PH (mPAP ≥ 40 mm Hg), intermediate PH (mPAP 21-39 mm Hg), and noPH (mPAP ≤20 mm Hg). The bioinformatics analysis showed that the upregulated genes in severe PH are associated with vascular remodeling and myofibroblast activation and proliferation. The upregulated genes in the no PH group were related to proinflammatory markers. Bioinformatic analysis identified 222 differentially expressed genes between severe PH and noPH groups, with 190 exhibiting higher expression in the severe PH group than in the noPH group. In contrast, 32 genes exhibited higher expression in the noPH group than in the severe PH group, including *ANKRD1* (D value = - 2.92; fold change vs the noPH group = - 2.56, q value = 0.025, fold change vs. IPAH group = 1.81, q value < 0.001) (Mura et al., 2012).

Another study examined the effect of moderate to severe PE using rat models to identify the effect of PE development on PH and the RV. The rat models were treated with 1.3 or 2.0 million microspheres/100 g body weight (referred to as PE1.3 and PE2.0, respectively), while the control rats group was treated with 0.15 mL/100 g of 0.01% Tween 20. The mean RVSP was 40 mmHg in the PE1.3 group and 50 mmHg in the PE2.0 group two hours after injection compared to 25 mmHg in the control rats group. Microarray analysis of RVs from the PE2.0 and control rats group at two hours post-injection revealed that while the gene expression patterns in the early stage of PE were not significantly changed, gene expression was decreased because of the trauma in the RV. Interestingly, only 11 genes were upregulated in the RV in the PE2.0 compared to the control rats group, of which *ANKRD1* was the most upregulated (p = 0.0386) (Zagorski et al., 2008).

A recent study integrated transcriptomic and proteomic approaches on RV samples categorized as cRV, dRV, and control based on patients' clinical parameters. Its bioinformatics analysis revealed that among the differentially upregulated proteins, ANKRD1 was upregulated in the dRV group compared to the control group (Boucherat et al., 2022).

1.14. Activating Transcription Factor 3 (ATF3)

ATF3 is a transcription factor and an ATF/cAMP-responsive element-binding (CREB) family member. It binds to the cAMP response element (CRE) in the promotors of interleukin 12B (*IL-12B/p40*), *CCL4*, *CCND1*, and *GADD153*. As the leucine zipper region of ATF3 is important

for making homo- and hetero-dimers with other proteins, such as activator protein 1 (AP-1) and CCAAT-enhancer-binding proteins (C/EBPs), it is also considered a member of the basic leucine zipper (bZIP) superfamily. JDP2 is a member of the bZIP family and a transcription factor that shares 90% identity with ATF3. The main differences between ATF3 and JDP2 are their regulatory form and bioavailability. *JDP2* is a ubiquitously expressed gene, whereas *ATF3* expression is undetectable in normal conditions but induced under physiological stimuli. JDP2 binds to the ATF/CRE element in the ATF3 promoter, suppressing *ATF3* expression. The double knockout of *ATF3* and *JDP2* in mice followed by transverse aortic constriction (TAC) surgery attenuated the maladaptive and hypertrophy condition in the heart and preserved contractility (Hai et al., 2010; Ku et al., 2020; Kalfon et al., 2019).

ATF3 is important in cell proliferation, apoptosis, migration, invasion, and angiogenesis. In vitro experiments using NP31/ATF3-Tet cells showed that ATF3 inhibits tubulogenic differentiation in ECs (Tamura et al., 2005; Chen et al., 2018; You et al., 2019; Okamoto et al., 2006). Acute exposure of ECs to hypoxia activated ATF3 via nitric oxide (Chen et al., 2008). One study showed that patients with high serum levels of ATF3 had a higher risk of colorectal cancer (Zhu et al., 2018).

ATF3 is involved in glucose homeostasis by modulating several mechanisms. In the liver, it inhibits gluconeogenesis by reducing gluconeogenic enzymes, such as fructose-1,6 bisphosphatase (FBP) and phosphoenolpyruvate carboxykinase (PEPCK). In adipose tissue, it downregulates solute carrier family 2 member 4 (*SLC2A4/GLUT4*), followed by adiponectin (*ADIPOQ*). In the pancreas, ATF3 increases the expression of the genes involved in peptide hormone synthesis (e.g., glucagon and proglucagon), apoptosis (e.g., BCL-2 interacting protein 3 [*BNIP3*]), and inflammation (e.g., *IL-6*, *IL-1B*, and C-C motif chemokine ligand 2 [*CCL2*]) (Ku et al., 2020).

1.14.1. Role of ATF3 in cardiovascular disease

ATF3 expression is very low under healthy conditions but elevated in various heart diseases (Hai et al., 2010). One study showed that deletion of *ATF3* in cardiomyocytes, followed by TAC surgery, resulted in a lower fibrotic response. Deletion of *ATF3* in activated cardiac FBs leads to a decrease in the hypertrophic gene expression (Soraya et al., 2020). Another study using conditional cardiac FB-specific ATF3 transgenic mice that had undergone TAC surgery found that cardiac FB-specific ATF3 bound to mitogen-activated protein kinase kinase 3 (*Map2k3*), increasing HF risk (Li et al., 2017). Recent cardiopulmonary bypass (CPB) studies have identified genes including *JUN*, *ATF3*, *EGR1*, and AP-1 are potentially involved in the

inflammatory response and post-surgical complications. (Qi et al., 2022). Another study found that ATF3 was detectable in the blood and urine, and its concentration was significantly high in patients who developed acute kidney injury after CPB compared to patients who did not develop acute kidney injury after CPB (Wu et al., 2021). ATF3 can be induced in vascular ECs by growth factors such as tumor necrosis factor-alpha (TNF-α) via the c-Jun N-terminal kinase (JNK) and ERK pathways (Inoue et al., 2004). ATF3 was recently reported to be among the major targets of the stiffness/Rac signaling pathway. The suppression of *ATF3* in mouse embryo FBs by ECM stiffness activated Rac via CCND1. Rac and Rho belong to the Rho family of GTPases and play important roles in mediating mechanical information from the ECM to cells (Dang et al., 2022).

1.14.2. Role of ATF3 in pulmonary hypertension

ATF3 dysregulation has been studied in pulmonary veno-occlusive disease (PVOD), which belongs to Group 1 PH. PVOD is related to a biallelic mutation in *EIF2AK4/GCN2*. *GCN2* deficiency attenuated the phosphorylation of ATF3-dependent p38 MAPKs in PVOD development. The p38 inhibitor SB203580 ameliorated the RV's hemodynamics and pulmonary vascular remodeling in rats with mitomycin C-induced PVOD (Chen et al., 2021). In another study, rat models have been used to study the effect of different treatment options on AFT3 expression. The rat models were classified as MCT (PH group), MCT plus aortocaval shunt (PH+shunt group), PH+shunt treated with prostacyclin analog iloprost (PH+shunt+Ilo group), and sham (control group). Increases in PAP and RVH were observed in the PH and PH+shunt groups, whereas a decrease in PAP without the effect on pulmonary vascular remodeling was observed in the PH+shunt+Ilo group. Microarray analyses of RV tissue from the rat models revealed that *ATF3* and *EGR1* expression was significantly higher in the PH+shunt and PH+shunt+Ilo groups than in the PH and CTRL groups. The higher ATF3 and EGR1 expression was related to flow-induced neointimal lesions, whereas in the PH group, it was related to enhanced mast cells (van Albada et al., 2010).

The nuclear transcription factor aryl hydrocarbon receptor (AHR) is important in the differentiation of different immune cells. To identify the role of AHR in PAH pathogenesis, AHR-dependent gene expression profiling was performed on peripheral blood mononuclear cells (PBMCs) from patients with Qing Dai-induced PAH and SU4516/hypoxia (SuHx) rats. Fifty-two upregulated genes were shared between the PBMCs of Qing Dai-treated patients and SuHx rats, including *CCL3*, *CCL2*, *IL-1B*, *EGR1*, *AFT3*, *PTGS2*, and *SOCS3* (Masaki et al., 2021).

1.15. Interleukin 7 Receptor (IL7R)

Interleukin 7 (IL7) is a member of the common γ-chain receptor (γc) family of cytokines and a shared receptor subunit of interleukins 2 (IL2), 4 (IL4), 9 (IL9), 15 (IL15), and 21 (IL21) (Wickham et al., 2007). IL7 is a cytokine secreted primarily by the thymus and bone marrow and secondarily by the spleen and lymph nodes. The organs producing the IL7 receptor (IL 7R) include the brain, skin epidermis, liver, and gut. IL7R is a heterodimeric receptor consisting of IL7Rα, encoded by the *IL7R* gene. Both IL7 and IL7R are involved in different disease pathogenesis induced by impaired lymphoid function. IL7 acts as a growth factor for T and B cells, and its regulatory role is already evident. Recently, the role of IL7 in the development of innate lymphoid cells (ILC) has been studied. The IL7 signaling pathway is crucial in the development of hematopoietic stem cells and common lymphoid progenitor cells. Lower *Il7r* expression levels in hypoxia-exposed rat catecholamine cells (PC-12) are calcium-dependent (Lu et al., 2009).

Experiments using *IL7R* knockout mice showed that IL7R is important in controlling lineage fate decisions for developing pre-T, pro-B, and ILC precursors in bone marrow. Development of pre-T cells to double-negative (DN)-1, 2, 3, 4, and single positive cells in the thymus depends on IL7R. The IL7 signaling pathway that promotes DN proliferation by regulating cell growth genes and inhibiting transcriptional repressor genes such as the BCL6 transcription repressor (Bcl6). In contrast, the proliferation of double-positive cells does not depend on IL7 signaling. ILCs are important in immune defense. IL7R is essential in the development of group 2 and 3 ILCs, and *Il7r* knockout mice completely lack these ILC sub-classes (Barata et al., 2019). The role of IL7R in T-cell acute lymphoblastic leukemia has been studied. High *IL7R* expression activated the phosphoinositide 3-kinase (PI3K)/protein kinase B (AKT) signaling pathway by upregulating the BCL2 apoptosis regulator (*BCL2*) (Silva et al., 2021).
The IL7/IL7R axis requires the AKT/NF-κB signaling pathway to activate cell migration (Qu et al., 2016). An anti-thymic stromal lymphopoietin (TSLP) monoclonal antibody inhibited IL 7Rα, blocking IL7 signaling in T cells ex vivo, reducing regulatory T cells and inhibiting effector T cells (Kern et al., 2016).

1.15.1. Role of IL7R in cardiovascular disease

IL7R plasma levels are elevated in patients with acute coronary syndrome. In addition, IL7R induced higher expression of inflammatory chemokines in PBMCs. Moreover, IL7R plasma levels were significantly reduced in HCs receiving a low dose of aspirin. However, aspirin did

not suppress IL7R secretion in patients with angina who had high IL7R plasma levels. Furthermore, IL7R plasma levels correlated significantly with plasma levels of prothrombin fragments and troponin I and serum levels of CRP (Damas et al., 2003).

Another study showed that after an MI, treatment with an IL7R antibody attenuated the lipid content of atherosclerotic plaques. Apolipoprotein E (*Apoe*) knockout mice with MI were found to have upregulated Il7 expression in cardiac tissue and increased inflammation in the aortic sinus. Interestingly, inhibition of IL7R reduced the lipid plague in the aortic sinus (Mihailovic et al., 2019).
The IL7 and IL7R signaling pathways are involved in cancer and chronic inflammatory and autoimmune diseases. Several clinical trials have examined therapeutically targeting the *IL7* and IL7R pathways (Cramer et al., 2016). One study showed that in rheumatoid arthritis, activation of proangiogenic factors by IL7 in endothelial cells and macrophages led to angiogenesis (Pickens et al., 2011). Coronary artery disease (CAD) is considered a chronic inflammatory disease, and IL7R has an important role in its development. In the Chinese Han population, those carrying the G allele (odds ratio [OR] = 1.20) or GG genotype (OR = 1.45) of the IL7R variant rs969129 had a higher genetic predisposition for CAD (Sun et al., 2020).

1.15.2. Role of IL7R in pulmonary hypertension

RNA-seq data for the RV of MCT-treated and SuHx rats revealed identical transcriptomic profiles. In both MCT-treated and SuHx rats, the top upregulated pathways in the RV were TNF-α signaling via NF-κB and the EMT, and the top downregulated pathways were fatty acid metabolism and oxidative phosphorylation. Validation of the RNA-seq data using quantitative reverse transcription-polymerase chain reactions (qRT-PCR) showed that the expression of IL 7R, which participates in TNF-α signaling via NF-κB, was significantly higher in SuHx compared to control rats, whereas IL7R expression did not differ significantly between MCT-treated and control rats (Park et al., 2021).

The plasma levels of IL7 were measured in children with and without PH. They were found to be significantly lower in blood collected from the superior vena cava, PA, and ascending aorta of children with PH compared to those without PH. In addition, IL7 plasma levels correlated negatively with the ratio of PVR to systemic vascular resistance (Diekmann et al., 2021).

Another study used microarrays to examine whole blood from patients with PAH, cystic fibrosis (CF), or pre-transplant COPD and HCs. Validation of the microarray results for patients with PAH or CF, HCs, and those with pre-transplant COPD identified three gene signatures related

to end-stage chronic respiratory diseases. The common signatures were T-cell factor 7 (*TCF7*) and *IL7R*. The mRNA levels of *IL7R* and *TCF7* were significantly lower in the PH, CF, and COPD groups than in the HC group. Downregulation of *IL7R* contributes to patients' susceptibility to infection (Chesne et al., 2014).

IL7R is connected to the proliferation of PASMCs. In addition, *Il7r* knockout and blocking IL7R using IL7R antibodies protected mice from hypoxia-mediated PH. Hypoxia exposure for four weeks followed by IL7R antibody treatment significantly reduced both RVSP (28.89 ± 0.87 vs. 34.43 ± 2.23 mmHg) and RVH (the ratio of RV to LV mass plus septum [RV/LV+S]: 0.290 ± 0.008 vs. 0.390 ± 0.014) compared to treatment with immunoglobulin G (Gao et al., 2016).

1.16. Inhibin Subunit Beta B (INHBB)

Inhibins and activins belong to the TGF-β family and are connected to various biological processes. The β subunit is shared by inhibins and activins. Inhibins are αβ heterodimers, and activins are ββ homodimers. Inhibin subunit beta B (INHBB) and inhibin subunit beta A (INHBA) are β monomers belonging to the inhibin group. The activin A and B complexes represent βA heterodimers and βB monomers, respectively. Activin C and activin E are also members of the activin family. Inhibin α is synthesized as a proprotein and contains a pro-domain and a mature domain. The cleavage of the proprotein by proprotein convertase contributes to the formation of inhibin A (αβA) and inhibin B (αβB) homodimers or heterodimers. The suppression of activin signaling is mediated by inhibin receptors, including type II and type III TGF-β receptors and betaglycan. Interestingly, activin A, B, and AB bind to betaglycan and type II and III TGF-β receptors, and inhibin competitively suppresses them. The suppression of activin signaling is associated with the single subunit of inhibin B and type II activin receptor. The single subunit of inhibin B is bound to betaglycan and directs the formation of the inactive inhibin-receptor complex. In addition to betaglycan, inhibin α and αβ can bind to activin receptor-like kinase (ALK), inhibiting activin signaling (Namwanje et al., 2016).

The structural resemblance between INHBB and other TGF-β families is based on the cysteine knot that preserves the cysteine between two subunits with a disulfide bond. Other similarities include the formation of dimers, bioactive peptides at the C-terminal, and intracellular similarities in signaling mechanisms (Risbridger et al., 2001). Simultaneous enhancement of INHBB and SRY-box transcription factor 9 (SOX9) showed that SOX9 regulates INHBB, and the SOX9/INHBB axis regulates renal fibrosis in humans (Sun et al., 2022).

INHBB is a secreted protein, and its secretion has been reported in patients with polycystic ovary syndrome (Tsigkou et al., 2008). One study investigated *INHBB* expression in cancer cell lines under hypoxia conditions, The Results showed no significant difference in *INHBB* expression under hypoxia and normoxia conditions (Horst et al., 2022).

1.16.1. Role of INHBB in cardiovascular disease

The role of INHBB in cardiovascular disease is poorly reported. One study conducted mRNA profiling of the dystrophin (DMD)-deficient mouse hearts (mdx). Their gene profiling data showed the activation of profibrotic genes such as NADPH oxidase 4 (*Nox4*) and lysyl oxidase (*Lox*), with fold changes of 3.47 and 3.44, respectively, compared to wild-type mice. The expression of *Inhbb* in the LV was 2.26-fold higher in old mdx mice than in wild-type mice (Spurney et al., 2008). Another study investigated the effect of physiological and surgical menopause on CAD markers. It showed a reduction in serum levels of inhibin A and B. Furthermore, INHBB serum levels were significantly higher in premenopausal women than in postmenopausal women (9.0 [0.5–33.0] ng/L vs. 0.5 [0.5–0.5] ng/L) (Verhoeven et al., 2009). A further study examined hypoplastic left heart syndrome (HLHS), a congenital heart defect characterized by the underdevelopment of the LV that leads to RV remodeling. The DEGs with a greater than two-fold difference between the HLHS-RV myocardium and normal RV and LV myocardium included *INHBB* (− 9.76 and −7.96), respectively (Ricci et al., 2010).

1.16.2. Role of INHBB in pulmonary hypertension

The mRNA levels of activins, inhibins, and follistatin (*FST*) were measured in idiopathic PF and control. The results of PCR array showed increased mRNA levels of *INHBB* and *FST*. Further analysis in animal models also showed that the mRNA levels of *Inhba*, *Inhbb*, and activin B are significantly higher in silica-exposed mice than in control mice (Myllärniemi et al., 2014). The mRNA levels of *INHBB* in ECs and SMCs isolated from different vascular beds, including human PAECs (HPAECs), coronary artery ECs (HCAECs), microvascular ECs in the dermis (HMVECs-D), and lung (HMVECs-L), and human PASMCs (HPASMCs), were compared. The mRNA levels of *INHBB* were markedly higher in HPAECs than in HCAECs, HMVECs-D, HMVECs-L, and HPASMCs (Ryanto et al., 2021). A recent study investigated the mRNA levels of INHBB in the RV of SuHx rat models of PAH given different treatments: vehicle (Veh), RAP-011 (2.5 mg/kg, subcutaneous, two times/week), sildenafil (30 mg/kg, per os, two times/day), and sildenafil+RAP-011. Their finding showed that the mRNA levels of *Inhbb* were significantly higher in the sildenafil group than in the RAP-011 and sildenafil+RAP-

011 groups. In contrast, the mRNA levels of *Inhbb* were significantly lower in the sildenafil+RAP-011 group than in the sildenafil and Veh groups. These results showed that activin receptor type IIA-Fc (ActRIIA-Fc) fusion can reverse RV remodeling in rats and be considered a therapeutic target (Joshi et al., 2022).

1.17. Serpin Family E Member 1 (SERPINE1)

SERPINE1, formerly called plasminogen activator inhibitor 1 (PAI1), belongs to the serine protease inhibitor (SERPIN) superfamily (Iwaki et al., 2012). A phylogenic and comprehensive alignment analysis of the SERPIN superfamily highlighted its structure-function relationships and conserved residues (Irving et al., 2000). The SERPIN superfamily is mainly involved in the physiological regulation of urokinase-type plasminogen activator (PLAU/uPA) and the activity of tissue-type plasminogen activator (PLAT/tPA) (Iwaki et al., 2012).

SERPINE1 is a secreted protein, and its structure consists of two interactive domains: a reactive center loop (RCL) in the C-terminal and vitronectin (VTN) binding sites in helixes D, E, and F in the N-terminal. The binding site for uPA/tPA is located in the RCL domain, contains the P1-P1′ peptide, and reacts with proteases. The cleavage of the P1-P1′ bond inactivates SERPINE1. SERPINE1 can be stimulated upon pro-fibrotic, pro-inflammatory, and pro-hormonal stimuli. Upon stimulation, SERPINE1 is secreted into the ECM, inhibiting uPA/tPA and then ECM degradation by suppressing the activation of MMPs. Plasmin and uPA/tPA are important in the cellular degradation of ECM proteins and tissue homeostasis. The proteolytic activities of uPA, tPA, plasmin, and MMP under normal conditions mainly depend on SERPINE1 whereas in disease conditions, high *SERPINE1* expression causes an accumulation of ECM proteins and collagen, leading to scars in the wound healing area. However, inhibiting SERPINE1 reduces wound closure (Simone et al., 2015). The binding of the active form of SERPINE1 to VTN prohibits its conversion to its latent state and reduces its binding to uPA/tPA. The interaction of SERPINE1 with uPA/tPA and lipoprotein receptor-related protein 1 (LRP1) results in its degradation (Rahman et al., 2020; Ghosh et al., 2012).

1.17.1. Role of SERPINE1 in cardiovascular disease

A systematic meta-analysis revealed that the highest quantile of blood levels of SERPINE1 was associated with CAD risk (Song et al., 2017). Elevated SERPINE1 and tPA levels in the blood of patients with acute ST-elevation MI were associated with abnormal glucose regulation

(Knudsen et al., 2011). Another study showed that SERPINE1 is secreted by impaired ECs in the resistance vessels of infarcted arteries into the coronary circulation (Shimizu et al., 2016).

While some studies have shown an association between the 4G/5G polymorphisms in SERPINE1 and coronary heart disease, others showed no association. A meta-analysis of 32 studies assessing common variants in *SERPINE1*, including the 4G/5G polymorphism, revealed no increased risk of MI in carriers of the 4G allele (OR = 1.07, 95% confidence interval = 0.99–1.16, p = 0.110) (Koch et al., 2010). Another meta-analysis of 19,559 subjects, including 10,796 from genome-wide association studies, examined associations between genetic variants and circulating levels of SERPINE1. Its results identified loci significantly associated with plasma levels of SERPINE1, including *SERPINE1*, basic helix-loop-helix ARNT like 1 (*BMAL1/ARNTL*), and mucin 3A, cell surface-associated (MUC3A/MUC3; Huang et al., 2012).

Immunohistochemistry analysis of the endomyocardial biopsies of patients with DCM and inflammatory DCM (DCMi; cluster of differentiation 3 [CD3]+ lymphocytes: >30 cells/mm2) showed significantly higher SERPINE1 levels in those with DCMi than with DCM (15.5% ± 0.4% vs. 1.0% ± 0.1%). High *SERPINE1* expression in patients with DCMi decreased cardiac fibrosis, TGF-β levels, and the number of activated cardiac FBs but increased the number of non-classically-activated M2 macrophages (Baumeier et al., 2021).

SERPINE1 was found to be a hypoxic molecule associated with abdominal aortic aneurysms (Teng et al., 2022). Moreover, activation of the advanced glycation end product (AGE)-AGE receptor (RAGE) signaling pathway activated the thrombogenic reaction in ECs via SERPINE1 and VEGF (Higashimoto et al., 2013).

1.17.2. Role of SERPINE1 in pulmonary hypertension

The micro RNA (miR)-17~92 cluster has been implicated in PH pathogenesis. Overexpression of the miR-17~92 cluster in PASMCs downregulated *SERPINE1*. SERPINE1 is also a target for miR-17~92 family members, including miR-19a/b. Interestingly, SERPINE1 has a miR-19a/b binding site in its 3′-untranslated region. MiR-17/20a are other members of the miR-17~92 cluster that can inhibit *SERPINE1* expression. These results showed that SERPINE1 acts as a miR-17~92 regulator and is important in the proliferation of PASMCs via SMAD family member 2 (SMAD2; Chen et al., 2018). A recent study applied various bioinformatics methods such as the R statistical software, STRING, DAVID, and Cytoscape to identify the potential mechanisms and biomarkers in PAH. It revealed various biomarker genes for PAH, including SLC4A1, AHSP, ALAS2, CA1, HBD, SNCA, HBM, SELENBP1, SERPINE1, and ITGA2B.

They also found significantly higher infiltration of immune cells such as monocytes, activation of natural killer cells, activation of memory CD4 molecule (CD4)+ T cells, and mast cells in the peripheral blood in patients with PAH than in HCs (Tang et al., 2022). Another study examined the transcriptomics of RV samples categorized based on the patients' clinical parameters into cRV, dRV, and CTRL groups. Its bioinformatics analysis revealed that SERPINE1 was upregulated in the dRV group compared to the cRV group, identifying it as a fibrosis marker (Boucherat et al., 2022). SERPINE1 is connected to the hypoxia-inducible factor 1 (HIF-1) signaling pathway, and the stimulation of primary human pulmonary FBs with TGF-β under hypoxic conditions increased the expression of *SERPINEI* (Senavirathna et al., 2020).

2. Aims and Objectives

CTEPH is a multifactorial disease with rapid RV remodeling leading to high morbidity and mortality. PEA is the only potentially curative treatment for operable patients with CTEPH. Patient's operability is determined by a multidisciplinary CTEPH team based mainly on the disease distribution (segmental vs subsegmental lesions), age, and concomitant disease. This study, investigated the gene expression profiles of hearts from patients with CTEPH, including the RV and IVS. The CTEPH cohort consisted of an exploratory and confirmatory cohort. The CTEPH cohort with biopsies from the RV free wall was considered as prePEA and the CTEPH cohort with biopsies from the IVS was considered as postPEA.

This study had the following aims:

- To classify patients with CTEPH in the exploratory and confirmatory cohorts before PEA (prePEA) into subgroups based on their clinical parameters and ESC/ERS guidelines.
- To discover the top regulated genes, Kyoto Encyclopedia of Genes and Genomes (KEGG) pathways, and gene ontology (GO) terms in the prePEA subgroups of the exploratory and confirmatory cohorts.
- To compare the gene expression profile of the prePEA subgroups in the exploratory and confirmatory cohorts.
- To validate the results of the exploratory cohort in the confirmatory cohort.
- To determine the effect of PEA on the clinical parameters of patients with CTEPH by comparing the prePEA and postPEA subgroups.
- To discover the top regulated genes, KEGG pathways, and GO terms between the prePEA and postPEA subgroups in the confirmatory cohort.
- To compare the gene expression profiles in prePEA and postPEA subgroups, focusing on paired patients.
- To discover the top common KEGG pathways and GO terms between the prePEA and postPEA subgroups.
- To correlate the clinical parameters of the patients with CTEPH with the expression profiles of candidate genes.

- To validate the candidate genes in human cardiac fibroblasts (HCFs) and human cardiac microvascular endothelial cells (HCMECs).
- To validate the candidate genes in HCFs and HCMECs stimulated by hypoxic, profibrotic, and proinflammatory stimuli.
- To investigate the effect of knocking down the candidate genes using siRNA on the proliferation of HCFs and HCMECs.
- To investigate the effect of knocking down the candidate genes using siRNA on HCFs proliferation and migration.
- To investigate the effect of knocking down the candidate genes by using siRNA on HCMECs angiogenesis.
- To investigate the effect of mechanical properties by the extracellular matrix (ECM) on the expression of candidate genes in HCFs.
- To validate the expression of candidate genes in MCT rat models compared to control rats.
- To correlate the gene expression profile of candidate genes with the hemodynamic parameters of MCT rat models and control rats.
- To validate the expression of candidate genes in PAB rat models compared to sham.
- To correlate the gene expression profile of candidate genes with hemodynamic parameters of PAB rat models and Sham

3. Materials and Methods

3.1. Materials

3.1.1. Reagents and chemicals

Table 3. List of reagents and chemicals

Reagent	Company
Acrylamide 30%	Sigma-Aldrich, Germany
Bovine serum albumin (BSA)	Carl Roth, Germany
Bromophenol Blue	Roche, Germany
Chloroform	Carl Roth, Germany
Dako fluorescence mounting media	Dako, Denmark
Dimethyl sulfoxide (DMSO)	Sigma-Aldrich, Germany
Ethanol absolute	Carl Roth, Germany
Glycine	Carl Roth, Germany
Goat Serum	Sigma-Aldrich, Germany
Halt Protease and Phosphatase Inhibitor Cocktail	Thermo Fisher Scientific, USA
Hydrochloric acid (HCl)	Carl Roth, Germany
Isopropanol	Carl Roth, Germany
iTaq™ Universal SYBR® Green Supermix	BioRad, USA
Lipofectamine™ 3000 Reagent	Invitrogen, USA
Matrigel® Growth Factor Reduced, Phenol Red-Free	Corning, USA
Methanol	Carl Roth, Germany
Milk powder	Carl Roth, Germany
N, N, N', N'-tetramethylethylenediamine (TEMED)	Sigma-Aldrich, Germany
Opti-MEM® I(1X)+GlutaMAX™	Gibco, Germany
Qiazol	Qiagen, Germany
Resolving Buffer, 1.5M Tris-HCL pH 8.8	BioRAD, USA
RIPA Lysis and Extraction Buffer	Thermo Fisher Scientific, USA
Rotiphorese® Gel 30(37.5:1)	Carl Roth, Germany
Sodium chloride	Carl Roth, Germany
Sodium dodecylsulfate 20% w/v (SDS)	Carl Roth, Germany
Stacking buffer, O.5M Tris-HCl pH-6.8	BioRAD, USA
Stripping buffer	Thermo Scientific, USA
Supersignal west femto	Thermo Scientific, USA
Tissue-Tek ® O.C.T.™	Sakura Finetek Europe, Poland
T-PER™ tissue protein extraction reagent	Thermo Fisher Scientific, USA
Tris-HCl (1.5 M, pH-8.9)	Amresco, Germany
Tris-HCl (2M, pH-6.8)	Amresco, Germany
Triton X-100	Carl Roth, Germany
Tween 20	Sigma, USA
β-Mercaptoethanol	Sigma-Aldrich, Germany
Normal Goat Serum	R&D Systems®, USA

3.1.2. Kits

Table 4. List of the used kits

Names	Company
Bio-Rad DC Protein Assay Kit 2	BioRad, USA
Brdu Incorporation assay kit	Roche, Germany
DuoSet ®Ancillary Reagent Kit 2	R&D Systems®, USA
DuoSet Elisa Development System ; Human Periostin/OSF-2	R&D Systems®, USA
DuoSet Elisa Development System; Human Serpine E1/PAI-1	R&D Systems®, USA
High-Capacity cDNA Reverse Transcription Kit with RNase Inhibitor	Thermo Fisher Scientific, USA
Human ANKRD1 (Ankyrin Repeat Domain 1) ELISA Kit	NOVUS Biologicals, USA
Human IL7R alpha/CD127 ELISA kit	Invitrogen, USA
miRNAeasy Microkit (50)	Qiagen, Germany
Precellys® Lysing kit	PeQLab, Germany
RNase-Free DNase Set	Qiagen, Germany
RNeasy® Mini Kit	Qiagen, Germany

3.1.3. Cell culture medium and reagents

Table 5. List of cell culture medium and reagents

Reagent	Company
Ascorbic Acid (AA)-500	PromoCell GmbH, Germany
Basic Fibroblast Growth Factor recombinant human (hbFGF-5)	PromoCell GmbH, Germany
Cryopreservation- Serum Free Medium (Cryo-SFM)	PromoCell GmbH, Germany
Dulbecco's phosphate buffer saline (DPBS)	Sigma, USA
Endothelial Cell Basal Medium MV2	PromoCell GmbH, Germany
Epidermal Growth Factor recombinant human (hEGF)-2.5	PromoCell GmbH, Germany
Fetal bovine serum (FBS)	Gibco®, UK
Fetal bovine serum (FBS)	ScienCell Research, USA
Fetal calf serum (FCS)-25	PromoCell GmbH, Germany
Fibroblast growth supplement (FGS)- 100X	ScienCell Research, USA
Fibroblast medium (FM)	ScienCell Research, USA
HEPES buffered Balanced Salt Solution (Hepes BSS)	PromoCell GmbH, Germany
Human cardiac fibroblast (HCF)	ScienCell Research, USA
Human cardiac microvascular endothelial cells (HCMEC)	PromoCell GmbH, Germany
Hydrocortisone (HC)-100	PromoCell GmbH, Germany
Long R3 Insulin-like Growth Factor-1 (R3IGF-1)	PromoCell GmbH, Germany
Penicillin/Streptomycin (Pen/Strep)	Gibco®, USA
Penicillin/Streptomycin (P/S) solution 100X	ScienCell Research, USA
Poly-L-Lysine	ScienCell Research, USA
Recombinant Human TNF-α	Peprotech, USA
Recombinant Human TGF-β1	Peprotech, USA
SupplementPack Endothelial Cell GM MV2	PromoCell GmbH, Germany
Trypsin-EDTA solution	Sigma-Aldrich, Germany
Trypsin/Ethylenediaminetetraacetic acid (EDTA)	PromoCell GmbH, Germany
Trypsin Neutralization Solution (TNS)	PromoCell GmbH, Germany
Vascular Endothelial Growth Factor recombinant human (hVEGF)-0.25	PromoCell GmbH, Germany

3.1.4. Other materials

Table 6. List of additionally used materials

Names	Company
Cell culture dishes (6cm, 10 cm)	Greiner bio-one, Germany
Cell culture dishes (6 well, 24 well, 48 well and 96 well)	Greiner bio-one, Germany
Cell culture flask, T-25, surface : standard, filter cap	SARSTEDT, Germany
Cell scraper	SARSTEDT, Germany
Centrifugal protein concentrators	Millipore, USA
CryoPure Tube	SARSTEDT, Germany
Filter tips (10, 100, 1000 µl)	Greiner bio-one, Germany
ibiTreat# 1.5 polymer coverslip, tissue culture treated, sterilized	Ibidi, Germany
Multiplate™ 96-Well Unskirted PCR Plates	BioRAD
Microseal B Adhesive Seals for PCR Plates	BioRAD, USA
milliTUBE 1 mL	Covaris, LLC, USA
Petrisoft ™ polystyrene dishes	Cell Guidance Systems, USA
Polyvinylidene fluoride (PVDF) membrane	Carl Roth, Germany
Precellys Tube with beads	PeQLab, Germany
QIAshredder	Qiagen, Germany
Real time PCR plates	BioRad, USA
SafeSeal micro tube	SARSTEDT, Germany
SafeSeal tube	SARSTEDT, Germany
Serological pipette	SARSTEDT, Germany
Triple-pure ™, high impact zirconium beads, Ø o.3 mm	Biozym, Germany
TT05 culture tubes	Covaris, LLC, USA
Tube 15 ml, 50 ml	Greiner bio-one, Germany
µ-Slide Angiogenesis, ibiTreat	Ibidi, Germany

3.1.5. Equipments

Table 7. List of the equipments

Names	Company
Bead bug 3 Homogenizer	Biozym Scientific, Germany
Cell culture incubator, Hera cell	Heraus, Germany
Centrifuge	Life Technologies, Germany
CFX 96™ Real Time PCR detection system	BioRAD, USA
CP02 cryoPREP Automated Dry Pulverizer (110V)	Covaris, LLC, USA
Homogenizers Precelly® 24	PeQLab, Germany
Image Quant LAS 4000	*GE* Healthcare, *Sweden*
KEYENCE Microscope	*KEYENCE, Germany*
Microplate reader Infinite 200	TECAN, Germany
NanoDrop 2000 Spectrophotometer	Thermo Scientific, USA
PCR thermocycler	Eppendorf, USA
Power supply	BioRAD, USA
Western blot chambers	BioRad, USA
Zeiss Primovert including Axiocam 208 color	Carl Zeiss Microscopy, Germany

3.2. Methods

3.2.1. Human heart tissue from the CTEPH cohort

The human heart samples from the RV and IVS were obtained from the patients with CTEPH at the Kerckhoff Heart and Thorax Center in Bad Nauheim, Germany, between 2016 and 2020. Each patient provided informed consent. This study was approved by the ethics board of Justus Liebig University of Giessen (AZ 44 /14, 144 /11, 145 /11, 146 /11, 199 /15) and conducted according to the declaration of Helsinki. The RV specimens were obtained from patients who underwent the PEA procedure at baseline (prePEA; $n = 75$). The RV biopsy was taken using a biopsy needle (1 mm) during the surgery, immediately following sternotomy and the patient's connection to the heart-lung machine, in the cooling phase as soon as the heart is fibrillating, before circulatory arrest and the endarterectomy procedure are performed. The septum biopsy from the IVS (pre-septal-PEA; $n = 3$) was taken one day before PEA. Additionally, the septum biopsy was taken from the IVS (postPEA; $n = 21$) 12 months after PEA. The septum biopsies were taken in the catheter lab while the patients were awake. The location and timing of the biopsies of the RV and septum of the patients with CTEPH are shown in Figure 5.

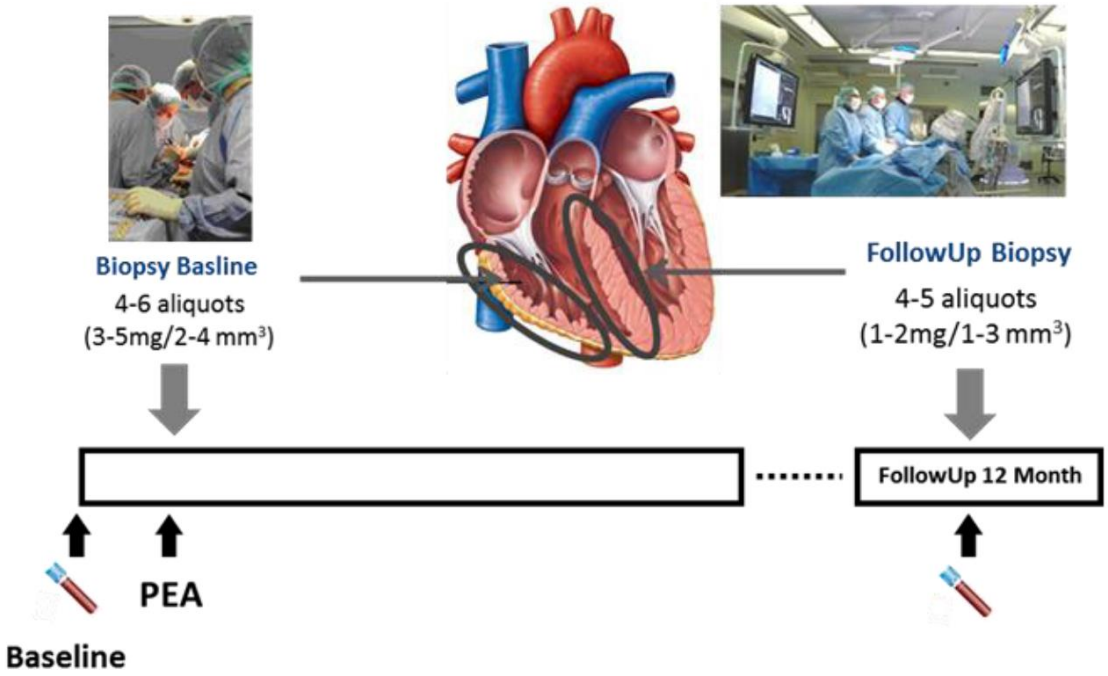

Figure 5. The location of RV (prePEA) and septum (postPEA) biopsies in the CTEPH cohort. RV biopsy was obtained before PEA, and the septum biopsy were obtained 12 months after PEA.

3.2.2. RNA isolation from the human RV free wall and IVS of patients with CTEPH

The RV biopsies were first cut longitudinally and then dissected horizontally. Both RV and septum biopsies were cut into 4 to 5 pieces and then stored in liquid nitrogen or as a paraffin section (Figure 6 A and B). RNA isolation was performed at the Deep Sequencing Platform Service Group at Max-Planck-Institute for Heart and Lung Research in Bad Nauheim, Germany, between 2017 and 2022 using two RNA isolation methods. The biopsy samples were stored in a liquid nitrogen tank and then transferred to the small, and portable liquid nitrogen tank for RNA isolation.

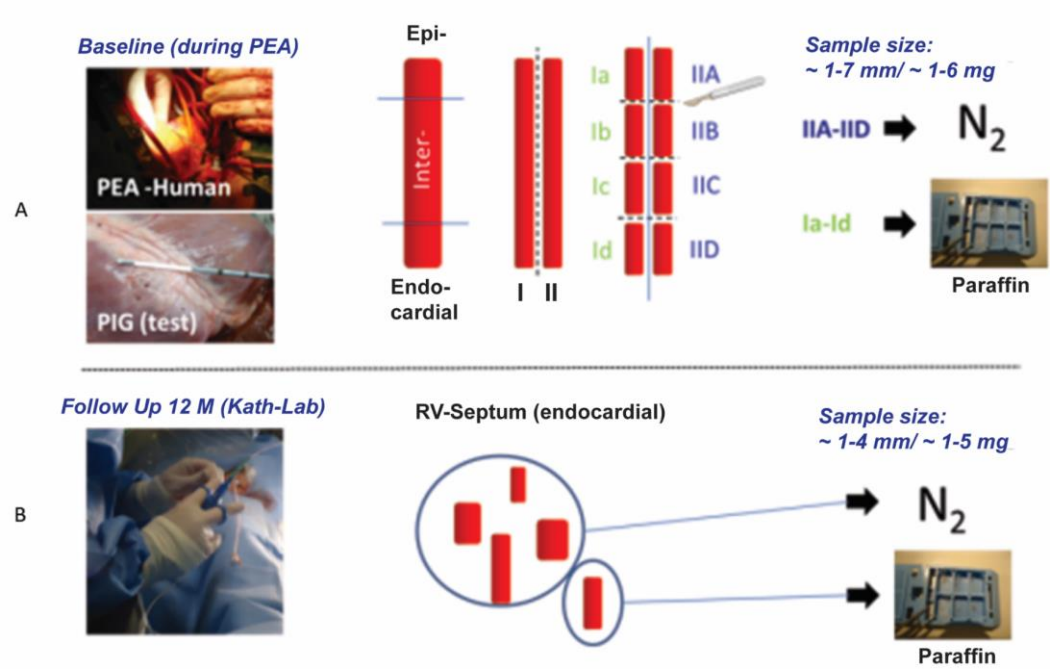

Figure 6. Biopsy procedure for the RV and septum of patients with CTEPH. (A) RV biopsy during PEA, and (B) septum biopsy 12 months after PEA.

3.2.2.1. Tissue homogenization using the bead beating method

The myocardial tissue samples were homogenized using the bead-beating method to lyse the samples and release the RNA. Briefly, the tissue samples were transferred to 2.0 mL non-skirted screw cap tubes containing Triple-pure™ high-impact zirconium beads (Ø = 0.3 mm) and 350 µL of QIAzol. Next, the tubes were placed on BeadBug 3 homogenizer, and tissue dissociation was performed at room temperature for two minutes at 400 revolutions per minute (rpm). Then, 350 µL of QIAzol was added to each tube before vortexing and brief centrifugation. Finally, the RNA was isolated using a miRNeasy Micro Kit (217084) according to the manufacturer's instructions. This RNA isolation method was used for nine RV tissue of the pre-PEA samples in the exploratory cohort.

3.2.2.2. Dry cryo-pulverization method

The dry cryo-pulverization method was used to isolate RNA from the heart tissue. In this method, biopsy samples were first transferred to a small, portable liquid nitrogen tank. Next, they were transferred to pre-chilled TT05 culture tubes, which were then screwed into 1 mL milliTUBEs. Then, the TT05 culture tubes were immediately snap-frozen in liquid nitrogen. Next, the TT05 culture tubes were placed on a CRYOPREP machine for pouching with CRYOPREP impact force set to level 3. Then, 700 µL of QIAzol was added to each TT05 culture tube and mixed with the tissue by pipetting up and down a few times. Finally, the RNA was isolated using a miRNeasy Micro Kit (217084) according to the manufacturer's instructions. This RNA isolation method was used for 71 pre-PEA RV samples and 21 post-PEA septum samples in the confirmatory cohort. Note that the exploratory cohort comprises nine patients, of which five overlapped with the confirmatory cohort. The total number of patients in each cohort, RNA isolation method, and RNA isolation data are shown in Table 8.

Table 8. The number of heart tissue samples in patients with CTEPH for RNA isolation

RNA isolation Method	CTEPH cohort	Type of sample	# samples	Date of RNA isolation
Beads beating homogenization	Exploratory	A-prePEA	9	2017-2018
Dry cryopulverization	Confirmatory	B-prePEA	71	2021-2022
		B-postPEA	21	2021-2022
		B-pre-septal-PEA	3	2021

3.2.3. Quality and Quantity of the isolated RAN from the samples

The RNA quality and quantity of the samples are very important to perform RNA sequencing. The size of the biopsy samples was around 0.001 to 0.01 grams and tried to obtain as much RNA as possible from these valuable samples. After RNA isolation the quality and quantity of the RNA samples were checked with different methods. RNA fragment size distribution was used to predict the quality of the samples. The total concentration of RNA samples was determined by the Qubit assay.

3.2.4. RNA sequencing

RNA sequencing was performed by the Deep Sequencing Platform Service Group at the Max Planck Institute for Heart and Lung Research in Bad Nauheim, Germany. The RNA-seq data for all patients with CTEPH has been deposited in the Gene Expression Omnibus database under

the accession number GSE249697. After isolation, the RNA samples underwent on-column DNase digestion to avoid genomic DNA contamination (DNase-Free DNase Set; Qiagen). Total RNA and library integrity were verified using a LabChip Gx Touch 24 nucleic acid analyzer (Perkin Elmer). About 100 ng of total RNA was used as input for the SMARTer Standard Total RNA Sample Prep Kit - HI Mammalian (Takara Bio). Sequencing was performed on an Illumina NextSeq 2000 system (P2 flowcell, v3 chemistry, and 1×72 bp single-end setup) or NextSeq 500 system (v2 chemistry, 1×75 bp single-end setup).

3.2.5. RNA-Seq analysis

Trimmomatic (version 0.39) was used to trim the reads based on a quality drop below a mean of Q15 in a 20-nucleotide window; only filtered reads longer than 15 nucleotides were retained (Bolger et al., 2014). The reads were aligned against the Ensembl human genome (version hg38, Ensembl release 104) using STAR (version 2.7.10a; Dobin et al., 2013). The aligned reads were filtered to remove duplicates with Picard (version 2.27.1). Gene counts were determined using featureCounts (version 2.0.2), considering only reads mapped to exons and aggregated per gene (Liao et al., 2014); reads overlapping multiple genes were excluded. The raw count was normalized using DESeq2 (version 1.30.1; Love et al., 2014). The groups were compared using DESeq2 based on the raw count matrix. DEGs were identified based on a mean expression ≥5 counts, $|\log_2$ fold change ($\log_2$FC)| ≥ 0.585, and *P* value ≤0.05. The Ensemble annotation was supplemented with UniProt data via the Ensemble gene identifiers (UniProt Consortium, 2014).

3.2.5.1. Downstream analysis of RNA-seq data

All downstream analyses were performed on the normalized gene count matrix. Volcano plots were generated to visualize DEG expression. A clustering heatmap of the samples was created based on the Euclidean distance of regularized logarithm transformation. Principal component analysis (PCA) as a dimension reduction analysis was performed on regularized logarithm-transformed count using an R package (Le et al., 2008). A maximum Benjamini-Hochberg corrected *P* value <0.05 was applied for the identified pathways. For further analysis, R (v4.2.0) and RStudio (v2023.03.0, Build 386) and several specialized R packages were used including:

- DESeq2 (v1.38.3) package for the differential gene expression analysis (Love et al., 2014) (Significant Genes = FDR < 0.05, $|\text{Log}_2\text{FC}| \geq 0.585$, base mean ≥5 and pathway analysis: all significant genes (FDR < 0.05)

- ClusteProfiler (v4.6.2) package for pathway analysis and enrichment analysis (for generating dot plots for GSE (KEGG and GO), bar plots/dot plots for OVA (KEGG/GO), a treeplots, and cnetplot (Wu et al., 2021; Yu et al. 2012)

- sva (v3.46.0), ComBat_seq () package for surrogate variable analysis and batchcorrection (Leek et al., 2022). The batch correction was applied to all the RNA-seq data analyses.
- Complexheatmap (v2.14.0) for Heatmaps (Gu, 2022; Gu et al., 2016)
- gplots (v3.1.3) -> Distance Matrix
- annotables (v.0.1.91) -> ensemble annotation tables; used for Gene Annotation
- EnhancedVolcano (v1.16.0) -> Volcanoplot

3.2.5.2. Pathway enrichment analysis:

Pathway enrichment analysis was carried out using Metascape (www.metascape.org). Pathway and process enrichment analysis was performed with the following ontology sources for each gene list: KEGG Pathway, GO Biological Processes, GO Cellular Components, GO Molecular Functions, Reactome Gene Sets, Canonical Pathways, CORUM, WikiPathways, and PANTHER Pathway. All genes in the genome were used as the enrichment background. Terms with a *P* value < 0.01, a minimum count of 3, and an enrichment factor > 1.5 were collected and grouped into clusters based on their membership similarities. Specifically, *P* values were calculated based on the cumulative hypergeometric distribution, and q-values were calculated using the Benjamini-Hochberg procedure to account for multiple testings. Kappa scores were used as the similarity metric when performing hierarchical clustering on the enriched terms, and sub-trees with a similarity of > 0.3 were considered a cluster. The most statistically significant term within a cluster was selected to exemplify the cluster. When multiple gene lists were provided, all lists were combined into one list called "_FINAL". A term may be found enriched in several individual gene lists and/or in the _FINAL gene list, and the best *P* value among them is chosen as the final *P* value (Zhou et al., 2019).

3.2.6. Cell culture

Cell culture experiments were carried out on human cardiac fibroblasts (HCFs) and -microvascular endothelial cells (HCMECs). HCFs were purchased from ScienCell Research laboratories and grown on poly-L-lysine (2µg/cm^2) coated dishes in Fibroblast medium (FM), supplemented with 2% FBS, 1% FGS, and 1% P/S solution provided by the company. HCMECs were obtained from PromoCell GmbH and maintained in Endothelial Cell Basal Medium MV2 supplemented with SupplementPack Endothelial Cell GM MV2 containing: FCS 0.05 mL/mL, hEGF 0.005 µg/mL, Hydrocortisone 0.2 µg/mL, hVEGF 500 ng/mL, hbFGF 0.01 µg/mL, R3IGF-1 0.02 µg/mL, Ascorbic Acid 1µg/mL and P/S containing penicillin 100 U/mL and streptomycin 0.1 mg/mL.

The cells were cultured at 37°C in a humidified chamber with 5% CO_2 until they reached 90-95% confluency for HCFs and 70-80% for HCMECs. For sub-culturing, the HCF cells were washed with DPBS and incubated with Trypsin/EDTA for 4-5 minutes. Trypsin/EDTA was neutralized by the addition of an equal volume of FCS, and for the HCMECs, PromoCell DetachKit was used. The cells were washed once with Hepes BSS and incubated with Trypsin/EDTA for 5-8 minutes followed by Trypsin Neutralization Solution (TNS). The HCF cells were centrifuged at 1200 rpm for 10 minutes and for HCMECs 220 x g for 3 minutes. The supernatant was removed, and the pellet was resuspended in a pre-warmed growth medium and plated according to the recommended seeding density into the new cell culture vessels. The medium was changed every two or three days. Cell freezing for HCMECs was performed using Cryo-SFM and for HCFs using 5% DMSO in FCS. When needed the cryovials were kept for two minutes in a water bath (37 °C) and the cells were transferred to the new cell culture vessels containing growth medium. The medium was replaced after 16-24 hours.

3.2.6.1. Treatment of human cardiac cells

HCF cells and HCMECs were seeded in 6 cm dishes and treated with different stimuli. Cells were kept in a serum starvation medium containing the corresponding basal medium, supplemented with 0.1% FBS and Pen Strep (penicillin 100 U/mL and streptomycin 0.1 mg/mL) for 24 hours, and then stimulated with varying concentrations of TGF-β1 (5, 10, and 50 ng), and TNF-α (5, 10, and 50 ng), for 48 hours.

3.2.6.2. Hypoxia treatment

For hypoxia treatment, HCFs and HCMECs were maintained in the medium supplemented with 1%FCS and 1% penicillin and streptomycin. The cells were kept in a humidified hypoxia chamber with 5% CO_2 and 1% O_2 at 37°C for 6h, 24h and 48 h. The normoxia condition was used as a control and the cells were maintained with the same medium in a cell culture incubator with 5% CO_2 and 21% O_2 at 37°C.

3.2.6.3. Enzyme-linked immunosorbent assay (ELISA)

Detection of the candidate proteins was conducted on cell culture supernatants by different ELISA kits according to the manufacturer's instructions. For SERPINE1 and PERIOSTIN DuoSet ELISA Development System (R&D System), ANKRD1 (Novus Biologicals), and IL7R(Invitrogen) were used. HCF cells and HCMECs were treated with different stimuli and supernatants were collected and centrifuged at 1000 x g for 20 minutes at 4 degrees.

3.2.6.3.1. DuoSet ELISA Development System

The ELISA plate was coated with the capture antibody and incubated overnight at room temperature. The wells were washed three times with washing buffer followed by blocking for 1h at room temperature. After the washing steps, 100 µl samples or standard were added and incubated for 2 hours at room temperature. The wells were washed, and the detection antibody (for SERPINE1 diluted with normal goat serum) was added to each well. After the washing steps, 100 µl Streptavidin-HRP was added to each well and incubated for 20 minutes in the dark at room temperature. The wells were washed and the Substrate solution (100 µl) was added to each well and incubated for 20 minutes in the dark at room temperature followed by adding a stop solution (50 µl) to each well. The optical density of each well was determined at 450 nm (nanometer) with the reference at 540 nm in the TECAN Infinite M200 plate reader. SERPINE1 concentration was plotted versus absorbance at 450 nm.

3.2.6.3.2. ANKRD1 (Novus Biologicals)

Standard and samples (100 µl) were added to each well and incubated for 90 minutes at 37°C followed by adding Biotinylated Detection Ab to each well and incubated for 1 h at 37°C. The wells were washed three times. HRP Conjugate was added to each well and incubated for 30 minutes at 37°C. After the washing steps, Substrate Reagent (90 µl) was added to each well and incubated for 15 minutes at 37°C followed by Stop solution (50 µl) to each well. The optical density of each well was determined at 450 nm in the TECAN Infinite M200 plate reader. ANKRD1 concentration was plotted versus absorbance at 450 nm. The detection range was 0.31-20 ng/ml.

3.2.6.3.3. IL7R (Invitrogen)

Standard and samples (100 µl) were added to each well and incubated overnight at 4° C followed by four times washing with wash buffer. Biotin Conjugated (100 µl) was added to each well and incubated at room temperature for 1 hour with gentle shaking. The wells were washed and Streptavidin -HRP solution (100 µl) was added to each well and incubated for 45 minutes at room temperature with gentle shaking. After the washing steps, TMB Substrate (100 µl) was added to the wells and incubated for 30 minutes at room temperature in the dark with gentle shaking. At the end stop solution (50 µl) was added to each well. The optical density of each sample was determined at 450 nm in the TECAN Infinite M200 plate reader. IL7R concentration was plotted versus absorbance at 450 nm. The minimum detectable concentration of IL7R is 0.14 ng/ml.

3.2.7. Animal experiments

All the animals (rats) were obtained from the project CP02, SFB CRC 1213 consortium. With the great support of project CP02 two independent groups of animals including monocrotaline (MCT) induced PH and pulmonary artery banding (PAB) rat models were included in this study. All the animal experiments were performed according to the National Institute of Health Guidelines on the Use of Laboratory Animals. The study protocols (GI 20/10 Nr G92/2017) were approved by the University Animal Care Committee and the Federal Authorities for Animal Research of the Regierungspräsidium Giessen, Hessen, Germany.

3.2.7.1. Experimental groups

In our study, 13 rats in the MCT group and 14 rats in the control group were included. Among them, there were 4 rats in the MCT group and 5 rats in the control group for the time point of 2 weeks, and for the 3 week time point, there were 4 rats in the MCT group and 5 rats in the control group. Finally, 5 rats in the MCT group and 4 rats in the control group were added for the time point of 5 weeks. One sample from the 3 weeks control group has been excluded from mRNA expression analysis of the target genes due to an extremely low RNA concentration.

Moreover, 8 rats in the PAB group and 8 rats in the sham group were included in the study. Specifically, there were 4 rats in the PAB group and 4 rats in the sham group for the time point of 35 days as well as 4 rats in the PAB group and 4 rats in the sham group for the time point of 53 days.

3.2.7.2. Pulmonary artery banding model (PAB)

The rats were anesthetized with subcutaneously analgesic buprenorphine hydrochloride (Temgesic ®, 0.1 mg/kg Sigma-Aldrich, Germany) and inhalation of 3-4% isoflurane mixed with oxygen. After intubation, the rats were connected to the ventilator, and the respiratory rate and the stork volume were adjusted based on the animal weight using MiniVent type 845 (Hugo Sachs Elektronik, March-Hugstetten, Germany). The left thoracic wall of the rats was depilated and disinfected with Braunoderm® (Braun, Melsungen, Germany), and a small incision of the skin was made at the axillary level. The thoracic muscles pulled apart to open the chest cavity by a small incision in the second intercostal space results in exposing the pulmonary artery, aorta, and left atrium. After the separation of the pulmonary artery from the aorta and left atrium, an L-shaped blunted needle was used around the pulmonary artery and tight against the needle. Titanium ligating clip (Hemoclip®, Edward Weck, and Research Triangle Park, NC, USA) was used to place around the pulmonary artery to produce 65-70 % constriction. The chest cavity was closed, and the muscles were put back in place. For the sham groups, dissection

of the pulmonary artery was performed by the L-shaped needle, without a ligating clip around the pulmonary artery and immediately was closed. After recovery from the surgery, the rats were kept in a standard rodent cage with free access to water and food at 23° C.

3.2.7.3. Monocrotaline (MCT)-induced PH rat model

Pyrrolizidine alkaloid MCT was dissolved in 1 mol/L HCL and the PH was adjusted to 7.4 with the final concentration of 20mg/ml. The adult rats were injected either with a single subcutaneous MCT (60 mg/kg body weight) or with the same volume of saline for the control group. Hemodynamic measurements and organ harvesting were performed on the 2 weeks, 3 weeks, and 5 weeks after MCT injection.

3.2.7.4. Hemodynamic, MRI, and RV hypertrophy measurements

All the invasive and non-invasive hemodynamics measurements were performed by SFB CRC 1213 consortium which is known as Project CPO2. The hemodynamics measurements were performed on the 2-, 3- and 5- weeks of MCT rats and for the PAB rats on the 35- and 53- days. The hemodynamic parameters include cardiac MRI, right heart catheterization, and RV hypertrophy measurements.

3.2.8. RNA isolation from the cells

Total mRNA was extracted from primary HCFs and HCMECs utilizing the RNeasy® Mini Kit. Media was aspirated, and the cells were washed with PBS. Then 350 µl RLT buffer (provided with the kit and supplemented with 1% β-ME) was added to the cells and lysates were loaded on QIAshredder for homogenization and centrifuged at high speed for 2 minutes at room temperature. An equal volume of 70% ethanol was added to the lysate, mixed, and transferred to the RNeasy Mini spin column. The column was centrifuged at 8000 x g for 15 seconds and the flow through was discarded. To each RNeasy Mini spin column, 350 µl buffer RW1 was added and centrifuged at 8000 x g for 15 seconds. DNase digestion was done by adding 70 µl of buffer RDD to 10 µl of DNase and then it was loaded on RNeasy Mini spin and incubated for 15 minutes at room temperature. Subsequently, 350 µl buffer RW1 was added and centrifuged at 8000 x g for 15 seconds. The flow through was discarded and the columns were washed two times with 500 µl of buffer RPE and centrifuged at 8000 x g for 15 seconds and 2 minutes. Finally, the RNeasy spin column was placed into a new 1.5 ml collection tube and 30 µl of RNase-free water was added to the center of the spin column membrane and centrifuged at 8000 x g for 1 minute. A NanoDrop 2000 Spectrophotometer was used to assess the RNA

concentration and purity. The RNA samples with a 260/280 ratio of around 1.8 were used for further experiments.

3.2.9. RNA isolation from the tissue

Total RNA was isolated from animal heart tissue using Qiagen RNeasy mini kit. 20 mg of heart tissue was transferred in a Precellys tube containing beads and 600µl of Qiazol. Precellys tubes were placed on the tissue homogenizer for 30 sec spins in two repeats. Afterward, the supernatant was transferred into a new tube. An equal volume of 70% ethanol was added to the lysate, mixed well, and transferred to the RNeasy spin column. The column was centrifuged at 8000 x g for 15 seconds and the flow through was discarded. To each RNeasy Mini spin column, 700 µl buffer RW1 was added and centrifuged at 8000 x g for 15 seconds. The flow through was removed and the columns were washed two times with 500 µl of buffer RPE and centrifuged at 8000 x g for 15 seconds and 2 minutes. Finally, the RNeasy spin column was placed into a new 1.5 ml collection tube and 30 µl of RNase-free water was added to the center of the spin column membrane and centrifuged at 8000 x g for 1 minute. A NanoDrop 2000 Spectrophotometer was used to assess the RNA concentration and purity. The RNA samples with a 260/280 ratio of around 1.8 were used for further experiments.

3.2.10. Reverse transcription of RNA

A total of 1000 ng of RNA was transcribed into complementary DNA using a High Capacity Synthesis Kit according to the manufacturer's instructions. The Reverse transcription master mix was prepared as follows:

Table 9. Composition of reverse transcription master mix

Component	Final concentration	Volume/ Reaction (µl)
10X RT Buffer	1X	2.0
25X dNTP Mix (100 mM)	4mM	0.8
10X RT Random Primers	1X	2.0
MultiScribe ™ Reverse Transcriptase (50U/µl)	50U	1.0
RNase Inhibitor (10 U/µl)	10U	1.0
Nuclease-free H_2O		3.2
Total volume of reaction		10.0

3.2.11. Quantitative real-time PCR

Quantitative real-time PCR (qRT-PCR) was performed from cDNA samples in 10 µl reactions using iTaq^{TM} Universal SYBR® Green Supermix. Intron-spanning human and rat-specific

primers genes were designed using sequence information from the NCBI database and were purchased from Metabion International AG (Martinsried, Germany) and Sigma-Aldrich, Merck KGaA (Darmstadt, Germany), respectively (Appendix, A-1 and A-2**)**. The PCR product size was 100-250 bp. The preparation of the qRT-PCR reaction mix is detailed in Table 10.

Table 10. qRT-PCR reaction mix components

Components	Volume (µl)
Forwards primer, 10 µM	0.25
Reverse Primer, 10 µM	0.25
iTaq ™Universal SYBR® Green Supermix (2x)	5
cDNA template	1
Nuclease free water	3.5

The qRT PCR was carried out in the CFX96™ Real-Time PCR detection system using the following program:

Table 11. Thermocycler steps for qRT PCR

qRT-PCR steps	Temperature	Time	Number of repeats
Initial denaturation	95°C	3 min	1
Denaturation	95°C	10 sec	
Annealing	60°C	30 sec	40
Elongation	72°C	30 sec	
Denaturation	95°C	10 sec	1
Melting curve	65°C to 95°C	Increment 0.5°C for 5 sec	1

Gene expression was determined using the ΔCt method. The Ct values of the target genes were normalized to the value of the housekeeping gene. HPRT was used as a housekeeping gene (endogenous control) using the equation $\Delta Ct = Ct_{reference} - Ct_{target}$ and expressed as ΔCt. The primer sequence used in this study is shown in Appendix A-1 and A-2**.**

3.2.12. Protein isolation from tissue

Protein extracted from the tissue using T-PER™ Tissue Protein Extraction Reagent and Precellys® Lysing kit. T-PER™ Tissue Protein Extraction Reagent was supplemented with Protease and Phosphatase Inhibitor. 30 mg of tissue was placed in a Precellys tube containing beads and 600µl T-PER™ Tissue Protein Extraction Reagent. The Precellys tube was transferred to the Precellys homogenizer for 30-second spins in two repeats. After homogenization, samples were centrifuged at 13000 x g for 30 minutes at 4°C. The supernatant was taken into the 1.5 ml tubes and either directly quantified or stored at -80°C.

3.2.13. Protein quantification

Protein estimation was conducted using the Bio-Rad DC Protein Assay kit. The assay is based on Lowry's method involving the reaction of peptide bonds in the protein under alkaline conditions with copper. The monovalent form of copper (Cu^{+}) then reacted with the Folin Ciocalteu reagent and that led to a subsequent reduction of the Folin Ciocalteu reagent giving rise to a blue color with absorbance at 750 nm. The standard curve was generated using different concentrations of BSA standards in the range of 0.125 to 2.0 mg/ml. The absorbance of the samples was plotted versus BSA at 750 nm using Infinite®M200 PRO Multimode Microplate Reader, TECAN.

3.2.14. Western blotting

An equal amount of protein samples was mixed with 5X gel loading buffer (Table 12) and denatured at 95°C for 10 minutes. Protein samples were separated according to their molecular weights using 10 % polyacrylamide gels (Table 13). The gels were run using a 1X running buffer (Table 14) in a vertical electrophoretic set-up at 80-120 V.

Table 12. Composition of 5X gel loading buffer

Components	Final Concentration
Tris-HCl (2M, pH-6.8)	375 mM
SDS	10% (w/v)
Glycerol	50% (v/v)
β-Mercaptoethanol	12,5% (v/v)
Bromophenol Blue	0.02% (w/v)
Water	Up to the final volume

Table 13. Composition of polyacrylamide gels

Stacking gel (6%)	
Components	Final concentration
Tris-HCl (1.5 M, pH-8.9)	375mM
Acrylamide 30%	6%
SDS 10% (w/v)	0.10%
APS 10%(w/v)	0.05%
TEMED	0.10%
Water	Up to the final volume
Resolving gel 10%	
Gel component	Final concentration
Tris-HCl (1.5 M, pH-8.9)	375mM
Acrylamide 30%	10%
SDS 10% (w/v)	0.10%
APS 10%(w/v)	0.05%
TEMED	0.10%
Water	Up to the final volume

Table 14. Composition of 1XSDS Running buffer

Components	**Final Concentration**
Tris	25 mM
Glycine	250 mM
SDS 10% (w/v)	0.1% (w/v)
Water	Up to the final volume

The proteins separated on polyacrylamide gels were transferred to the Polyvinylidene Difluoride (PVDF) membrane by an electrophoretic transfer system. The transfer was conducted for 1 h and 20 minutes at 100V in a blotting buffer (Table 15).

Table 15. Composition of 1X blotting buffer

Components	**Final concentration**
Tris	50 mM
Glysine	40 mM
Methanol	20% (v/v)
Water	Up to the final volume

After blotting the membranes were incubated in a blocking buffer containing 5% non-fat dry milk or BSA in 1X TBST buffer (Table 16) for 1 h with gentle shaking at room temperature.

Table 16. Composition of TBST buffer

Components	Final concentration
Tris	20 mM
Sodium chloride	137 mM
Tween 20(v/v)	0.1%
HCl	to adjust the pH to 7.4
Water	Up to the final volume

The membranes were incubated with one of the following primary antibodies overnight at 4°C (Table 17), then the membranes were washed with TBST buffer and subsequently incubated with secondary HRP-conjugated antibodies (Table 17) diluted in blocking buffer for 1h at room temperature. The membrane was incubated with Supersignal West Femto maximum sensitivity substrate and the signal was detected by Image Quant LAS 4000. To re-probe the membranes, they were stripped with stripping buffer for 20 minutes at room temperature, then washed with TBST and probed with another primary antibody.

Table 17. List of antibodies

Antibody	Catalog number	Company	Dilution
PAI-1	ab66705	abcam	1:200
ANKRD1	BS-8074R	BIOSS ANTIBODIES	1:200
GAPDH	MA5-15738	Invitrogen	1:1000

3.2.15. RNA interference and treatment of the cells

HCFs cells and HCMECs transfected with different isoform-specific SMARTpool siRNAs (targeting ANKRD1, SERPINE1, IL7R, INHBB, and ATF3) using Lipofectamine™ 3000 Reagent in Opti-MEM serum-free medium. Cells were seeded in 6 cm dishes or 48 well plates. The transfection reagent and siRNA were diluted in an Opti-MEM medium and mixed with a 1:2 ratio of siRNA (µg) to the transfected reagent (µl). The mixture was incubated for 15 minutes at room temperature and added dropwise onto the cells cultured in a complete medium for 48 hours. For HCFs, after 48 hours of siRNA transfection, cells were starved for 6 hours and then treated with basal medium or stimulated with TGF-β1 (10 ng), and TNF-α (10 ng) for 24 hours. siRNAs were purchased from Dharmacon™, Horizon Discovery Ltd. and as

a negative control, nontargeting siRNA was used (Appendix A-3). The effects of siRNA-mediated knockdown on proliferation, migration, tube formation (for HCMECs) gene and protein expression were evaluated.

3.2.16. Cell proliferation assay

Cellular proliferation of HCFs and HCMECs was determined using a colorimetric BrdU Cell Proliferation ELISA Kit according to the manufacturer's instructions. The kit is based on the detection of 5-bromo-2′-deoxyuridine (BrdU) incorporated into DNA during DNA synthesis through an anti-BrdU antibody conjugated with the Peroxidase enzyme.

HCF cells and HCMECs were seeded in 48 well plates at a density of 10000 and 8000 cells/ well, respectively. For HCFs before seeding the plates were coated with poly-L-lysine. After siRNA transfection for 48 hours, cells were serum starved for 24. Then they incubated with BrdU labeling solution for 2 hours. Cells were washed with PBS and fixed with FixDenat solution for 30 minutes. Fixed cells were subsequently incubated with Tetramethyl-benzidine (TMB) solution until color development. Absorbance was measured at a wavelength of 370 nm with reference at 492 nm in the TECAN Infinite M200 plate reader. Cell proliferation was plotted as a percentage of absorbance compared to the control.

3.2.17. Wound healing assay

The cultured HCFs and HCMECs were transfected with siRNA as described. After 48 hours the cell suspension was prepared from siRNA transfected cells at the cell concentration of $5x10^5$ cells/ml. 70µl of the cell suspension was applied to each well of the Culture-Inserts 2 Well and the cells were incubated at 37°C and 5% CO_2 to achieve cell confluency after 24 hours. The Culture-Inserts 2 Well was removed gently with sterile tweezers. The cells were washed with PBS and 1 ml of cell culture medium was added to each well. The images were acquired at different time points (1h, and 24h) using a 4x objective lens of Leica DM 6000B microscope. The microscopic pictures were analyzed by Image J using the wound healing plugin.

3.2.18. Tube formation assay

The cultured HCMECs were transfected with siRNA for 48 hours as described. Before seeding the cells in µ-slide angiogenesis, the Matrigel (10µl) was applied to each well and the µ-slide was placed into the incubator for polymerization for 30 minutes. Afterward, the cell suspension was prepared from siRNA-transfected cells at the cell concentration of $2x10^5$ cells/ml. 50µl of

the cell suspension was added to each well of µ-slide and an image was collected after seeding the cells. Moreover, the cells were incubated at 37°C and 5% CO_2 and they were taken out from the incubator at distinct time points. As recommended the small magnification (4x) of Leica DM 6000B microscope was used to collect the images at different time points (1h and 24h). The microscopic pictures were analyzed by Image J using the angiogenesis plugin.

3.2.19. Matrix stiffness-dependent cell culture experiments

To mimic the stiffness in the pathogenesis of CTEPH, a Matrix stiffness experiment was performed using ready-to-use hydrogel dishes containing rat tail collagen type 1 attached to the petrisoft ™ polystyrene dishes (Cell Guidance Systems Ltd). The primary human cardiac fibroblasts (HCFs), (700,000 cells per dish) was seeded on Petrisoft™ dishes with 1kPa (soft matrix) and 50 kPa (stiff matrix). The cells were harvested at the time points of 12, 24, and 48 hours. The cells were used for RNA extraction.

3.2.20. Statistical analysis

Statistical analyses were performed using GraphPad Prism version 9.1.0 (GraphPad Software, Inc., San Diego, CA). Several tests were applied for the statistical analysis.

Normally distributed variables are shown as mean± standard deviation (sd) and the comparison between two groups was performed using unpaired t-tests, while paired t-tests were used where applicable. Non-normally distributed variables are presented as median (interquartile range, IQR). The comparison between the two groups was performed using the Mann-Whitney U-test, while the Wilcoxon test was used where applicable.

For the comparisons involving more than two groups, one-way ANOVA (analysis of variance) was used for the normally distributed variables. For the non-normally distributed variables, the Kruskal-Wallis test was used. Additionally, the categorical variables are shown as counts and percentages and Fisher's exact test was performed to compare the categorical variables.

Pearson's correlation analysis was used to show the relationship between the regularized logarithm transformation (r-log) read counts of the selected genes and the clinical parameters of the patients.

4. Results

4.1. Classification of the patients with CTEPH based on the ECS/ERS guidelines

This study included 75 patients with CTEPH who underwent PEA. Their risk factors and comorbidities are presented in Table 18. The number of patients, biopsy locations, and sample labeling in the exploratory and confirmatory cohorts of CTEPH patients are summarized in Figure 7. Patients entered the study in the exploratory cohort, (A-prePEA, n = 9; Figure 7 A), with five overlapping with the confirmatory cohort (B-prePEA, n = 71; Figure 7 B).

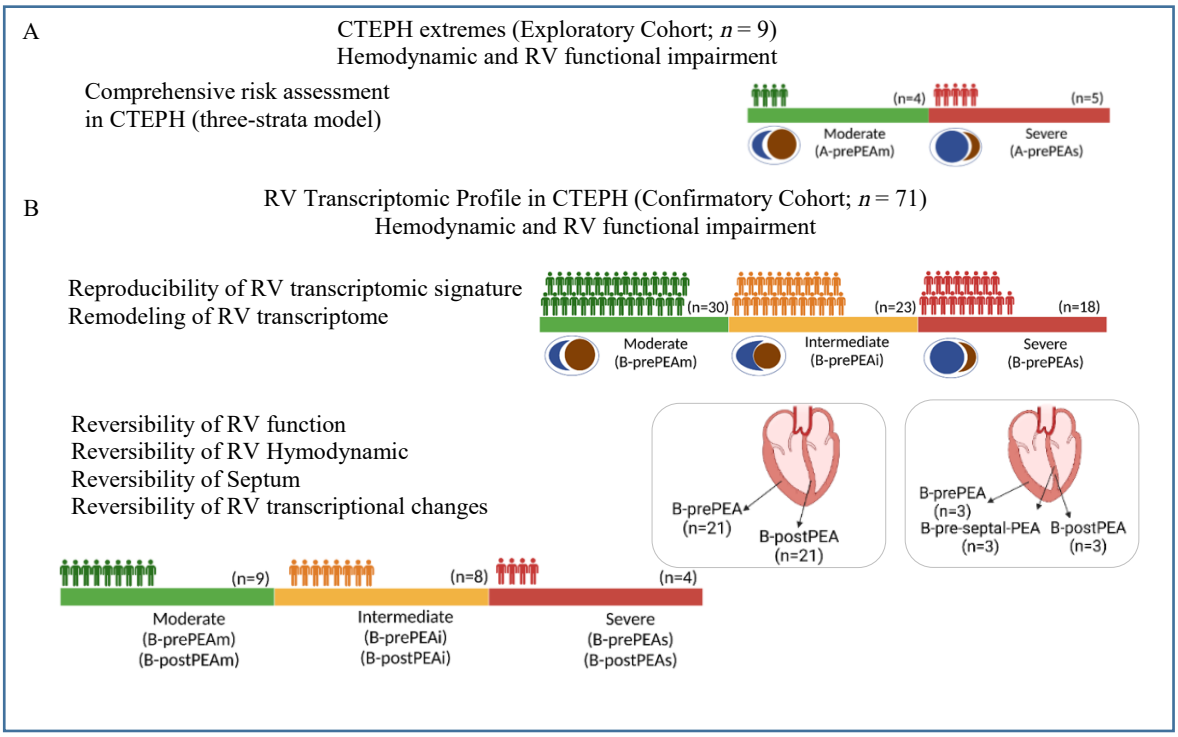

Figure 7. Study population in the CTEPH cohort. The patients with CTEPH were classified into the (A) exploratory cohort and (B) confirmatory cohort. Created with BioRender.com.

In both cohorts, patients with CTEPH were classified based on their clinical parameters and according to the ESC/ERS risk stratification before PEA (Humbert et al., 2022). The risk assessment of patients with CTEPH was conducted according to a three-strata model using three variables: N-terminal-pro hormone BNP (NT-proBNP, pg/ml), cardiac index (CI, l/min/m²) and the ratio of tricuspid annular plane systolic excursion to systolic pulmonary artery pressure (TAPSE/sPAP, mm/mmHg). Each variable was graded into moderate, intermediate, and severe according to the cutoffs defined in Figure 8, and the patients were placed in the corresponding group.

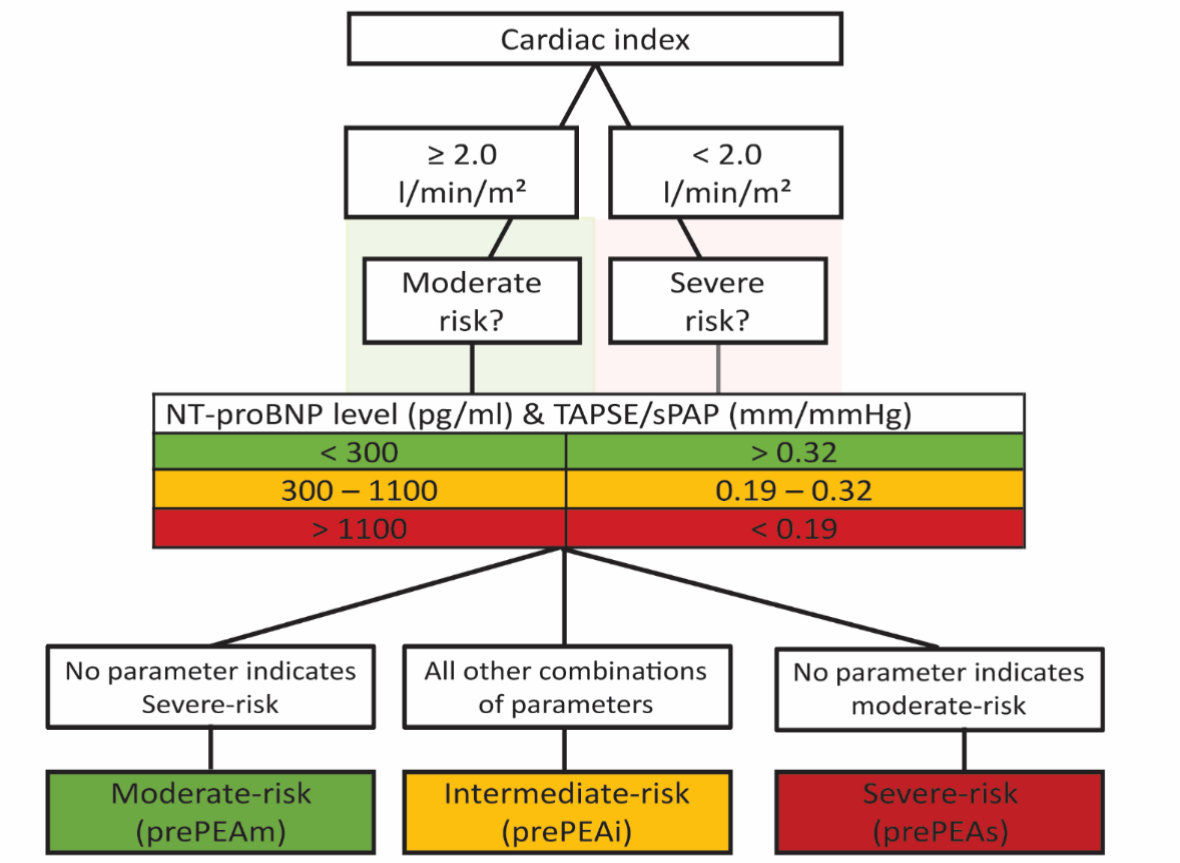

Figure 8. A flowchart of the classification of the patients with CTEPH. An ESC/ERS three-strata model was used to classify the patients with CTEPH. Abbreviations: NT-proBNP: N-terminal-pro hormone BNP; ratio of tricuspid annular plane systolic excursion to systolic pulmonary artery pressure (TAPSE/sPAP) mm/mmHg; CI: cardiac index.

The patients in the exploratory cohort were placed into moderate (A-prePEAm, n = 4) and severe (A-prePEAs, n = 5) risk groups based on their clinical parameters (Table 19), similarly, the patients in the confirmatory cohort (B-prePEA, n = 71), were classified into moderate (B-prePEAm, n = 30), intermediate (B-prePEAi, n = 23), and severe (B-prePEAs, n = 18) risk groups (Figure 7 B). The clinical parameters of the patients are shown in Table 20.

Moreover, in the confirmatory cohort, the gene expression profiles of patient-paired samples were compared between prePEA and postPEA (i.e., the pre and post PEA biopsies belonged to the same patient (Table 21 and Figure 7 B). Additionally, for the three patients who underwent septal biopsies prior to PEA- labeled as B-pre-septal PEA (n = 3) - the gene expression profile of the septum were compared with their corresponding RV (B-prePEA, n = 3) and septum (B-postPEA, n = 3) (Table 22 and Figure 7 B).

Table 18. Risk factors and comorbidities of the patients with CTEPH before PEA. The risk factors and comorbidities of all patients with CTEPH at study entry in both exploratory and confirmatory cohorts.

	All study patients (*n* = 75)
Risk factors for CTEPH	
History of VTE	20 (30.30%), *n* = 66
History of DVT	25 (40.32%), *n* = 62
Acute PE	28 (45.16%), *n* = 62
Antiphospholipid syndrome	2 (3.22%), *n* = 62
History of splenectomy	1 (1.33%), *n* = 75
Chronic inflammatory disease[1]	75 (1.06%), *n* = 75
VA shunt	75 (0), *n* = 75
Pacemarker	1 (1.51%), *n* = 66
Blood group non-0	61 (87.14%), *n* = 70
Group A	42 (60%)
Group B	8 (11.42 %)
Group AB	11 (15.71%)
Thyroid dysfunction	13 (19.40%), *n* = 67
Known hypothyroidism	8 (11.94%), *n* = 67
Comorbidities	
Cancer over than 5 years ago	2 (2.85%), *n* = 70
Cancer less than 5 years ago	3 (4.28%), *n* = 70
Coronary heart disease	5 (6.66%), *n* = 75
History of myocardial infarction	0, *n* = 70
Atrial fibrillation	10 (14.28%), *n* = 70
Valvular heart diseasee	17 (25%), *n* = 68
Atrial septal defect	1 (1.49%), *n* = 67
Diabetes mellitus	4 (5.33%), *n* = 75
Chronic pulmonary disease	19 (26.76%), *n* = 71
Renal insufficiency	18 (24%), *n* = 75
Smoking	*n* = 75
Smoker	15 (20%)
Former smoker	24 (32%)
Non-smoker	36 (48%)
Anemia[2]	6 (8%), *n* = 75

n = refers to the number of patients with available data
Data are presented as n (%)
Abbreviations: VTE, venous thromboembolism; DVT, deep vein thrombosis; PE, pulmonary embolism; VA, ventriculo-atrial.
[1]Chronic inflammatory bowel disease (Crohn's disease and ulcerative colitis)
[2] haemoglobin concentration <12 g/dl in female and <13 g/dl in male.

Table 19. Clinical characteristics of the patients with CTEPH in the exploratory cohort. The patients with CTEPH were classified based on their clinical parameters and ESC/ERS guidelines as Moderate (A-prePEAm, $n = 4$) and severe (A-prePEAs, $n = 5$).

Parameter	Total ($n = 9$)	A-prePEAm ($n = 4$)	A-prePEAs ($n = 5$)	*P* value
General characteristics				
Female gender, n (%)	5(35.71)	3 (75)	0 (0)	0.047
Age at PEA, y	55± 14.9	58.78± 12.3	51.97 ± 17.53	
BMI, kg/m²	25.6 ± 4.66	24.6 ± 3.63	26.39 ± 5.64	
Laboratory				
GFR, ml/min/1.73m^2 *	82.71 (79.87-93.3)	88.23 (83-106.5)	80.29(51.81-88.34)	
Creatinine, µmol/l *	0.96 (0.73-1.1)	0.73 (0.61-0.91)	1.02(0.93-2.05)	0.031
NT-proBNP, pg/ml *	468.9(113.4-1658)	113.4 (43.75-390.9)	1466 (544-3825)	0.031
Functional status				
6-MWD, m	362 ± 165.7	378± NA	356.7 ± 202.5	NA
WHO FC, n (%) I	0 (0)	0 (0)	0 (0)	
II	2 (14.3)	1 (25)	0 (0)	
III	8 (57.1)	2 (50)	4 (80)	
IV	4 (28.6)	1 (25)	1 (20)	
VO2max, ml/min/kg	15.12±6.12	21±NA	12.18±3.71	NA
Hemodynamics				
sPAP, mmHg	71.79 ± 19.58	47.75 ± 13.6	86.2 ± 6.9	0.0008
mPAP, mmHg	39.89 ± 14.14	25.25 ± 6.85	50.8 ± 5.45	0.0005
mRAP, mmHg	7.37 ±3.54	4.75 ±2.21	10 ±2.44	0.019
PVR, WU	7.65 ±4.96	2.93 ±2.39	11.44 ±2.24	0.0008
CI, L/min/m²	2.29 ± 0.402	2.4 ± 0.35	1.79 ± 0.16	0.011
CO, L/min	3.82±0.59	4.34±0.77	3.60±0.43	
Echocardiography				
RV basal diameter, mm	43±11.6	36.5±7.55	49.5±12.18	
LVEF, % *	60 (55-60)	60 (60-60)	55 (55-60)	
TAPSE, mm *	19 (12-22)	20 (19-22.5)	12 (11.5-22)	
TAPSE/sPAP, mm/mmHg *	0.26 (0.15-0.43)	0.43 (0.35-0.55)	0.16 (0.12-0.24)	0.015

Data are presented as n (%), median (interquartile range, IQR) *, and mean ± (standard deviation, SD). Abbreviations: BMI, Body mass index; GFR, glomerular filtration rate; NT-proBNP, N-terminal pro-B-type natriuretic peptide; 6-MWD, 6-minute-walk distance; WHO FC, World health organization functional class; VO2 max, peak oxygen uptake; sPAP, systolic pulmonary arterial pressure; mPAP, mean pulmonary arterial pressure; mRAP, mean right atrial pressure; PVR, pulmonary vascular resistance; WU, wood units; CI, cardiac index; CO, cardiac output; LVEF, left ventricular ejection fraction; TAPSE, tricuspid annular plane systolic excursion; NA, not applicable.

Table 20. Clinical characteristics of the patients with CTEPH in the confirmatory cohort. The patients with CTEPH were classified based on their clinical parameters and ESC/ERS guidelines as moderate (B-prePEAm, *n* = 30), intermediate (B-prePEAi, *n* = 23), and severe (B- prePEAs, *n* = 18).

Parameter	Total (*n* = 71)	B-prePEAm (*n* = 30)	B-prePEAi (*n* = 23)	B-prePEAs (*n* = 18)	*P* value[1]	*P* value[2]	*P* value[3]
General characteristics							
Female gender, n (%)	22 (30.99)	11 (36.67)	7 (30.43)	4 (22.22)			
Age at PEA, y	58.7± 14.7	57.7 ± 15	59.6 ± 14	59.5 ± 15.8			
BMI, kg/m²	27.81 ± 6.01	28.18 ± 5.25	27.41 ± 7.01	27.71 ± 6.16			
Laboratory							
GFR, ml/min/1.73m² *	80.29 (63.71-92.57)	89.26 (79.40-96.68)	78.33 (62.53-96.86)	71.1 (49.19-82.17)		0.007	
Creatinine, µmol/l *	0.96 (0.82-1.12)	0.9 (0.72-1)	1.03 (0.82-1.2)	1.14 (0.99-1.2)		0.002	
NT-proBNP, pg/ml *	1046 (354.7-2047)	361.8 (133.5-702.7)	1890 (1312-2620)	2079 (1254-4756)	<0.0001	<0.0001	
Functional status							
6-MWD, m	415.8 ± 110.13	452.6 ± 90.85	401.7 ± 111.2	336 ± 128.7			
WHO FC, n (%) I	0 (0)	0 (0)	0 (0)	0 (0)			
II	8 (11.3)	5 (16.6)	4 (17.4)	0 (0)			
III	50 (70.4)	20 (66.66)	16 (69.6)	13 (72.2)			
IV	13 (18.3)	5 (16.7)	3 (13)	5 (27.8)			
VO2max, ml/min/kg	11.89±4.01	15.21±4.79	10.6 ±2.8	10.13±2.43	0.008	0.008	
Hemodynamics							
sPAP, mmHg	72.39 ± 19.33	63.27 ± 19.02	81.48 ± 18.13	76 ± 14.95		0.04	0.001
mPAP, mmHg	41.42 ± 10.21	36.07 ± 9.34	45.74 ± 9.88	44.83 ± 8.12	0.001	0.006	
mRAP, mmHg	7.4 ±3.81	6.33 ±2.63	6.84 ±4.1	10.71 ±4.03		0.02	
PVR, WU	7.54 ±3.16	5.72 ±2.59	7.7 ±1.98	10.33 ±3.14	0.03	<0.0001	0.008
CI, L/min/m²	2.29 ± 0.57	2.66 ± 0.44	2.30 ± 0.45	1.63 ± 0.20	0.007	<0.0001	<0.0001
CO, L/min	4.54± 1.24	5.30± 1.13	4.45± 0.93	3.47± 0.78	0.02	<0.0001	0.002
Echocardiography							
RV basal diameter, mm	44.25±8.1	38.83±9.96	47.45±8.4	49.35±11.42	0.002	0.0006	
LVEF, % *	60 (55-60)	60 (55-60)	57 (55-60)	55 (55-60)			
TAPSE, mm *	19 (16-23)	20.5 (19-24.5)	18 (15-22)	15.5 (11.75-18.25)		<0.0001	
TAPSE/sPAP, mm/mmHg *	0.25 (0.19-0.35)	0.34 (0.23-0.47)	0.21 (0.18-0.33)	0.22 (0.16-0.25)	0.002	0.0001	

[1]B-prePEAm versus B-prePEAi
[2]B-prePEAm versus B-prePEAs
[3]B-prePEAi versus B-prePEAs

Data are presented as n (%), median (interquartile range, IQR)*, and mean ± (standard deviation, SD). Abbreviations: BMI, Body mass index; GFR, glomerular filtration rate; NT-proBNP, N-terminal pro-B-type natriuretic peptide; 6-MWD, 6-minute-walk distance; WHO FC, World health organization functional class; VO2 max, peak oxygen uptake; sPAP, systolic pulmonary arterial pressure; mPAP, mean pulmonary arterial pressure; mRAP, mean right atrial pressure; PVR, pulmonary vascular resistance; WU, wood units; CI, cardiac index; CO, cardiac output; LVEF, left ventricular ejection fraction; TAPSE, tricuspid annular plane systolic excursion.

4.2. Effect of PEA on the clinical parameters in the confirmatory cohort: B-prePEA versus B-postPEA

The clinical parameters of the patients with CTEPH in the confirmatory cohort before and after PEA are presented in Table 21. NT-proBNP (pg/ml), sPAP (mmHg), mPAP (mmHg), PVR (WU), and RV basal diameter (mm) were significantly decreased after PEA. In contrast, CO L/min, and TASPE/sPAP (mm/Hg) were significantly increased after PEA. However, CI (L/min/m²) did not change significantly after PEA (Table 21).

Table 21. The effect of PEA on the clinical parameters of CTEPH patients in the confirmatory cohort of B-PrePEA versus B-postPEA.

Parameter	B-prePEA (*n* = 21)	B-postPEA (*n* = 21)	*P* value
Laboratory			
NT-proBNP, pg/ml*	1074 (194-2338)	259 (123-962.7)	0.038
Hemodynamics			
sPAP, mmHg	70.71 ± 21.34	39.48 ± 21.87	<0.0001
mPAP, mmHg	40.43 ± 11.08	28.48 ± 11.48	<0.0001
mRAP, mmHg	7.07 ±3.42	6.23 ±4.51	
PVR, WU	7.5 ±3.29	3.54 ±2.73	0.0005
CI, l/min/m²	2.19 ± 0.41	2.38 ± 0.41	
CO, L/min	4.12±0.79	4.87±0.96	0.034
Echocardiography			
RV basal diameter (mm)	43.56±9.90	36.78±7.72	0.039
LVEF, % *	57.5 (55-60)	55 (55-60)	
TAPSE, mm *	19 (15.75-21)	17 (16-19)	
TAPSE/sPAP, mm/mmHg *	0.25 (0.19-0.35)	0.57 (0.36-0.7)	<0.0001

Data are presented as median (interquartile range, IQR)*, and mean ± (standard deviation, SD). Abbreviations: NT-proBNP, N-terminal pro-B-type natriuretic peptide; sPAP, systolic pulmonary arterial pressure; mPAP, mean pulmonary arterial pressure; mRAP, mean right atrial pressure; PVR, pulmonary vascular resistance; WU, wood units; CO, cardiac output; CI, cardiac index; LVEF, left ventricular ejection fraction; TAPSE, tricuspid annular plane systolic excursion.

Additionally, the clinical parameters of three patients who underwent septal biopsies prior to PEA (B-pre-septal PEA), the gene expression profile of the septum were compared with their corresponding RV (B-prePEA) and septum (B-postPEA) are presented in Table 22.

Table 22. The effect of PEA on the clinical parameters of patients with CTEPH in the confirmatory cohort comparing B-prePEA and B-postPEA (three paired patients)

Parameter	B-prePEA (*n* = 3)	B-postPEA (*n* = 3)	*P* value
Laboratory			
NT-proBNP, pg/ml*	7595 (1074-9505)	548.5 (60.7-2067)	
Hemodynamics			
sPAP, mmHg	81.33±15.31	39.67±20.43	
mPAP, mmHg	46.67±7.31	28±14.73	
mRAP, mmHg	11±NA	8.33±7.57	NA
PVR, WU	7.51±1.26	3.19±1.23	
CI, l/min/m²	2.03±0.37	2.53±0.30	
CO, L/min	4.12±NA	5.24±0.97	NA
Echocardiography			
RV basal diameter (mm)	41.33±9.29	38±11.27	
LVEF, % *	55 (45-55)	55 (50-55)	
TAPSE, mm *	18 (10-24)	16 (14-17)	
TAPSE/sPAP, mm/mmHg *	0.24 (0.13-0.25)	0.54 (0.22-0.64)	

Data are presented as median (interquartile range)*, or mean ± standard deviation.

Abbreviations: NT-proBNP, N-terminal pro-brain natriuretic peptide; sPAP, systolic pulmonary artery pressure; mPAP, mean pulmonary artery pressure; mRAP, mean right atrial pressure; PVR, pulmonary vascular; CI, Cardiac index; resistance; CO, cardiac output; LVEF, left ventricular ejection fraction; TAPSE, Tricuspid annular plane systolic excursion; NA, not applicable.

4.3. RNA quality and quantity of human heart tissue

The quantity of the RNA samples of heart tissue was determined by Qubit assay. The samples with RNA concentration >50 ng were included for library preparation and subsequent RNA-seq. The electropherograms showed different peaks for pre-PEA RNA samples extracted using both bead-beating homogenization and dry cryo-pulverization methods (Figures 9 and 10).

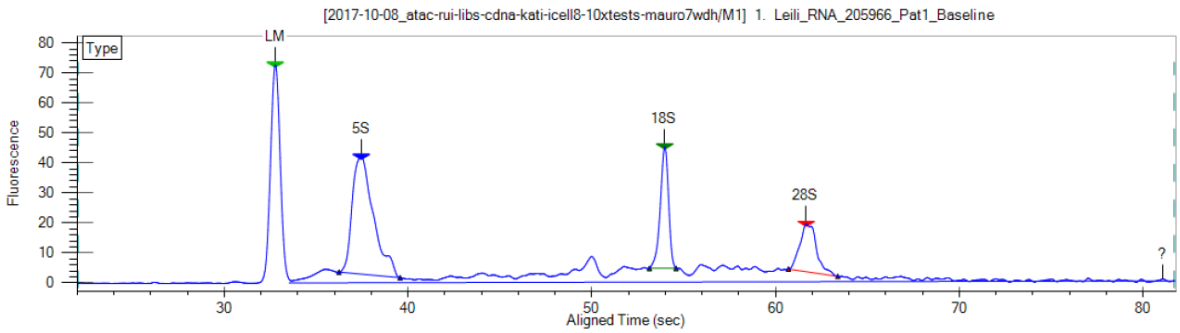

Figure 9. An electropherogram showing the regions that indicate the quality of RNA from the heart tissue of the patients with CTEPH. The RNA quality of one pre-PEA sample with a clear distribution of 5-, 18-, and 28-S peaks with the bead-beating homogenization RNA isolation method.

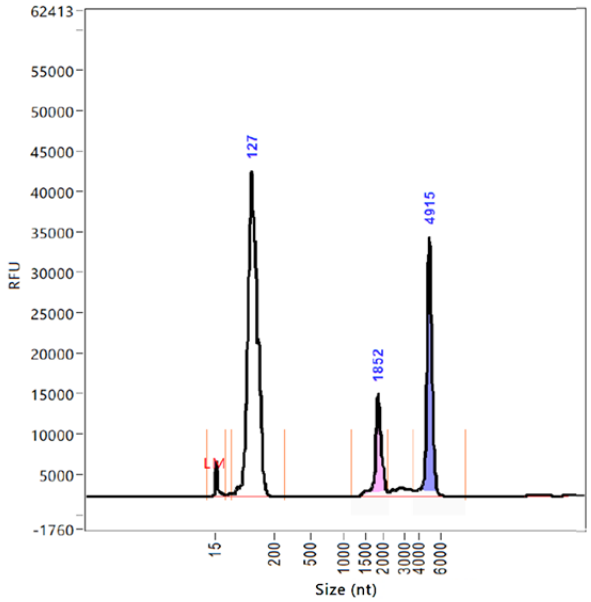

Figure 10. Segments of the electropherogram showing the peak distribution of RNA from the pre-PEA sample. The RNA integrity assessment of the pre-PEA sample showed that RNA isolated using the dry cryo-pulverization method was intact.

4.4. Transcriptomic profiling of the RV and septum in patients with CTEPH before and after PEA

The sample preparation steps (total RNA isolation, RNA quality, and quantity control), library preparation, next-generation sequencing, and bioinformatics analysis are illustrated in Figure 11. The bioinformatics analysis was performed after RNA-seq. Multiple comparisons were conducted in the CTEPH cohort.

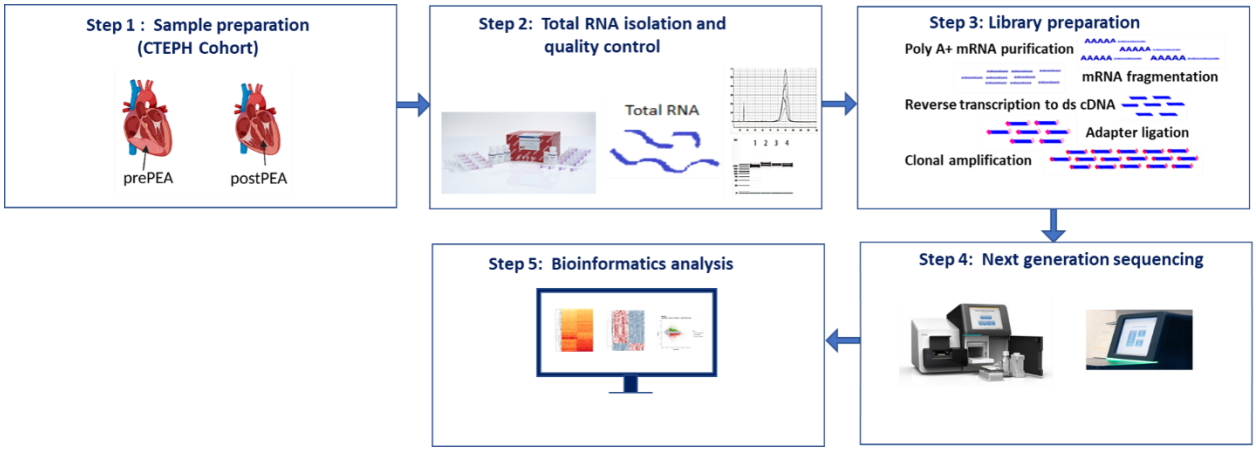

Figure 11. Schematic of the approach used to examine CTEPH heart tissue. (1) Heart tissue samples from patients with CTEPH were prepared, (2) total RNA was isolated and subjected to quality control, (3) library preparation, (4) next-generation sequencing, and (5) bioinformatics analysis. Created with BioRender.com.

4.5. Principal component analysis of RNA-seq data

Transcriptome profiles were compared in the CTEPH cohorts using principal component analysis (PCA) of normalized counts. The distinct clustering of the prePEAm and prePEAs samples is evident in both the exploratory (Figure 12 A) and confirmatory (Figure 12 B) cohorts.

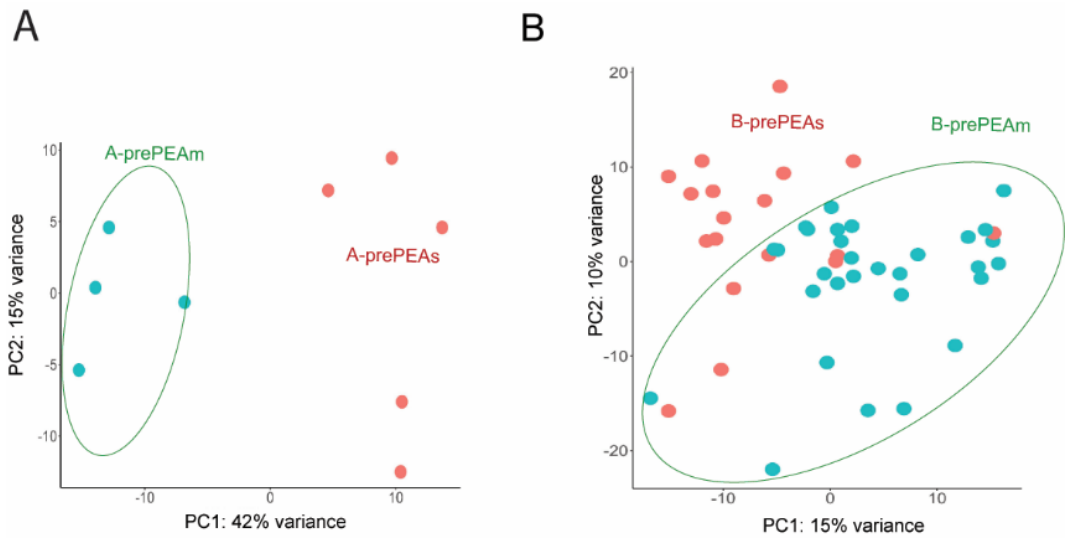

Figure 12. PCA of the RNA-seq data. Changes in gene expression were investigated in the (A) exploratory cohort (A-prePEAm [n = 4] and A-prePEAs [n = 5]) and (B) in the confirmatory cohort (B-prePEAm [n = 30] and B-prePEAs [n = 18]).

4.6. Volcano plots of the differentially expressed genes in the exploratory and confirmatory cohorts of patients with CTEPH

The bioinformatic analysis was performed on both exploratory and confirmatory cohorts. The volcano plots show the distribution of the DEGs in the CTEPH cohorts. The total number of DEGs between the prePEAm and prePEAs groups was 814 in the exploratory (347 upregulated and 467 downregulated, Figure 13 A) and 358 in the confirmatory cohort (161 upregulated and 197 downregulated Figure 13 B). Furthermore, in the confirmatory cohort, the overall count of DEGs between prePEAm and prePEAi was 88 (26 upregulated and 62 downregulated, Figure 13 C). Whereas, there were 15 DEGs between prePEAi and prePEAs, all of which were found to be upregulated (Figure 13 D).

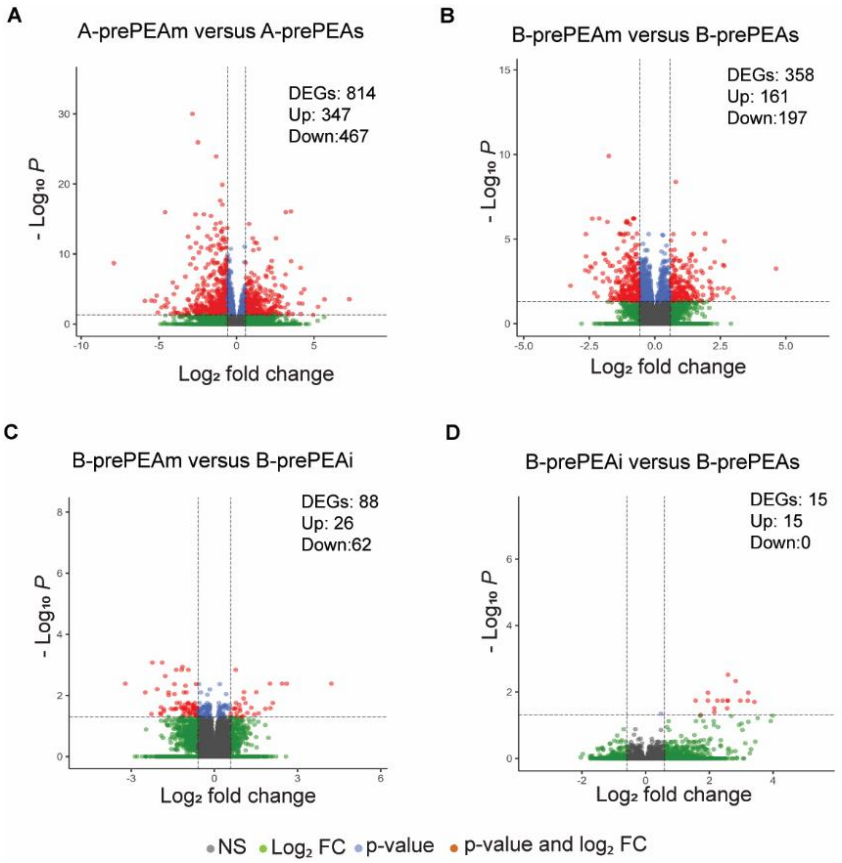

Figure 13. Volcano plots of differentially expressed genes. The volcano plot shows the DEGs in (A) exploratory cohort (A-prePEAm [*n* = 4] versus A-prePEAs [*n* = 5]) and (B) confirmatory cohort (B-prePEAm [*n* = 30] versus B-prePEAs [*n* = 18]), (C) B-prePEAm [*n* = 30] versus B-prePEAi [*n* = 18], and (D) B-prePEAi [*n* = 23] versus B-prePEAs [*n* = 18].The significantly differentially expressed genes (DEGs) were defined in both the exploratory cohort and the confirmatory cohort using the following criteria: for the exploratory cohort, $|\log_2 FC| \geq 0.585$ and P adj ≤ 0.05 (two-sided); for the confirmatory cohort, base mean ≥ 5, $|\log_2 FC| \geq 0.585$, and P-adjusted value (Padj) ≤ 0.05 (two-sided). The DEGs were identified based on the *P* value < 0.05 and $|\log_2 FC| > 0.585$ (in red), only *P* value (blue), $\log_2 FC$ (green), and not significant in grey dots.

4.7. Heatmaps of the differentially expressed genes in the exploratory and confirmatory cohorts

The heatmaps show the top 50 DEGs between the pre-PEAm and pre-PEAs groups. The top 50 DEGs between the A-prePEAm (*n* = 4) and A-prePEAs (*n* = 5) groups in the exploratory cohort and the B-prePEAm (*n* = 30) and B-prePEAs (*n* = 18) groups in the confirmatory cohort are shown in Figures 14 A and 14 B, respectively. The top 50 DEGs in both cohorts showed the upregulation of heart disease-associated genes, including *NPPA*, *NPPB*, and proenkephalin (*PENK*). In the exploratory cohort, the DEGs also included ECM-related genes, including *TNC*, *POSTN*, and collagen type IX alpha 1 chain (*COL9A1*). In the confirmatory cohort, the DEGs also included *COMP*. In addition, Figure 14 C shows the top 50 DEGs between B-prePEAm (*n* = 30) and B-prePEAi (*n* = 23).

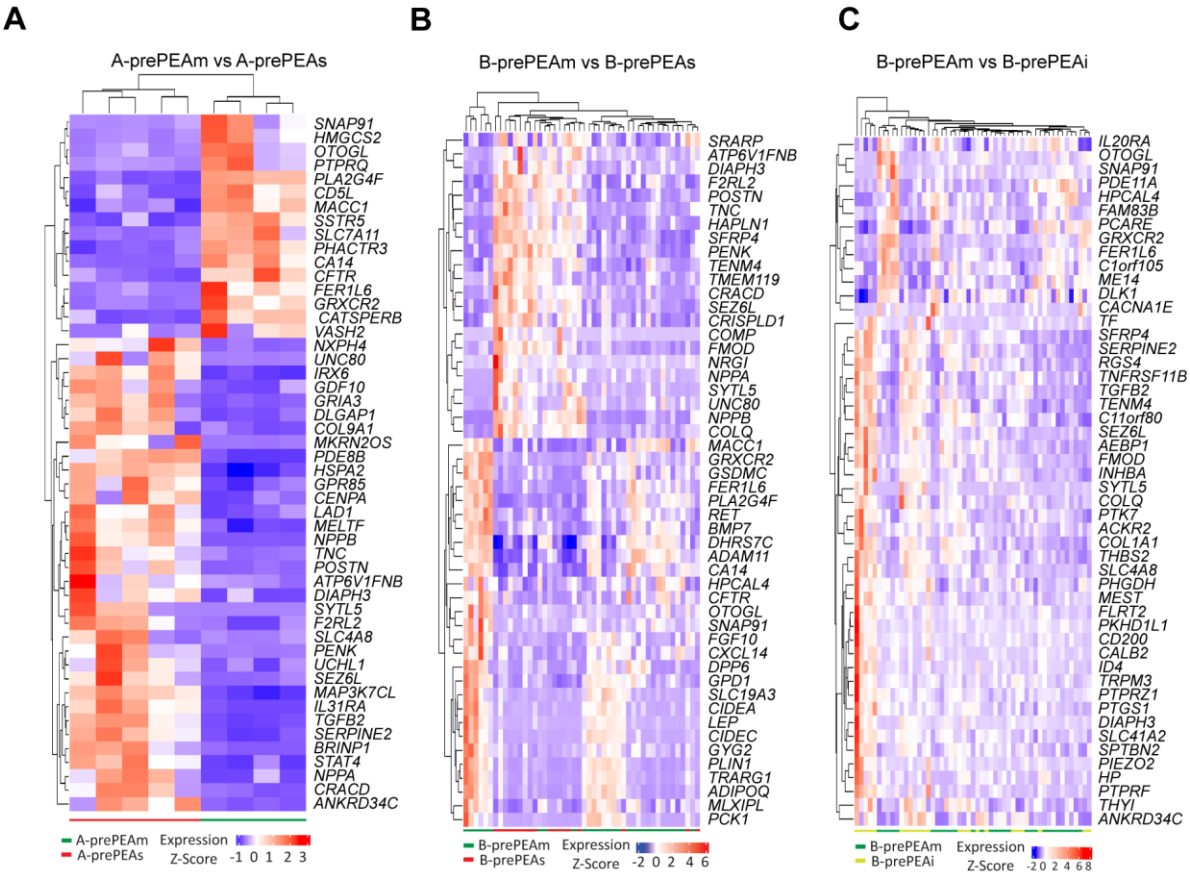

Figure 14. Heatmaps of DEGs in the RNA-Seq data. Heatmaps showing the z-score of the top DEGs in the (A) exploratory cohort (A-prePEAm [n = 4] versus A-prePEAs [n = 5)], (B) confirmatory cohort (B-prePEAm [n = 30] versus B-prePEAs [n = 18]) and (C) comparison between (prePEAm [n = 30] versus B-prePEAi [n = 23]).

4.8. Tree plots showing the hierarchical clustering of enriched terms in the exploratory and confirmatory cohorts

The hierarchical clustering of enriched terms among the DEGs between the pre-PEAm and pre-PEAs groups was performed in the exploratory and confirmatory cohorts. The most significantly enriched terms were extracellular region and extracellular space in the exploratory cohort (Appendix A-4) and multicellular organismal process, system development, developmental process, and anatomical structure development in the confirmatory cohort (Appendix A-5).

4.9. Gene set enrichment analysis in the exploratory and confirmatory cohort

For the pathway analysis, distinctive clusters have been defined for different cohorts: in the exploratory cohort, A-prePEAm vs. A-prePEAs is determined as cluster 1. Within the confirmatory cohort, B-prePEAm vs. B-prePEAs is identified as cluster 2, B-prePEAm vs. B-

prePEAi as cluster 3, and B-prePEAi vs. B-prePEAs builds cluster 4. The pathway analysis was performed using the DEGs from each cluster, with the filter criteria of base mean ≥ 5; $|\log_2(FC)| \geq 0.585$; Padj ≤ 0.05, two-sided. The top 20 and 100 overrepresented terms between clusters 1 and 2 are presented in Figure 15 A and B. The top regulated terms are associated with various forms of ECM, including its organization, glycosaminoglycan binding, and structural constituents. The ECM categories further include collagen fibril organization, the presence of ECM proteoglycans, and the formation of collagen trimers. Additionally, the process of conferring tensile strength via ECM structural constituents is also notably regulated. Other significant categories include the degradation of ECM, interactions at the integrin cell surface, collagen degradation, as well as protein digestion and absorption. Among the GO terms, various processes including actin filament-based processes, organization of actin cytoskeleton, regulation of muscular system functionalities, regulation of sodium ion transport, collagen binding, and focal adhesion, are specifically expressed in the exploratory cohort (cluster 1). In contrast, the confirmatory cohort distinctly shows processes linked to the metabolism of fatty acids, the condition of familial partial lipodystrophy, and the regulatory mechanisms governing protein processing.

A

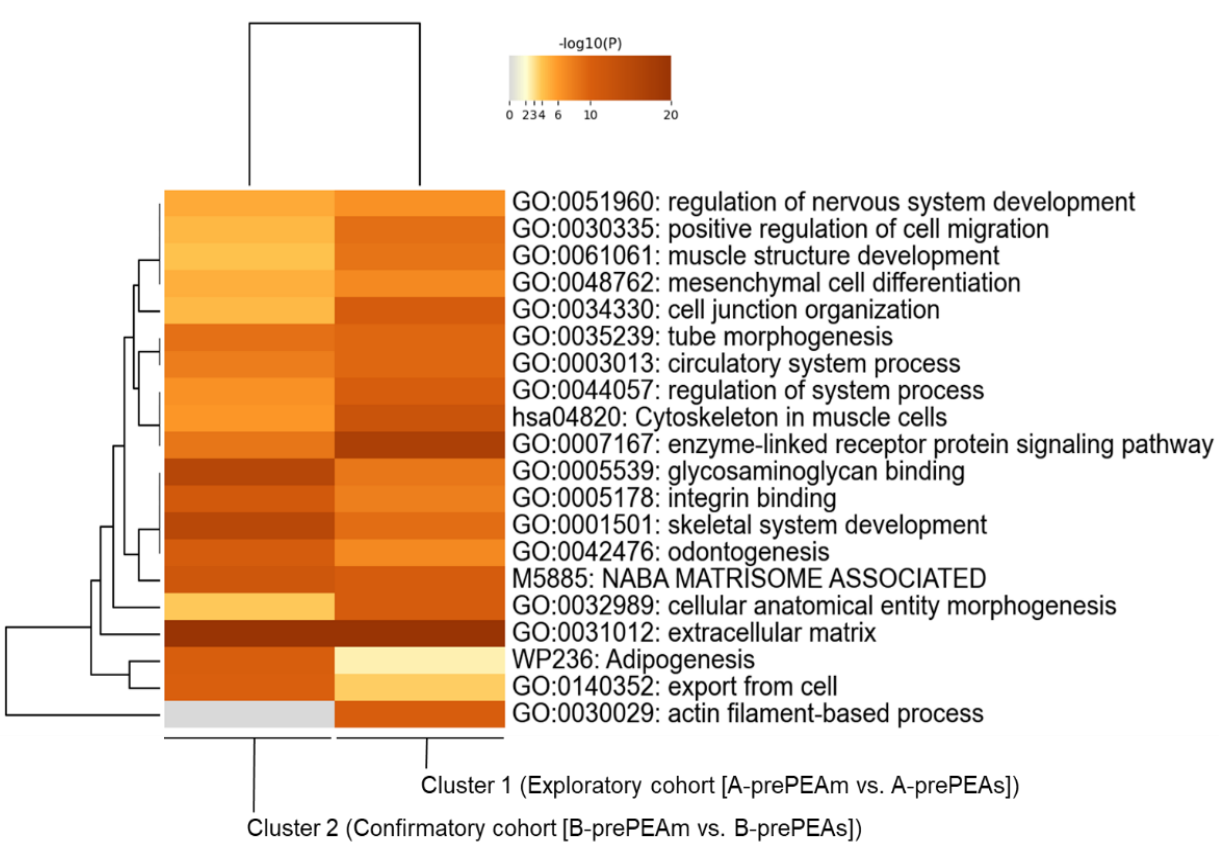

B

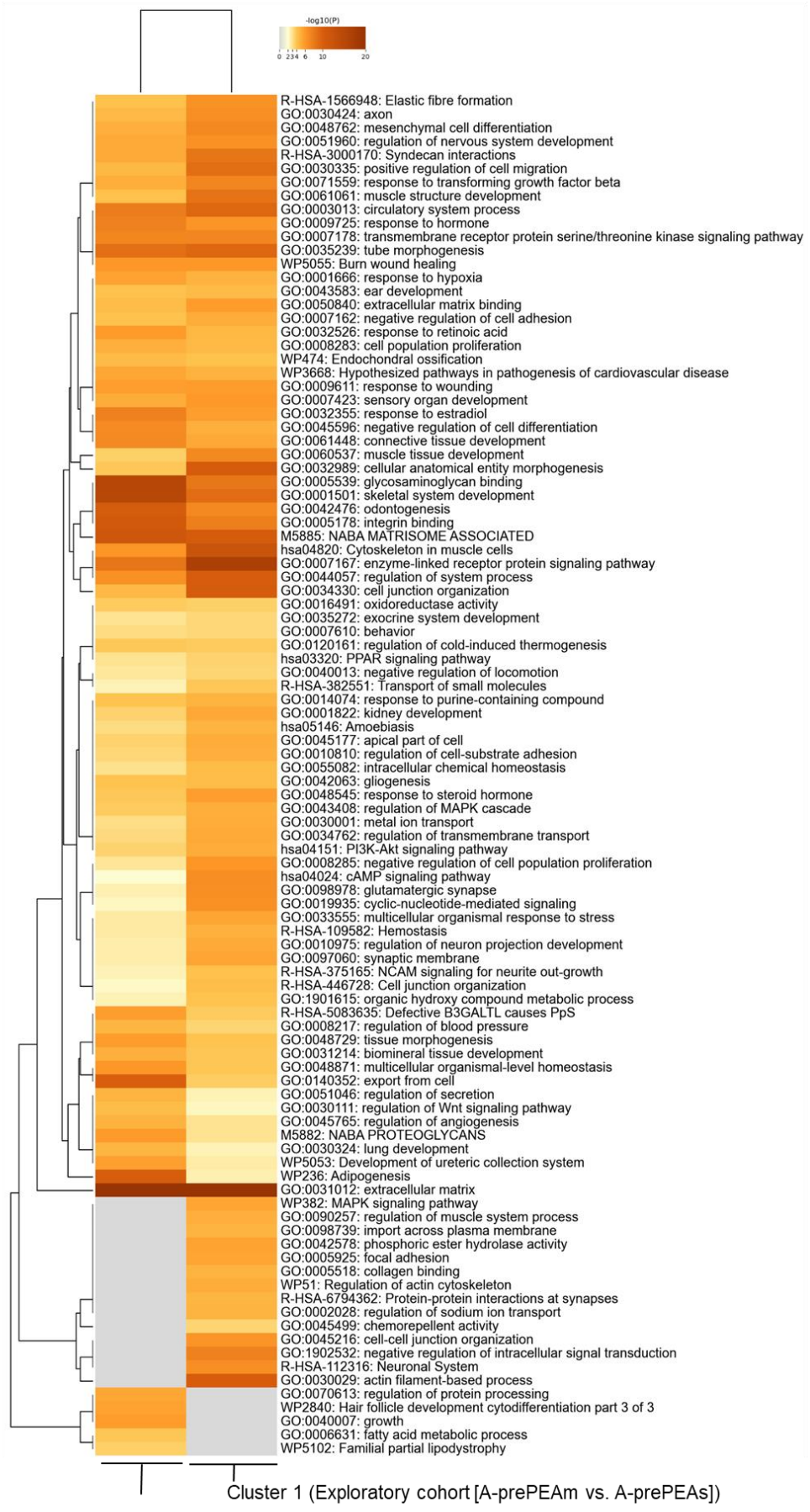
-log10(P)
0 2 3 4 6 10 20
R-HSA-1566948: Elastic fibre formation
GO:0030424: axon
GO:0048762: mesenchymal cell differentiation
GO:0051960: regulation of nervous system development
R-HSA-3000170: Syndecan interactions
GO:0030335: positive regulation of cell migration
GO:0071559: response to transforming growth factor beta
GO:0061061: muscle structure development
GO:0003013: circulatory system process
GO:0009725: response to hormone
GO:0007178: transmembrane receptor protein serine/threonine kinase signaling pathway
GO:0035239: tube morphogenesis
WP5055: Burn wound healing
GO:0001666: response to hypoxia
GO:0043583: ear development
GO:0050840: extracellular matrix binding
GO:0007162: negative regulation of cell adhesion
GO:0032526: response to retinoic acid
GO:0008283: cell population proliferation
WP474: Endochondral ossification
WP3668: Hypothesized pathways in pathogenesis of cardiovascular disease
GO:0009611: response to wounding
GO:0007423: sensory organ development
GO:0032355: response to estradiol
GO:0045596: negative regulation of cell differentiation
GO:0061448: connective tissue development
GO:0060537: muscle tissue development
GO:0032989: cellular anatomical entity morphogenesis
GO:0005539: glycosaminoglycan binding
GO:0001501: skeletal system development
GO:0042476: odontogenesis
GO:0005178: integrin binding
M5885: NABA MATRISOME ASSOCIATED
hsa04820: Cytoskeleton in muscle cells
GO:0007167: enzyme-linked receptor protein signaling pathway
GO:0044057: regulation of system process
GO:0034330: cell junction organization
GO:0016491: oxidoreductase activity
GO:0035272: exocrine system development
GO:0007610: behavior
GO:0120161: regulation of cold-induced thermogenesis
hsa03320: PPAR signaling pathway
GO:0040013: negative regulation of locomotion
R-HSA-382551: Transport of small molecules
GO:0014074: response to purine-containing compound
GO:0001822: kidney development
hsa05146: Amoebiasis
GO:0045177: apical part of cell
GO:0010810: regulation of cell-substrate adhesion
GO:0055082: intracellular chemical homeostasis
GO:0042063: gliogenesis
GO:0048545: response to steroid hormone
GO:0043408: regulation of MAPK cascade
GO:0030001: metal ion transport
GO:0034762: regulation of transmembrane transport
hsa04151: PI3K-Akt signaling pathway
GO:0008285: negative regulation of cell population proliferation
hsa04024: cAMP signaling pathway
GO:0098978: glutamatergic synapse
GO:0019935: cyclic-nucleotide-mediated signaling
GO:0033555: multicellular organismal response to stress
R-HSA-109582: Hemostasis
GO:0010975: regulation of neuron projection development
GO:0097060: synaptic membrane
R-HSA-375165: NCAM signaling for neurite out-growth
R-HSA-446728: Cell junction organization
GO:1901615: organic hydroxy compound metabolic process
R-HSA-5083635: Defective B3GALTL causes PpS
GO:0008217: regulation of blood pressure
GO:0048729: tissue morphogenesis
GO:0031214: biomineral tissue development
GO:0048871: multicellular organismal-level homeostasis
GO:0140352: export from cell
GO:0051046: regulation of secretion
GO:0030111: regulation of Wnt signaling pathway
GO:0045765: regulation of angiogenesis
M5882: NABA PROTEOGLYCANS
GO:0030324: lung development
WP5053: Development of ureteric collection system
WP236: Adipogenesis
GO:0031012: extracellular matrix
WP382: MAPK signaling pathway
GO:0090257: regulation of muscle system process
GO:0098739: import across plasma membrane
GO:0042578: phosphoric ester hydrolase activity
GO:0005925: focal adhesion
GO:0005518: collagen binding
WP51: Regulation of actin cytoskeleton
R-HSA-6794362: Protein-protein interactions at synapses
GO:0002028: regulation of sodium ion transport
GO:0045499: chemorepellent activity
GO:0045216: cell-cell junction organization
GO:1902532: negative regulation of intracellular signal transduction
R-HSA-112316: Neuronal System
GO:0030029: actin filament-based process
GO:0070613: regulation of protein processing
WP2840: Hair follicle development cytodifferentiation part 3 of 3
GO:0040007: growth
GO:0006631: fatty acid metabolic process
WP5102: Familial partial lipodystrophy
Cluster 1 (Exploratory cohort [A-prePEAm vs. A-prePEAs])
Cluster 2 (Confirmatory cohort [B-prePEAm vs. B-prePEAs])

Figure 15. Top 20 and 100 overrepresented GO terms and pathways in moderate and severe risk groups. The Heatmap displays the top 20 (A) and 100 (B) overrepresented GO terms and for all the DEGs between the following comparisons: cluster 1 (exploratory cohort [A-prePEAm vs. A-prePEAs], and cluster 2 (confirmatory cohort [B-prePEAm vs. B-prePEAs]).

The top 20 and 100 overrepresented GO terms among clusters 2, 3, and 4 are illustrated in Figure 16 A and B. The top common regulated terms are linked with adipogenesis, a process related to the regulation of fat cell differentiation. This includes the differentiation of white and brown adipocytes, the transcriptional regulation of white adipocytes, as well as processes involved in metabolism such as fatty acid, monocarboxylic acid, and lipid catabolism. The TGF-beta, BMP, and Hippo signaling pathways are identified in clusters 2 and 3. Shared ECM-related terms between clusters 2 and 3 include external encapsulating structure, ECM proteoglycan, and integrin binding.

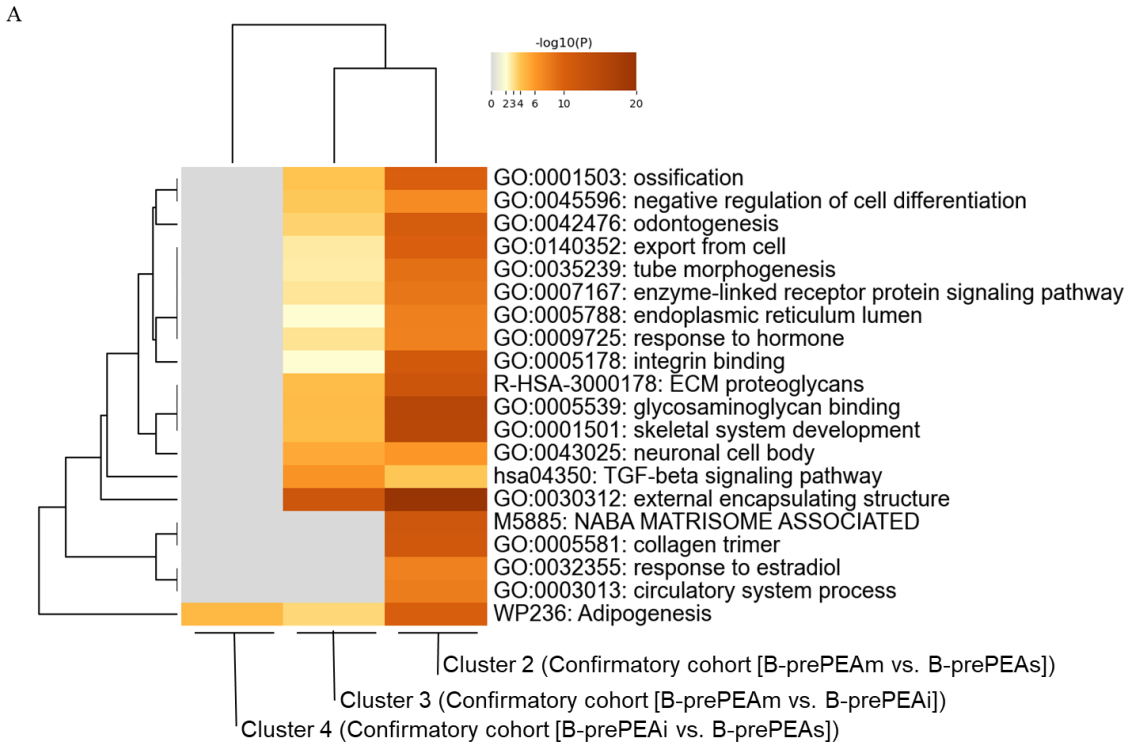

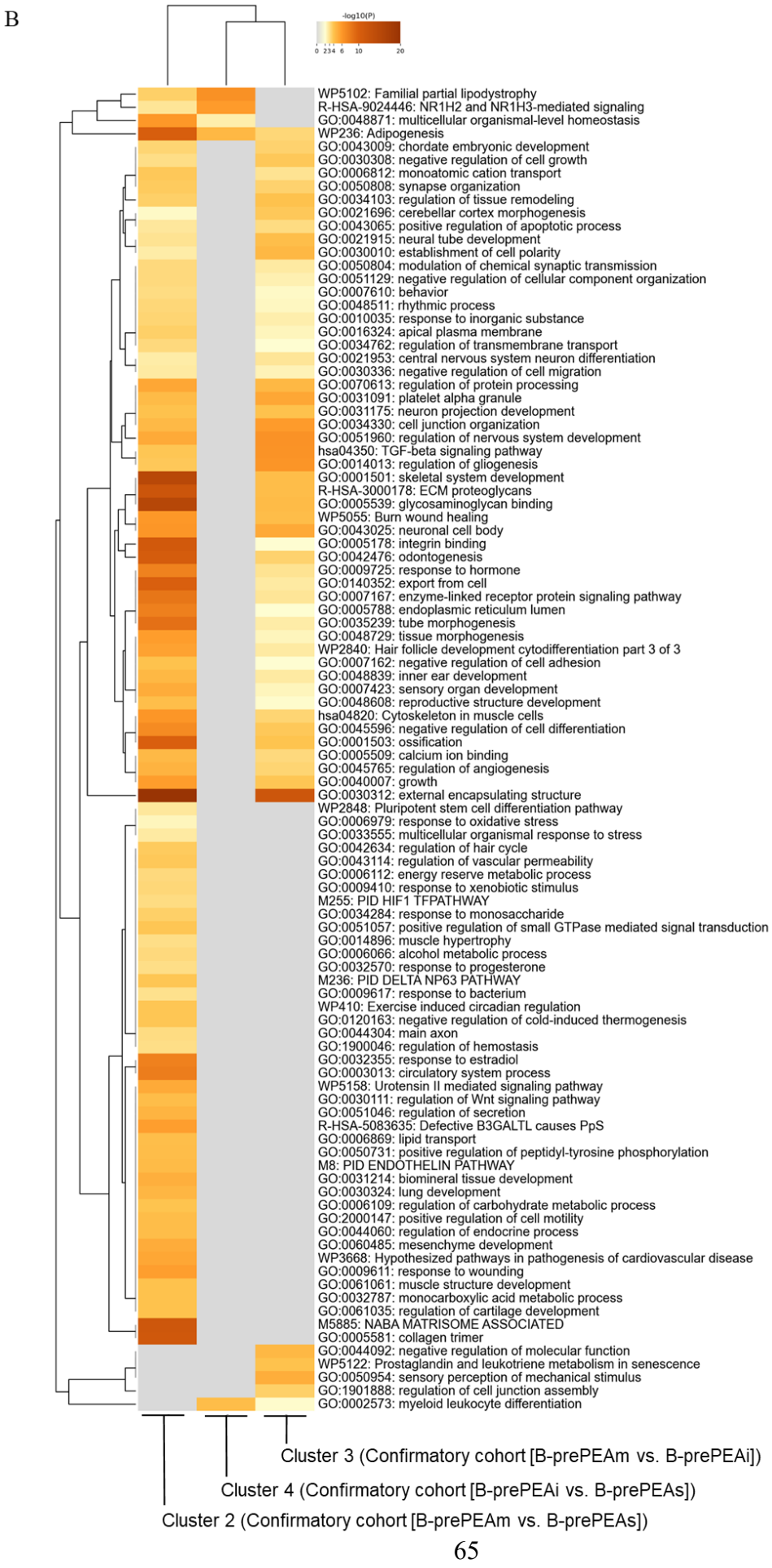
B
-log10(P)
0 2 3 4 6 10 20
WP5102: Familial partial lipodystrophy
R-HSA-9024446: NR1H2 and NR1H3-mediated signaling
GO:0048871: multicellular organismal-level homeostasis
WP236: Adipogenesis
GO:0043009: chordate embryonic development
GO:0030308: negative regulation of cell growth
GO:0006812: monoatomic cation transport
GO:0050808: synapse organization
GO:0034103: regulation of tissue remodeling
GO:0021696: cerebellar cortex morphogenesis
GO:0043065: positive regulation of apoptotic process
GO:0021915: neural tube development
GO:0030010: establishment of cell polarity
GO:0050804: modulation of chemical synaptic transmission
GO:0051129: negative regulation of cellular component organization
GO:0007610: behavior
GO:0048511: rhythmic process
GO:0010035: response to inorganic substance
GO:0016324: apical plasma membrane
GO:0034762: regulation of transmembrane transport
GO:0021953: central nervous system neuron differentiation
GO:0030336: negative regulation of cell migration
GO:0070613: regulation of protein processing
GO:0031091: platelet alpha granule
GO:0031175: neuron projection development
GO:0034330: cell junction organization
GO:0051960: regulation of nervous system development
hsa04350: TGF-beta signaling pathway
GO:0014013: regulation of gliogenesis
GO:0001501: skeletal system development
R-HSA-3000178: ECM proteoglycans
GO:0005539: glycosaminoglycan binding
WP5055: Burn wound healing
GO:0043025: neuronal cell body
GO:0005178: integrin binding
GO:0042476: odontogenesis
GO:0009725: response to hormone
GO:0140352: export from cell
GO:0007167: enzyme-linked receptor protein signaling pathway
GO:0005788: endoplasmic reticulum lumen
GO:0035239: tube morphogenesis
GO:0048729: tissue morphogenesis
WP2840: Hair follicle development cytodifferentiation part 3 of 3
GO:0007162: negative regulation of cell adhesion
GO:0048839: inner ear development
GO:0007423: sensory organ development
GO:0048608: reproductive structure development
hsa04820: Cytoskeleton in muscle cells
GO:0045596: negative regulation of cell differentiation
GO:0001503: ossification
GO:0005509: calcium ion binding
GO:0045765: regulation of angiogenesis
GO:0040007: growth
GO:0030312: external encapsulating structure
WP2848: Pluripotent stem cell differentiation pathway
GO:0006979: response to oxidative stress
GO:0033555: multicellular organismal response to stress
GO:0042634: regulation of hair cycle
GO:0043114: regulation of vascular permeability
GO:0006112: energy reserve metabolic process
GO:0009410: response to xenobiotic stimulus
M255: PID HIF1 TFPATHWAY
GO:0034284: response to monosaccharide
GO:0051057: positive regulation of small GTPase mediated signal transduction
GO:0014896: muscle hypertrophy
GO:0006066: alcohol metabolic process
GO:0032570: response to progesterone
M236: PID DELTA NP63 PATHWAY
GO:0009617: response to bacterium
WP410: Exercise induced circadian regulation
GO:0120163: negative regulation of cold-induced thermogenesis
GO:0044304: main axon
GO:1900046: regulation of hemostasis
GO:0032355: response to estradiol
GO:0003013: circulatory system process
WP5158: Urotensin II mediated signaling pathway
GO:0030111: regulation of Wnt signaling pathway
GO:0051046: regulation of secretion
R-HSA-5083635: Defective B3GALTL causes PpS
GO:0006869: lipid transport
GO:0050731: positive regulation of peptidyl-tyrosine phosphorylation
M8: PID ENDOTHELIN PATHWAY
GO:0031214: biomineral tissue development
GO:0030324: lung development
GO:0006109: regulation of carbohydrate metabolic process
GO:2000147: positive regulation of cell motility
GO:0044060: regulation of endocrine process
GO:0060485: mesenchyme development
WP3668: Hypothesized pathways in pathogenesis of cardiovascular disease
GO:0009611: response to wounding
GO:0061061: muscle structure development
GO:0032787: monocarboxylic acid metabolic process
GO:0061035: regulation of cartilage development
M5885: NABA MATRISOME ASSOCIATED
GO:0005581: collagen trimer
GO:0044092: negative regulation of molecular function
WP5122: Prostaglandin and leukotriene metabolism in senescence
GO:0050954: sensory perception of mechanical stimulus
GO:1901888: regulation of cell junction assembly
GO:0002573: myeloid leukocyte differentiation
Cluster 3 (Confirmatory cohort [B-prePEAm vs. B-prePEAi])
Cluster 4 (Confirmatory cohort [B-prePEAi vs. B-prePEAs])
Cluster 2 (Confirmatory cohort [B-prePEAm vs. B-prePEAs])

Figure 16. Top 20 and 100 verrepresented GO terms and pathways in B-prePEA patinets of confirmatoy cohort. The Heatmap displays the top 20 (A) and 100 (B) overrepresented GO terms for all the DEGs between the following comparisons: cluster 2 (confirmatory cohort [B-prePEAm vs. B-prePEAs]), cluster 3 (confirmatory cohort [B-prePEAm vs. B-prePEAi]), and cluster 4 (confirmatory cohort [B-prePEAi vs. B-prePEAs]).

Furthermore, Figure 17 A-B, shows the common and specific terms and pathways across clusters 1, 2 3, and 4. Adipogenesis is common in all the clusters. The term external encapsulating structure is predominantly expressed in clusters 1, 2, and 3. In addition, terms related to the heart muscle, such as cytoskeleton in muscle cells, and skeletal system development are also detected in clusters 1, 2, and 3. In cluster 4, B-prePEAi versus B-prePEAs, adipogenesis, familial partial lipodystrophy, NR1H2 and NR1H3- mediated signaling, oxidoreductase activity, intracellular chemical homeostasis, and multicellular organismal-level homeostasis are detected among 100 terms (Figure 17 B).

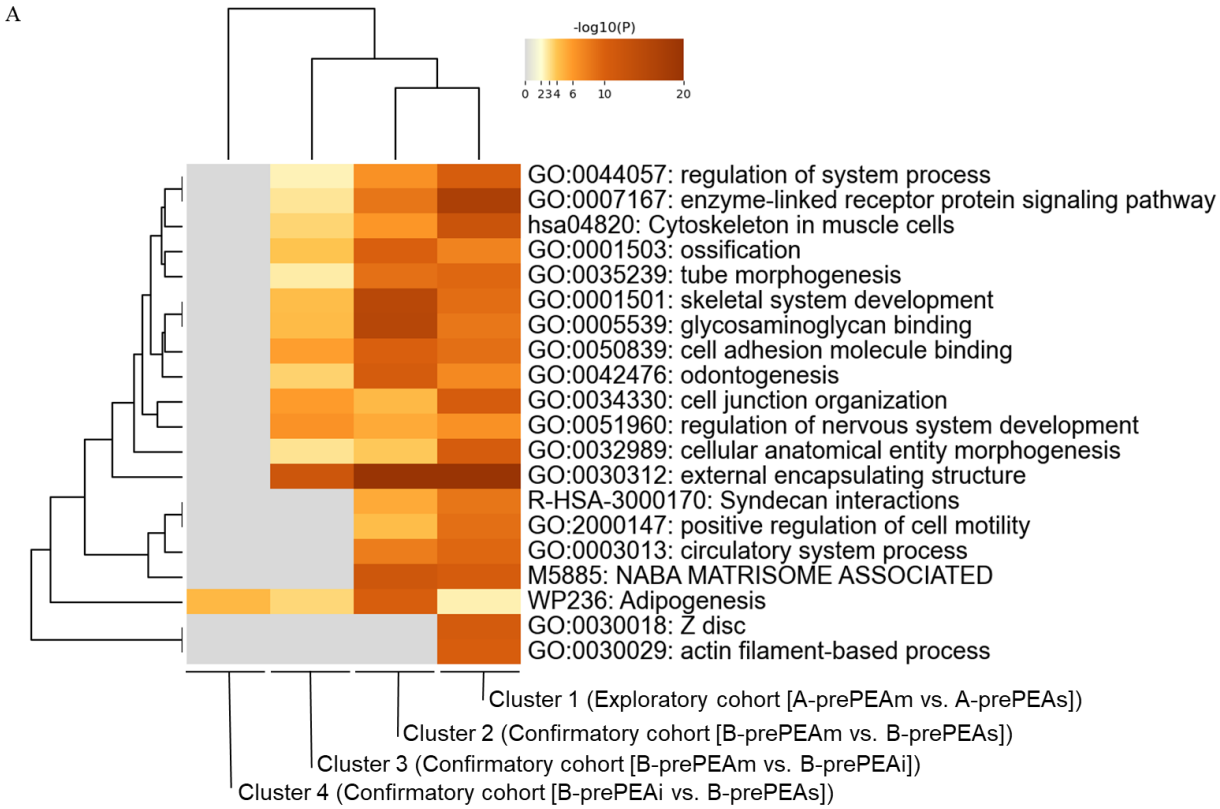

B

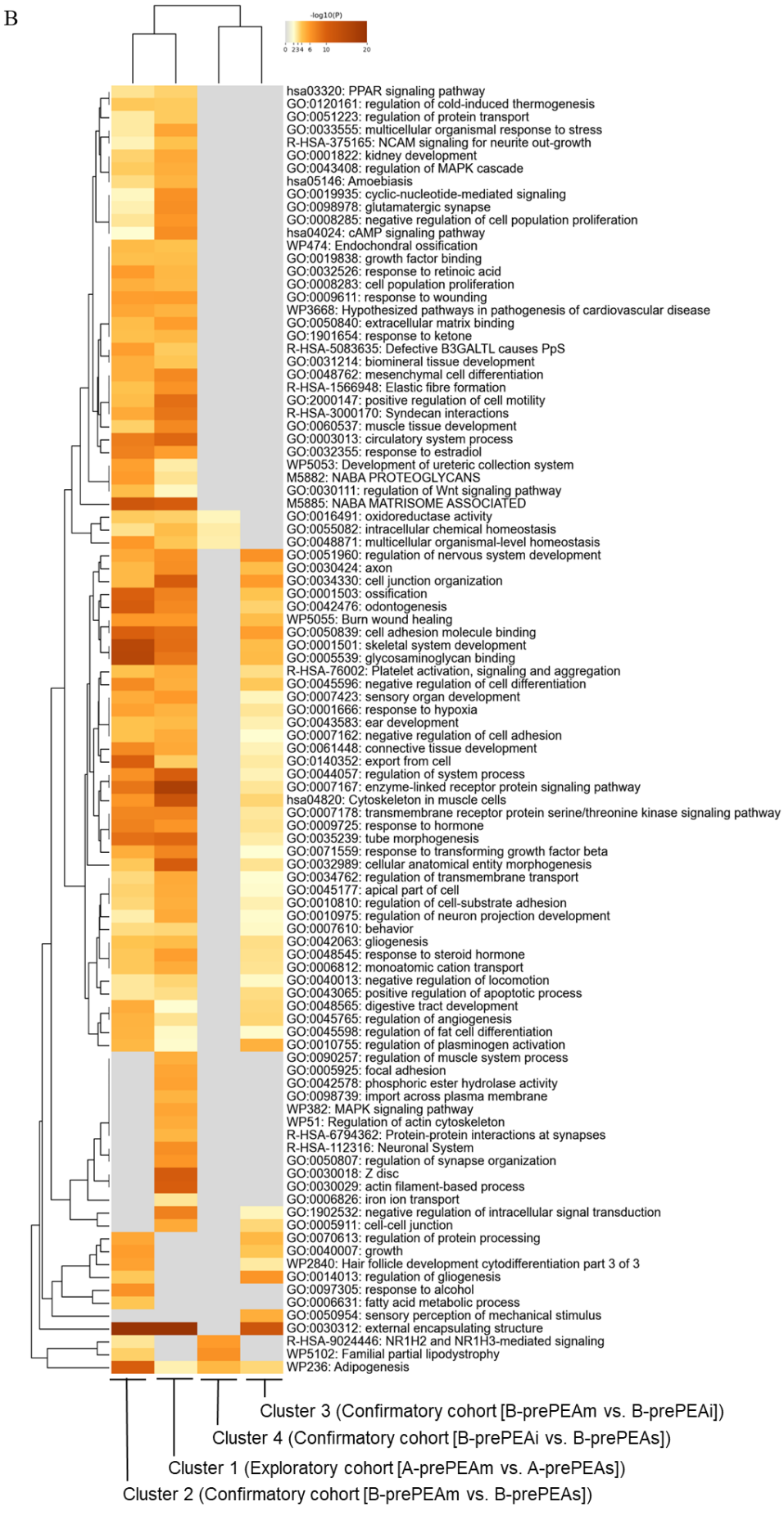
-log10(P)
0 2 3 4 6 10 20
hsa03320: PPAR signaling pathway
GO:0120161: regulation of cold-induced thermogenesis
GO:0051223: regulation of protein transport
GO:0033555: multicellular organismal response to stress
R-HSA-375165: NCAM signaling for neurite out-growth
GO:0001822: kidney development
GO:0043408: regulation of MAPK cascade
hsa05146: Amoebiasis
GO:0019935: cyclic-nucleotide-mediated signaling
GO:0098978: glutamatergic synapse
GO:0008285: negative regulation of cell population proliferation
hsa04024: cAMP signaling pathway
WP474: Endochondral ossification
GO:0019838: growth factor binding
GO:0032526: response to retinoic acid
GO:0008283: cell population proliferation
GO:0009611: response to wounding
WP3668: Hypothesized pathways in pathogenesis of cardiovascular disease
GO:0050840: extracellular matrix binding
GO:1901654: response to ketone
R-HSA-5083635: Defective B3GALTL causes PpS
GO:0031214: biomineral tissue development
GO:0048762: mesenchymal cell differentiation
R-HSA-1566948: Elastic fibre formation
GO:2000147: positive regulation of cell motility
R-HSA-3000170: Syndecan interactions
GO:0060537: muscle tissue development
GO:0003013: circulatory system process
GO:0032355: response to estradiol
WP5053: Development of ureteric collection system
M5882: NABA PROTEOGLYCANS
GO:0030111: regulation of Wnt signaling pathway
M5885: NABA MATRISOME ASSOCIATED
GO:0016491: oxidoreductase activity
GO:0055082: intracellular chemical homeostasis
GO:0048871: multicellular organismal-level homeostasis
GO:0051960: regulation of nervous system development
GO:0030424: axon
GO:0034330: cell junction organization
GO:0001503: ossification
GO:0042476: odontogenesis
WP5055: Burn wound healing
GO:0050839: cell adhesion molecule binding
GO:0001501: skeletal system development
GO:0005539: glycosaminoglycan binding
R-HSA-76002: Platelet activation, signaling and aggregation
GO:0045596: negative regulation of cell differentiation
GO:0007423: sensory organ development
GO:0001666: response to hypoxia
GO:0043583: ear development
GO:0007162: negative regulation of cell adhesion
GO:0061448: connective tissue development
GO:0140352: export from cell
GO:0044057: regulation of system process
GO:0007167: enzyme-linked receptor protein signaling pathway
hsa04820: Cytoskeleton in muscle cells
GO:0007178: transmembrane receptor protein serine/threonine kinase signaling pathway
GO:0009725: response to hormone
GO:0035239: tube morphogenesis
GO:0071559: response to transforming growth factor beta
GO:0032989: cellular anatomical entity morphogenesis
GO:0034762: regulation of transmembrane transport
GO:0045177: apical part of cell
GO:0010810: regulation of cell-substrate adhesion
GO:0010975: regulation of neuron projection development
GO:0007610: behavior
GO:0042063: gliogenesis
GO:0048545: response to steroid hormone
GO:0006812: monoatomic cation transport
GO:0040013: negative regulation of locomotion
GO:0043065: positive regulation of apoptotic process
GO:0048565: digestive tract development
GO:0045765: regulation of angiogenesis
GO:0045598: regulation of fat cell differentiation
GO:0010755: regulation of plasminogen activation
GO:0090257: regulation of muscle system process
GO:0005925: focal adhesion
GO:0042578: phosphoric ester hydrolase activity
GO:0098739: import across plasma membrane
WP382: MAPK signaling pathway
WP51: Regulation of actin cytoskeleton
R-HSA-6794362: Protein-protein interactions at synapses
R-HSA-112316: Neuronal System
GO:0050807: regulation of synapse organization
GO:0030018: Z disc
GO:0030029: actin filament-based process
GO:0006826: iron ion transport
GO:1902532: negative regulation of intracellular signal transduction
GO:0005911: cell-cell junction
GO:0070613: regulation of protein processing
GO:0040007: growth
WP2840: Hair follicle development cytodifferentiation part 3 of 3
GO:0014013: regulation of gliogenesis
GO:0097305: response to alcohol
GO:0006631: fatty acid metabolic process
GO:0050954: sensory perception of mechanical stimulus
GO:0030312: external encapsulating structure
R-HSA-9024446: NR1H2 and NR1H3-mediated signaling
WP5102: Familial partial lipodystrophy
WP236: Adipogenesis
Cluster 3 (Confirmatory cohort [B-prePEAm vs. B-prePEAi])
Cluster 4 (Confirmatory cohort [B-prePEAi vs. B-prePEAs])
Cluster 1 (Exploratory cohort [A-prePEAm vs. A-prePEAs])
Cluster 2 (Confirmatory cohort [B-prePEAm vs. B-prePEAs])

Figure 17. Top 20 and 100 verrepresented GO terms and pathways in the exploratory and confirmatory of CTEPH patients before PEA. The Heatmap displays the top 20 (A) and 100 (B) overrepresented GO terms for all the DEGs between the following comparisons: cluster 1 (exploratory cohort [A-prePEAm vs. A-prePEAs], cluster 2 (confirmatory cohort [B-prePEAm vs. B-prePEAs]), cluster 3 (confirmatory cohort [B-prePEAm vs. B-prePEAi]), and cluster 4 (confirmatory cohort [B-prePEAi vs. B-prePEAs]).

4.10. DEGs between the B-prePEA and B-postPEA groups in the confirmatory cohort

Among the B-prePEA patients, there was a subgroup of patients (n = 21) with a biopsy from the septum (postPEA, n = 21) that was collected 12 months after PEA (Table 21). RNA-seq analysis was performed on the RV (B-prePEA, n = 21) and septum (B-postPEA, n = 21). The patients in the B-prePEA group were placed into moderate (B-prePEAm, n = 9), intermediate (B-prePEAi, n = 8), and severe (B-prePEAs, n = 4) risk groups based on their clinical parameters and following ECS/ERS guidelines. PCA determines the kinetics of RV and septum in B-prePEA and B-postPEA, B-prePEAm and B-postPEAm, B-prePEAi and B-postPEAi, B-prePEAs and B-postPEAs (Figure 18 A-D). The PCA plots illustrate the discrimination of RV and septum through the PC1.

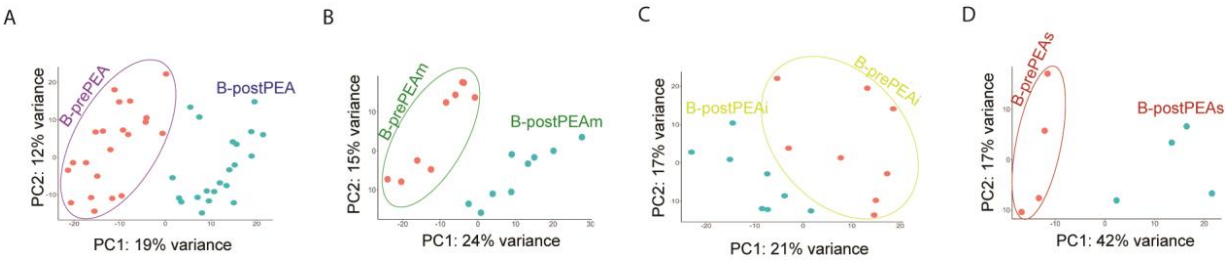

Figure 18. PCA of the RNA-seq data. Changes in gene expression were investigated in the confirmatory cohort of (A) B-prePEA [n = 21] and B-postPEA [n = 21], (B) B-prePEAm [n = 9] and B-postPEAm [n = 9], (C) B-prePEAi [n = 8] and B-postPEAi [n = 8], (D) B-prePEAs [n = 4] and B-postPEAs [n = 4].

The RNA-seq analysis revealed that the total number of DEGs (base mean ≥ 5; $|\log_2(FC)| \geq 0.585$; Padj ≤ 0.05, two-sided) in B-postPEA vs. B-prePEA were 1492 with 891 upregulated genes and 601 down-regulated genes (Figure 19 A). In the contrast between B-postPEAm and B-prePEAm 1082 DEGs were identified, of which 615 were observed upregulated and 467 were downregulated (Figure 19 B). When assessing B-postPEAi versus B-prePEAi, the total number of DEGs amounted to 701, comprising 306 upregulated genes and 395 downregulated genes (Figure 19 C). In the comparison of B-postPEAs to B-prePEAs, a total of 1026 genes were found to be differentially expressed, including 520 genes that were upregulated and 506 genes that were downregulated (Figure 19 D).

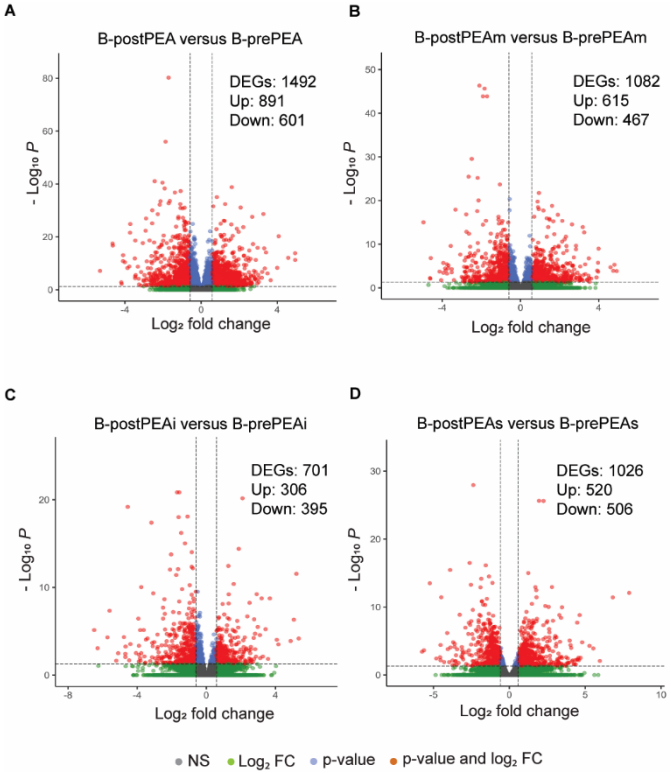

Figure 19. Volcano plots of differentially expressed genes. The volcano plot shows the DEGs in the confirmatory cohort of (A) B-postPEA [n = 21] versus B-prePEA [n = 21], (B) B-postPEAm [n = 9] versus B-prePEAm [n = 9], (C) B-postPEAi [n = 8] versus B-prePEAi [n = 8], (D) B-postPEAs [n = 4] versus B-prePEAs [n = 4]. The significant DEGs (base mean expression ≥ 5; $|\log_2(FC)| \geq 0.585$; Padj ≤ 0.05, two sided) were classified based on $P < 0.05$ and $|\log_2(FC)| > 0.585$ (red dots), only P value (blue dots), $\log_2(FC)$ (green dots) and not significant (gray dots).

The heatmaps show the top 50 DEGs between the postPEA versus pre-PEA, postPEAm versus pre-PEAm, postPEAi versus pre-PEAi, postPEAs versus pre-PEAs (Figure 20 A-D).

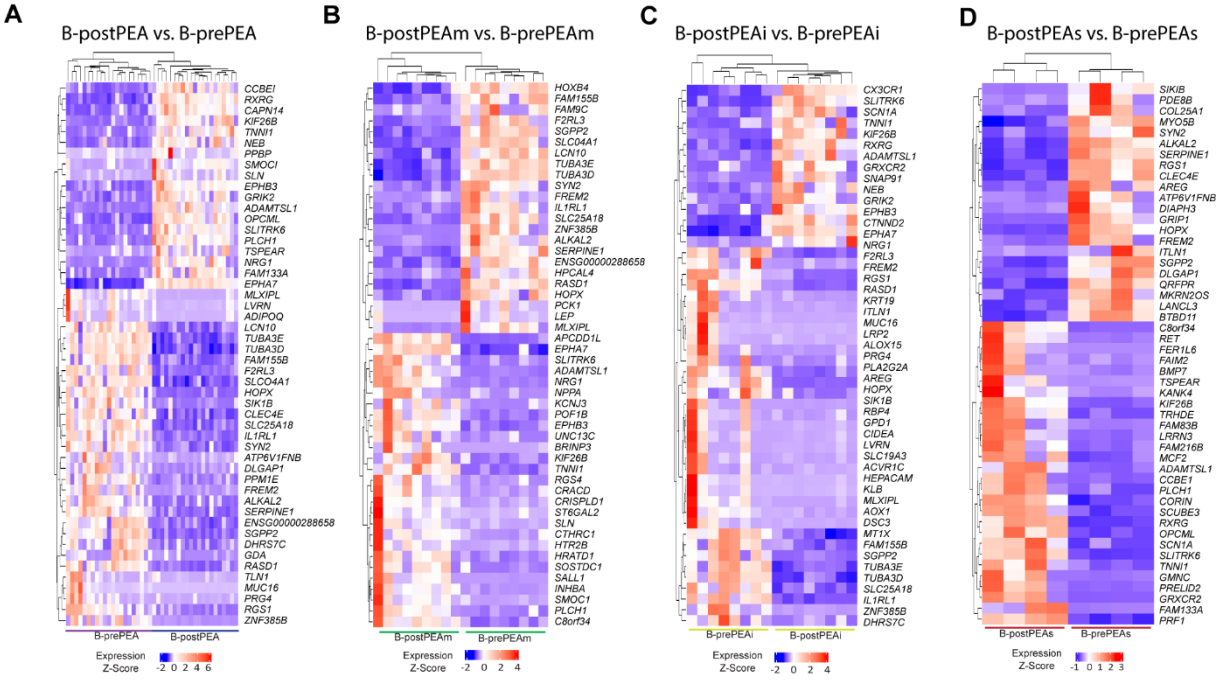

Figure 20. Heatmaps of DEGs in the RNA-seq data. Heatmaps showing the z-score of the top DEGs in the confirmatory cohort of (A) B-postPEA [n = 21] versus B-prePEA [n = 21], (B) B-postPEAm [n = 9] versus B-prePEAm [n = 9], (C) B-postPEAi [n = 8] versus B-prePEAi [n = 8], (D)B-postPEAs [n = 4] versus B-prePEA [n = 4].

4.11. Pathway analysis in the confirmatory cohort of B-postPEA versus B-prePEA

For the pathway analysis, distinctive clusters have been assigned to post and pre PEA: in the confirmatory cohort, B-postPEA vs. B-prePEA is identified as cluster 5, B-postPEAs vs. B-prePEAs is designated as cluster 6, B-postPEAm vs. B-prePEAm is defined as cluster 7, and B-postPEAi vs. B-prePEAi builds cluster 8. The pathway analysis was performed taking into account the DEGs from each cluster, with specific criteria of a base mean expression ≥ 5; $|\log_2(FC)| \geq 0.585$; $P\text{adj} \leq 0.05$.

The top 20 and 100 overrepresented GO terms among clusters 5,6,7, and 8 are illustrated in Figure 21 A-D. Tube morphogenesis, vascular development, and angiogenesis are expressively prevalent across clusters 5,6,7 and 8. Interestingly, among the top 100 GO terms and patheway, the inflammatory response was absent in cluster 6 (B-postPEAs vs. B-prePEAs). In contrast, the expression of the AGE-RAGE signaling pathway, VEGFA VEGFR2 signaling, PI3K Akt signaling pathway, and cytokine signaling in the immune system, were elevated in cluster 6 compared to the other clusters. The terms external encapsulating structure, ECM organization, and NABA MATRISOME ASSOCIATED- an Ensemble of genes that encode ECM-associated proteins such as ECM-affiliated proteins, ECM regulators, and secreted factors - are expressed throughout all the clusters.

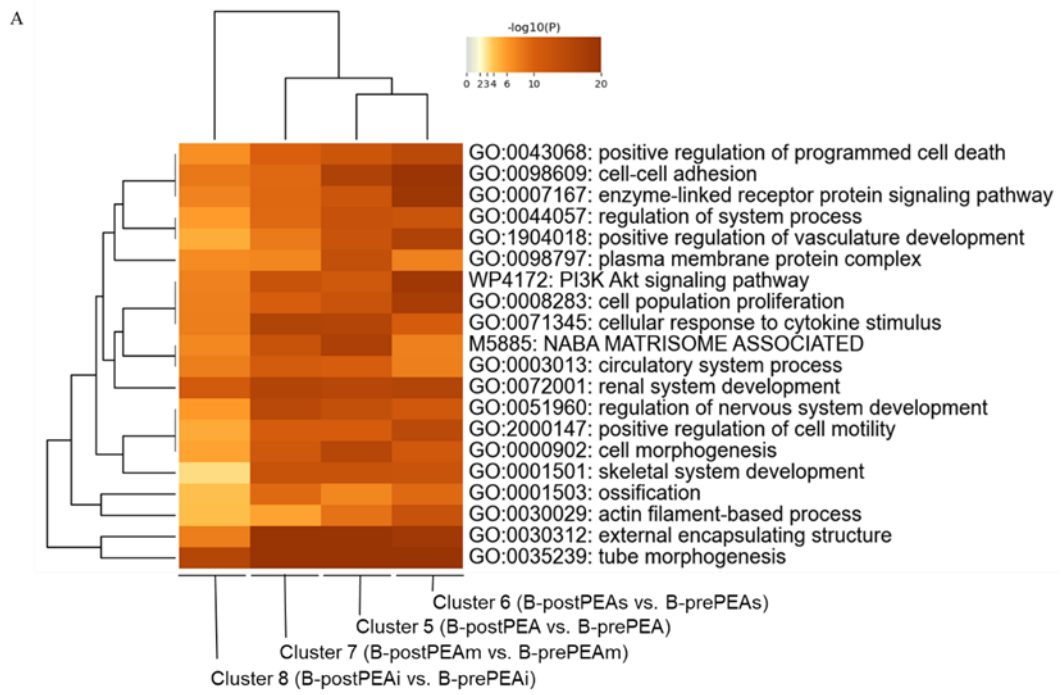
A
-log10(P)
0 234 6 10 20
GO:0043068: positive regulation of programmed cell death
GO:0098609: cell-cell adhesion
GO:0007167: enzyme-linked receptor protein signaling pathway
GO:0044057: regulation of system process
GO:1904018: positive regulation of vasculature development
GO:0098797: plasma membrane protein complex
WP4172: PI3K Akt signaling pathway
GO:0008283: cell population proliferation
GO:0071345: cellular response to cytokine stimulus
M5885: NABA MATRISOME ASSOCIATED
GO:0003013: circulatory system process
GO:0072001: renal system development
GO:0051960: regulation of nervous system development
GO:2000147: positive regulation of cell motility
GO:0000902: cell morphogenesis
GO:0001501: skeletal system development
GO:0001503: ossification
GO:0030029: actin filament-based process
GO:0030312: external encapsulating structure
GO:0035239: tube morphogenesis
Cluster 6 (B-postPEAs vs. B-prePEAs)
Cluster 5 (B-postPEA vs. B-prePEA)
Cluster 7 (B-postPEAm vs. B-prePEAm)
Cluster 8 (B-postPEAi vs. B-prePEAi)

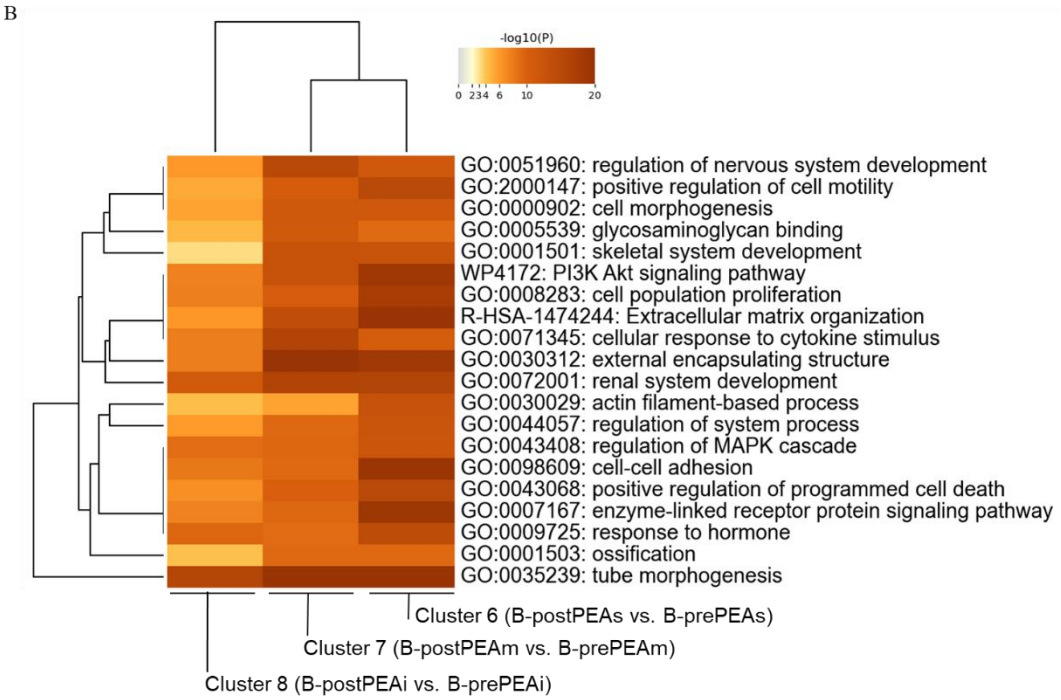
B
-log10(P)
0 234 6 10 20
GO:0051960: regulation of nervous system development
GO:2000147: positive regulation of cell motility
GO:0000902: cell morphogenesis
GO:0005539: glycosaminoglycan binding
GO:0001501: skeletal system development
WP4172: PI3K Akt signaling pathway
GO:0008283: cell population proliferation
R-HSA-1474244: Extracellular matrix organization
GO:0071345: cellular response to cytokine stimulus
GO:0030312: external encapsulating structure
GO:0072001: renal system development
GO:0030029: actin filament-based process
GO:0044057: regulation of system process
GO:0043408: regulation of MAPK cascade
GO:0098609: cell-cell adhesion
GO:0043068: positive regulation of programmed cell death
GO:0007167: enzyme-linked receptor protein signaling pathway
GO:0009725: response to hormone
GO:0001503: ossification
GO:0035239: tube morphogenesis
Cluster 6 (B-postPEAs vs. B-prePEAs)
Cluster 7 (B-postPEAm vs. B-prePEAm)
Cluster 8 (B-postPEAi vs. B-prePEAi)

C

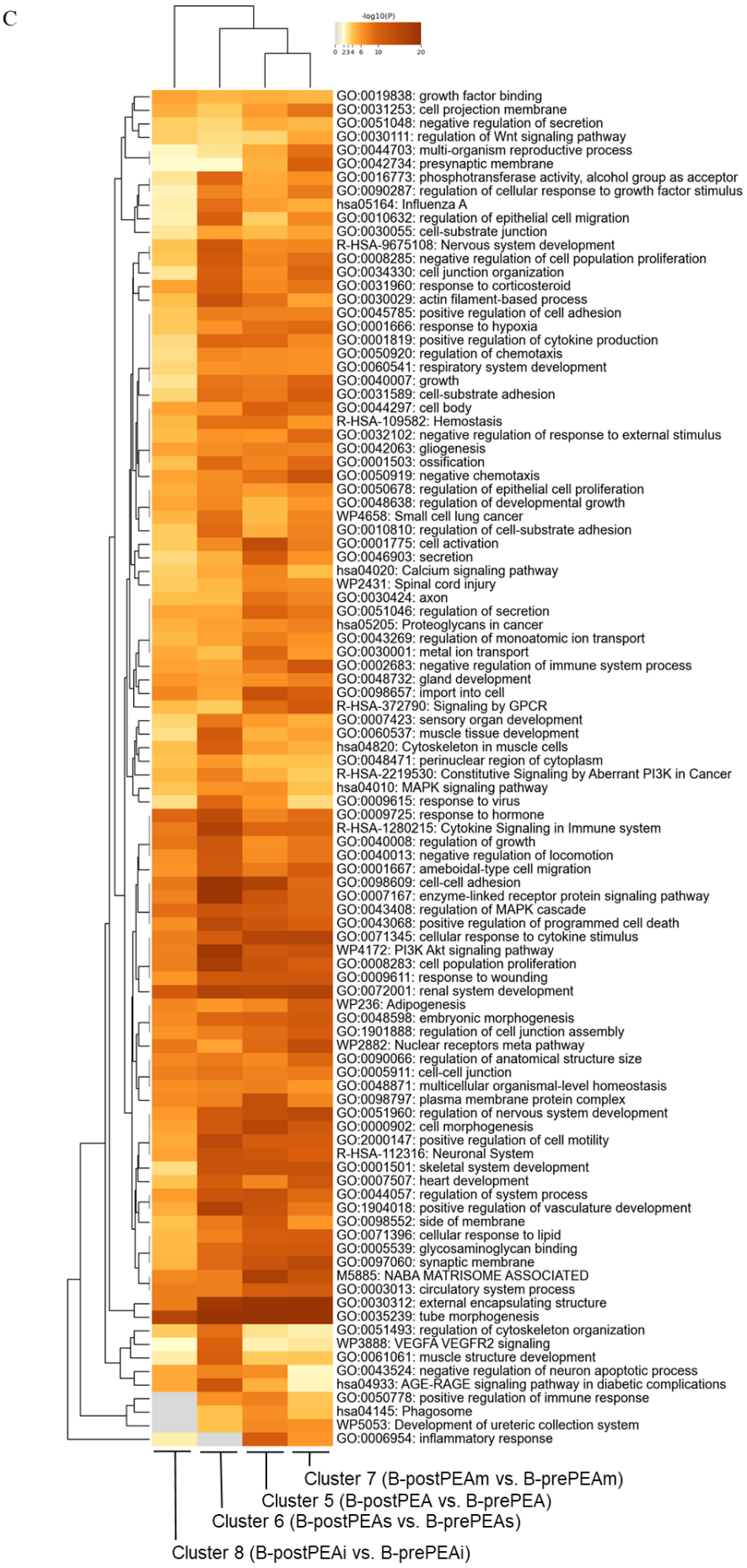
-log10(P)
0 2 3 4 6 10 20
GO:0019838: growth factor binding
GO:0031253: cell projection membrane
GO:0051048: negative regulation of secretion
GO:0030111: regulation of Wnt signaling pathway
GO:0044703: multi-organism reproductive process
GO:0042734: presynaptic membrane
GO:0016773: phosphotransferase activity, alcohol group as acceptor
GO:0090287: regulation of cellular response to growth factor stimulus
hsa05164: Influenza A
GO:0010632: regulation of epithelial cell migration
GO:0030055: cell-substrate junction
R-HSA-9675108: Nervous system development
GO:0008285: negative regulation of cell population proliferation
GO:0034330: cell junction organization
GO:0031960: response to corticosteroid
GO:0030029: actin filament-based process
GO:0045785: positive regulation of cell adhesion
GO:0001666: response to hypoxia
GO:0001819: positive regulation of cytokine production
GO:0050920: regulation of chemotaxis
GO:0060541: respiratory system development
GO:0040007: growth
GO:0031589: cell-substrate adhesion
GO:0044297: cell body
R-HSA-109582: Hemostasis
GO:0032102: negative regulation of response to external stimulus
GO:0042063: gliogenesis
GO:0001503: ossification
GO:0050919: negative chemotaxis
GO:0050678: regulation of epithelial cell proliferation
GO:0048638: regulation of developmental growth
WP4658: Small cell lung cancer
GO:0010810: regulation of cell-substrate adhesion
GO:0001775: cell activation
GO:0046903: secretion
hsa04020: Calcium signaling pathway
WP2431: Spinal cord injury
GO:0030424: axon
GO:0051046: regulation of secretion
hsa05205: Proteoglycans in cancer
GO:0043269: regulation of monoatomic ion transport
GO:0030001: metal ion transport
GO:0002683: negative regulation of immune system process
GO:0048732: gland development
GO:0098657: import into cell
R-HSA-372790: Signaling by GPCR
GO:0007423: sensory organ development
GO:0060537: muscle tissue development
hsa04820: Cytoskeleton in muscle cells
GO:0048471: perinuclear region of cytoplasm
R-HSA-2219530: Constitutive Signaling by Aberrant PI3K in Cancer
hsa04010: MAPK signaling pathway
GO:0009615: response to virus
GO:0009725: response to hormone
R-HSA-1280215: Cytokine Signaling in Immune system
GO:0040008: regulation of growth
GO:0040013: negative regulation of locomotion
GO:0001667: ameboidal-type cell migration
GO:0098609: cell-cell adhesion
GO:0007167: enzyme-linked receptor protein signaling pathway
GO:0043408: regulation of MAPK cascade
GO:0043068: positive regulation of programmed cell death
GO:0071345: cellular response to cytokine stimulus
WP4172: PI3K Akt signaling pathway
GO:0008283: cell population proliferation
GO:0009611: response to wounding
GO:0072001: renal system development
WP236: Adipogenesis
GO:0048598: embryonic morphogenesis
GO:1901888: regulation of cell junction assembly
WP2882: Nuclear receptors meta pathway
GO:0090066: regulation of anatomical structure size
GO:0005911: cell-cell junction
GO:0048871: multicellular organismal-level homeostasis
GO:0098797: plasma membrane protein complex
GO:0051960: regulation of nervous system development
GO:0000902: cell morphogenesis
GO:2000147: positive regulation of cell motility
R-HSA-112316: Neuronal System
GO:0001501: skeletal system development
GO:0007507: heart development
GO:0044057: regulation of system process
GO:1904018: positive regulation of vasculature development
GO:0098552: side of membrane
GO:0071396: cellular response to lipid
GO:0005539: glycosaminoglycan binding
GO:0097060: synaptic membrane
M5885: NABA MATRISOME ASSOCIATED
GO:0003013: circulatory system process
GO:0030312: external encapsulating structure
GO:0035239: tube morphogenesis
GO:0051493: regulation of cytoskeleton organization
WP3888: VEGFA VEGFR2 signaling
GO:0061061: muscle structure development
GO:0043524: negative regulation of neuron apoptotic process
hsa04933: AGE-RAGE signaling pathway in diabetic complications
GO:0050778: positive regulation of immune response
hsa04145: Phagosome
WP5053: Development of ureteric collection system
GO:0006954: inflammatory response
Cluster 7 (B-postPEAm vs. B-prePEAm)
Cluster 5 (B-postPEA vs. B-prePEA)
Cluster 6 (B-postPEAs vs. B-prePEAs)
Cluster 8 (B-postPEAi vs. B-prePEAi)

D


-log10(P)
0 2 3 4 6 10 20
GO:0071396: cellular response to lipid
GO:0005539: glycosaminoglycan binding
GO:0097060: synaptic membrane
GO:0002683: negative regulation of immune system process
GO:0048863: stem cell differentiation
GO:0031589: cell-substrate adhesion
GO:0048471: perinuclear region of cytoplasm
GO:0042391: regulation of membrane potential
GO:0036293: response to decreased oxygen levels
R-HSA-109582: Hemostasis
GO:0030097: hemopoiesis
GO:0032103: positive regulation of response to external stimulus
GO:0048638: regulation of developmental growth
GO:0042063: gliogenesis
GO:0001503: ossification
GO:0098552: side of membrane
GO:0005178: integrin binding
GO:0030424: axon
GO:0051046: regulation of secretion
GO:0045178: basal part of cell
GO:0007162: negative regulation of cell adhesion
hsa05205: Proteoglycans in cancer
GO:0044283: small molecule biosynthetic process
GO:0043269: regulation of monoatomic ion transport
GO:0046903: secretion
WP2431: Spinal cord injury
GO:0048598: embryonic morphogenesis
GO:0003013: circulatory system process
WP236: Adipogenesis
M5885: NABA MATRISOME ASSOCIATED
GO:1901888: regulation of cell junction assembly
WP2882: Nuclear receptors meta pathway
GO:0048732: gland development
GO:0098657: import into cell
GO:0048871: multicellular organismal-level homeostasis
GO:0005911: cell-cell junction
GO:0098797: plasma membrane protein complex
WP4172: PI3K Akt signaling pathway
GO:0001667: ameboidal-type cell migration
GO:0071345: cellular response to cytokine stimulus
GO:0008283: cell population proliferation
GO:0009611: response to wounding
R-HSA-1474244: Extracellular matrix organization
GO:0072001: renal system development
GO:0009725: response to hormone
R-HSA-1280215: Cytokine Signaling in Immune system
GO:0040008: regulation of growth
GO:0007167: enzyme-linked receptor protein signaling pathway
GO:0040013: negative regulation of locomotion
GO:0042327: positive regulation of phosphorylation
GO:0098609: cell-cell adhesion
GO:0043408: regulation of MAPK cascade
GO:0043068: positive regulation of programmed cell death
GO:0051960: regulation of nervous system development
GO:0000902: cell morphogenesis
GO:2000147: positive regulation of cell motility
R-HSA-112316: Neuronal System
GO:0007507: heart development
GO:0030029: actin filament-based process
hsa04820: Cytoskeleton in muscle cells
GO:0044057: regulation of system process
GO:0048545: response to steroid hormone
GO:0061061: muscle structure development
R-HSA-913531: Interferon Signaling
hsa04072: Phospholipase D signaling pathway
hsa05164: Influenza A
GO:0030055: cell-substrate junction
R-HSA-9675108: Nervous system development
GO:0008285: negative regulation of cell population proliferation
GO:0001501: skeletal system development
GO:0034330: cell junction organization
GO:0016773: phosphotransferase activity, alcohol group as acceptor
GO:0090287: regulation of cellular response to growth factor stimulus
GO:0001819: positive regulation of cytokine production
GO:0045785: positive regulation of cell adhesion
GO:0050920: regulation of chemotaxis
GO:0060541: respiratory system development
GO:0010810: regulation of cell-substrate adhesion
GO:0048589: developmental growth
GO:0001775: cell activation
hsa04010: MAPK signaling pathway
GO:0007423: sensory organ development
GO:0030312: external encapsulating structure
GO:0035239: tube morphogenesis
GO:0044703: multi-organism reproductive process
GO:0030111: regulation of Wnt signaling pathway
R-HSA-372790: Signaling by GPCR
GO:0031253: cell projection membrane
GO:0043292: contractile fiber
hsa04210: Apoptosis
WP3888: VEGFA VEGFR2 signaling
GO:0051493: regulation of cytoskeleton organization
GO:0051896: regulation of phosphatidylinositol 3-kinase/protein kinase B signal transduction
GO:0019199: transmembrane receptor protein kinase activity
R-HSA-397014: Muscle contraction
hsa04933: AGE-RAGE signaling pathway in diabetic complications
GO:0043523: regulation of neuron apoptotic process
WP5053: Development of ureteric collection system
GO:0090100: positive regulation of transmembrane receptor protein serine/threonine kinase signaling pathway
GO:0098644: complex of collagen trimers
Cluster 6 (B-postPEAs vs. B-prePEAs)
Cluster 7 (B-postPEAm vs. B-prePEAm)
Cluster 8 (B-postPEAi vs. B-prePEAi)

Figure 21. Top 20 and 100 overrepresented GO terms and pathways of pre and post PEA. (A) The Heatmap displays the top 20 overrepresented GO terms for all the DEGs between the following comparisons: cluster 5 (B-postPEA vs. B-prePEA), cluster 6 (B-postPEAs vs. B-prePEAs), cluster 7 (B-postPEAm vs. B-prePEAm), and cluster 8 (B-postPEAi vs. B-prePEAi). (B) The heatmap depicts the top 20 overrepresented GO terms between cluster 6 (B-postPEAs vs. B-prePEAs), cluster 7 (B-postPEAm vs. B-prePEAm), and cluster 8 (B-postPEAi vs. B-prePEAi). (C) The heatmap shows 100 overrepresented GO terms between cluster 5 (B-postPEA vs. B-prePEA), cluster 6 (B-postPEAs vs. B-prePEAs), cluster 7 (B-postPEAm vs. B-prePEAm), and cluster 8 (B-postPEAi vs. B-prePEAi). (D) The heatmap represents the top 100 overrepresented GO terms between cluster 6 (B-postPEAs vs. B-prePEAs), cluster 7 (B-postPEAm vs. B-prePEAm), and cluster 8 (B-postPEAi vs. B-prePEAi).

4.12. Analysis of the transcriptomic profile of the right ventricle and septum at prePEA and comparing it to the septum at postPEA in patient-paired samples

In a subgroup of B-prePEA patients, we had three unique patients with biopsies obtained from both the septum and RV prior to PEA (B-pre-septal-PEA, $n = 3$ and B-prePEA, $n = 3$), as well as septum biopsy collected 12 months after PEA (B-postPEA; $n = 3$). RNA-seq was performed to uncover the impact of PEA on the gene expression of RV and septum. PCA plot shows a clear segregation between RV and septum through the PC1. Whereas, the B-pre-septal-PEA and B-postPEA clusters are separable through the PC2 (Figure 22).

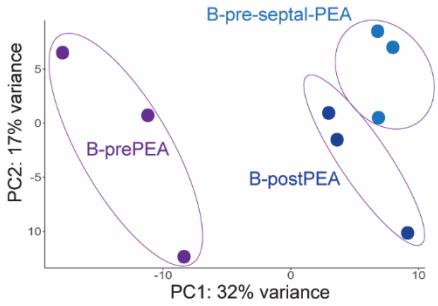

Figure 22. PCA of the RNA-seq data. Changes in gene expression were investigated in the confirmatory cohort of B-prePEA [$n = 3$], B-pre-septal-PEA [$n = 3$], and B-postPEA [$n = 3$].

The RNA-seq analysis identified a total of 394 DEGs between B-prePEA and B-pre-septal-PEA with 221 upregulated genes and 173 down-regulated genes (Figure 23 A), using a stringent threshold of base mean ≥ 5; $|\log_2(FC)| \geq 0.585$; and $P\text{adj} \leq 0.05$ (two-sided). In contrast, the comparison between B-postPEA and B-pre-septal-PEAm revealed 27 DEGs, with 12 upregulated and 15 downregulated (Figure 23 B). Additionally, when comparing B-postPEA to B-prePEA, we identified 301 DEGs, consisting of 128 upregulated genes and 173 downregulated genes (Figure 23 C).

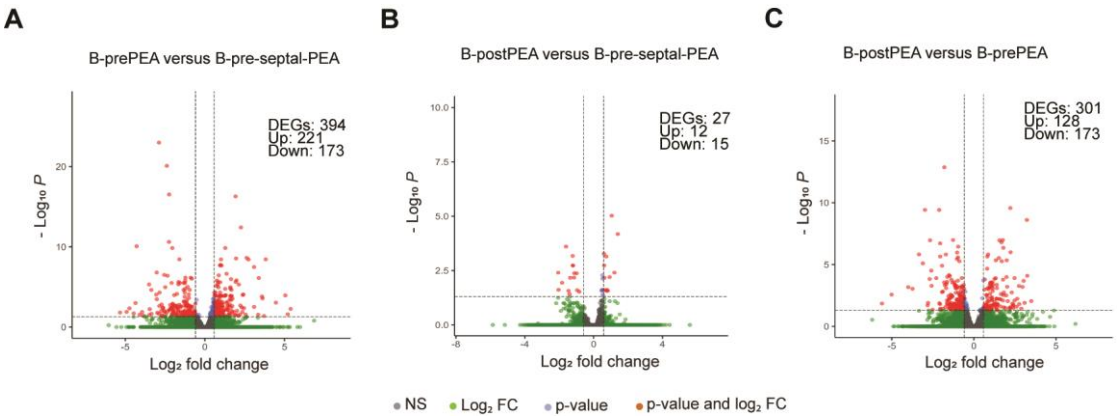

Figure 23. Volcano plots of differentially expressed genes. The volcano plot shows the DEGs in the confirmatory cohort of (A) B-prePEA [n = 3] versus B-pre-septal-PEA [n = 3], (B) B-postPEA [n = 3] versus B-pre-septal-PEA [n = 3], (C) B-postPEA [n = 3] versus B-prePEA [n = 3]. The DEGs were classified based on $P < 0.05$ and $|\log_2(FC)| > 0.585$ (red dots), only P value (blue dots), log2(FC) (green dots) and not significant (gray dots).

The heatmaps show the top 50 DEGs between the B-prePEA versus B-pre-septal-PEA, B-postPEA versus B-pre-septal-PEA, B-postPEA versus B-pre-PEA (Figure 24 A-C).

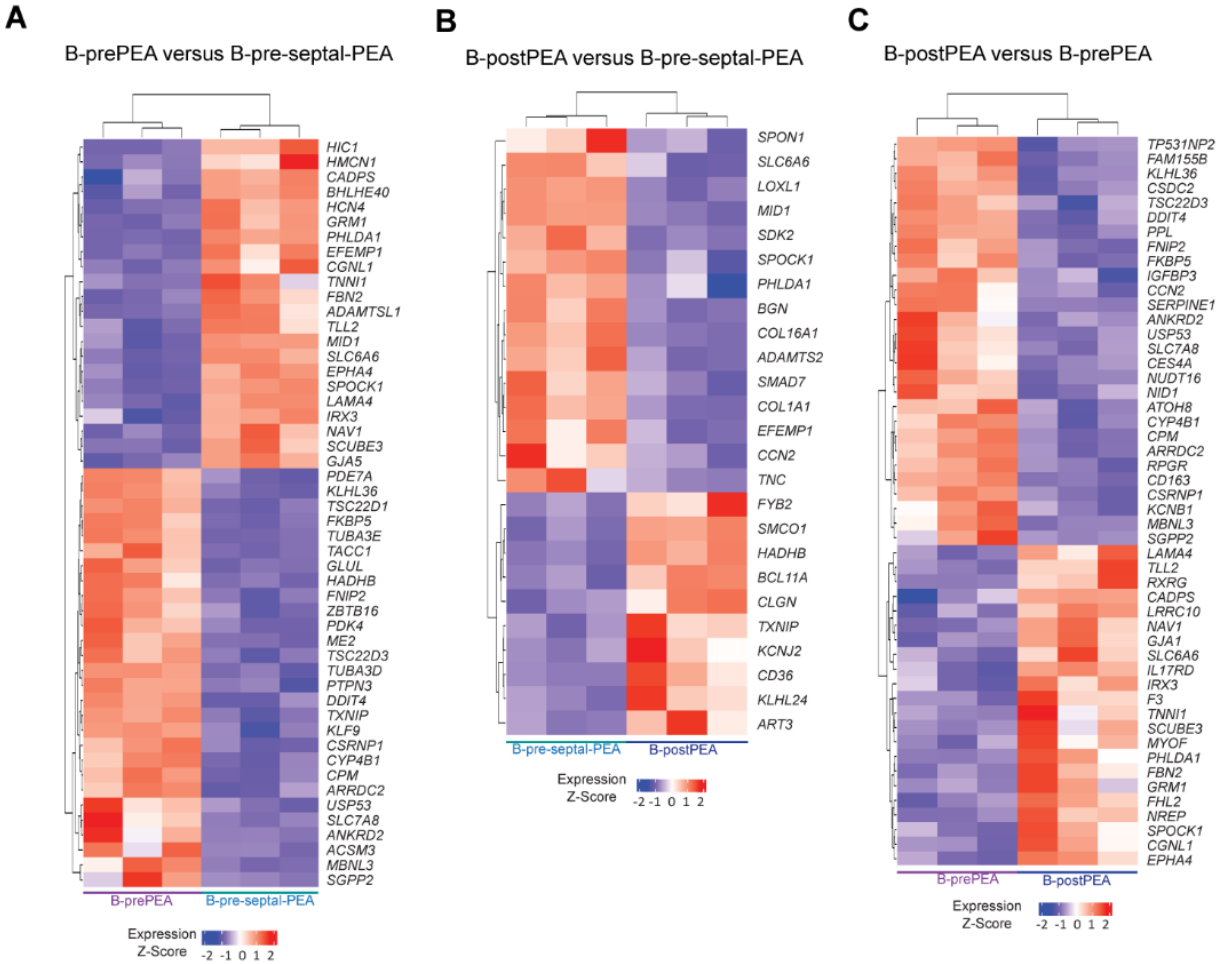

Figure 24. Heatmaps of DEGs in the RNA-seq data. Heatmaps showing the z-score of the top DEGs in the confirmatory cohort of (A) B-prePEA [n = 3] versus B-pre-septal-PEA [n = 3], (B) B-postPEA [n = 3] versus B-pre-septal-PEA [n = 3], (C) B-postPEA [n = 3] versus B-prePEA [n = 3].

4.13. Pathway enrichment analysis

For the pathway analysis, distinctive clusters have been identified within the confirmatory cohort. The comparison between B-postPEA and B-pre-septal-PEA is labeled as cluster 9, B-postPEA in contrast to B-prePEA builds cluster 10, and B-postPEA versus B-pre-septal-PEA is defined as cluster 11. The pathway analysis was performed by using the DEGs from each cluster, with specific criteria of a base mean ≥ 5; $|\log_2(FC)| \geq 0.585$; and P adj ≤ 0.05 (two-sided).

The top 20 and 100 overrepresented GO terms between clusters 9, 10, and 11 are presented in Figure 25 A and B. The external encapsulating structure, a term related to ECM, is expressed across all the clusters. The expression of contractile fiber is notably high within cluster 9 as compared to cluster 10. The term A band is specifically expressed in cluster 9, with related terms including structural constituents of muscle, cardiac myofibril, and myosin heavy chain binding.

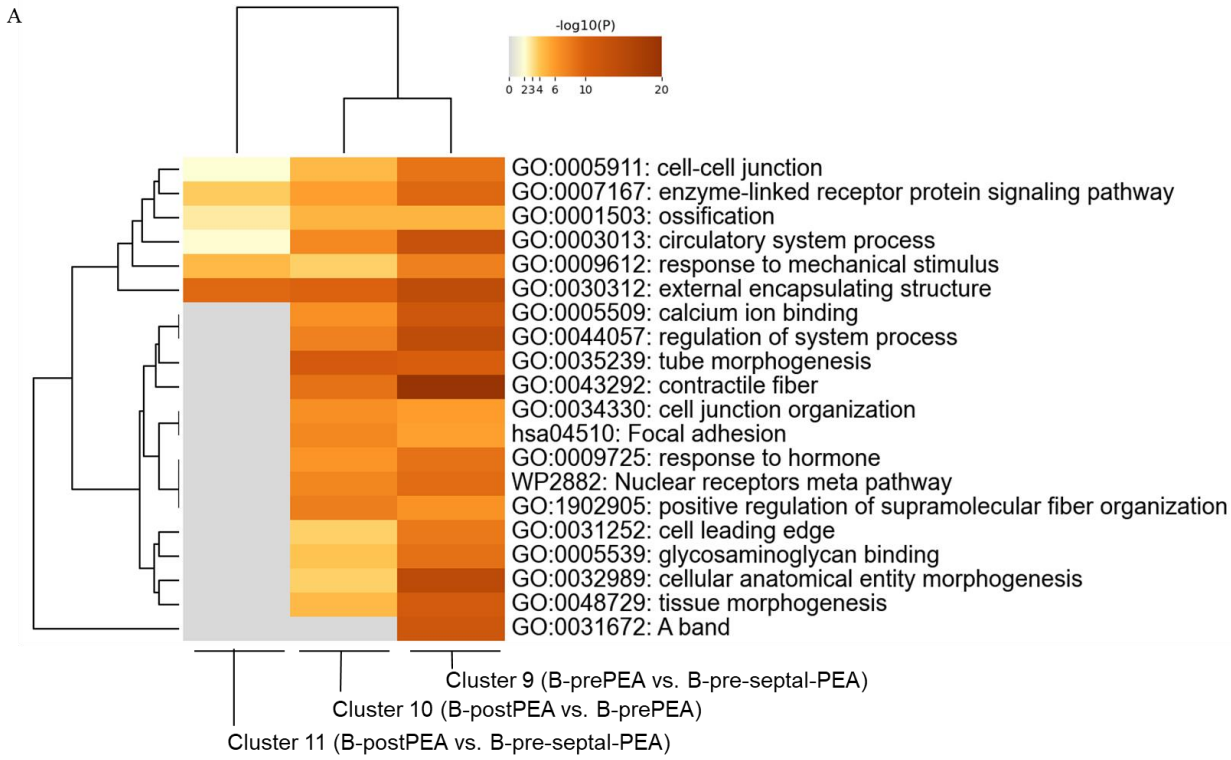

B

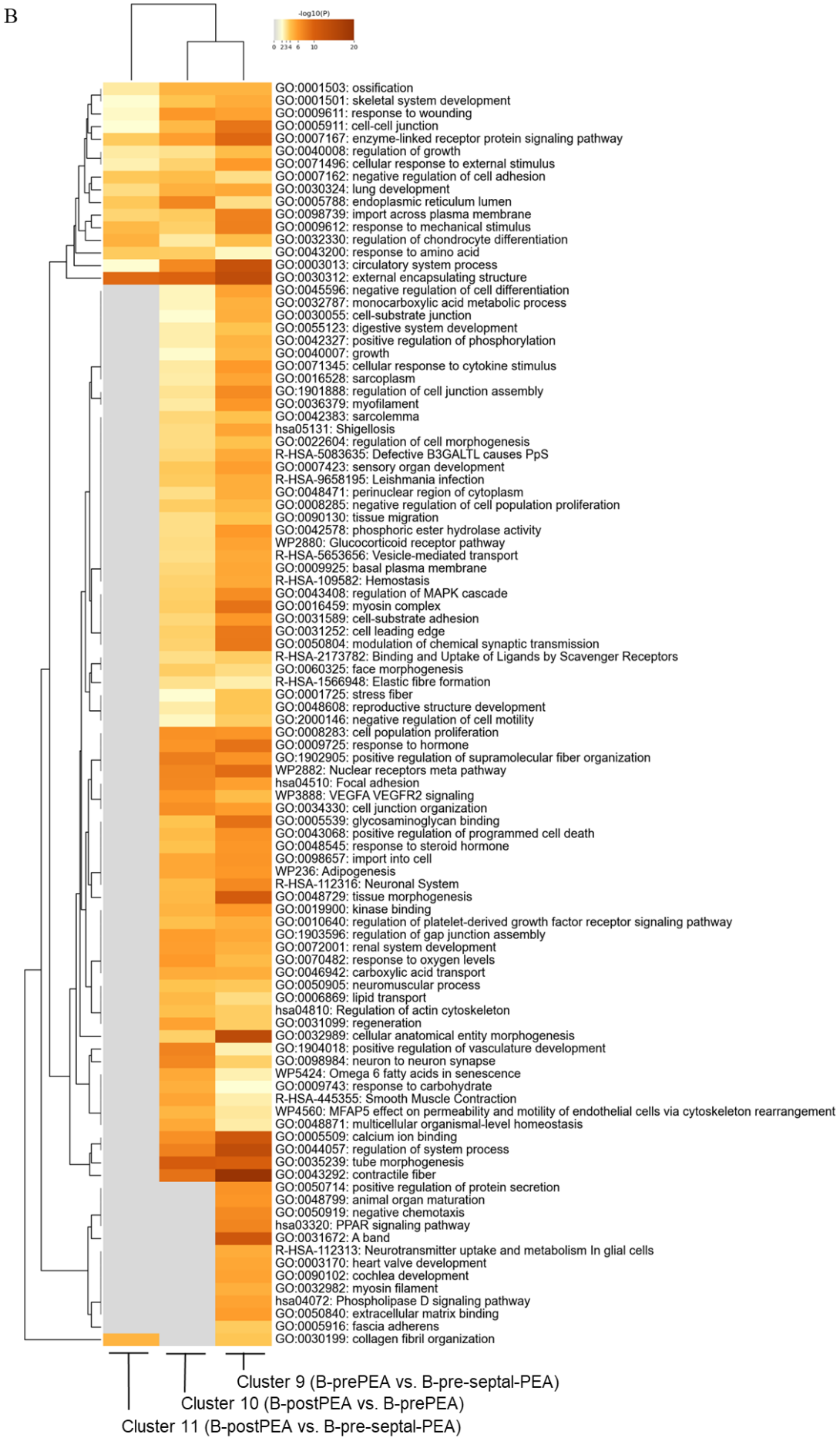
-log10(P)
0 2 3 4 6 10 20
GO:0001503: ossification
GO:0001501: skeletal system development
GO:0009611: response to wounding
GO:0005911: cell-cell junction
GO:0007167: enzyme-linked receptor protein signaling pathway
GO:0040008: regulation of growth
GO:0071496: cellular response to external stimulus
GO:0007162: negative regulation of cell adhesion
GO:0030324: lung development
GO:0005788: endoplasmic reticulum lumen
GO:0098739: import across plasma membrane
GO:0009612: response to mechanical stimulus
GO:0032330: regulation of chondrocyte differentiation
GO:0043200: response to amino acid
GO:0003013: circulatory system process
GO:0030312: external encapsulating structure
GO:0045596: negative regulation of cell differentiation
GO:0032787: monocarboxylic acid metabolic process
GO:0030055: cell-substrate junction
GO:0055123: digestive system development
GO:0042327: positive regulation of phosphorylation
GO:0040007: growth
GO:0071345: cellular response to cytokine stimulus
GO:0016528: sarcoplasm
GO:1901888: regulation of cell junction assembly
GO:0036379: myofilament
GO:0042383: sarcolemma
hsa05131: Shigellosis
GO:0022604: regulation of cell morphogenesis
R-HSA-5083635: Defective B3GALTL causes PpS
GO:0007423: sensory organ development
R-HSA-9658195: Leishmania infection
GO:0048471: perinuclear region of cytoplasm
GO:0008285: negative regulation of cell population proliferation
GO:0090130: tissue migration
GO:0042578: phosphoric ester hydrolase activity
WP2880: Glucocorticoid receptor pathway
R-HSA-5653656: Vesicle-mediated transport
GO:0009925: basal plasma membrane
R-HSA-109582: Hemostasis
GO:0043408: regulation of MAPK cascade
GO:0016459: myosin complex
GO:0031589: cell-substrate adhesion
GO:0031252: cell leading edge
GO:0050804: modulation of chemical synaptic transmission
R-HSA-2173782: Binding and Uptake of Ligands by Scavenger Receptors
GO:0060325: face morphogenesis
R-HSA-1566948: Elastic fibre formation
GO:0001725: stress fiber
GO:0048608: reproductive structure development
GO:2000146: negative regulation of cell motility
GO:0008283: cell population proliferation
GO:0009725: response to hormone
GO:1902905: positive regulation of supramolecular fiber organization
WP2882: Nuclear receptors meta pathway
hsa04510: Focal adhesion
WP3888: VEGFA VEGFR2 signaling
GO:0034330: cell junction organization
GO:0005539: glycosaminoglycan binding
GO:0043068: positive regulation of programmed cell death
GO:0048545: response to steroid hormone
GO:0098657: import into cell
WP236: Adipogenesis
R-HSA-112316: Neuronal System
GO:0048729: tissue morphogenesis
GO:0019900: kinase binding
GO:0010640: regulation of platelet-derived growth factor receptor signaling pathway
GO:1903596: regulation of gap junction assembly
GO:0072001: renal system development
GO:0070482: response to oxygen levels
GO:0046942: carboxylic acid transport
GO:0050905: neuromuscular process
GO:0006869: lipid transport
hsa04810: Regulation of actin cytoskeleton
GO:0031099: regeneration
GO:0032989: cellular anatomical entity morphogenesis
GO:1904018: positive regulation of vasculature development
GO:0098984: neuron to neuron synapse
WP5424: Omega 6 fatty acids in senescence
GO:0009743: response to carbohydrate
R-HSA-445355: Smooth Muscle Contraction
WP4560: MFAP5 effect on permeability and motility of endothelial cells via cytoskeleton rearrangement
GO:0048871: multicellular organismal-level homeostasis
GO:0005509: calcium ion binding
GO:0044057: regulation of system process
GO:0035239: tube morphogenesis
GO:0043292: contractile fiber
GO:0050714: positive regulation of protein secretion
GO:0048799: animal organ maturation
GO:0050919: negative chemotaxis
hsa03320: PPAR signaling pathway
GO:0031672: A band
R-HSA-112313: Neurotransmitter uptake and metabolism In glial cells
GO:0003170: heart valve development
GO:0090102: cochlea development
GO:0032982: myosin filament
hsa04072: Phospholipase D signaling pathway
GO:0050840: extracellular matrix binding
GO:0005916: fascia adherens
GO:0030199: collagen fibril organization
Cluster 9 (B-prePEA vs. B-pre-septal-PEA)
Cluster 10 (B-postPEA vs. B-prePEA)
Cluster 11 (B-postPEA vs. B-pre-septal-PEA)

Figure 25. Top 20 and 100 overrepresented GO terms and pathways. The Heatmap displays the top 20 (A) and 100 (B) overrepresented GO terms for all the DEGs between the following comparisons: cluster 9 (B-prePEA vs. B-pre-septal-PEA), cluster 10 (B-postPEA vs. B-prePEA), cluster 11 (B-postPEA vs. B-pre-septal-PEAm).

4.14. Pathway analysis for target selection

Target selection was performed based on the top terms and pathways expressed within the clusters. Figure 26 shows the eleven distinct clusters and the comparison between clusters.

Clusters	Contrast
Cluster 1	Exploratory cohort (A-prePEAm vs A-prePEAs)
Cluster 2	Confirmatory cohort (B-prePEAm vs B-prePEAs)
Cluster 3	Confirmatory cohort (B-prePEAm vs B-prePEAi)
Cluster 4	Confirmatory cohort (B-prePEAi vs B-prePEAs)
Cluster 5	Confirmatory cohort (B-postPEA vs B-prePEA)
Cluster 6	Confirmatory cohort (B-postPEAs vs B-prePEAs)
Cluster 7	Confirmatory cohort (B-postPEAm vs B-prePEAm)
Cluster 8	Confirmatory cohort (B-postPEAi vs B-prePEAi)
Cluster 9	Confirmatory cohort (B-prePEA vs B-pre-septal-PEA)
Cluster 10	Confirmatory cohort (B-postPEA vs B-prePEA)
Cluster 11	Confirmatory cohort (B-postPEA vs B-pre-septal-PEA)
Comparison of clusters: 1,2 / 2,3,4 / 1,2,3,4 / 5,6,7,8 / 6,7,8 / 9,10,11	

Figure 26. Comparison of clusters for target selection. Eleven clusters were incorporated into the pathway analysis. Additionally, within both exploratory and confirmatory cohorts, prePEA clusters (1,2,3, and 4) underwent contrasting include 1,2 /2,3,4/ and 1,2,3,4. In the confirmatory cohort, contrasts were drawn between pre and post-PEA clusters (5,6,7, and 8) using sequences of 5,6,7,8 and 6,7,8. Furthermore, clusters 9,10,11, belonging to three special samples, were examined through a contrast of 9,10, and 11.

Upon conducting the pathway analysis, five targets were identified. These include *SERPINE1*, *ATF3*, *IL7R*, *INHBB*, and *ANKRD1*. Figure 27 A-E illustrates the enrichment of various GO terms and pathways across different clusters and the association of each selected target with its respective cluster.

SERPINE1 plays important roles in various GO terms and pathways related to ECM such as ECM formation, external encapsulating structure, collagen-containing extracellular matrix and ECM organization, ECM proteoglycans, NABA MATRISOME ASSOCIATED, and collagen trimer formations. *SERPINE1* expression within clusters 5,6,7, and 8 which is related to postPEA and prePEA contrasts, primarily influences tube morphogenesis, angiogenesis, as well as blood vessel development and morphogenesis (Figure 27 A).

ATF3 is associated with the terms and pathways characterizing the postPEA versus prePEA within clusters 5,6,7, and 8. It plays a critical role in the PI3K Akt signaling pathway. Specifically, in clusters 6,7, and 8, ATF3 is mainly involved in the regulation of MAPK, ERK1, and ERK2 cascade (Figure 27 B).

IL7R shows a significant association with the terms and pathways of the postPEA versus prePEA within clusters 5,6,7, and 8. IL7R has critical connections to the PI3K-Akt signaling pathway, regulation of the nerve system, as well as to the PI3K Akt mTOR signaling pathway in relation to focal adhesion. Furthermore, IL7R is involved in the cellular response to cytokine stimulus, as illustrated in Figure 27 C.

INHBB is linked to the terms and pathways indicative of the contrast between postPEA versus prePEA within clusters 5,6,7, and 8. INHBB is connected to enzyme-linked receptor protein signaling pathway, regulation of system process, and modulating cellular response to cytokine stimuli (Figure 27 D).

ANKRD1 is linked to the terms and pathways within clusters 9, 10, and 11. ANKRD1 is predominantly connected with cardiac muscle and plays a role in the assembly of contractile fibers, myofibrils, and sarcomeres, as well as the processes based on actin filaments and the organization of the actin cytoskeleton (Figure 27 E).

A

SERPINE1 is associated with the top enriched terms in clusters 1,2,3,4,5,6,7,8,9,10, and 11

GO term	Description	Clusters					
		1,2	2,3,4	1,2,3,4	5,6,7,8	6,7,8	9,10,11
GO:0031012	extracellular matrix						
GO:0030312	external encapsulating structure						
GO:0062023	collagen-containing extracellular matrix						
R-HSA-1474244	Extracellular matrix organization						
R-HSA-3000178	ECM proteoglycans						
M5885	NABA MATRISOME ASSOCIATED						
GO:0035239	tube morphogenesis						
GO:0001944	vasculature development						
GO:0001568	blood vessel development						
GO:0048514	blood vessel morphogenesis						
GO:2000147	positive regulation of cell motility						
WP236	Adipogenesis						
hsa04350	TGF Smad signaling pathway						
GO:0005581	collagen trimer						
GO:0042476	odontogenesis						
GO:0001525	angiogenesis						
hsa04510	Focal adhesion						
hsa04933	AGE-RAGE signaling pathway in diabetic complications						

log 10 enrichment *P* value

-45 -5

B

ATF3 is associated with the top enriched terms in clusters 5,6,7 and 8

GO term	Description	Clusters	
		5,6,7,8	6,7,8
GO:0043068	positive regulation of programmed cell death		
GO:0043065	positive regulation of apoptotic process		
WP5087	Pleural mesothelioma		
GO:0070372	regulation of ERK1 and ERK2 cascade		
WP289	Myometrial relaxation and contraction pathways		

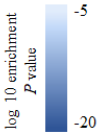

C

IL7R is associated with the top enriched terms in clusters 5,6,7 and 8

GO term	Description	Clusters	
		5,6,7,8	6,7,8
hsa04151	PI3K-Akt signaling pathway		
WP3932	Focal adhesion PI3K Akt mTOR signaling pathway		
hsa05200	Pathways in cancer		
GO:0008283	cell population proliferation		
GO:0000902	cell morphogenesis		
GO:0071345	cellular response to cytokine stimulus		
GO:0019221	cytokine-mediated signaling pathway		
GO:0004896	cytokine receptor activity		
hsa04060	Cytokine-cytokine receptor interaction		
GO:0070233	negative regulation of T cell apoptotic process		
GO:0043029	T cell homeostasis		

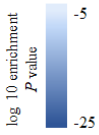

D

INHBB is associated with the top enriched terms in clusters 5,6,7 and 8

GO term	Description	Clusters
		5,6,7,8
GO:0007167	enzyme-linked receptor protein signaling pathway	
GO:0044057	regulation of system process	
GO:0071345	cellular response to cytokine stimulus	
GO:0043068	positive regulation of programmed cell death	
GO:0043065	positive regulation of apoptotic process	
GO:0060322	head development	
GO:0007420	brain development	

E

ANKRD1 is associated with the top enriched terms in clusters 9,10 and 11

GO term	Description	Clusters
		9,10,11
GO:0043292	contractile fiber	
GO:0030016	myofibril	
hsa04820	Cytoskeleton in muscle cells	
GO:0030017	sarcomere	
GO:0030029	actin filament-based process	
GO:0097435	supramolecular fiber organization	
GO:0030036	actin cytoskeleton organization	
GO:0032989	cellular anatomical entity morphogenesis	
GO:0007507	heart development	

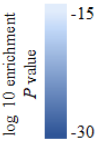

Figure 27. Pathway enrichment analysis for selected targets in the CTEPH cohort. The graphical representation of the top enriched pathways within each cluster, accompanied by their respective Log10 enrichment *P* values (highlighted in blue). The association of *SERPINE1* (A), *ATF3* (B), *IL7R* (C), *INHBB* (D), and *ANKRD1* (E) with the top enriched terms within their corresponding cluster is illustrated.

4.15. Correlations between *ANKRD1, ATF3, IL7R, INHBB,* and *SERPINE1* expression and clinical parameters in the confirmatory cohort

In the confirmatory cohort, the clinical parameters of the patients in the B-prePEAm and B-prePEAs groups and the B-prePEA and B-postPEA groups were correlated with gene expression levels of *ANKRD1*, *ATF3*, *IL7R*, *INHBB*, and *SERPINE1*.

4.15.1. Correlation between *SERPINE1* expression and clinical parameters of B-prePEAm and B-prePEAs groups

SERPINE1 expression was significantly positively correlated with mPAP, sPAP, PVR, NT-proBNP, and RV basal diameter and negatively correlated with CI, TAPSE, and TAPSE/sPAP (Figure 28).

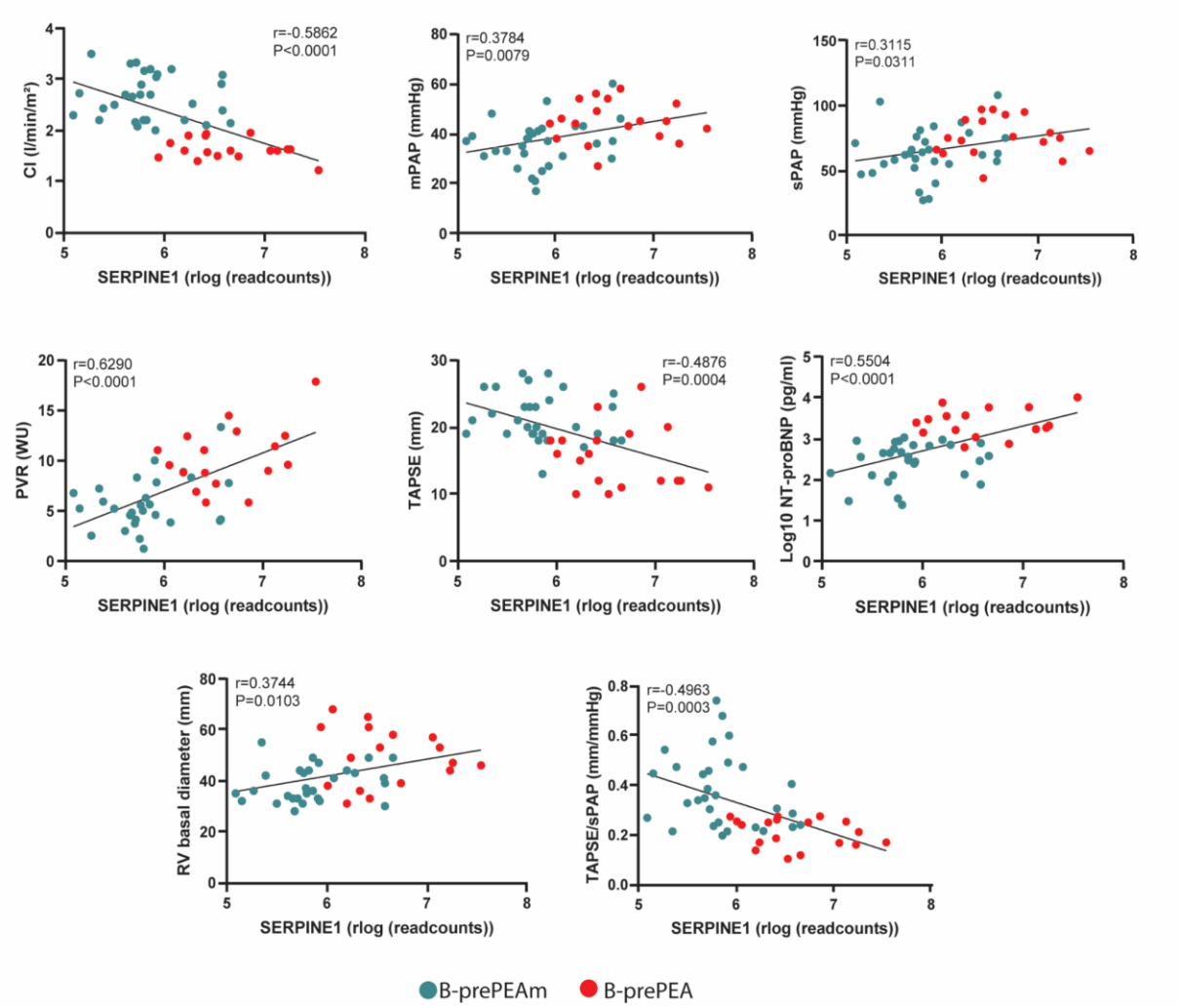

Figure 28. Correlation between *SERPINE1* expression and clinical parameters in the B-prePEAm and B-prePEAs groups. Pearson's correlation coefficient (r) with the associated *P* value are shown in each graph. A *P* <0.05 indicates the statistical significance. Abbreviations: CI, cardiac index; mPAP, mean pulmonary artery pressure; sPAP, systolic pulmonary artery pressure; PVR, pulmonary vascular resistance; TAPSE, tricuspid annular plane systolic excursion; NTproBNP, N-terminal pro-B-type Natriuretic peptide; RV basal diameter; TAPSE/sPAP, ratio of tricuspid annular plane systolic excursion to systolic pulmonary artery pressure.

4.15.2. Correlation between *IL7R* expression and clinical parameters in the B-prePEAm and B-prePEAs groups

IL7R expression was negatively correlated with mRAP (Figure 29).

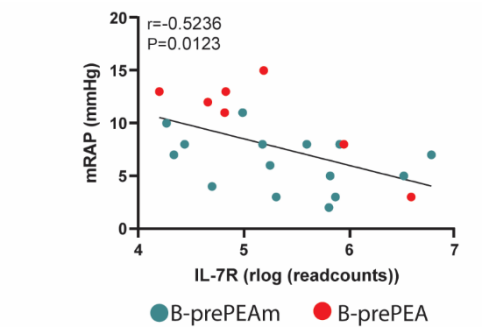

Figure 29. Correlation between *IL7R* expression and clinical parameters in B-prePEAm and prePEAs. Pearson's correlation coefficient (r) with the associated *P* value is shown in each graph. A $P < 0.05$ is statistically significant. Abbreviations: mRAP, mean right atrial pressure.

4.15.3. Correlation between *INHBB* expression and clinical parameters in the B-prePEAm and B-prePEAs groups

INHBB expression was significantly negatively correlated with mPAP, mRAP, PVR, and sPAP and positively correlated with VO_2 max (Figure 30).

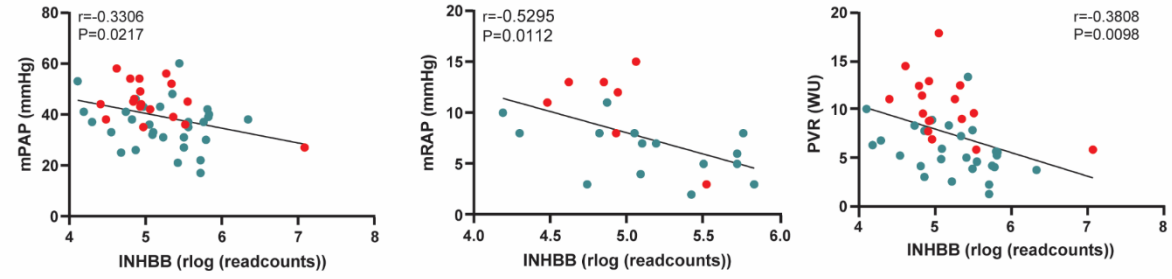

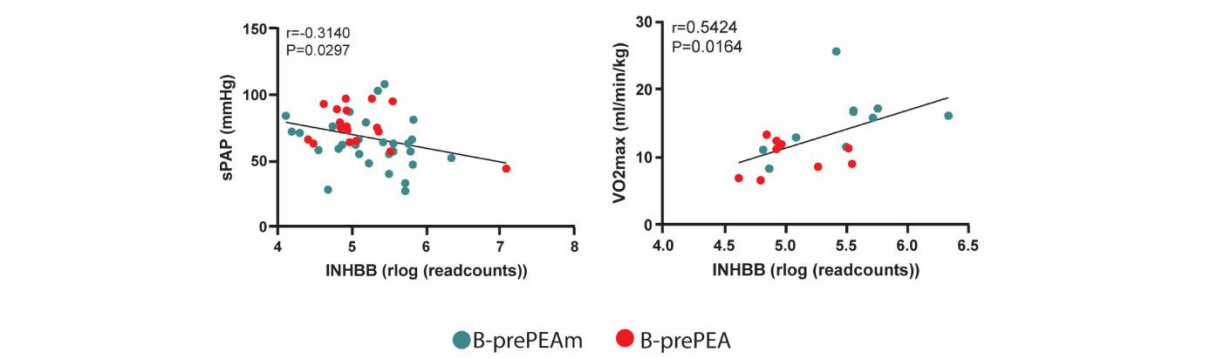

Figure 30. Correlation between *INHBB* expression and clinical parameters in the B-prePEAm and prePEAs groups. Pearson's correlation coefficient (r) with the associated *P* value are shown in each graph. A $P < 0.05$ is statistically significance. Abbreviations: mPAP, mean pulmonary artery pressure; mRAP, mean right atrial pressure; PVR, pulmonary vascular resistance; sPAP, systolic pulmonary artery pressure; VO2 max.

4.15.4. Correlation between *ANKRD1* expression and clinical parameters in the B-prePEA and B-postPEA groups

ANKRD1 expression was significantly positively correlated with mPAP and PVR (Figure 31).

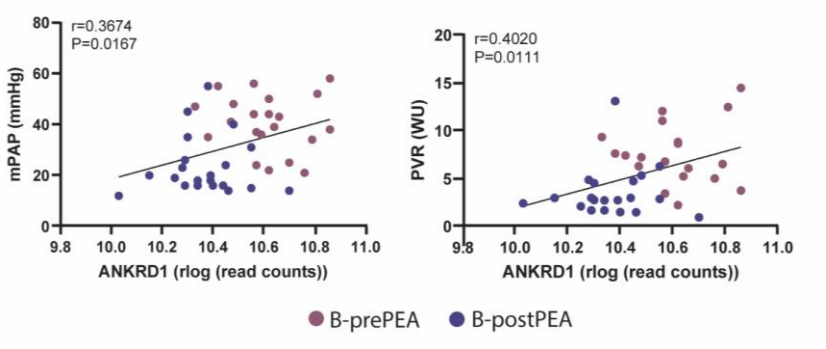

Figure 31. Correlation between *ANKRD1* expression and clinical parameters in the B-prePEA and B-postPEA groups. Pearson's correlation coefficient (r) with the associated *P* value is shown in each graph. $P < 0.05$ indicates the statistical significance. Abbreviations: mPAP, mean pulmonary artery pressure; PVR, pulmonary vascular resistance.

4.15.5. Correlation between *IL7R* expression and clinical parameters in the B-prePEA and B-postPEA groups

IL7R expression was significantly positively correlated with mPAP and sPAP (Figure 32).

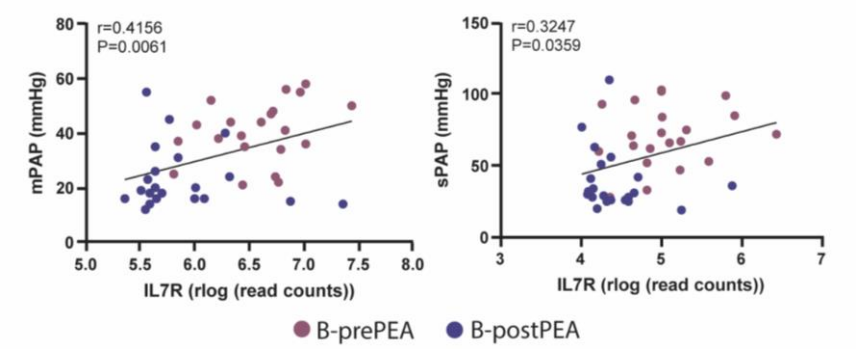

Figure 32. Correlations between *IL7R* expression and clinical parameters in the B-prePEA and B-postPEA groups. Pearson's correlation coefficient (r) with the associated *P* value are shown in each graph. A $P < 0.05$ is statistically significant. Abbreviations: mPAP, mean pulmonary artery pressure; sPAP, systolic pulmonary artery pressure.

4.15.6. Correlation between *INHBB* expression and clinical parameters in the B-prePEA and B-postPEA groups

INHBB expression was significantly positively correlated with sPAP and negatively correlated with TAPSE/sPAP (Figure 33).

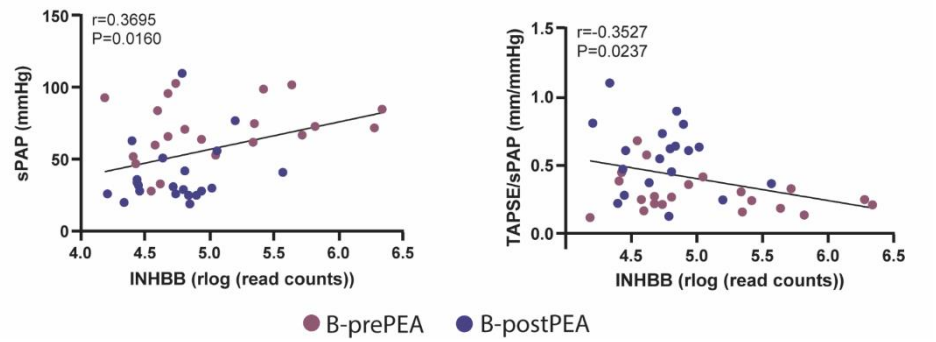

Figure 33. Correlations between *INHBB* expression and clinical parameters in the B-prePEA and B-postPEA groups. Pearson's correlation coefficient (r) with the associated *P* value is shown in each graph. A $P < 0.05$ is statistically significant. Abbreviations: sPAP, systolic pulmonary artery pressure; mPAP, mean pulmonary artery pressure.

4.15.7. Correlation between *SERPINE1* expression and clinical parameters in the B-prePEA and B-postPEA groups

SERPINE1 expression was significantly positively correlated with mPAP, PVR, RV basal diameter, and TAPSE and significantly negatively correlated with TAPSE/sPAP (Figure 34).

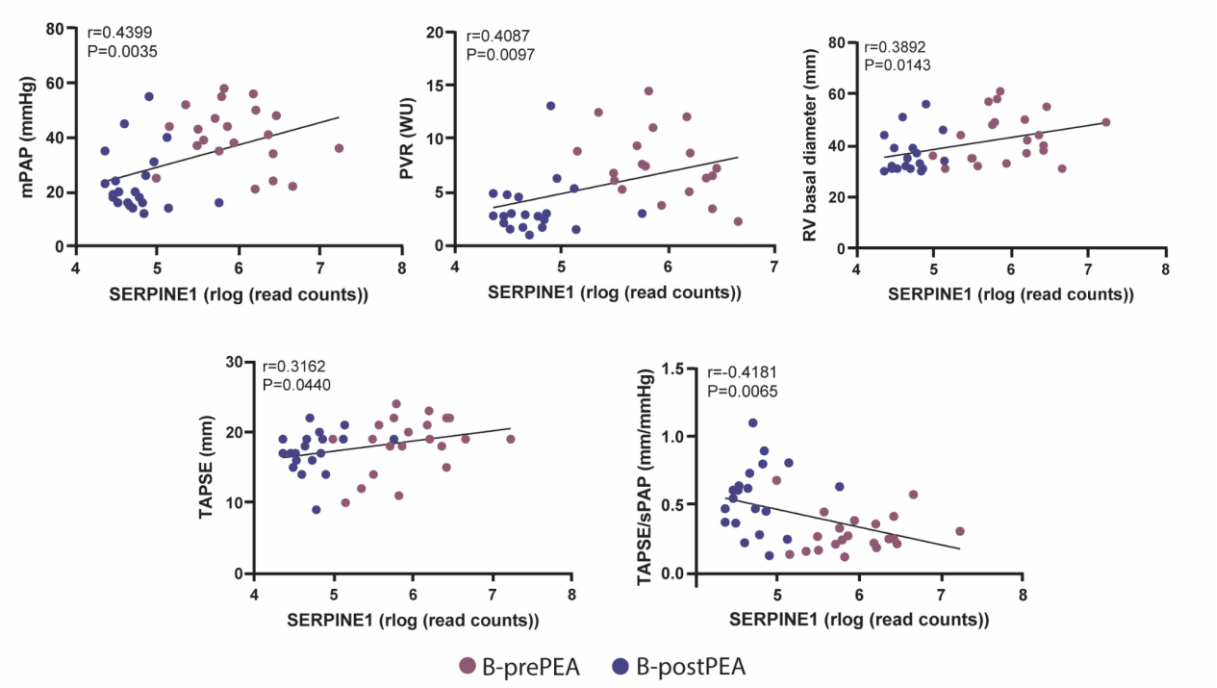

Figure 34. Correlations between *SERPINE1* expression and clinical parameters in the B-prePEA and B-postPEA groups. Pearson's correlation coefficient (r) with the associated *P* value is shown in each graph. A $P < 0.05$ is statistically significant. Abbreviations: mPAP, mean pulmonary artery pressure; PVR, pulmonary vascular resistance; RV basal diameter; TAPSE, tricuspid annular plane systolic excursion; TAPSE/sPAP, Ratio of tricuspid annular plane systolic excursion to systolic pulmonary artery pressure.

4.16. The effect of different growth factors on *ANKRD1, ATF3, CILP1, IL7R, INHBB,* and *SERPINE1* expression in human cardiac cells

The effect of profibrotic and proinflammatory growth factors on human cardiac fibroblasts (HCFs) and human cardiac microvascular endothelial cells (HCMECs) was evaluated. The cells were stimulated in culture media supplemented with serum (containing 2% FBS), without FBS (basal), transforming growth factor-β1 (TGF-β1), a profibrotic stimulus, and tumor necrosis factor-alpha (TNF-α) as a proinflammatory stimulus.

4.16.1. The effect of TGF-β1 and TNF-α stimulation on CILP1 expression in HCFs

Cardiac fibroblasts are the main source of CILP1. Therefore, *CILP1* mRNA levels were significantly higher in HCFs after stimulation with TFGβ-1 (10 ng) than in basal and serum media (Figure 35 A). In contrast, *CILP1* mRNA levels were significantly lower in HCFs stimulated with TNF-α than in basal medium. However, *CILP1* mRNA levels did not differ significantly between HCFs cultured in media containing TNF-α and in serum media (Figure 35 B).

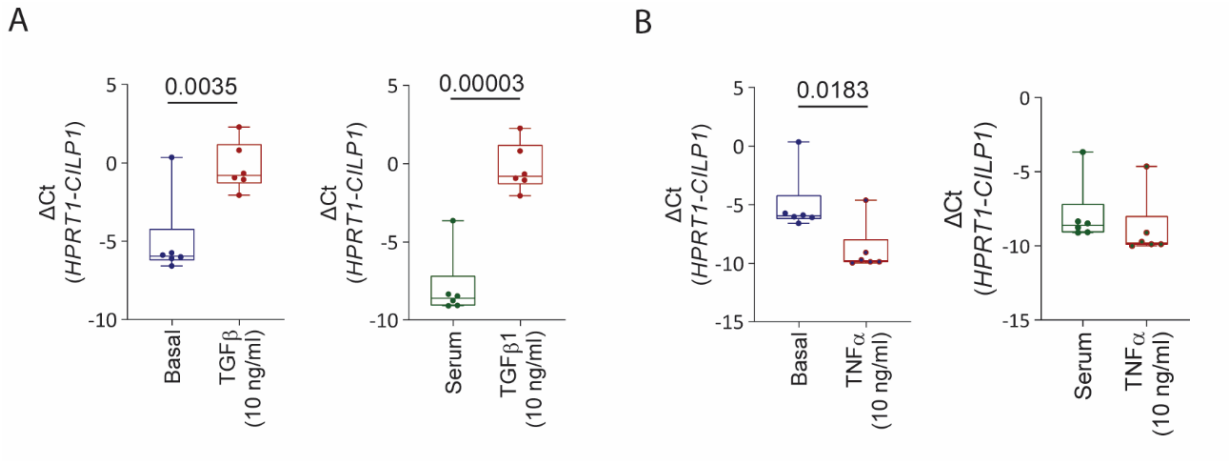

Figure 35. Stimulation of primary HCFs with profibrotic and proinflammatory stimuli induced *CILP1* expression. Relative mRNA levels of *CILP1* in HCF after stimulation with TGF-β1 (A) and TNF-α (B) for 48h compared to basal medium and serum were determined by qPCR. *HPRT* was used as the endogenous control. Bars indicate the mean ± SEM across *n* =3 independent experiments from 3 biological replicates and each with 2 technical replicates. The statistical significance of differences is defined using the two-tailed unpaired t-test. *P* values are reported when the results reach statistical significance ($p < 0.05$).

4.16.2. The effect of TGF-β1 and TNF-α stimulation on *ANKRD1, ATF3, IL7R, INHBB,* and *SERPINE1* expression in HCFs

ANKRD1 mRNA levels were significantly higher in HCFs cultured in media containing TGF-β1 or TNF-α than in basal or serum media after 48 hours (Figure 36 A and B). *ATF3* mRNA levels were significantly higher in HCFs stimulated with TGF-β1 than in basal or media. In contrast, no significant changes were observed in mRNA levels of ATF3 when HCFs were stimulated with TNF-α (Figure 36 C and D). *IL7R* mRNA levels were significantly lower in HCFs cultured in media containing TGF-β1 than in basal or serum media, while they were significantly higher in HCFs cultured in media containing TNF-α than in basal and serum medium (Figure 36 E and F). While *INHBB* mRNA levels did not differ significantly between HCFs cultured in media containing TGF-β1 than in basal and serum medium, they were significantly lower in HCFs cultured in media containing TNF-α than in basal and serum media (Figure 36 G and H). TGF-β1 stimulation did not induce the mRNA expression levels of *INHBB* versus basal medium and serum, whereas TNF-α stimulation significantly reduced the mRNA expression levels of *INHBB* (Figure 36 G and H). Finally, *SERPINE1* mRNA levels were

significantly higher in HCFs cultured in media containing TGF-β1 or TNF-α than in basal or serum media (Figure 36 I, J).

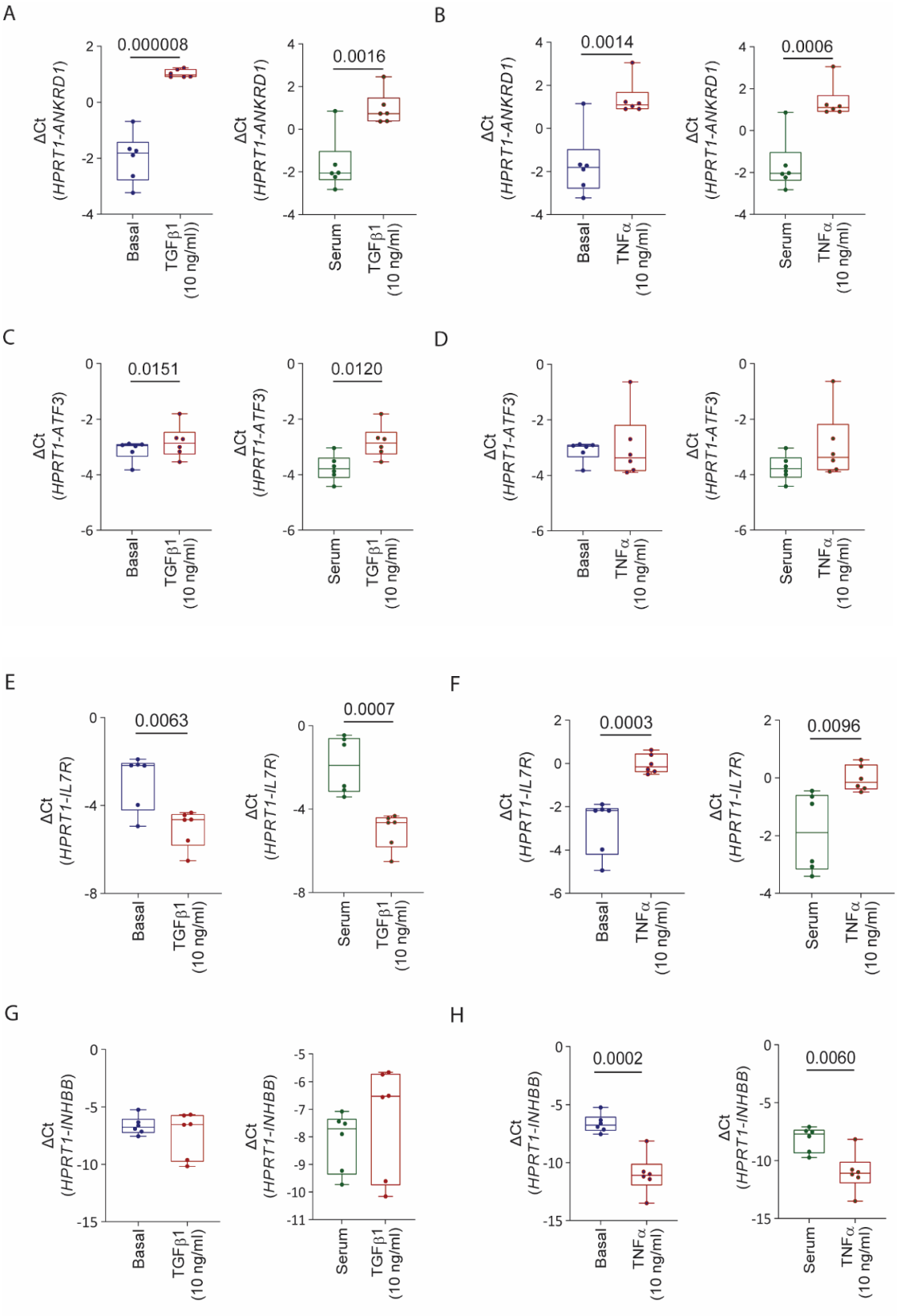

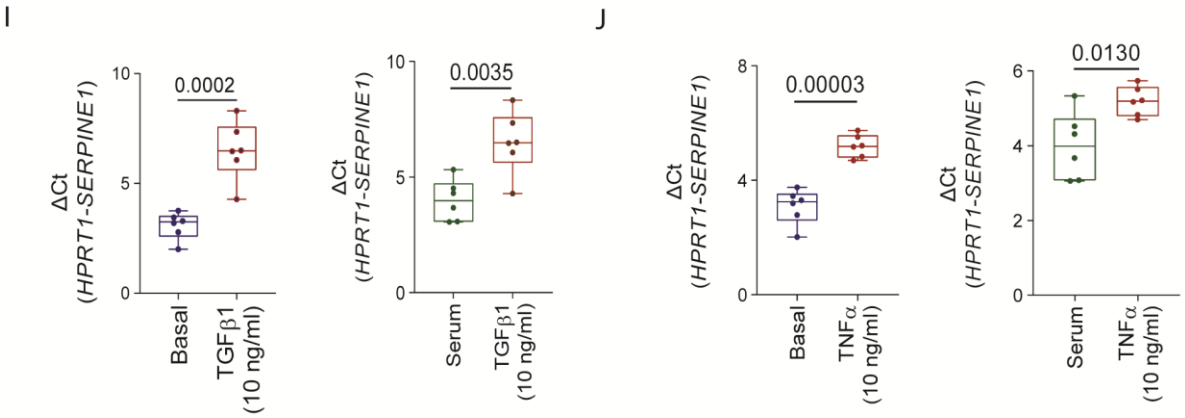

Figure 36. Stimulation of primary HCFs with profibrotic and proinflammatory stimuli induced *ANKRD1, ATF3, IL7R, INHBB,* and *SERPINE1* expression. Relative mRNA levels of *ANKRD1* (A and B), *ATF3* (C and D), *IL7R* (E and F), *INHBB* (G and H), and *SERPINE1* (I and J) in HCFs after stimulation with TGF-β1 and TNF-α for 48h compared to basal medium or serum media were determined by qPCR. *HPRT* was used as the endogenous control. Bars indicate the mean ± SEM across three independent experiments with three biological and each with two technical replicates. The statistical significance of differences is defined using the two-tailed unpaired t-test. *P* values are reported when the results reach statistical significance ($p < 0.05$).

4.16.3. The effect of TNF-α stimulation on *ANKRD1, ATF3, IL7R, INHBB,* and *SERPINE1* expression in HCMECs

HCMECs were stimulated with TNF-α (10 ng) for 48 hours. ANKRD1 mRNA levels did not differ significantly between HCMECs cultured in media containing TNF-α than in basal media while, they were significantly higher in HCMECs cultured in media containing TNF-α than in serum media (Figure 37 A). Similarly, ATF3 mRNA levels in HCMECs cultured in media containing TNF-α were significantly higher than in HCMECs cultured in serum media but did not differ significantly from HCMECs cultured in basal media (Figure 37 B). IL7R mRNA levels were significantly higher in HCMECs cultured in media containing TNF- α than in basal or serum media (Figure 37 C). Stimulated HCMECs with TNF-α significantly reduced the mRNA expression levels of INHBB compared to basal medium or serum (Figure 37 D). SERPINE1 mRNA levels in HCMECs cultured in media containing TNF-α were significantly higher than HCMECs cultured in serum media but did not differ significantly from HCMECs cultured in basal media (Figure 37 E).

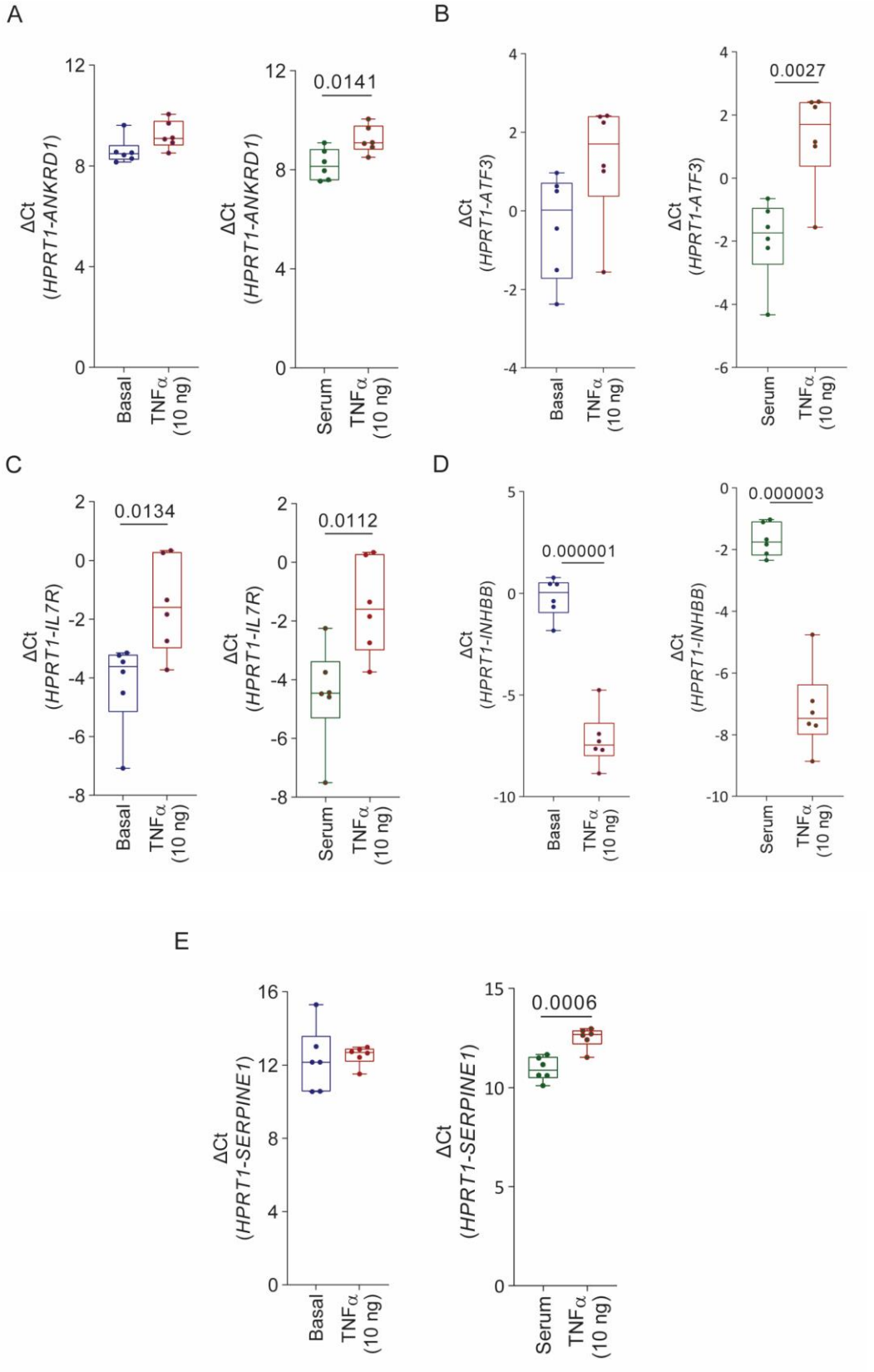
A
ΔCt (HPRT1-ANKRD1)
12
8
4
0
Basal
TNFα (10 ng)
ΔCt (HPRT1-ANKRD1)
0.0141
Serum
TNFα (10 ng)
B
ΔCt (HPRT1-ATF3)
4
2
0
-2
-4
Basal
TNFα (10 ng)
ΔCt (HPRT1-ATF3)
0.0027
-6
Serum
TNFα (10 ng)
C
ΔCt (HPRT1-IL7R)
2
0
-2
-4
-6
-8
0.0134
Basal
TNFα (10 ng)
ΔCt (HPRT1-IL7R)
0.0112
Serum
TNFα (10 ng)
D
ΔCt (HPRT1-INHBB)
5
0
-5
-10
0.000001
Basal
TNFα (10 ng)
ΔCt (HPRT1-INHBB)
0
-2
-4
-6
-8
-10
0.000003
Serum
TNFα (10 ng)
E
ΔCt (HPRT1-SERPINE1)
16
12
8
4
0
Basal
TNFα (10 ng)
ΔCt (HPRT1-SERPINE1)
15
10
5
0
0.0006
Serum
TNFα (10 ng)

Figure 37. Stimulation of primary HCMECs with proinflammatory stimuli induced *ANKRD1*, *ATF3*, *IL7R*, *INHBB*, and *SERPINE1* expression. Relative mRNA expression analysis of *ANKRD1* (A), *ATF3* (B), *IL7R* (C), *INHBB* (D), and *SERPINE1* (E) in HCMEC after stimulation with TNF-α (10 ng) for 48 hours compared to basal or serum media was determined by qPCR. HPRT was used as the endogenous control. Bars indicate the mean ± SEM across three independent experiments with three biological and each with two technical replicates. The statistical significance of differences is defined using the two-tailed unpaired t-test. *P* value are reported when the results reach statistical significance ($p < 0.05$).

4.17. Screening of *ANKRD1, ATF3, IL7R, INHBB,* and *SERPINE1* expression in hypoxia-exposed HCFs and HCMECs

Primary HCFs and HCMECs were exposed to hypoxia (Hox) to uncover the regulation of *ANKRD1*, *ATF3*, *IL7R*, *INHBB*, and *SERPINE1* under the physiological conditions of PH and by stimuli that drive PH. The cells were exposed to hypoxia for 6, 24, and 48 hours to delineate the time-dependent regulation of *ANKRD1*, *ATF3*, *IL7R*, *INHBB*, and *SERPINE1*. The mRNA levels were determined by qPCR and normalized to normoxia (Nox).

ANKRD1: *ANKRD1* mRNA levels in HCFs did not differ significantly from Nox after exposure to Hox for 6, 24, and 48 hours. However, after exposure to Hox for 24 and 48 hours, they were significantly higher in HCMECs than Nox (Figure 38 A and B).

ATF3: *ATF3* mRNA levels in HCFs and HCMECs did not differ significantly from Nox after exposure to Hox (Figure 38 C and D).

IL7R: mRNA levels of *IL7R* did not significantly change by hypoxia in HCF and HCMEC, compared to Nox (Figure 38 E and F).

INHBB: *INHBB* mRNA levels in HCFs did not differ significantly from Nox after exposure to Hox (Figure 38 G). However, in HCMEC the mRNA expression of *INHBB* was downregulated significantly compared to Nox at the 24 and 48 hour time points (Figure 38 H).

SERPINE1: *SERPINE1* mRNA levels in HCFs and HCMECs did not differ significantly from Nox after exposure to Hox for 6, 24, and 48 hours, although they tended to be higher (Figure 38 I and J).

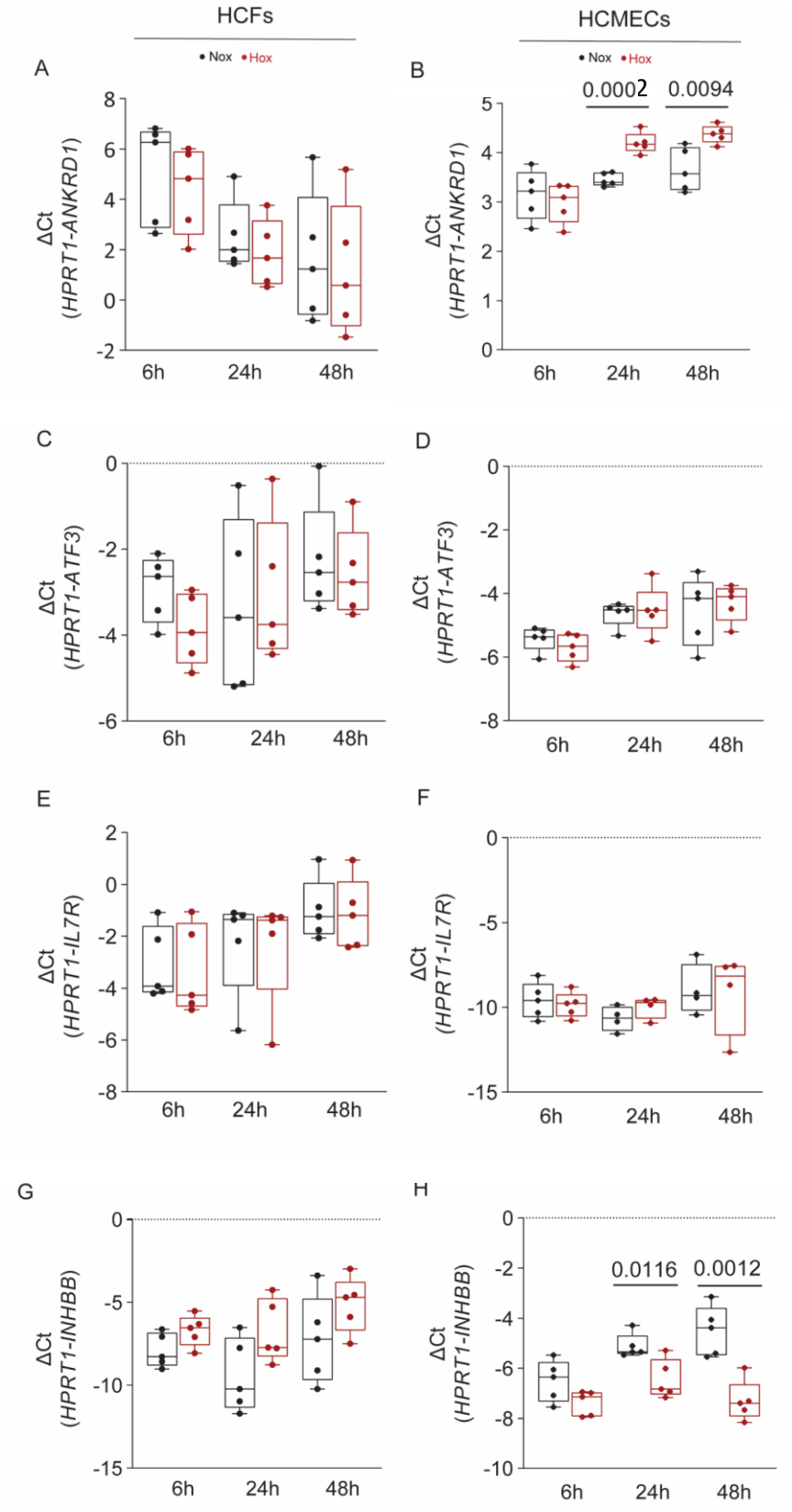
HCFs
HCMECs
A
B
C
D
E
F
G
H
Nox
Hox
ΔCt (HPRT1-ANKRD1)
ΔCt (HPRT1-ATF3)
ΔCt (HPRT1-IL7R)
ΔCt (HPRT1-INHBB)
0.0002
0.0094
0.0116
0.0012
6h
24h
48h

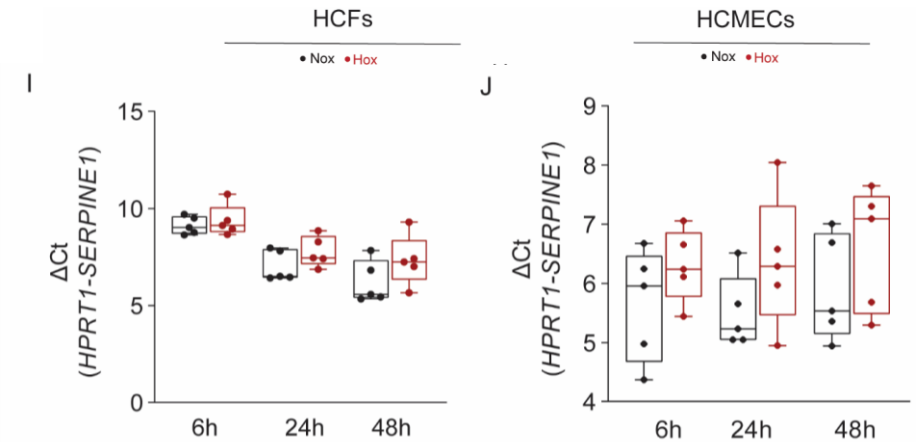

Figure 38. Hypoxia exposure in primary HCFs and HCMECs changed the mRNA expression levels of *ANKRD1*, *ATF3*, *IL7R*, *INHBB*, and *SERPINE1*. Relative mRNA levels of *ANKRD1* (A, B), *ATF3* (C, D), *IL7R*(E, F), *INHBB* (G, H), *SERPINE1*(I, J) in HCF and HCMEC were determined by qPCR. The cells were exposed to Hox and Nox for 6, 24, and 48h. Data are presented as mean ± SEM, for HCFs n = 5 independent experiments with n = 5 biological replicates, and for HCMECs n = 3 independent experiments with n = 3 biological replicates, and only two had two technical replicates (for *IL7R* at 24h and 48h, only one biological replicate has two technical replicates). Normoxia was used as a control, and *HPRT* was used as the endogenous control. The statistical significance of differences is defined using the two-tailed unpaired t-test. *P* values are reported when the results reach statistical significance ($p < 0.05$).

4.18. Detection of SERPINE1 and POSTN secretion in cell culture supernatant by Enzyme-linked immunosorbent assay

Enzyme-linked immunosorbent assays (ELISAs) were used to investigate the secretion of SERPINE1, POSTN, and IL7R into cell culture supernatants. The supernatants were collected at 6, 24, and 48 hours for HCFs and at 48 hours for HCMECs after TNF-α and TGF-β treatment. The SERPINE1 and POSTN concentrations were measured using the DuoSet ELISA kit from R&D Systems, and the IL7R concentration was measured using a kit from Invitrogen, according to the manufacturer's protocol.

4.18.1. SERPINE1 secretion from HCFs and HCMECs

A schematic representation of the experimental design in HCF is shown in Figure 39 A. Treatment of HCFs with different TGF-β1 concentrations (10, 20, and 50 ng/ml) for 48 hours significantly increased the SERPINE1 concentration in cell culture supernatant compared to serum or basal. However, the increase in SERPINE1 concentration in the supernatant was not dose-dependent (Figure 39 B and C). Furthermore, treating HCFs with different TNF-α concentrations (10, 50, and 200 ng/ml) significantly increased the SERPINE1 concentration in the supernatant compared to basal but not compared to serum (Figure 39 D and E).

A schematic representation of the experimental design for HCMECs is shown in Figure 39 F. Treatment of HCMECs with different doses of TNFα (10 and 200 ng/ml) significantly increased the SERPINE1 concentration in the cell culture supernatant compared to serum or basal (Figure 39 G and H).

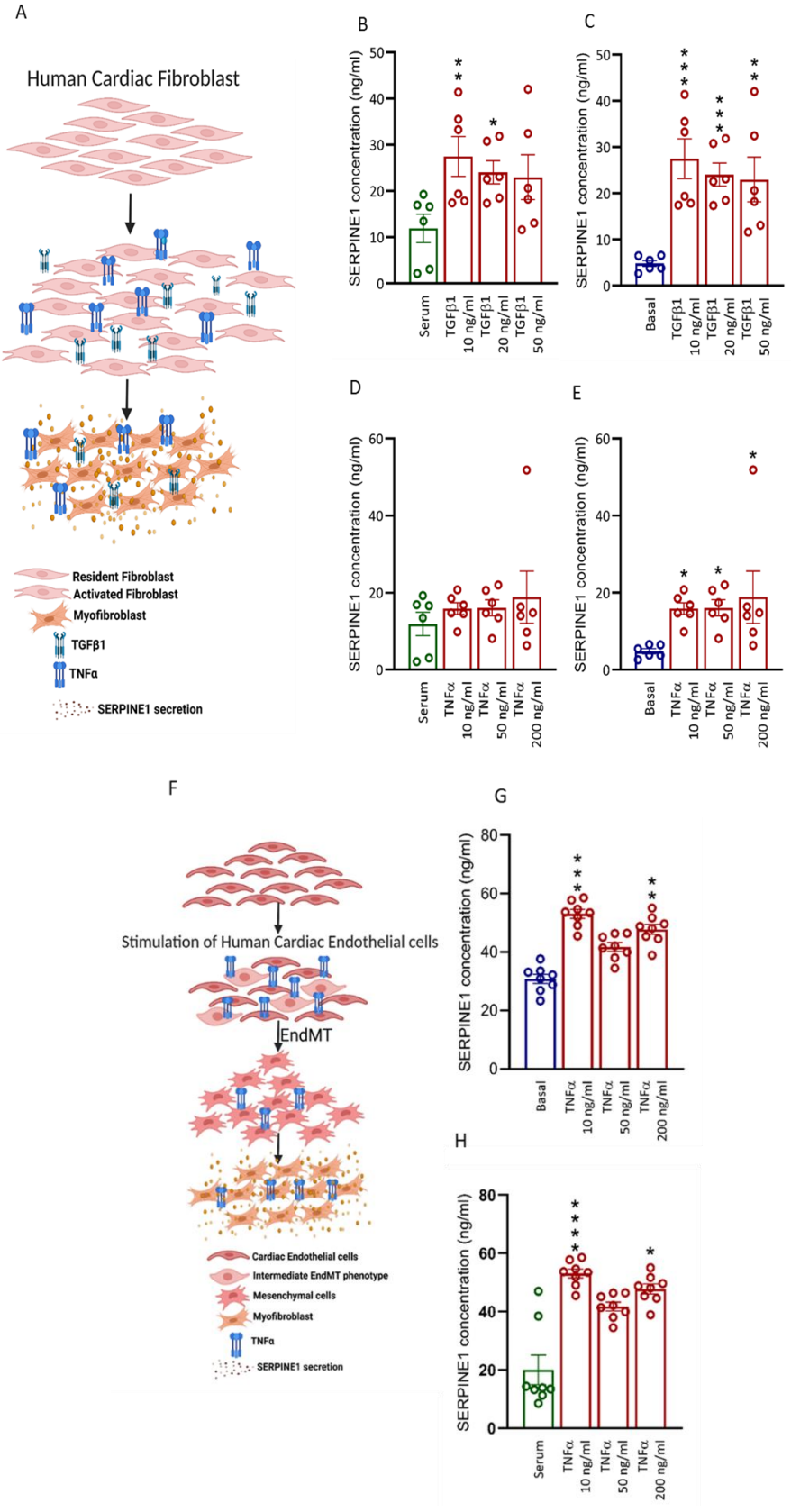

Figure 39. Detection of SERPINE1 levels in conditioned media of cultured HCFs and HCMECs. (A) Schematic representation of experimental design for HCFs (Created with BioRender.com). The SERPINE1 concentration in the supernatant increased when HCFs were cultured with TGF-β1 (B, C) or TNF-α (D, E) for 48 hours. Schematic representation of the experimental design for HCMECs (F) Created with BioRender.com. The SERPINE1(G, H) concentration in the supernatant of HCMECs cultured with different TGF-β1 and TNFα concentrations for 48 hours. The concentrations were measured by ELISA. The bars indicate as mean ± SEM across three independent experiments with three biological replicates and each with two technical replicates for HCF, and three biological replicates (two with three technical replicates and one with two technical replicates), for HCMECs. The serum or basal media was used as a control. Data were compared between groups using one-way analysis of variance (ANOVA) with Tukey's multiple comparison test. Key: *, $p < 0.05$; **, $p < 0.01$; ***, $p < 0.001$; ****, $p < 0.0001$ compared to the serum or basal medium.

4.18.2. POSTN secretion from HCFs and HCMECs

Treating HCFs and HCMECs with different TGF-β1 (10, 20, and 50 ng/mL) and TNF-α (10 and 200 ng/mL) concentrations for 48 hours significantly decreased the POSTN concentration in the supernatant compared to serum (Figure 40 A-D) but not compared to basal (Figure 40 E- H), although they tended to increase with the different TGF-β1 concentrations.

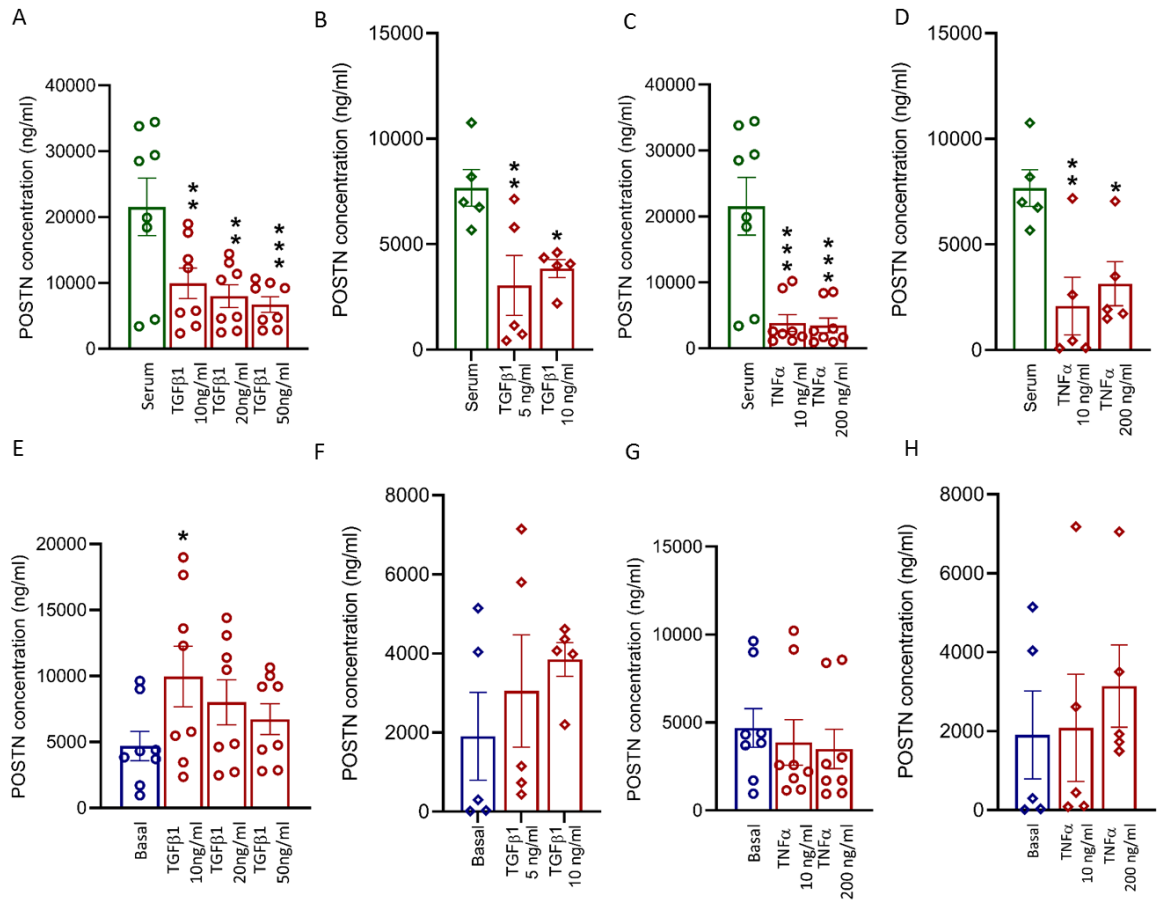

Figure 40. Detection of POSTN concentrations in the conditioned media of cultured HCFs and HCMECs. (A-H) POSTN concentrations in the supernatant of cultured HCFs and HCMECs treated with different TGF-β1 and TNF-α concentrations for 48 hours. The concentrations were measured by ELISA. The bars indicate the mean ± SEM across four independent experiments with four biological replicates and two technical replicates for HCFs and three independent experiments with three biological replicates and two of them with two technical replicates for HCMECs. Data were compared between groups using one-way ANOVA with Tukey's multiple comparison test. Key: *, $p < 0.05$; **, $p < 0.01$; ***, $p < 0.001$; ****, $p < 0.0001$ compared to serum or basal medium. Circles represent HCFs, and diamonds represent HCMECs.

4.18.3. IL7R secretion from HCFs

Treatment of HCF with different doses of TNFα (10, 50, and 200 ng/ml) did not significantly change the IL7R concentration in cell culture supernatant compared to serum (figure 41). In contrast, the IL7R concentrations was not detectable when HCFs were treated with different TGF-β1 concentrations (10, 20, and 50 ng/ml) and basal medium. These results show that IL 7R is mainly secreted upon stimulation with TNFα.

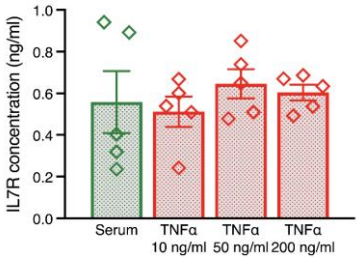

Figure 41. Detection of IL7R concentrations in the conditioned media of cultured HCFs. The IL7R concentration in the supernatant of HCFs cultured with different TNF-α concentrations for 48 hours compared to serum. The concentrations were measured by ELISA. The bars indicate the mean ± SEM across three independent experiments with three biological replicates (two technical replicates were conducted for one). Data were compared between groups using one-way ANOVA with Tukey's multiple comparison test.

4.18.4. ANKRD1 secretion from HCFs

The ANKRD1 concentration in the supernatant was undetectable when HCFs were treated with different TNF-α (10, 50, and 200 ng/mL) and TGF-β1 (10, 20, and 50 ng/mL) concentrations. These results revealed that ANKRD1 is not a secreted protein.

4.19. Transient knockdown of ANKRD1, ATF3, IL7R, INHBB, and SERPINE1 by siRNA SMARTpool in HCFs

ANKRD1, *ATF3*, *IL7R*, *INHBB*, and *SERPINE1* were effectively downregulated in HCFs using the siRNA SMARTpool method. The siRNA-mediated knockdown of ANKRD1, ATF3, IL7R, INHBB, and SERPINE1 was performed for 48 hours, and the cells were kept in a

serum starvation medium for 24 hours. Next, the cells were treated with TNFα (10 ng), TGF-β1 (10 ng), and basal medium. Knockdown efficiency was validated by qPCR and a scrambled siRNApool was used as a negative control. The mRNA levels of *ANKRD1* in HCFs were significantly inhibited by siRNA against it (siANRKD1; Figure 42 A). The mRNA levels of *ATF3* in HCFs were significantly inhibited by the siRNA against it (siATF3) and treatment with basal medium and TGF-β1, whereas, mRNA expression levels were not significantly inhibited with TNFα (Figure 42 B). Finally, the mRNA levels of *IL7R* (Figure 42 C), *INHBB* (Figure 42 D), and *SERPINE1* (Figure 42 E) were significantly inhibited by the siRNAs against them (siIL7R, siINHBB, and siSERPINE1, respectively).

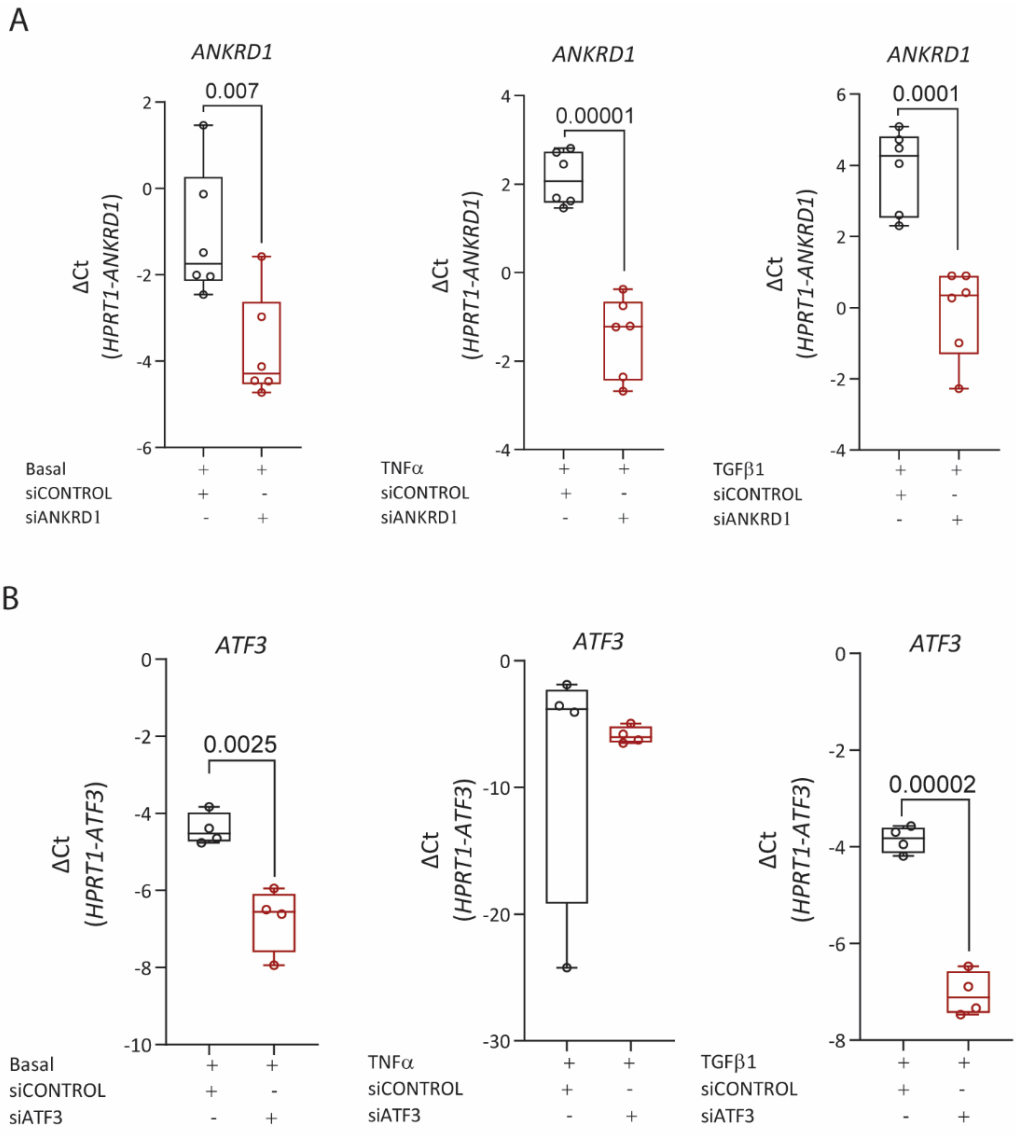

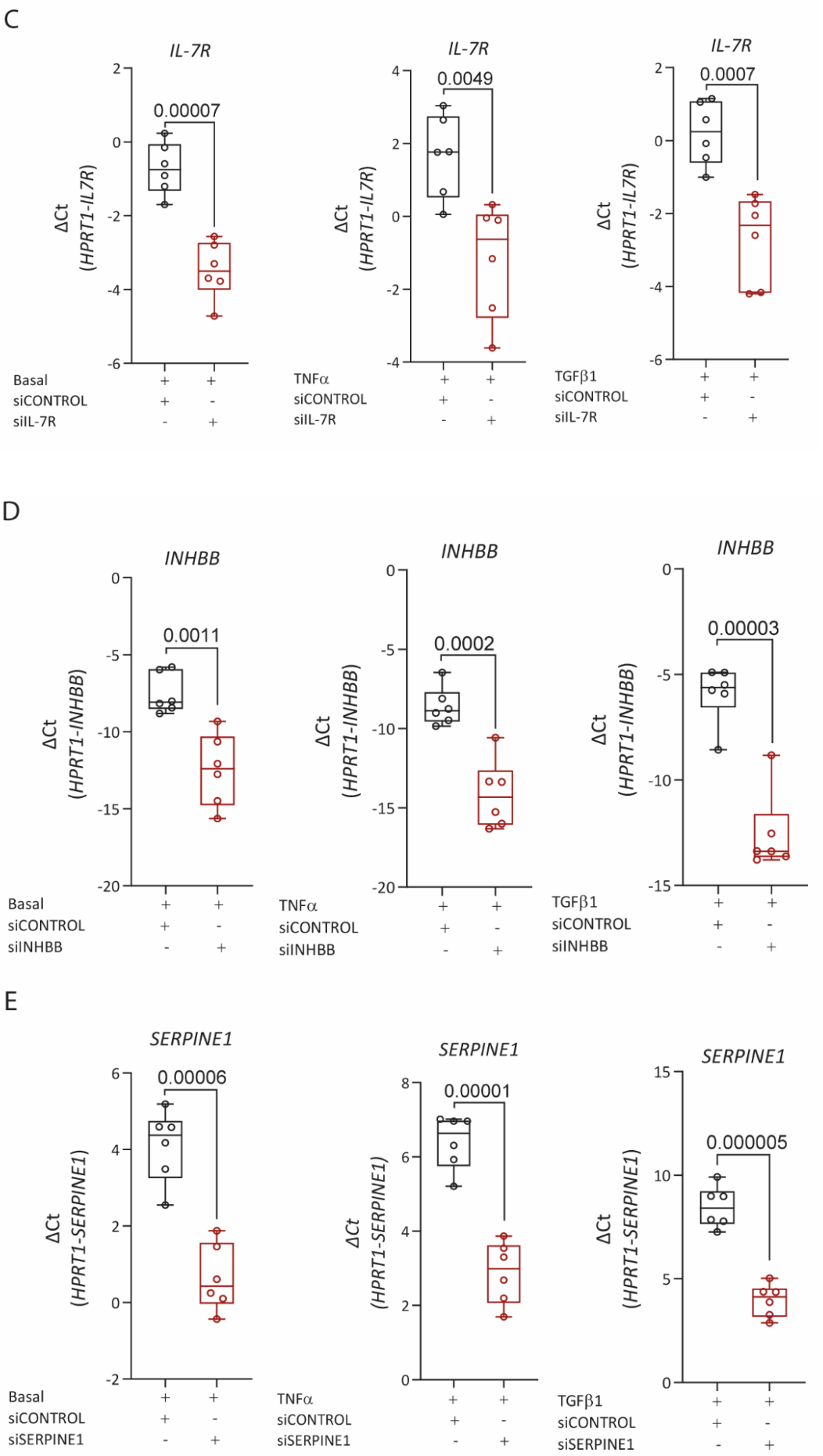
C
IL-7R
0.00007
ΔCt (HPRT1-IL7R)
Basal
siCONTROL
siIL-7R
IL-7R
0.0049
TNFα
siCONTROL
siIL-7R
IL-7R
0.0007
TGFβ1
siCONTROL
siIL-7R
D
INHBB
0.0011
ΔCt (HPRT1-INHBB)
Basal
siCONTROL
siINHBB
INHBB
0.0002
TNFα
siCONTROL
siINHBB
INHBB
0.00003
TGFβ1
siCONTROL
siINHBB
E
SERPINE1
0.00006
ΔCt (HPRT1-SERPINE1)
Basal
siCONTROL
siSERPINE1
SERPINE1
0.00001
ΔCt (HPRT1-SERPINE1)
TNFα
siCONTROL
siSERPINE1
SERPINE1
0.000005
ΔCt (HPRT1-SERPINE1)
TGFβ1
siCONTROL
siSERPINE1

Figure 42. Knockdown of ANKRD1, ATF3, IL7R, INHB*B, and* SERPINE1 in HCFs. *ANKRD1*, *ATF3*, *IL7R, INHBB*, and *SERPINE1* were downregulated via transient knockdown using the siRNA SMARTpool method in HCF treated with TNFα (10 ng), TGF-β1 (10 ng) and basal medium. Relative mRNA levels of *ANKRD1* (A), *ATF3* (B), *IL7R* (C), *INHBB* (D), and *SERPINE1* (E) were determined by qPCR 48 hours after transfection followed by treatment with TNFα (10 ng), TGF-β1 (10 ng) and basal medium. A scrambled siRNApool was used as a negative control. Bars indicate mean ± SEM across three independent experiments with three biological replicates and each with two technical replicates for *ANKRD1*, *IL7R*, *INHBB*, and *SERPINE1*; for *ATF3* four independent experiments from four biological replicates. *HPRT* was used as the endogenous control. The statistical significance of differences is defined using the two-tailed unpaired t-test. *P* values are reported when the results reach statistical significance ($p < 0.05$).

4.20. Transient knockdown of ANKRD1, ATF3, IL7R, INHBB, and SERPINE1 by siRNA SMARTpool in HCMECs

ANKRD1, *ATF3*, *IL7R, INHBB*, and *SERPINE1* were effectively downregulated in HCMECs using the siRNA SMARTpool method. The cells were harvested after 48 hours of siRNA-mediated knockdown of ANKRD1, ATF3, IL7R, INHBB, and SERPINE1. Knockdown efficiency was validated by qPCR and a scrambled siRNApool was used as a negative control. The mRNA levels of *ANKRD1* (Figure 43 A), *ATF3* (Figure 43 B), *IL7R* (Figure 43 C), *INHBB* (Figure 43 D), and *SERPINE1* (Figure 43 E) were significantly inhibited by *si*ANRKD1, siATF3, siIL7R, siINHBB, and siSERPINE1, respectively.

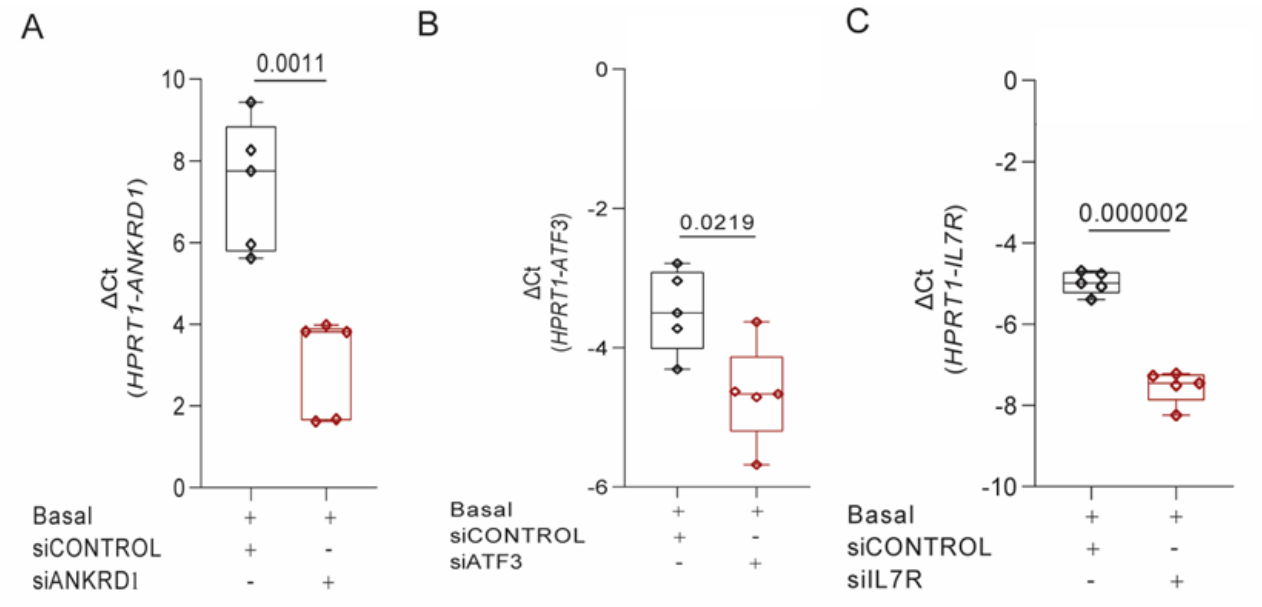

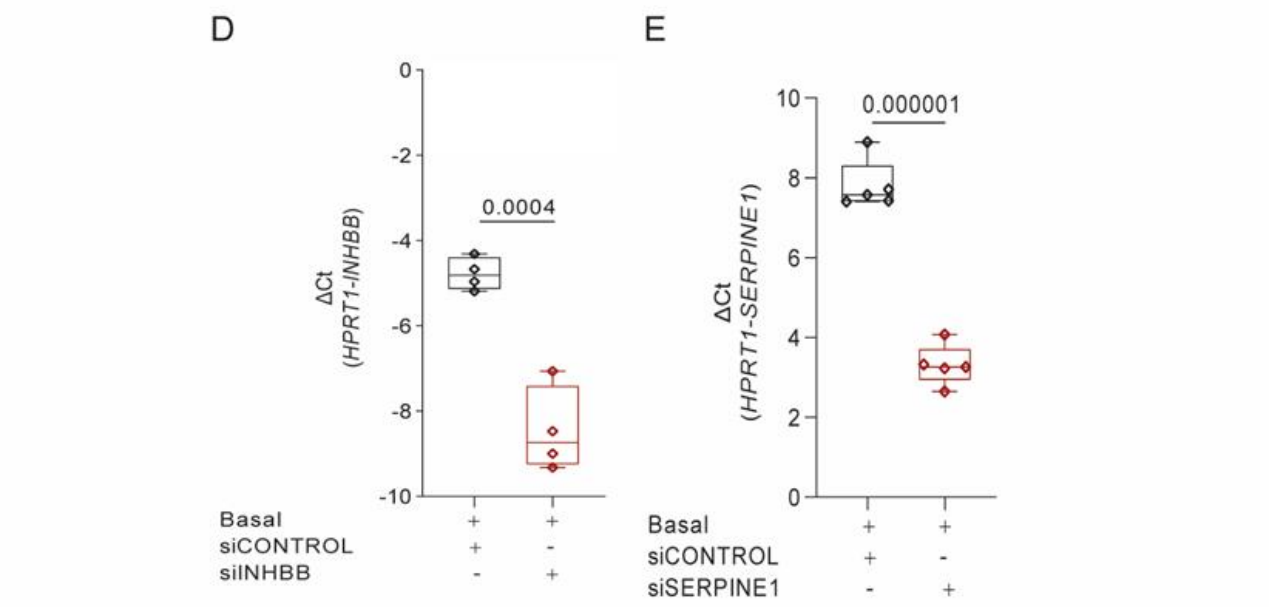

Figure 43. Knockdown of *ANKRD1*, *ATF3*, *IL7R*, *INHBB*, and *SERPINE1* in HCMECs. *ANKRD1*, *ATF3*, *INHBB*, and *SERPINE1* were downregulated in HCMECs by transient knockdown using the siRNA SMARTpool method. Relative mRNA levels of *ANKRD1* (A), *ATF3* (B), *IL7R* (C), *INHBB* (D), and *SERPINE1* (D) were determined by qPCR 48 hours after transfection. A siCONTROL was used as a negative control. The values were normalized to negative control. The bars indicate the mean ± SEM across three independent experiments with three biological replicates (two with two technical replicates) for *ANKRD1*, *ATF3*, *IL7R*, and *SERPINE1*. For INHBB, three independent experiments with three biological replicates (one with one technical replicate). The statistical significance of differences is defined using the two-tailed unpaired t-test. *P* values are reported when the results reach statistical significance ($p < 0.05$).

4.21. Inhibition of both ANKRD1 and SERPINE1 attenuates their expression in HCFs and HCMECs

Since SERPINE1 and ANKRD1 are the main targets of SMAD/YAP/TAZ pathway, the effects of single and double knockdown of *ANKRD1* and *SERPINE1* on their mRNA levels were investigated. In HCFs, a single knockout of *ANKRD1* and *SERPINE1* did not significantly affect the mRNA levels of *SERPINE1* (Figure 44 A - C) or *ANKRD1* (Figure 44 E and G), respectively. However, mRNA levels of *ANKRD1* were significantly increased in HCFs with siRNA knockdown of SERPINE1 in TNFα treatment (Figure 44 F). However, in HCMECs. the mRNA levels of *SERPINE1* and *ANKRD1* were not significantly affected by siANRKD1 or siSERPINE1 (Figure 44 D and H). Interestingly, double knockdown of ANKRD1 and SERPINE1 in HCFs significantly reduced the mRNA levels of *SERPINE1* (Figure 44 I-K) and *ANKRD1* (Figure 44 N and O). The mRNA levels of *ANKRD1* did not significantly change in HCFs with double knockdown of ANKRD1 and SERPINE1 in basal treatment (Figure 44 M). In contrast,

in HCMECs, double knockdown of both ANKRD1 and SERPINE1 significantly reduced the mRNA levels of *ANKRD1* (Figure 44 P) but not *SERPINE1* (Figure 44 L), despite the tendency to decrease *SERPINE1* mRNA levels.

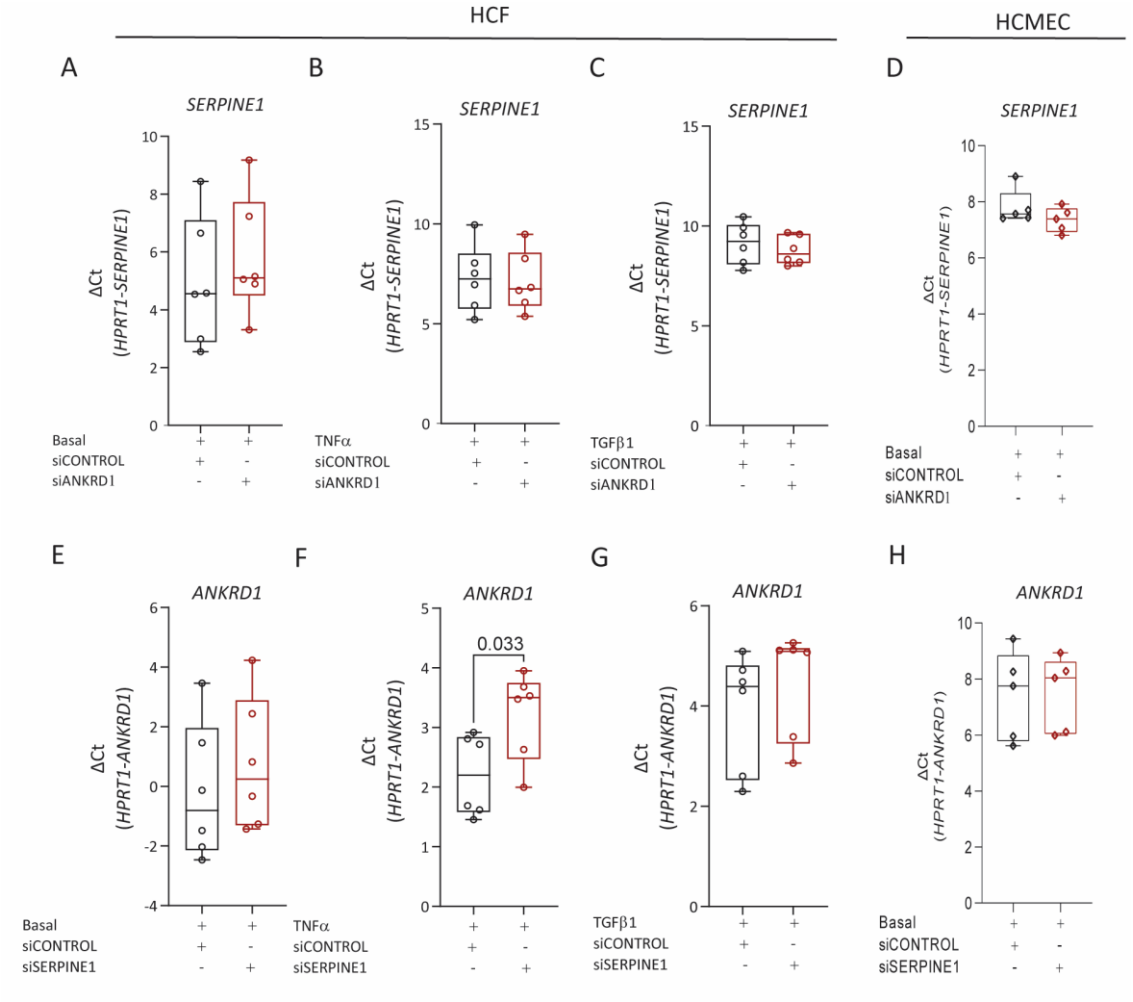

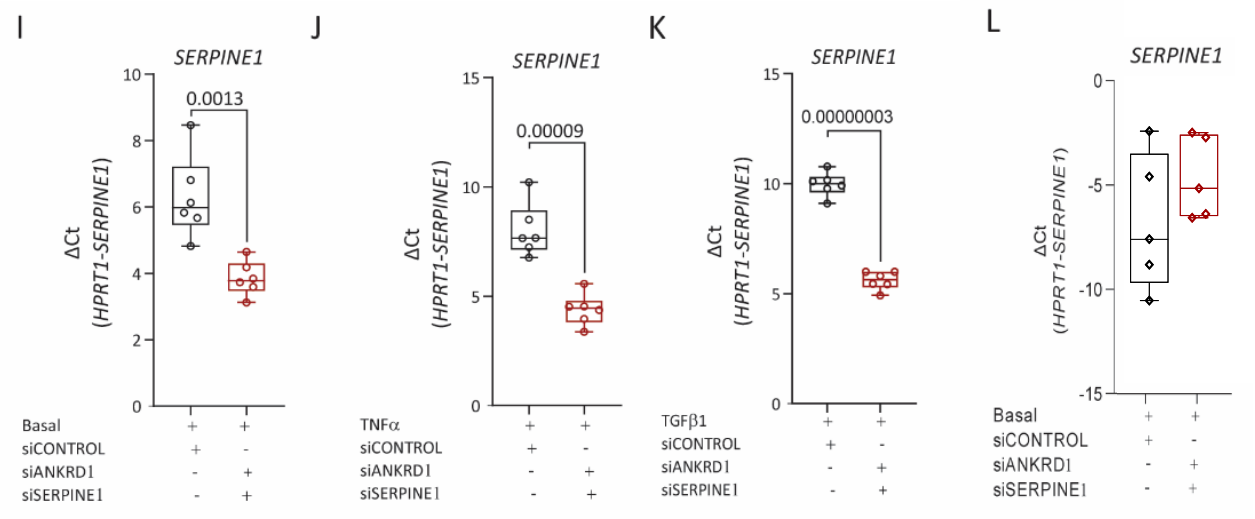

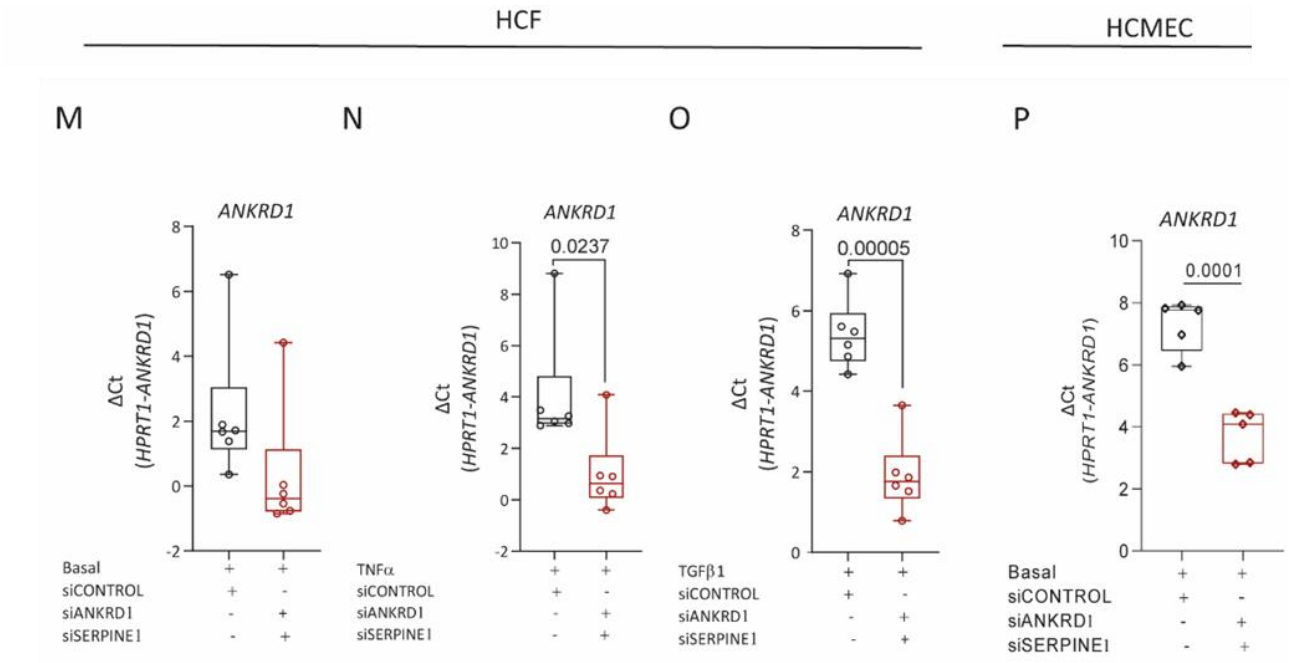

Figure 44. Single and double knockdown of *ANKRD1* and *SERPINE1* in HCFs and HCMECs. Relative mRNA expression of *SERPINE1* (A- D) and *ANKRD1* (E- H) was achieved by transient transfection with siANKRD1 or siSERPINE1 followed by treatment with TNFα (10 ng), TGF-β1 (10 ng), and basal medium. The mRNA levels of *SERPINE1* (I-L) and *ANKRD1* (M-P) in HCFs and for HCMECs after double knockdown via transient transfection with siANKRD1 and siSERPINE1 followed by treatment with TNFα (10 ng), TGF-β1 (10 ng) and basal medium. A scrambled siRNApool was used as a negative control. The values were normalized to the negative control. The Bars indicate mean ± SEM across three independent experiments with three biological replicates, each with two technical replicates for HCFs and three independent experiments with three biological replicates (only two with two technical replicates) for HCMECs. The statistical significance of differences is defined using the two-tailed unpaired t-test. *P* values are reported when the results reach statistical significance ($p < 0.05$).

4.22. Effects of ANKRD1, SERPINE1, ATF3, IL7R, and INHBB knockdown on HCFs and HCMECs proliferation

In vitro studies were performed in primary HCFs and HCMECs using transient siRNA SMARTpool transfection to investigate the functional role of ANKRD1, SERPINE1, ATF3, IL7R, and INHBB in modulating cell proliferation. The proliferation of HCFs and HCMECs were examined 48 hours after siRNA transfection (siANKRD1, siSERPINE1, siATF3, siIL7R, and siINHBB) using the bromodeoxyuridine (BrdU) incorporation assay. A scrambled siRNApool was used as the control. Single and double knockdown of ANKRD1 and SERPINE1 significantly reduced the proliferation of HCFs and HCMECs (Figure 45 A-C). Additionally, the knockdown of ATF3, IL7R, and INHBB significantly reduced the proliferation of HCFs and HCMECs (Figure 45 D-F).

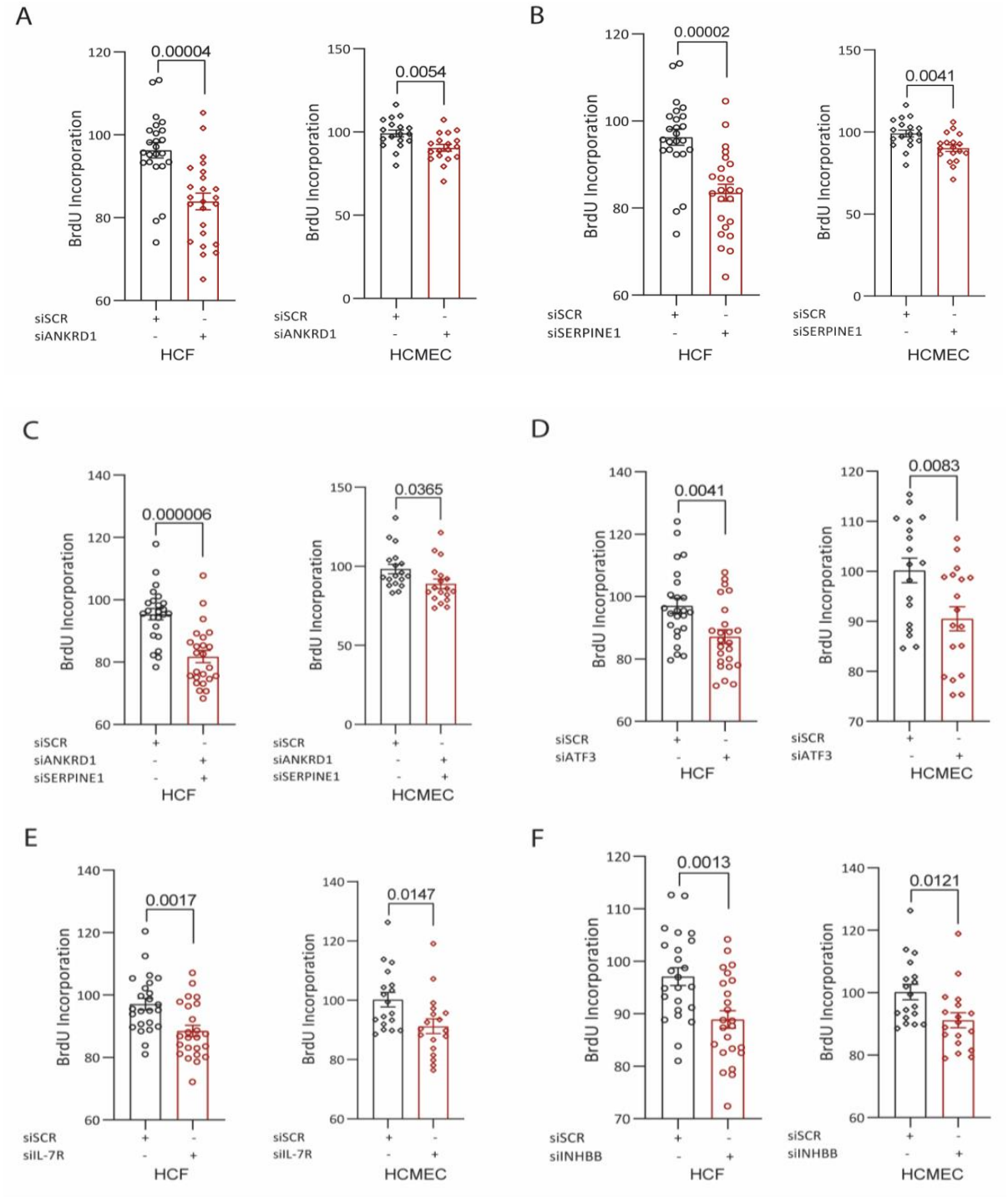

Figure 45. Effect of siRNA knockdown of *ANKRD1, SERPINE1*, *SERPINE1/ANKRD1*, *ATF3, IL7R*, and *INHBB* on HCFs and HCMECs proliferation. Primary HCFs and HCMECs were transfected with siRNA SMARTpools against *ANKRD1* (A), *SERPINE1* (B), *SERPINE1/ANKRD1* (C), *ATF3* (D), *IL7R* (E), *IHBB* (F), and control siRNA (siSCR) for 48 then proliferation was measured by BrdU incorporation assay. Bars indicate mean ± SEM across four independent experiments from four biological replicates and six technical replicates for HCFs. And three independent experiments from three biological replicates and six technical replicates for HCMECs. The data are expressed as the percentage of the control and the statistical significance of differences is defined using the two-tailed unpaired t-test. *P* values are reported when the results reach statistical significance ($p < 0.05$).

4.23. The effects of mechanical cues induced by extracellular matrix stiffness on *ANKRD1, ATF3, IL7R, INHBB,* and *SERPINE1* expression

In order to investigate *ANKRD1*, *ATF3*, *IL7R*, *INHBB*, and *SERPINE1* expression under mechanical cues induced by extracellular matrix (ECM) stiffness, primary HCFs were cultured on a soft (1 kPa) and stiff (50 kPa) matrix for different time point (Figure 46). After 12 hours, there were no significant changes in the mRNA levels of *ANKRD1* (Figure 47 A), *IL7R* (Figure 47 C), and *SERPINE1* (Figure 47 E). However, the mRNA levels of *ATF3* and *INHBB* were lower in cells grown on the stiff matrix than on the soft matrix (Figure 47 B and D). However, after 24 and 48 hours, the mRNA levels of *ANKRD1* were significantly higher in cells grown on the stiff matrix than on the soft matrix(Figure 47 A). However, after 24 and 48 hours, the mRNA levels of *ATF3* (Figure 47 B), IL7R (Figure 47 C), *INHBB* (Figure 47 D), and *SERPINE1* (Figure 47 E) were not significantly different.

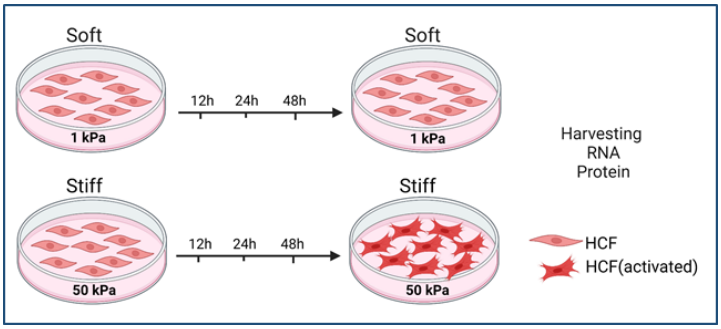

Figure 46. Schematic representation of the experimental design. Primary HCFs were cultured on 1kPa (soft matrix) and 50 kPa (stiff matrix) dishes coated with collagen and harvested at different time points (12, 24, and 48 hours). Created with BioRender.com.

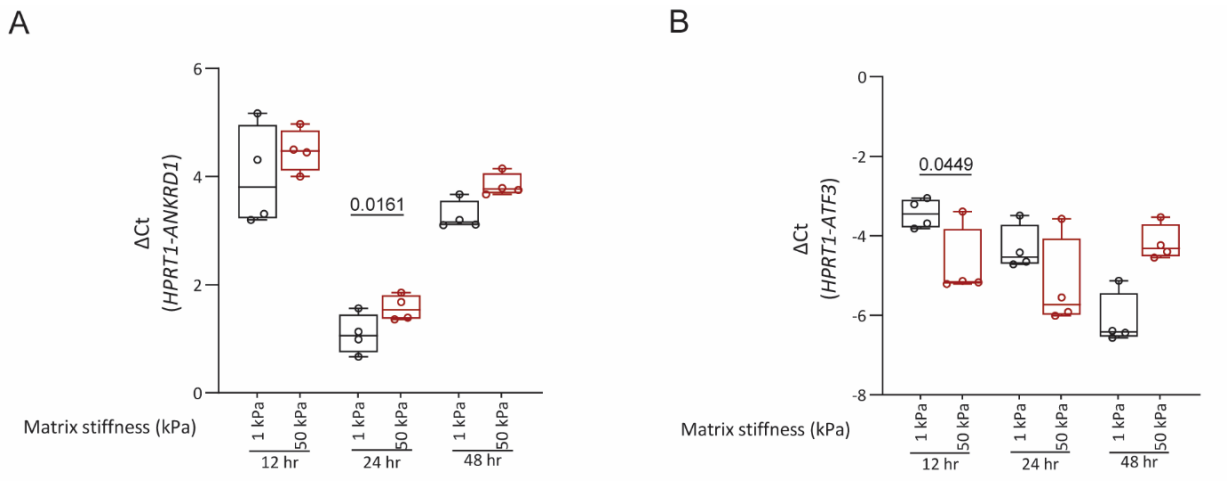

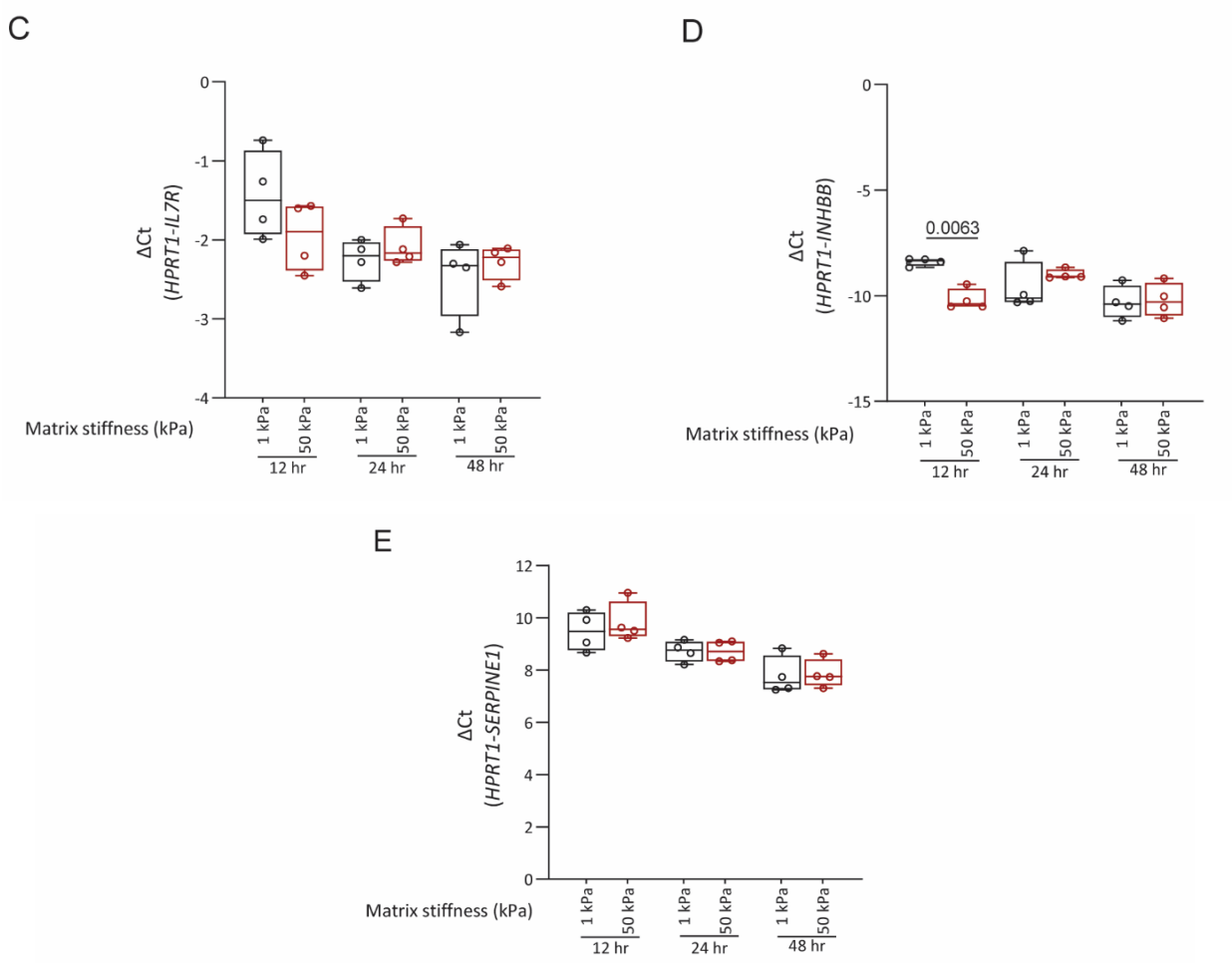

Figure 47. HCFs were cultured on 1kPa (soft matrix) and 50 kPa (stiff matrix) harvested after 12, 24 and 48 hours. Relative mRNA levels of *ANKRD1* (A), *ATF3* (B), *IL7R* (C), *INHBB* (D), and *SERPINE1* (E) were determined by qPCR. *HPRT* was used as the endogenous control. The bars indicate the mean ± SEM across four independent experiments from four biological replicates. A soft matrix (1kPa) was used as the control. Data were compared between groups using a non-parametric unpaired two-tailed *t*-test. Key: $P < 0.05$ compared to the supple matrix (1 kPa).

4.24. siRNA knockdown of ANKRD1, SERPINE1, ANKRD1/SERPINE1, ATF3, IL7R, and INHB*B* induced tube structure formation in HCMECs

A tube formation assay was used to further investigate the involvement of ANKRD1, SERPINE1, ANKRD1/SERPINE1, ATF3, IL7R, and INHBB in angiogenesis. The tube formation assay was performed on HCMECs 48 hours after transfection with si-ANKRD1, si-SERPINE1, si-ANKRD1/si-SERPINE1, si-ATF3, si-IL7R, and si-INHBB using µ-slide angiogenesis coated with corning matrigel matrix as a soluble basement membrane. A scrambled siRNApool was used as the negative control. Images were obtained after 1 and 24 hours (Figure 48 A-G). There were significantly fewer junctions in HCMECs transfected with si-ANKRD1 than with si-CONTROL (Figure 48 H). Total tube lengths were significantly

shorter in HCMECs transfected with si-ANKRD1 than with si-CONTROL (Figure 48 I). Furthermore, total segment lengths were significantly shorter in HCMECs transfected with si-ANKRD1 than with si-CONTROL (Figure 48 J). Knockdown of ANKRD1 and IL7R in HCMECs significantly decreased the total mesh area compared to the control but did not significantly affect total branch lengths (Figure 48 K and M).

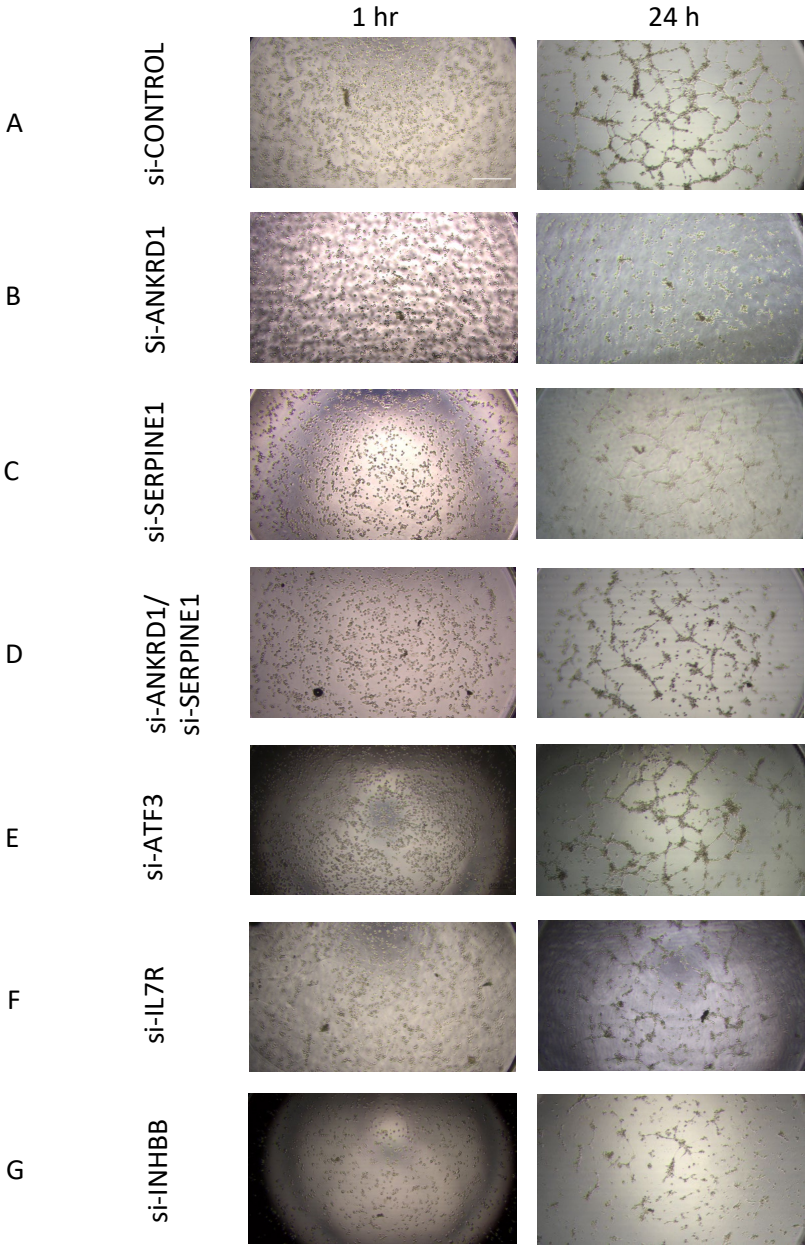

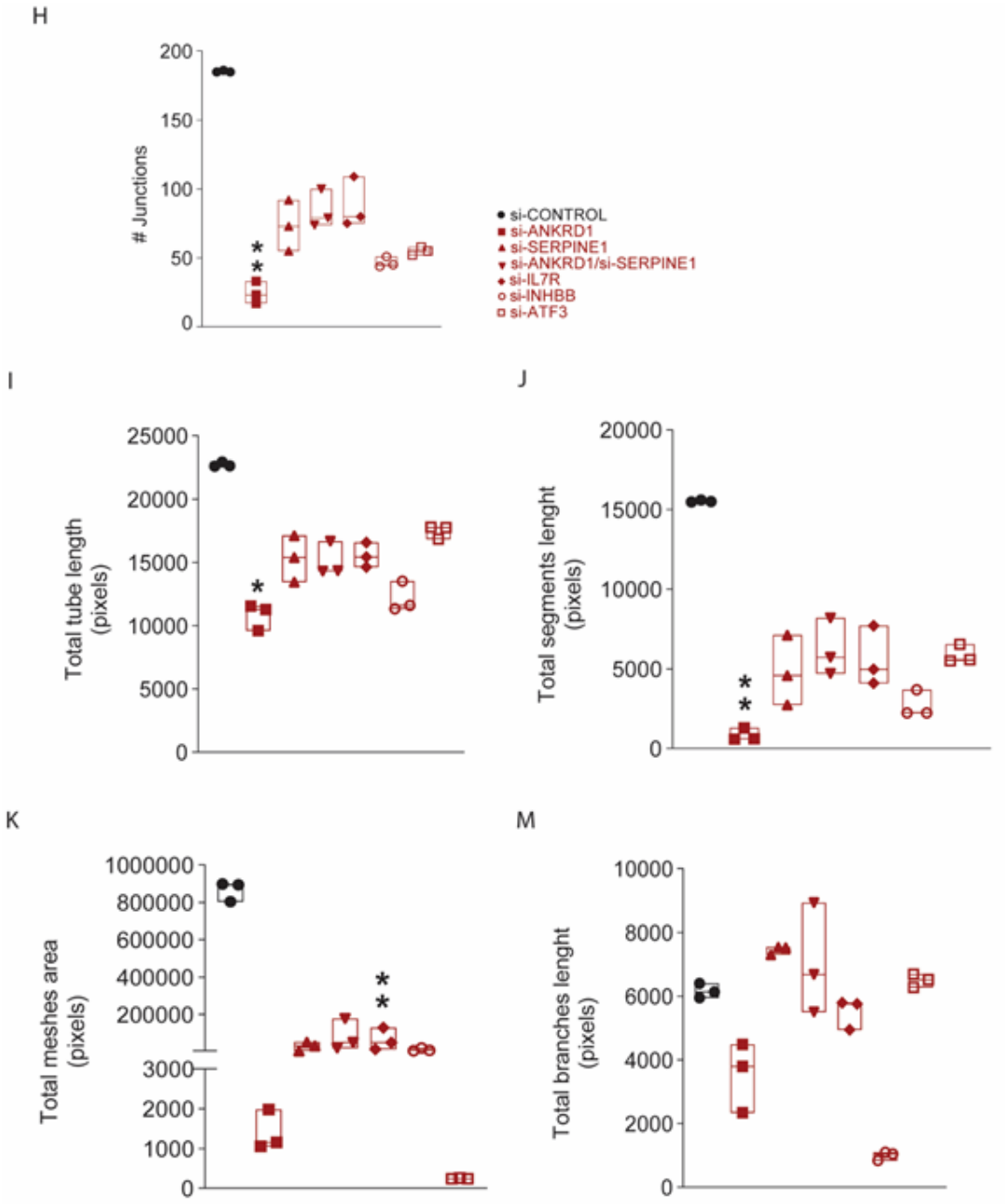

Figure 48. siRNA knockdown of ANKRD1, SERPINE1, ANKRD1/SERPINE1, ATF3, IL7R, and INHBB affected tube formation in HCMECs. The HCMECs were transfected with respective si-CONTROL, si-ANKRD1, si-SERPINE1, si-ANKRD1/si-SERPINE1, si-IL7R, si-INHBB or si-ATF3 for 48 hours. Tube formation assay were performed for 24 hours. Representative images of HCMECs tube formation at 1 hour (left) and 24 hours (right) (A-G). The number of junctions (H), Total tube length (pixels) (I), Total segment length (pixels) (J), Total mesh area (pixels) (K), and total branch length (pixels) (M) were analyzed and quantified using the Image J software with the angiogenesis analyzer plugin. A scrambled siRNApool was used as a negative control. The bars indicate mean ± SEM across three independent experiments from three biological replicates. Data were compared between groups using a non-parametric Kruskal–Wallis test. Scale bar, 1 mm. Key: *, $P < 0.05$; **, $P < 0.01$, compared to the scrambled siRNApool.

4.25. siRNA knockdown of ANKRD1, SERPINE1, ANKRD1/SERPINE1, ATF3, IL7R, and INHBB induced the migration of HCFs

Wound healing assays were performed using HCFs to further investigate the involvements of ANKRD1, SERPINE1, ATF3, IL7R, and INHBB in migration. The wound healing assay was performed after transfection with si-ANKRD1, si-SERPINE1, si-ANKRD1/si-SERPINE1, si-ATF3, si-IL7R, and si-INHBB using culture-insert 2 of 24-well plates. A scrambled siRNApool (si-CONTROL) was used as the negative control. Images were after 1, 3, 6, 18 and 24 hours. The images at 1 and 24 hours are shown in Figure 49 A-G. The percentage of wound closure was significantly smaller in HCFs transfected with si-SERPINE1, si-IL7R, or si-INHBB than with si-CONTROL. However, the percentage of wound closure did not differ significantly between HCFs transfected with si-ANKRD1, si-ANKRD1/si-SERPINE1, or si-ATF and those transfected with si-CONTROL (Figure 49 H).

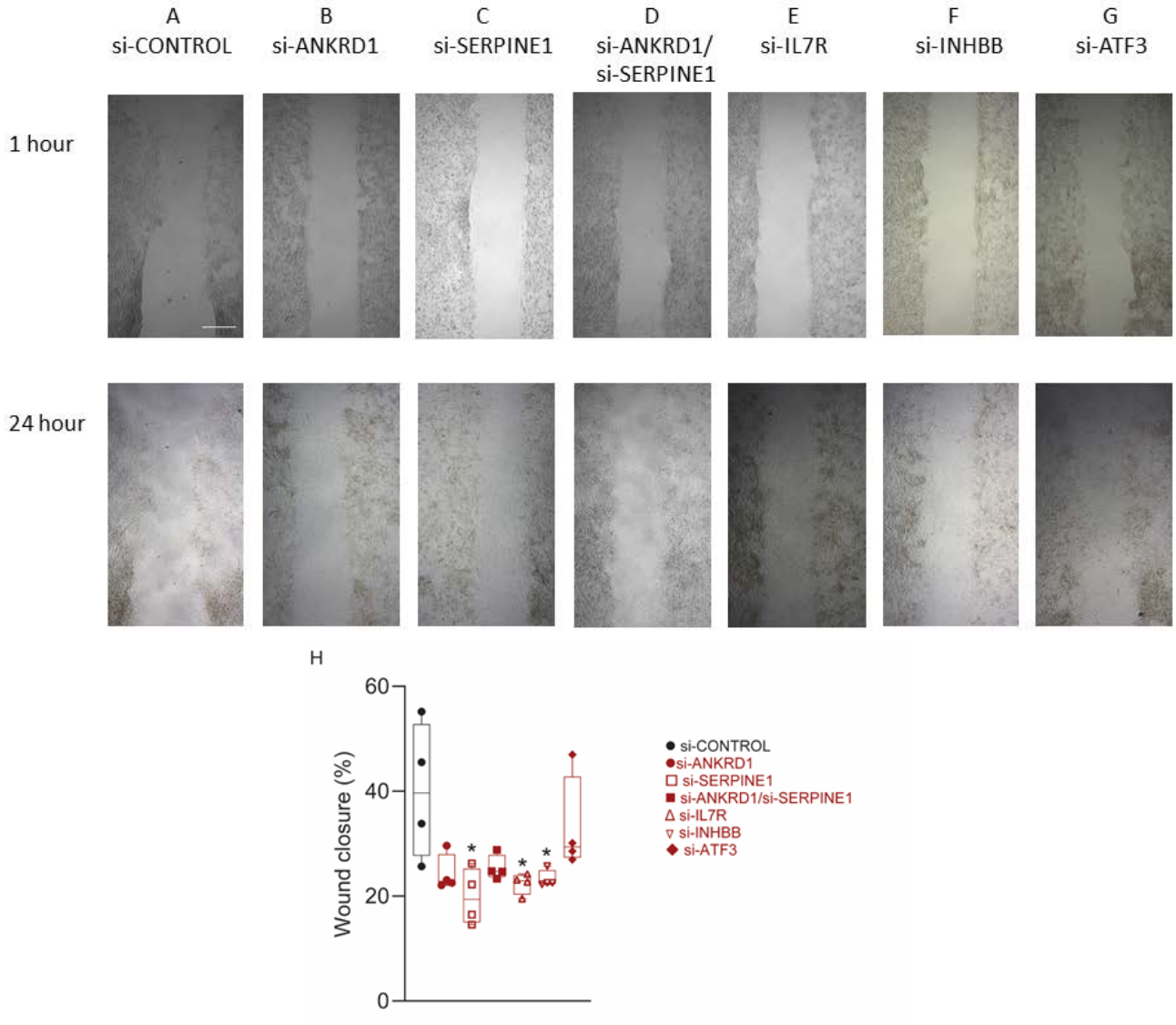

Figure 49. siRNA knockdown of ANKRD1, SERPINE1, ANKRD1/SERPINE1, ATF3, IL7R, and INHBB induced migration in HCFs by effecting wound closure. The HCFs were transfected with si-CONTROL, si-ANKRD1, si-SERPINE1, si-ANKRD1/si-SERPINE1, si-IL7R, si-INHBB, and si-ATF3 for 48 hour followed by a 24 hour migration assay. Representative images of HCFs migration at 1 hour (up) and 24 hour (down) (A-G). The percentage of wound closure (H) was analyzed and quantified using Image J software with the wound healing analyzer plugin. A scrambled siRNApool was used as a negative control. The bars indicate mean ± SEM across three independent experiments with three biological replicates with only one having one technical replicates. Data were compared between groups using an two-tailed unpaired t-test. * P <0.05 compared to scrambled siRNApool. Scale bar, 1mm.

4.26. Evaluation of right ventricle function using invasive and noninvasive methods in MCT-induced PH rats

A schematic representation of the experimental design for MCT-induced PH rats and RV dysfunction is shown in Figure 50. At 5W (weeks), the RV ejection fraction (RVEF %) was significantly smaller among MCT-treated rats (37.60% ±3.82%) than among control (saline treated) rats at 5 weeks (70.50% ± 2.25%). However, the RVEF did not differ significantly between MCT-treated and control rats at 2W (65.75% ± 3.56% vs. 66% ± 1.58%) and 3W (64.50% ± 2.10% vs. 71% ± 2.70%) (Figure 51 A). The ratio of RV to LV mass plus septum (RV/LV+S), was significantly higher in MCT-treated rats (0.269 ± 0.005) than in control rats (0.60 ± 0.01) at 5W (Figure 51 B). RV systolic pressure (RVSP mmHg) was significantly higher in MCT-treated rats than in control rats at 2W (33.05 ± 1.08 vs 25.66 ± 0.72 mmHg), 3W (42.31 ± 2.58 vs 27.80 ± 0.81 mmHg), and 5W (59.10 ± 3.30 vs. 23.32 ± 1.28 mmHg) (Figure 51 C).

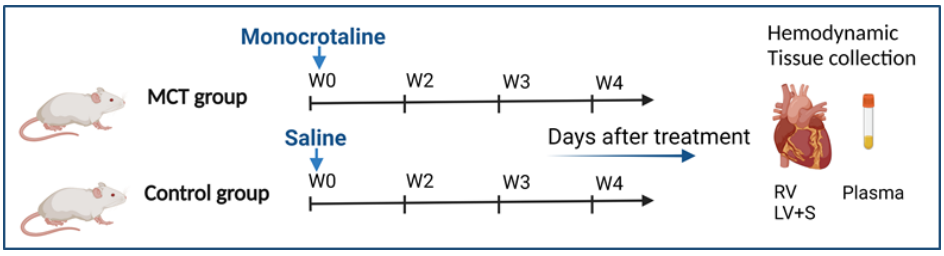

Figure 50. Schematic representation of the experimental design. The experiment involved MCT-induced PH rats and control rats examined via organ harvest at three time points (2, 3, and 5 weeks). Created with BioRender.com.

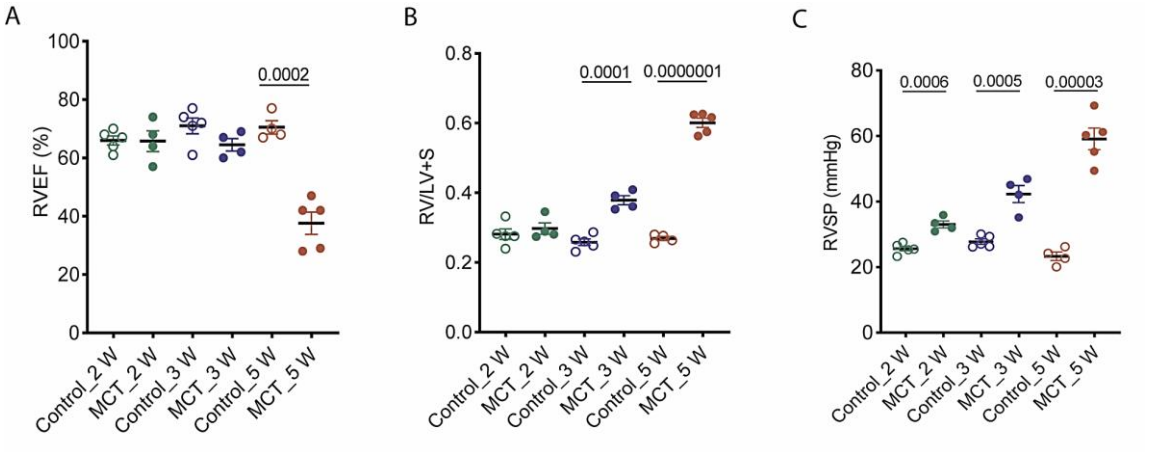

Figure 51. Cardiac function measured by noninvasive MRI or invasive hemodynamics via right heart catheterizations in MCT-induced PH rats. (A) RVEF(%) was measured by noninvasive MRI. (B) The ratio of RV mass to LV mass plus septum mass (RV/LV+S) was measured by gross weight. (C) RVSP was measured by invasive hemodynamics via RHC. Data are presented as the mean ± SEM at 2W (Control, n = 5; MCT, n = 4), at 3W (Control, n = 5; MCT, n = 4), and at 5W (Control, n = 4; MCT, n = 5). The data were compared between groups using an unpaired two-tailed t-test.

4.26.1. mRNA expression of *Ankrd1, Atf3, Il7r, Inhbb,* and *Serpine1* in MCT-induced PH rats

The mRNA expression levels of *Ankrd1*, *Atf3*, *Il7r*, *Inhbb*, and *Serpine1* were measured in RV of MCT-induced PH rats and control rats after 2, 3, and 5 weeks (W). The mRNA levels of *Ankrd1*, *Il7r*, *Inhbb*, and *Serpine1* were significantly higher in MCT-treated rats than in control rats after 5W(Figure 52 A, C, D, and E). However, only the mRNA levels of *Ankrd1* were significantly higher in MCT-treated rats than in control rats after 2W (Figure 52 A). For the time point of 2- and 3- weeks, only *Ankrd1* exhibited a strong upregulation in mRNA expression in RV of MCT rats 2W compared to the control 2W and other genes didn't show significant changes (Figure 52 B, C, D, and E).

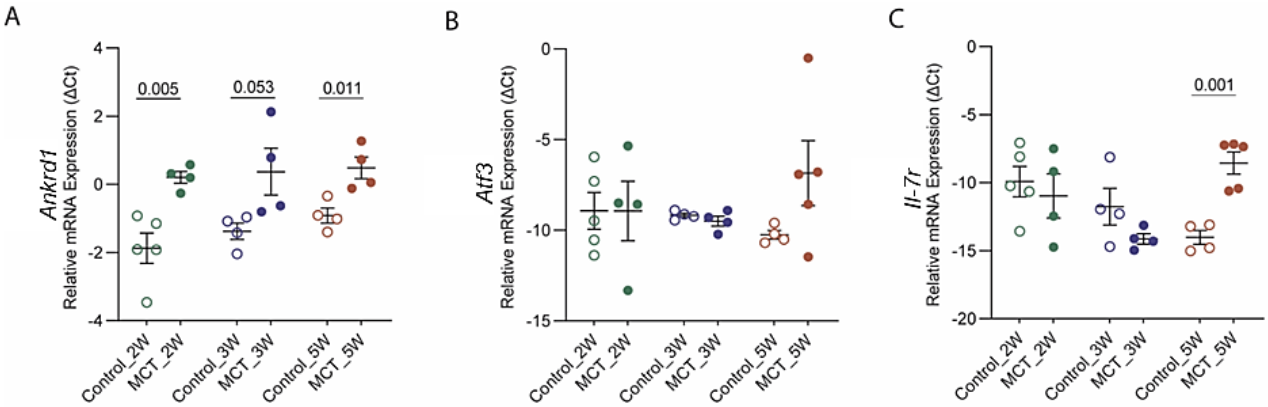

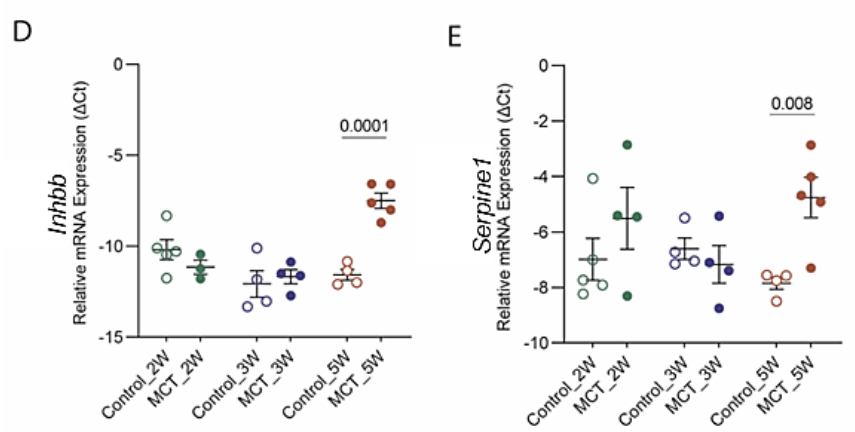

Figure 52. mRNA levels of *Ankrd1, Atf3, Il7r, Inhbb,* and *Serpine1* in the right ventricle of MCT-induced PH rats. The mRNA levels of *Ankrd1* (A), *Atf3* (B), *Il7r* (C), *Inhbb* (D), and *Serpine1* (E) in the RV of MCT-induced PH rats and control rats at 2, 3, and 5 weeks (W) post MCT injection. The mRNA levels were measured by real-time PCR and the values were normalized to the housekeeping gene, GAPHD. The data presented as the mean ± SEM. *n* (Control_2W: A, B, C, D, E) = 5, *n* (MCT_2W: A, B, C, E) = 4, *n* (MCT_2W: D) = 3, *n* (Control_3W: A, B, C, D, E) = 4, *n* (MCT_3W: A, B, C, D, E) = 4, *n* (Control_5W: A, B, C, D, E) = 4, *n* (MCT_5W: B, C, D, E) = 5, *n* (MCT_5W: A) = 4. The data were compared between groups using an unpaired two-tailed t-test.

4.26.2. Protein levels of ANKRD1 and SERPINE1 in the RV of MCT-induced PH rats

The protein levels of ANKRD1 and SERPINE1 in RV were measured in MCT-induced PH rats and control rats after 2, 3, and 5 weeks (W). The protein levels of ANKRD1 (Figure 53 A and B) and SERPINE1 (Figure 53 C and D) did not differ significantly between MCT-treated rats and control rats.

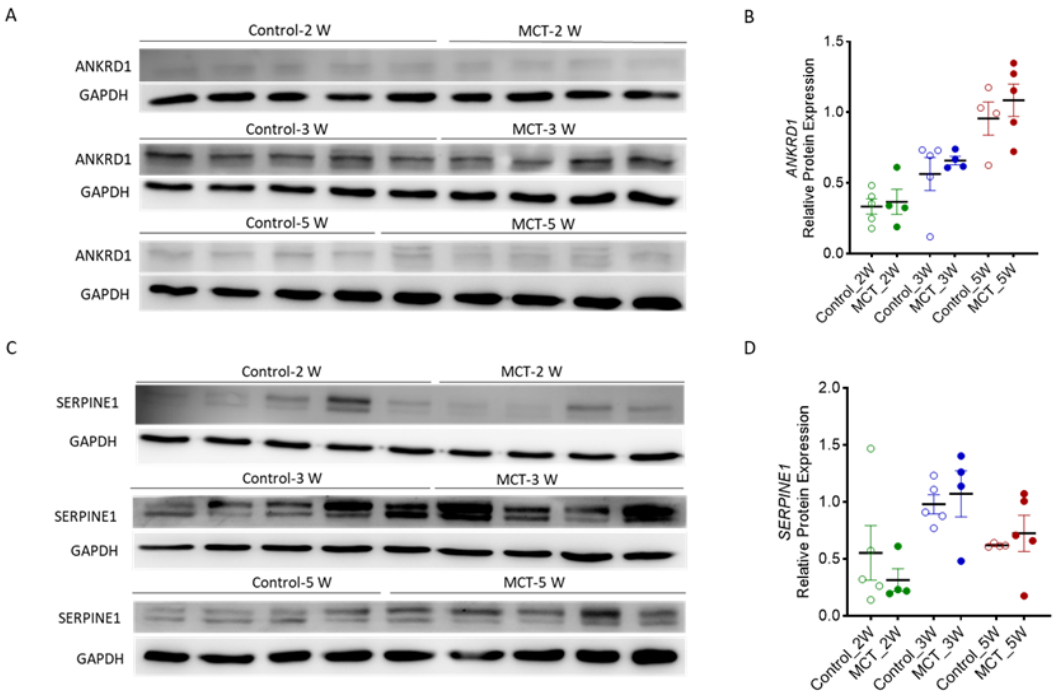

Figure 53. Protein levels of ANKRD1 and SERPINE1 in the RV of MCT-induced PH rats. Western blot analysis and immunoblot quantification of ANKRD1 (A, B) and SERPINE1 (C, D) in the RV of MCT-induced PH rats and control rats at 2, 3, and 5 weeks(W) post MCT injection. GAPDH was used as a loading control. The data are presented as mean ± SEM at 2W (weeks) animal (Control, n = 5; MCT, n = 4), for 3W (Control, n = 5; MCT, n = 4), and for 5W (Control, n = 4; MCT, n = 5). The data were compared between groups using an unpaired two-tailed t-test.

4.26.3. Correlations between *Ankrd1, Atf3, Il7r, Inhbb,* and *Serpine1* mRNA levels and the hemodynamic parameters of the RV in MCT-induced PH rats

The mRNA levels of *Ankrd1*, *Atf3*, *Il7r*, *Inhbb*, and *Serpine1* correlated with the RV hemodynamics parameters of MCT-treated rats. The mRNA levels of *Ankrd1*, *Inhbb*, and *Serpine1* correlated significantly with RVSP, RV/LV+S, and RVEF of MCT treated (Figure 54 A, D, and H).

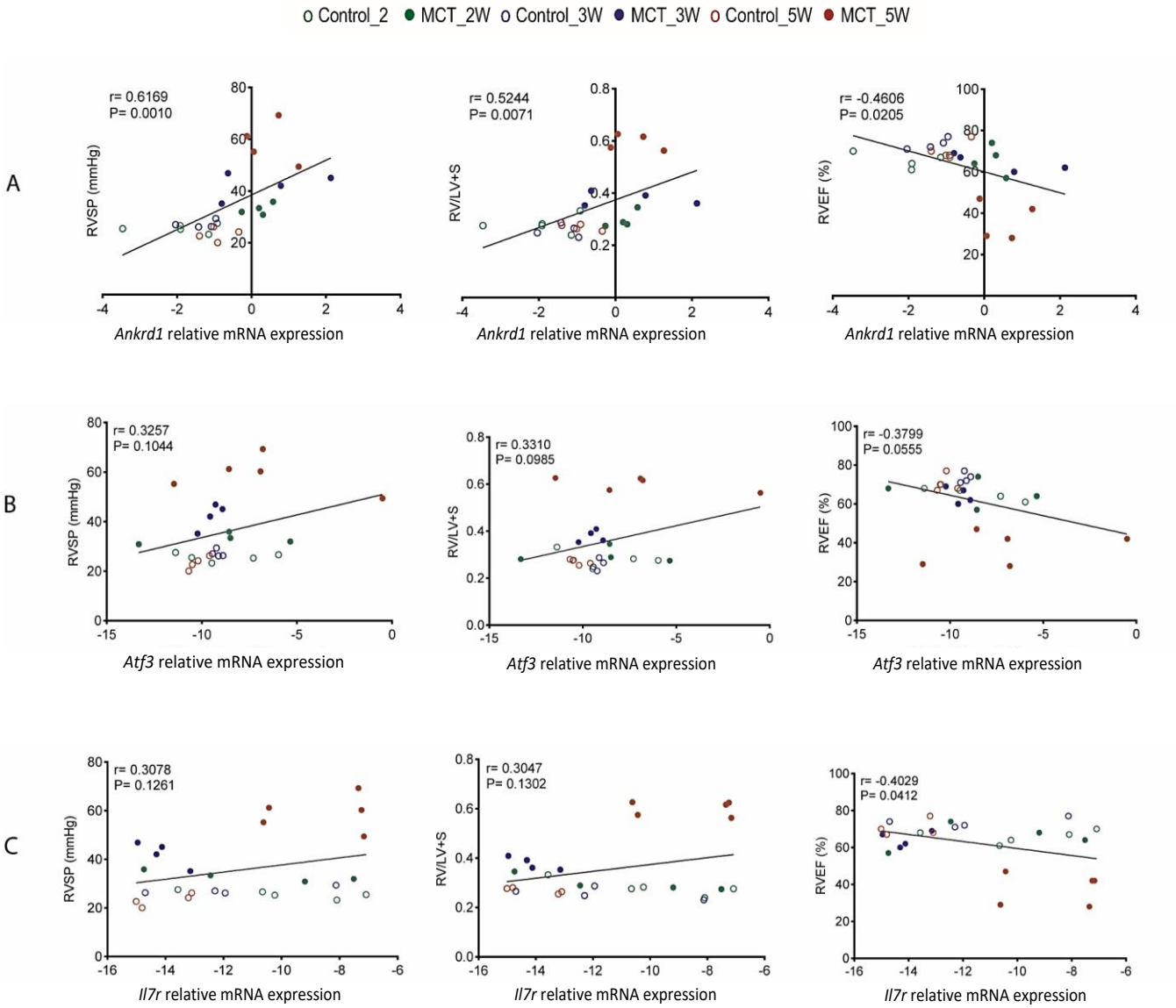

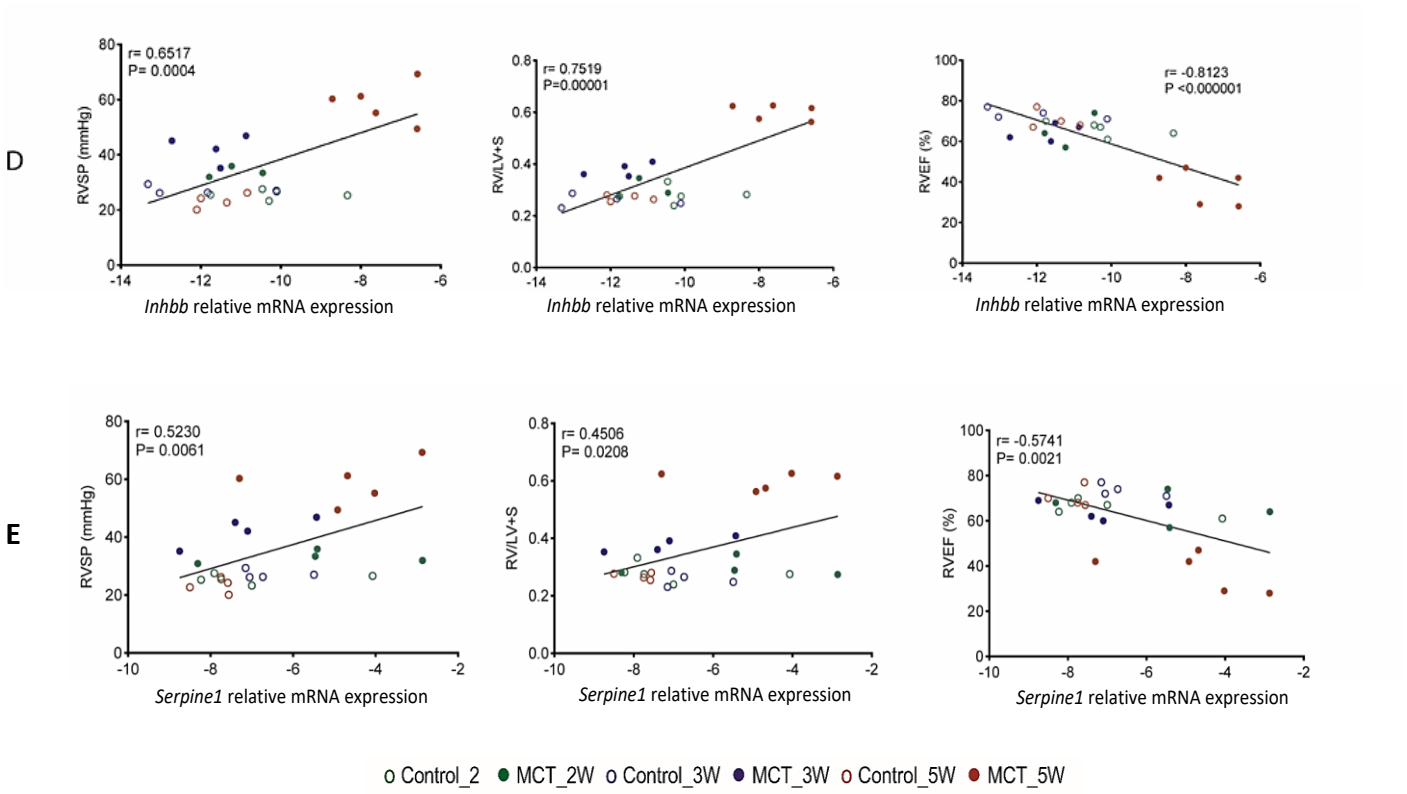

Figure 54. Correlations between *Ankrd1*, *Atf3*, *Il7r, Inhbb*, and *Serpine1* mRNA levels and the RV hemodynamics parameters of MCT-induced PH rats. The mRNA levels of *Ankrd1* (A), *Atf3* (B), *Il7r* (C), *Inhbb* (D), and *Serpine1* (E) were plotted against RV systolic pressure (RVSP mmHg), the ratio of RV mass to LV mass plus septum mass (RV/LV+S), and RV ejection fraction (RVEF). Pearson's correlation coefficient (r) and associated *P* value are shown in each graph.

4.27. Evaluation of right ventricle function by invasive and noninvasive methods in rat PAB models

A schematic representation of the experimental design for the PAB rats is shown in Figure 55. The RVEF was significantly smaller in the PAB rats (49.50% ± 2.98%) than in the sham rats (66.25% ± 2.32%) at 53 days (d). However, the RVEF did not differ significantly between the PAB and sham rats at 35d (61.50% ± 1.44% vs. 66.25% ± 1.75%)(Figure 56 A).

The RV/LV+S was higher in PAB rats than in sham rats at 35d (0.46 ± 0.006 vs. 0.26 ± 0.01) and 53d (0.59 ± 0.03 vs. 0.27 ± 0.01) (Figure 56 B). Compared to the sham rats, in the PAB operated rats, the RVSP significantly increased after 35d (44.86 ± 7.59 vs. 20.96 ± 1.43 mmHg) and 53d (42.90 ± 7.31 vs. 25.67 ± 1.69 mmHg) (Figure 56 C).

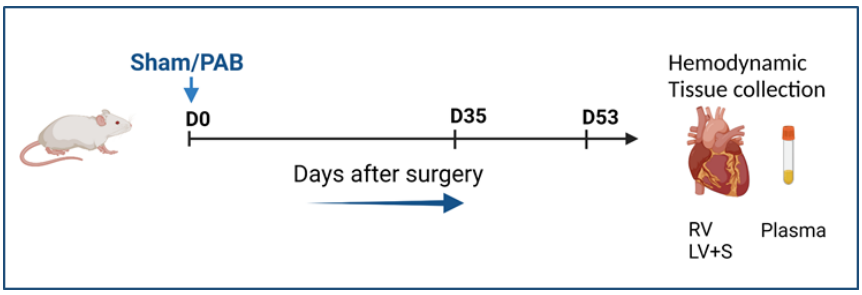

Figure 55. Schematic representation of the experimental design. The experiment was performed on the pulmonary artery banding (PAB) model of rat RV hypertrophy and Sham at different time points (35 and 53 days) with organ harvest. Created with BioRender.com.

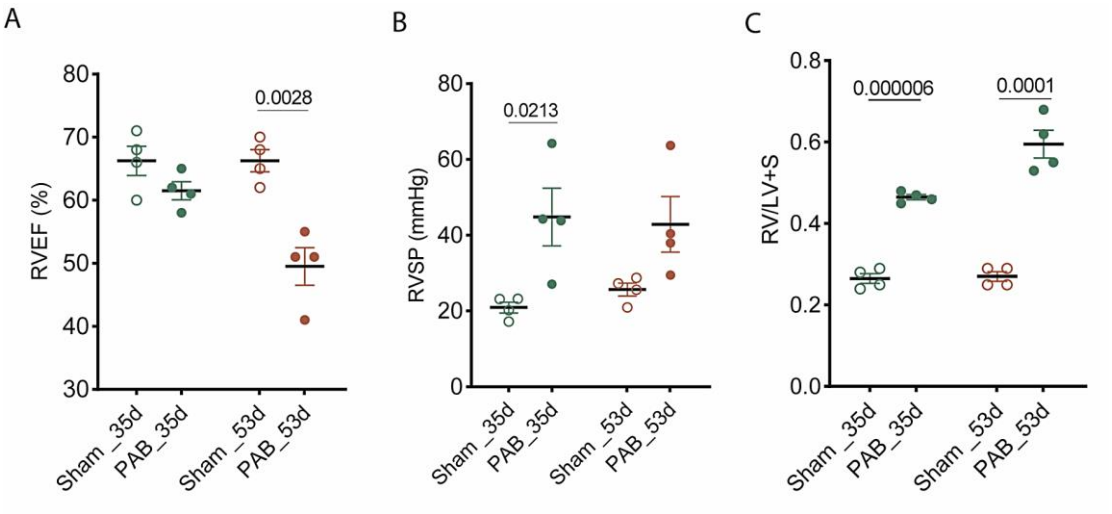

Figure 56. Measurements of cardiac function by noninvasive MRI or invasive hemodynamics via right heart catheterizations in rats PAB model of RV hypertrophy. RV ejection fraction (RVEF %) was measured by noninvasive MRI (A). RV systolic pressure (RVSP mmHg) was measured by invasive hemodynamics via RHC (B), and the ratio of RV mass to LV mass plus septum mass (RV/LV+S) was measured by gross weight (C). The data are presented as mean ± SEM at 35d (days) (Sham, $n = 4$; PAB, $n = 4$); for 53d (Sham, $n = 4$; PAB, $n = 4$). The data were compared between groups using an unpaired two-tailed t-test.

4.27.1. *Ankrd1, Atf3, Il7r, Inhbb,* and *Serpine1* mRNA levels in the RV of rats PAB model

The mRNA levels of *Ankrd1*, *Atf3*, *Il7r*, *Inhbb*, and *Serpine1* in the RV were measured in PAB and sham rats after 35 and 53 days. The mRNA levels of *Ankrd1*, *Atf3*, *Il7r*, *Inhbb*, and *Serpine1* did not differ significantly between the PAB and sham rats (Figure 57 A-E).

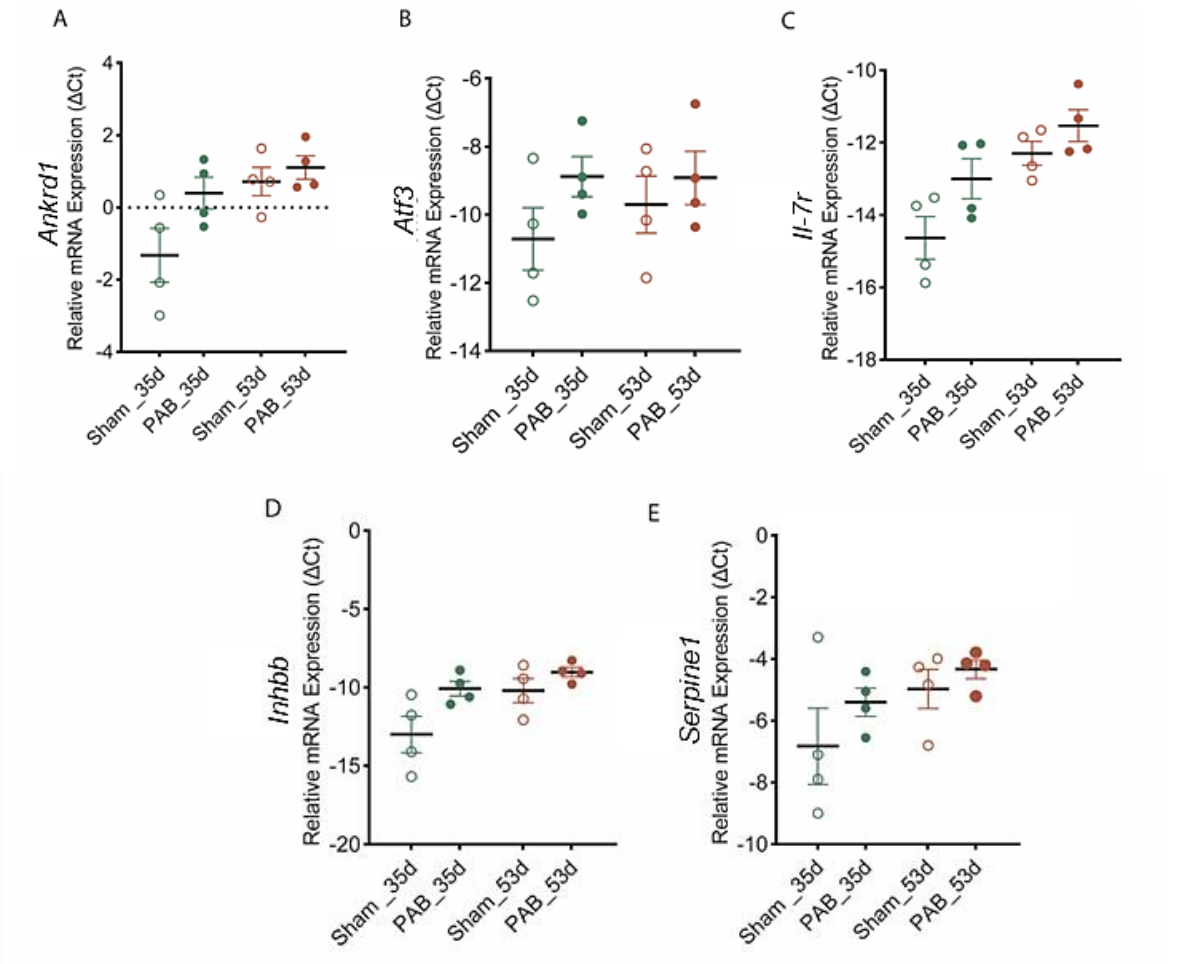

Figure 57. *Ankrd1, Atf3, Il7r, Inhbb,* and Serpine1 mRNA levels in the RV of the rats PAB model. mRNA levels of *Ankrd1* (A), *Atf3* (B), *Il7r* (C), *Inhbb* (D), and *Serpine1* (E) in the RV of PAB and sham at 35 and 53 days after surgery. The mRNA levels were measured by real-time PCR and the values were normalized to the housekeeping gene, GAPHD. The data presented as the mean ± SEM for 35d (days) (Sham, n = 4; PAB, n = 4), and 53d (Sham, n = 4; PAB, n = 4). The data were compared between groups using an unpaired two-tailed t-test.

4.27.2. Protein levels of ANKRD1 and SERPINE1 in the RV of rats PAB model

The protein levels of ANKRD1 and SERPINE1 were measured in the RV of PAB and sham rats at 35 and 53 days after surgery. Protein levels of ANKRD1 were significantly higher in PAB rats than in sham rats at 53d (Figure 58 A, B). Similarly, protein levels of SERPINE1 were significantly higher in PAB rats than in sham rats at 35 days (Figure 58 C, D).

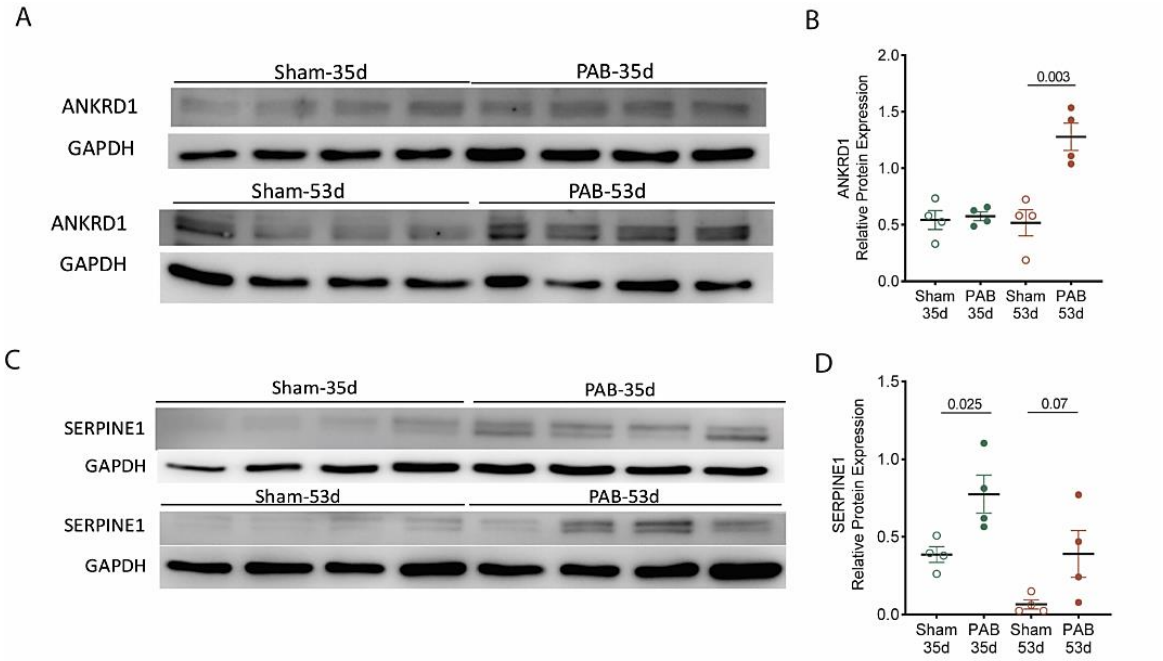

Figure 58. Protein levels of ANKRD1 and SERPINE1 in the RV of the rats PAB model. Western blot and immunoblot quantification ANKRD1 (A, B) and SERPINE1 (C, D). GAPDH was used as a loading control. Data are presented as mean ± SEM for 35d (days) (Sham, *n* = 4; PAB, *n* = 4), and for 53d (Sham, *n* = 4; PAB, *n* = 4). The data were compared between groups using an unpaired two-tailed t-test.

4.27.3. Correlation between *Ankrd1, Atf3, Il7r, Inhbb,* and *Serpine1* mRNA levels and the hemodynamic parameters of the RV in the rats PAB model

The mRNA levels of *Ankrd1*, *Atf3*, *Il7r*, *Inhbb*, and *Serpine1* correlated with the hemodynamics parameters of the RV in PAB and sham rats at 35 and 53 days post-surgery. The mRNA levels of *Ankrd1* correlated significantly with the RVSP, RV/LV+S, and RVEF (Figure 59 A). In contrast, the mRNA levels of *Atf3* did not correlate significantly with the hemodynamics parameters of the RV (Figure 59 B). However, the mRNA levels of Il7r correlated significantly with RVSP (Figure 59 C). In addition, the mRNA levels of *Inhbb* correlated significantly with RVSP and RV/LV+S (Figure 60 D). Finally, the mRNA levels of *Serpine1* correlated significantly with RV/LV+S and RVEF (Figure 59 E).

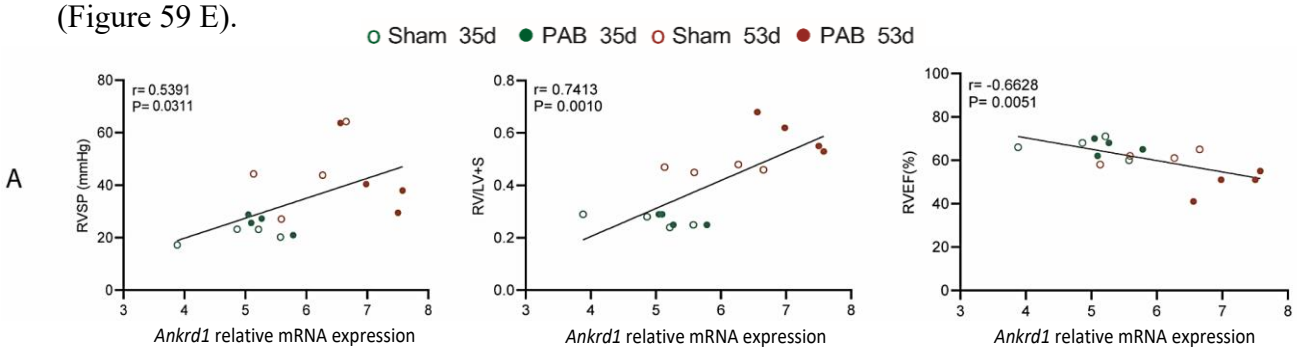

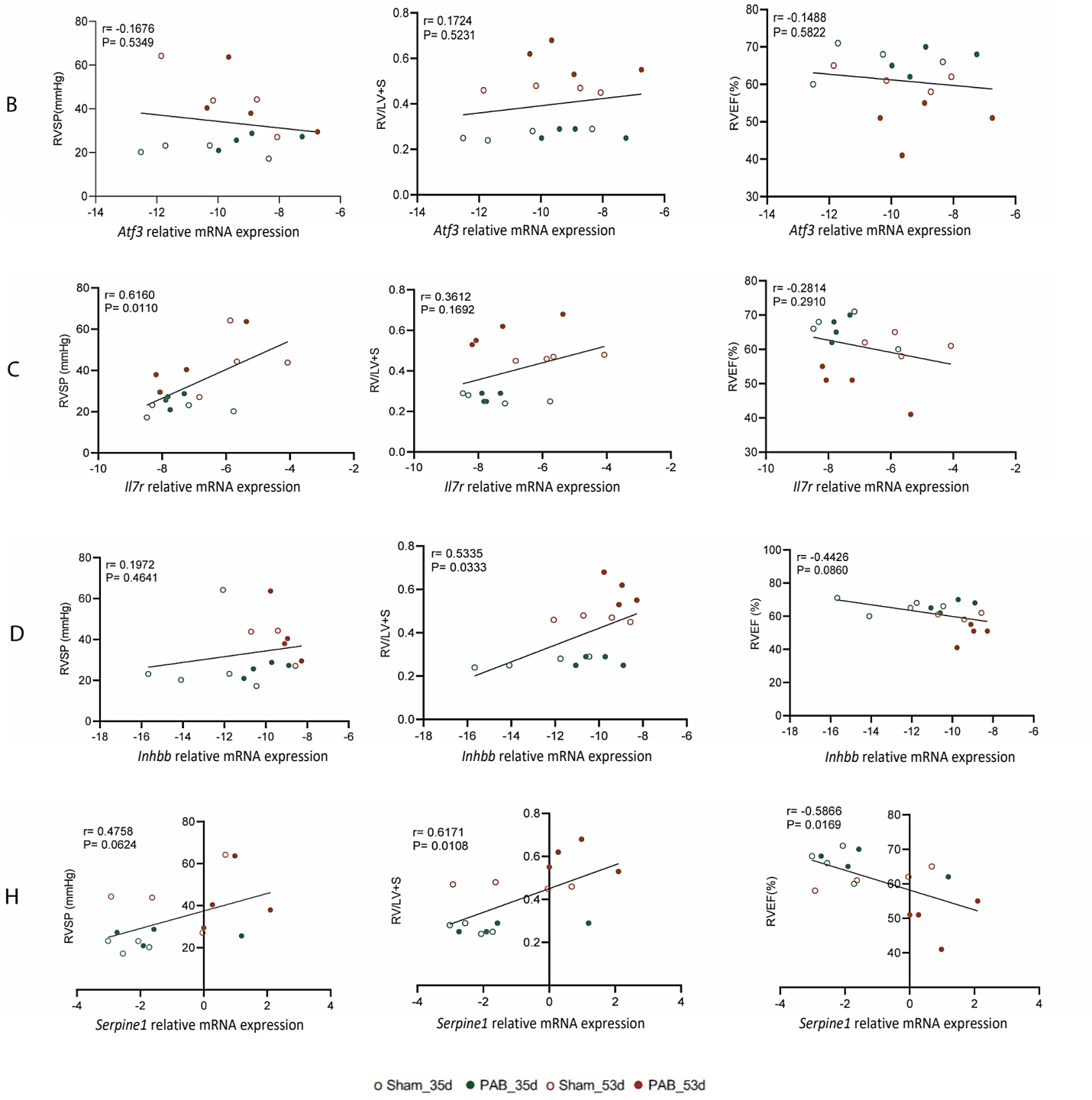

Figure 59. Correlations between *Ankrd1*, *Atf3*, *Il7r*, *Inhbb*, and *Serpine1* mRNA levels and the hemodynamics parameters of the RV in the rats PAB model. The mRNA levels of *Ankrd1* (A), *Atf3* (B), *Il7r* (C), *Inhbb* (D), and *Serpine1* (E) were plotted against RVSP, RV/LV+S, and RVEF. Pearson's correlation coefficient (r) and associated *P* value are presented in each graph.

5. Discussion

CTEPH is a complex and multifactorial pulmonary vascular disease that leads to RV remodeling. The operability of patients with CTEPH depends mainly on the accessibility of PA lesions. After successful PEA, a significant decrease in mPAP and PVR and a significant increase in 6MWD were achieved after five months (Lang et al., 2016; Madani et al., 2012; Czerner et al., 2020; Hsieh et al., 2018).

Multi-cardiac assessment approaches in CTEPH, such as MRI, RHC, serum biomarkers, and ultrasound, have contributed to some extent to reducing RV afterload. However, they are ineffective in attenuating the progression of RV remodeling (Liu et al., 2022).

The molecular mechanism of the RV in the pathophysiology of CTEPH is poorly studied and understood. RV remodeling in PH has been studied in several human cohorts, but many aspects remain to be explored. Based on the published data, some similarities and differences exist between RV remodeling in patients with CTEPH and other right heart diseases that remain to be comprehensively investigated (Liu et al., 2022). Studying the RV in CTEPH is vital because of the rapid transition from RV adaption to maladaptation in RV failure (McCabe et al., 2014). Previous studies have performed RNA-seq on RV tissues from human patients with different disease states or aetiologies (di Salvo et al., 2015; Pollmann et al., 2021). In one study, patients with RV insufficiency, based on their clinical parameters, were divided into two different RV remodeling groups (cRV and dRV). They used RNA-seq or a combination of other techniques, such as proteomics and plasma proteomics, to investigate the gene expression profile of the RV under disease conditions compared with control (Boucherat et al., 2022).

5.1. Significance of living CTEPH human cohort

Our CTEPH cohort is one of the most valuable human cohorts worldwide because it comprises biopsies from living patients with CTEPH from the RV obtained via RHC during PEA and from the ventricular septum 12 months later. Our study is the first study that applied RNA-seq to the RV of living patients with CTEPH before PEA. It provides new insights into RV pathophysiology and molecular mechanisms in patients with CTEPH who have undergone PEA. Our study investigated the molecular mechanisms of the RV and septal pathophysiology in patients with CTEPH to identify potential protein biomarkers or regulators involved in CTEPH. In addition, we applied one of the most advanced technologies, beads beating homogenization, and dry cryo-pulverization to isolate a high quality and quantity of RNA from

the RV and ventricular septum of patients with CTEPH. In the patients with CTEPH undergoing PEA, we applied an unbiased RNA-seq approach using poly-A-selected mRNA. Then, we performed a comprehensive bioinformatics analysis to determine gene expression profiles before and after PEA, which revealed a shift in gene expression from before to after PEA and confirmed the gene-specific expression patterns of the RV and septum. In addition, we identified three RV remodeling subgroups based on the patients' clinical parameters and ESC/ERS guidelines in the prePEA group, revealing shifts in gene expression patterns across the prePEAm (moderate risk), prePEAi (intermediate risk), and prePEAs (severe risk) subgroups.

5.2. Influence of RNA isolation method on the gene expression profile

In this study, the bead-beating method was used for RNA isolation in the exploratory cohort, whereas we used the dry cryo-pulverization method in the confirmatory cohort. In both methods, the size of the biopsy samples was very small, and we tried to recover as much RNA as possible from the samples using sophisticated technology.

5.3. Importance of the transcriptomic profiling of the RV and septum in CTEPH patients

Cardiac remodeling is characterized by a shift in gene expression profile triggered by thousands of genes and transcription factors that lead to the heart's response to various environmental factors (Soraya et al., 2020). In RV hypertrophy, impaired angiogenesis and reduced capillaries due to the damaged microvascular endothelial cells have been reported (Stam et al., 2019; Klinke et al., 2020).

The RNA-seq data analysis comparing post-PEA with pre-PEA revealed the role of five differentially regulated genes (*ANKRD1*, *ATF3*, *IL7R*, *INHBB*, and *SERPINE1*) both in vitro and ex vivo. SERPINE1 was significantly upregulated both pre-PEA versus post-PEA and pre-PEAs versus pre-PEAm. In addition, the clinical parameters of the well-annotated cohort of patients with CTEPH were bioinformatically correlated with gene expression profiles in the pre-and post-PEA groups. In the confirmatory cohort, *ANKRD1*, *ATF3*, *IL7R*, *INHBB*, and *SERPINE1* expression correlated significantly with some clinical parameters.

5.4. Activation of main KEGG Pathways in CTEPH cohort

The AMPK signaling pathway is mainly detected in prePEAm versus prePEAs of both exploratory and confirmatory cohorts. In the confirmatory cohort, the Hippo signaling pathways were expressed within the B-prePEA subgroups. The main KEGG pathways

that show differential expression when comparing B-postPEA to B-prePEA include the PI3k-Akt signaling pathways, focal adhesion, pathways implicated in cancer, the TGF-beta signaling pathway, the AMPK signaling pathway, and the Hippo signaling pathway.

The PI3K-Akt pathway is the common signaling pathway for postPEA compared to prePEA. IL7R is connected to the PI3K-Akt pathway. As it is reported in another study, higher expression of IL7R leads to activation of the PI3K/Akt pathway (Silva et al., 2021). Our results also confirm that IL7R is a gene associated with the PI3K-Akt signaling pathway in the CTEPH cohort.

The AGE-RAGE signaling pathway was expressed in the clusters of B-postPEA versus B-prePEA. A high expression level of the AGE-RAGE signaling pathway was observed in the cluster of postPEAs versus prePEAs. Additionally, the AGE-RAGE signaling pathway was expressed not only within the B-prePEA subgroups, but also within clusters of 9,10, and 11.

Based on the RNA-seq data of the CTEPH cohort, SERPINE1 is the gene connected to this pathway. However, the results of one study showed that activation of the AGE-RAGE pathway activates SERPINE1 in endothelial cells (Higashimoto et al., 2013). These data confirmed our finding that SERPINE1 is associated with the AGE-RAGE signaling pathway.

5.5. Role of ANKRD1 and SERPINE1 in Hippo signaling pathway

Hippo and TGF-β signaling pathways are the common pathways in B-prePEA subgroups. SERPINE1 plays an important role in the Hippo signaling pathway. The Hippo signaling pathway plays a key role in respiratory diseases. YAP/TAZ are known to be downstream effectors of the Hippo signaling pathway, and interestingly, *SERPINE1* and *ANKRD1* are the target genes of YAP/TAZ (Strippoli et al., 2020; Tang et al., 2022). Our RNA seq data showed that SERPINE1 is also involved in the Hippo signaling pathway in CTEPH RV. Our findings also demonstrated that the dual knockdown of ANKRD1 and SERPINE1 in both cardiac FBs and microvascular ECs results in a reduction of ANKRD1 and SERPINE1. However, the knockdown of *SERPINE1* leads to an increase in *ANKRD1* expression.

5.6. TGF-beta signaling pathway

The TGF-β signaling pathway is one of the most comprehensively studied pathways. To investigate the expression of *ANKRD1* , *SERPINE1* , *IL7R* , *INHBB* , and *ATF3* in HCF, we used *CILP1* as a positive control to monitor the HCF efficiency. We previously found that

CILP1 expression increased in HCFs after stimulation with TGF-β1 and that its expression was strongly correlated with TGF-β1. It appears that a functional feedback loop exists between CILP1 and TGF-β1 that leads to cardiac fibrosis. Furthermore, CILP1 plasma levels were defined as a biomarker in the same patients with CTEPH who underwent RNA-seq. Additionally, TGF-β signaling was an important pathway in prePEAm compared to prePEAs in both the exploratory and confirmatory cohorts (Keranov et al., 2021). It indicates that it may also be an important signaling pathway in postPEA versus prePEA because genes such as *ANKRD1*, *SERPINE1*, and *IL7R* are significantly affected by TGF-β1 stimulation in cardiac fibroblasts. The role of SERPINE1 in the pathogenesis of fibrosis using different animal models showed that the TGF-β/PAI-1 axis plays a crucial role in the pathogenesis of fibrosis (Ghosh et al., 2012).

5.7. Pathway enrichment analysis in prePEAm versus prePEAs in the exploratory and confirmatory cohorts

GO Terms related to the ECM, including ECM, external encapsulating structure, collagen-containing ECM, NABA CORE MATRISOME, glycosaminoglycan binding, extracellular matrix organization, and extracellular matrix structural constituent predominantly exhibit expression in prePEAm as compared to prePEAs within both exploratory and confirmatory cohorts. These terms exhibit an association with SERPINE1.

Notably, in the confirmatory cohort, cellular lipid metabolism, carboxylic acid metabolism, oxoacid metabolism, lipid metabolism, and glucose homeostasis were significantly activated in B-prePEAm compared to B-prePEAs. SERPINE1 is implicated in the biological processes underlying adipogenesis.

In contrast, within the exploratory cohort when comparing A-prePEAm to A-prePEAs, particular expressions are observed in processes and pathways such as actin filament-based process, regulation of sodium ion transport, regulation of actin cytoskeleton, regulation of muscle system process, the MAPK signaling pathway, focal adhesion, and collagen binding.

5.8. Expression of selected targets in postPEA vs. prePEA in the confirmatory cohort

The external encapsulating structure, the organization of the ECM, and the structuring of the ECM components are demonstrated expression in both the RV and the septum of the CTEPH patients. These terms exhibit an association with SERPINE1.

The expression of *ATF3* in postPEA, as compared to prePEA, is associated with regulation of the apoptotic process and programmed cell death. Furthermore, ATF3 exhibits a link to the regulation of appoptotic process and ERK1 and ERK2 cascade. ANKRD1 is connected to contractile fiber, myofibril, muscle tissue development, and actin filament organization in B-pre-septal-PEA, as compared to B-prePEA. IL7R plays a role in the regulation of nervous system development and is implicated in cancer-related pathways. IL7R is associated with the PI3K-Akt signaling pathway and focal adhesion PI3K Akt mTOR signaling pathways. SERPINE1, on the other hand, is significantly involved in tube and blood vessel morphogenesis, vascular development, angiogenesis, and terms related to the ECM. INHBB is associated with the enzyme-linked receptor protein signaling pathway, and also is involved in the cellular response to cytokine stimuli, the regulation of system processes, and the positive regulation of the apoptotic process.

5.9. Pro-PH stimuli induce *ANKRD1, ATF3, IL7R, INHBB* and *SERPINE1* expression in cardiac cells

Two types of human primary cardiac cells were used to validate the RNA-seq data: HCFs and HCMECs. A previous study demonstrated the involvement of these cells in PH pathophysiology (Frangogiannis 2017). Our study examined *CILP1*, *ANKRD1*, *ATF3*, *IL7R*, *INHBB*, and *SERPINE1* expression levels after stimulation with pro-inflammatory (TNF-α) and profibrotic (TGF-β1) stimuli, which are mainly associated with PH pathophysiology. Each gene responded differently to profibrotic and proinflammatory stimuli. While different concentrations of TGF-β1 and TNF-α were examined, the changes in *ANKRD1*, *SERPINE1*, *ATF3*, *INHBB*, *IL7R*, and *CILP1* expression were not dose-dependent, so only one concentration was presented.

Our findings revealed that the gene expression patterns of *CILP1*, *ANKRD1*, and *SERPINE1* in HCFs were the same with profibrotic stimuli. Interestingly, they also showed that ANKRD1 and *SERPINE1* expression in HCFs had the same pattern with proinflammatory stimuli, but *CILP1* expression was attenuated with pro-inflammatory stimulation. Kanai et al. (2001) showed that *ANKRD1* expression increased in vascular SMCs obtained from balloon injury after TGF-β stimulation, indicating that *ANKRD1* is a downstream target of the TGF-β/SMAD pathway.

High *SERPINE1* expression decreased TGF-β levels in DCM (Baumeier et al., 2021). *SERPINE1* was upregulated in primary human lung FBs after TGF-β stimulation under hypoxia conditions (Senavirathna et al., 2020).

Our findings revealed that *IL7R* expression in HCFs was differentially affected by profibrotic and pro-inflammatory stimuli. Park et al. (2021) showed that IL7R was associated with the TNF-α signaling pathway and expressed more highly in SuHx than in control rodents.

In renal fibrosis, the upregulation of *INHBB* depends on SOX9, a transcription factor identified as a biomarker in early kidney injury (Kumar et al., 2015; Li et al., 2018). Our results showed that INHBB expression was mainly affected by pro-inflammatory stimuli in HCFs and HCMECs. Myllaerniemi et al. (2014) found that *INHBB* expression levels were high in TGF-β/BMP pathways in the RCR array of idiopathic PF.

The upregulation of *ATF3* in cardiac FBs under hypertensive stimuli is beneficial in cardiac remodeling and hypertrophy due to the inhibition of the MAP2K3 and p38/TGF-β signaling pathways (Li et al., 2017). We found that *ATF3* expression was mainly affected by proinflammatory stimuli in HCMECs. Inoue et al. (2004) also confirmed our finding that *ATF3* can be induced by TNF-α in vascular ECs, indicating that *ATF3* expression is regulated by the JNK and ERK signaling pathways.

5.10. *Ankrd1, Serpine1, Atf3, Il7r,* and *Inhbb* expression in an experimental animal model of PH

The selection of animal models for CTEPH depends on the aim of the study. The complex pathophysiology of CTEPH makes it difficult to select a single method for its study (Mulchrone et al., 2019; Karpov et al., 2021). To study the RV remodeling in PH, MCT, and PAB are the common animal models. Due to the off-target effects of MCT and myocarditis in both the right and LV models, these animal models have limitations. Moreover, PAB as a model for RV pressure overload causes fewer RV maladaptation or failure instances than MCT (Maarman et al., 2013; Abe et al., 2010; Akazawa et al., 2020).

Our study used two different rat models: MCT and PAB. High mRNA levels of *Ankrd1*, *Atf3*, *Il7r*, *Inhbb*, and *Serpine1* were found in five-week-old MCT-treated rats, which was considered RV maladaptation, indicating that these genes were involved in the late onset of the disease. Of these genes, only Ankrd1 was upregulated in the early onset of the disease. The mRNA levels of *Ankrd1* continuously increased from the early onset to the late onset of the disease. Interestingly, the mRNA levels of *Ankrd1, Atf3, Il7r*, *Inhbb*, and *Serpine1* were not significantly altered in PAB models, and it seems that they require more than 7–8 weeks to develop a more severe RV phenotype in which they may be differentially expressed. However,

mRNA levels of *Ankrd1, Atf3, Il7r*, *Inhbb*, and *Serpine1* in PAB models continuously increased from early to late onset after PAB surgery at 53 days as a dRV.

Ankrd1, *Serpine1*, and *Inhbb* expression in the RV of animal models has not been previously investigated. For the first time, we investigated their expression in animal models of PH. Van Albada et al. (2010) examined *Atf3* expression in the RV of rat models ~36 days after MCT treatment. Their results showed no significant change in Atf3 expression in MCT-treated compared to control rats. In contrast, Atf3 expression in the MCT+shunt and MCT+shunt+Ilo groups compared to the MCT and control groups. In our MCT-treated rat models, Atf3 expression was significantly higher than in the control rats after 35 days. *Il7r* expression in the RV was higher in SuHx rats than in control rats but not in MCT-treated rats compared to control rats ~30 days after MCT treatment (Park et al., 2021). We measured *Il7r* expression at 14, 21, and 35 days after MCT treatment, but its expression was only higher in MCT-treated than in control rats at 35 days after MCT treatment.

5.11. Hypoxia induces *ANKRD1, SERPINE1, ATF3, IL7R* and *INHBB* expression in cardiac cells

As a pathological stimulus, hypoxia is important in PH pathophysiology and triggers the downstream signaling pathways of specific transcription factors. Our study examined *ANKRD1*, *ATF3*, *IL7R*, *INHBB*, and *SERPINE1* expression under hypoxia conditions for the first time using HCFs and HCMECs. Most studies on ANKRD1 focused on the stress response to stretch, and its changes under hypoxia conditions remain poorly studied.

Band et al. (2010) showed that *ANKRD1* expression correlates with the hypoxia tolerance of different animal species; for example, *Ankrd1* expression is higher in Rattus compared to Spalax species. Shinjo et al. (2017) found that *HIF1A* expression correlated with the overexpression of *ANKRD1* in dermatomyositis, a systemic idiopathic inflammatory myopathy with muscle weakness. Our findings showed, the mRNA levels of *ANKRD1* in HCMECs continuously increased after 24 and 48 hours of hypoxia exposure.

Several studies have reported high *ATF3* expression in acute hypoxia in the heart via vascular ECs (Rohini et al., 2018). In ECs, acute hypoxia was shown to increase *ATF3* expression via nitric oxide and the activation of the JNK pathway (Chen et al., 2008). Our results showed that short- and long-hypoxia exposure did not change the expression of *ATF3* in both HCFs and HCMECs.

The role of IL7R in hypoxia has been poorly studied. showed that *IL7R* expression was downregulated in PC12 cells under hypoxia conditions (Lu et al. 2009). However, our findings showed no significant changes in *IL7R* expression in both HCFs and HCMECs.

The expression of *INHBB* in hypoxia has been investigated in a few studies. In one study, no significant changes in the expression of *INHBB* under hypoxia conditions were detected (Horst et al., 2022). Our observation indicates that the expression of INHBB differs between HCFs and HCMECs. Under hypoxia conditions, *INHBB* expression was higher in HCFs but significantly lower in HCMECs.

SERPINE1 is a hypoxic molecule, and its expression has been associated with abdominal aortic aneurysms (Teng et al., 2022). Stimulation of human lung FBs with TGF-β under hypoxia increased *SERPINE1* expression, which is involved in the HIF signaling pathway (Senavirathna et al., 2020). Our findings confirmed an increased expression of *SERPINE1* under hypoxic conditions as compared to normoxic conditions in both HCFs and HCMECs. However, these changes were not statistically significant.

5.12. ANKRD1 regulates diverse cellular processes

Bogomolovas et al. (2015) showed a correlation between *ANKRD1* expression and shorter E-wave delay time, an index of LV stiffness. Our findings affirmed that ANKRD1 is connected to stiffness, with a stiff matrix increasing *ANKRD1* expression in HCFs.

The role of ANKRD1 in proliferation has been previously investigated. Beyer et al. (2016) showed that siRNA knockdown of *ANKRD1* in satellite cells led to larger cell clusters without affecting their differentiation. Interestingly, our findings revealed reduced HCF and HCMEC proliferation. Samaras et al. (2015) reported that deleting *ANKRD1* impaired wound healing and collagen contraction. *ANKRD1* was strongly induced (157.1-fold) on the first day of wound formation and is crucial in angiogenesis and wound healing (Shi et al., 2005). Our results indicated that ANKRD1 induces tube formation in HCMECs.

5.13. ATF3 regulates diverse cellular processes

ATF3 in hepatocellular carcinoma (HCC) cells, suppressed the cell proliferation and mobility both *in vitro* and *in vivo* (Chen et al., 2018). Deletion of *ATF3* inhibited the proliferation in MYC proto-oncogene bHLH transcription factor (MYC/c-Myc)-deficient cells (Tamura et al., 2005). whereas, siRNA transfection of ATF3 in cholangiocarcinoma cells, leads to an increase

in cell proliferation and decreased in cell apoptosis via inhibiting the p53 pathway (You et al., 2019). Our results indicate that *ATF3* deletion decreased the proliferation of both HCFs and HCMECs. Moreover, deleting *ATF3* in HCFs did not induce wound closure.

ATF3 is considered as a main target of the stiffness/Rac signaling pathway, and its expression on stiff hydrogel was inversely correlated with *CCND1* expression (*ATF3* expression was lower when *CCND1* expression was higher) (Dang et al., 2022). Our findings also revealed that the stiff matrix did not significantly induce *ATF3* expression in HCFs.

Okamoto et al. (2006) investigated the role of ATF3 in angiopathy in NP31/ATF3-Tet cells, showing that siRNA knockdown of *ATF3* suppressed tubulogenic differentiation. We showed that deleting ATF3 in HCMECs did not significantly induce the angiogenesis parameters.

5.14. IL7R regulates diverse cellular processes

IL7R was found to be important in the proliferation of PASMCs (Gao et al., 2016). Our results showed that deleting *IL7R* decreased the proliferation of HCFs and HCMECs. IL7R regulates the production of proangiogenic factors in ECs and macrophages (Pickens et al., 2011). We found that deleting IL7R in HCMECs significantly decreased the total meshes area, an angiogenesis parameter. Upregulation of matrix metallopeptidases 3 (MMP3) and 7 (MMP7) and activation of the AKT/NF-κB signaling pathway activated the IL7/IL7R axis and cell migration (Qu et al., 2016). Our results indicated that deleting IL7R in HCFs impairs wound closure.

5.15. INHBB regulates diverse cellular processes

Downregulating *INHBB* via small-hairpin RNAs in anoikis-resistant nasopharyngeal carcinoma (NPC) cells decreased the number of apoptotic cells; upregulated *MMP9*, vimentin (*VIM*), VEGF A (*VEGFA*); and downregulated cadherin 1 (*CDH1*/E-cadherin). Furthermore, INHBB could inhibit NPC cell migration via the TGF-β signaling pathway (Zou et al., 2018). These data confirm our findings that deleting *INHBB* in HCFs decreased wound closure. While the role of INHBB in angiogenesis and stiffness has been poorly studied, two studies have investigated the roles of the other activin family members (Kaneda et al., 2011; Ervolino De Oliveira et al., 2020). Downregulating *INHBB* via siRNA suppressed hepatocyte proliferation (Chen et al., 2011). These results also confirmed our finding that the siRNA knockdown of *INHBB* decreased cell proliferation. While the role of INHBB in stiffness has not yet been

studied, our results indicate that a stiff matrix induces *INHBB* expression in HCFs within 12 hours.

5.16. SERPINE1 regulates diverse cellular processes

Under normal conditions, SERPINE1/PAI-1 acts as a proangiogenic factor while under disease conditions it acts as an antiangiogenic factor. The aortic ring test using vessels from gene-inactivated mice showed that the absence of SERPINE1/PAI-1 suppresses angiogenesis, and underscores the role of SERPINE1/PAI-1 in proteolysis. Interestingly, recombinant SERPINE1 induced an angiogenic response in the vessels of *SERPINE1*-inactivated mice (Devy et al., 2002).

Under disease conditions, high expression of *SERPINE1* leads to ECM and collagen organization and impaired in wound healing, whereas inhibition of SERPINE1 attenuates wound closure (Rahman et al., 2020; Ghosh et al., 2012; Simone et al., 2015). Our results also showed that the deletion of *SERPINE1* in cardiac fibroblasts leads to a decrease in wound closure.

5.17. Circulation of ANKRD1, SERPINE1, ATF3, IL7R, and INHBB in Plasma

ANKRD1 is not a secreted protein. Our results showed that after stimulating HCFs and HCMECs with TGF-β1 or TNF-α, the concentration of ANKRD1 in the cell culture supernatant was undetectable. ATF3 is a secreted protein and a potential diagnostic biomarker in patients with colorectal cancer (Zhu et al., 2018). Studies in humans showed that while INHBB is barely detectable in healthy kidneys, it is detectable in kidney biospecimens from patients with immunoglobulin A nephropathy or diabetic nephropathy (Sun et al., 2022). INHBB is defined as a biomarker for various diseases, and its secretion has been reported in women with polycystic ovary syndrome (Tsigkou et al., 2008). To date, measuring INHBB is useful in the clinic to monitor ovarian tumors (Risbridger et al., 2001). It is also reported that INHBB is secreted from the ovary in a few species, and its circulating plasma levels are reduced after gonadectomy (Woodruff et al., 1996; Robertson et al., 1988). It has been reported that IL7R is a secreted protein, and its secretion is affected by patient medication (Damas et al., 2003). Plasma levels of SERPINE1 in mice and humans ranged from 10 to 20 ng/mL. Plasma levels of SERPINE1 are reported to be elevated in disease (Ghosh et al., 2012; Devy et al., 2002). Our results show that both HCFs and HCMECs secrete SERPINE1 into the cell culture supernatant.

6. Limitations

Despite our rigid efforts and work, our study had a few limitations. First, the number of consecutive patients enrolled in the exploratory cohort was small. However, our data was sufficient to identify the significant differences in RNA-seq profiles between the moderate and severe risk groups for CTEPH, which were validated in the confirmatory cohort.

Second, it used a right heart-focused risk stratification model adapted from the ESC/ERS PH guidelines. This model has not yet been validated in a clinical outcome study. However, all recommended diagnostic aspects (hemodynamic, biomarker, and imaging) of right heart assessment were addressed.

Third, it classified the patients with CTEPH using the ESC/ERS guidelines, which were designed to comprehensively assess risk in PAH. Based on the ESC/ERS guidelines, patients with PAH are classified as low (<5% estimated one-year mortality), intermediate (5%–20%), and high (>20%) risk. Since CTEPH is considered as Group 4 PH, and PAH is classified as Group 1, we could not incorporate the PAH classification into the CTEPH category to predict the mortality rate. Nonetheless, the death of one patient with CTEPH in the high-risk (severe) group was reported.

Fourth, our study obtained biopsy samples from two distinct locations within the heart. Our findings showed distinct gene expression profiles between the RV and septum. While the timing of the biopsy differed between the RV (baseline, pre-PEA) and septum (follow-up, post-PEA), our data clearly demonstrated several overlapping results between them, underscoring the significance of these findings.

Fifth, the RV biopsy was obtained during surgery, immediately following sternotomy and the patient’s connection to the heart-lung machine, in the cooling phase as soon as the heart was fibrillating, before the circulatory arrest and the endarterectomy procedure were performed. The septum biopsy was taken in the catheter lab from awake patients. Therefore, our study did not investigate the impact of factors such as the timing of biopsy removal, surgical procedures, and patient medication on the RNA-seq profiling of patients with CTEPH.

Sixth, due to the ethical issues regarding taking myocardial biopsies from healthy individuals our study lacks the healthy control RV and septum tissue. Most available data consists of transplanted heart tissue, making comparing them with our dataset difficult. The surgical procedures, biopsy location, and RNA isolation method complicate incorporating these samples into our study. Nonetheless, we compared the RNA profiles between patients with CTEPH and

healthy controls (transplanted heart tissue). A PCA plot showed significant segregation between the RNA profiles of patients with CTEPH and healthy controls. The precise cause of this segregation (i.e., PEA or varying RNA isolation methods) remains uncertain (these results have not been included in my thesis). To ensure appropriate control in our study, we explored subgroups within our patients with CTEPH (e.g., pre-PEAm, pre-PEAi, and pre-PEAs).

Notably, the transcriptomic data from our CTEPH cardiac tissue (RV and septum) exhibited heterogeneity because they comprised various cell types in the heart, such as cardiomyocytes, cardiac FBs, ECs, and macrophages.

Nonetheless, as a human model of RV remodeling and reverse remodeling after PEA, our CTEPH cohort is superior to other datasets derived from transplanted hearts.

7. Outlook

The data presented here are the first to examine the gene expression profiles of cardiac tissue in living patients with CTEPH. The biopsies were obtained from the RV and septum of the same patients. Our results demonstrated that comparing the gene expression profiles of the septum and RV may provide new insights into the pathophysiology of CTEPH.

CTEPH is a unique model of right ventricular failure that can recover after PEA. The transition of the maladaptive RV to failure is a very individualized process, and individualized risk stratification is crucial for optimal patient management. However, comparing our datasets with others is difficult due to differences in RNA-seq data and disease etiologies across studies. Therefore, subdividing CTEPH into moderate, intermediate, and severe groups is very important. It is essential to identify additional subgroups for the intermediate risk group.

Patients with CTEPH should be classified according to their sex to determine sex-specific gene expression profiles. It is important to study the impact of sex on disease progression in patients with CTEPH.

It is infeasible to collect cardiac biopsies from healthy subjects as a control due to ethical issues. Therefore, our results can be validated in animal studies.

Despite differences in the timing of the RV and septum biopsies, examining the relationship between the gene expression profiles of the RV and septum is vital, especially between pre-PEA and post-PEA. Notably, these samples were paired and belonged to the same patients, reducing variation between the RV and septum. Another important aspect is that we found that the RV and septum had common signaling pathways and genes that are very important in CTEPH pathophysiology.

A few studies have described the key roles of ATF3, IL7R, INHBB, and SERPINE1 as biomarkers. Their plasma/serum concentrations should be measured in the CTEPH cohort.

Since ANKRD1, ATF3, IL7R, INHBB, and SERPINE1 have been reported as therapeutic targets, their therapeutic role should be validated in PH animal models. In addition, studies should identify the roles and molecular mechanisms of ANKRD1, ATF3, IL7R, INHBB, and SERPINE1, particularly in cardiomyocytes.

Based on RNA-seq, ANKRD1, ATF3, IL7R, INHBB, and SERPINE1 are involved in various signaling pathways in CTEPH patients. Therefore, it would be important to investigate the exact role of these genes in the specific signaling pathways in which they are involved in the pathophysiology of CTEPH.

The expression of ANKRD1, ATF3, IL7R, INHBB, and SERPINE1 should be studied in the left ventricle or septum of MCT-treated and PAB rats.

Immunofluorescence staining of RV and septal tissue from CTEPH patients should be performed to localized ANKRD1, ATF3, IL7R, INHBB, and SERPINE1.

Summary

Chronic thromboembolic pulmonary hypertension (CTEPH) is a complex and multifactorial disease with progressive right ventricular (RV) failure. CTEPH, which is associated with high morbidity and mortality, is classified as group 4 pulmonary hypertension (PH) according to the WHO classification. Pulmonary endarterectomy (PEA) is a potentially curative treatment for operable CTEPH patients, leading to a reduction in RV afterload and improvement in interventricular septum (IVS) asynchrony. The effect of PEA in operable CTEPH patients on the RV and the transition from chronic impairment to normal RV function makes it a unique model for study.

The molecular mechanism and RV dynamics were investigated in different subgroups of patients with CTEPH before and after PEA. In addition, RNA-sequencing (RNA-seq) was performed on the RV tissue of both the exploratory (A-prePEA) and confirmatory cohorts (B-prePEA). In addition, patients in both the exploratory and confirmatory cohorts were classified as moderate (A-prePEAm, n = 4; B-prePEAm, n = 30) and severe-risk (A-prePEAs, n = 5; B-prePEAs, n = 18) based on their clinical parameters and ESC/ERS guidelines before PEA surgery. Furthermore, a group in the confirmatory cohort was classified as intermediate-risk (B-prePEAi, n = 23). The gene expression patterns of the septum before (B-pre-septal-PEA, n = 3) and after PEA (B-postPEA, n = 21) were compared with RV (B-prePEA, n = 3 and B-prePEA, n = 21) in pairwise comparisons in the same patients to determine the reversal effect of PEA. Pathway Enrichment Analysis was performed to determine the differences between prePEA subgroups. In addition, molecular and biological approaches were used to determine the role of differentially regulated genes. The functional roles of Ankyrin Repeat Domain 1 (ANKRD1), Activating Transcription Factor 3 (ATF3), Interleukin 7 Receptor (IL7R), Inhibin Subunit Beta B (INHBB), and Serpin Family E Member 1 (SERPINE1) were determined in various experimental models including *in vitro*, *ex vivo*, and *in vivo*.

The results of this study showed that first, the RNA profile of prePEA separates prePEAm from postPEAs in both the exploratory and confirmatory cohorts, confirming the classification of patients based on their clinical parameters and ESC/ERS guidelines.

Second, the results of the RNA profile in the exploratory cohort can be validated in the confirmatory cohort with a large number of patients.

Third, ECM-related terms were significantly activated in prePEAm versus prePEAs of both cohorts. Adipogenesis was detected in all the subgroups of prePEA whereas, oxidoreductase

activity was not observed in prePEAm versus prePEAi. The TGF-beta signaling pathway, BMP signaling pathway, and Hippo signaling pathways were identified in B-prePEAm versus B-prePEAs and B-prePEAm versus B-prePEAi.

Fourth, pathway enrichment analysis in B-prePEA and B-postPEA in the same patients revealed the following signaling pathways: MAPK, PI3K-Akt, and AGE-RAGE are common pathways between moderate, intermediate, and severe risk groups.

Fifth, bioinformatics analysis showed that the high expression of SERPINE1 in prePEAs compared with prePEAm plays an important role in triggering the disease in CTEPH. Furthermore, activation of the AGE-RAGE pathway in prePEAs compared to prePEAm with SERPINE1 involvement confirmed the importance of SERPINE1 in the pathogenesis of CTEPH.

Sixth, the comparison of the gene expression profile of septum (pre and post PEA) with that of RV (prePEA), revealed that in addition to ECM changes, simultaneous alterations in the myocardium, including sarcomere organization, and contractile fiber, were induced and ANKRD1 was associated with actin filament organization. ATF3, INHBB, and IL7R are the genes related to the PI3K-Akt signaling pathway.

Seventh, investigation of the functional role of ANKRD1, AFT3, IL7R, INHBB, and SERPINE1 molecules in *in vitro* and *in vivo* models related to these signaling pathways highlights the crucial role of these molecules in modulating cardiac cell proliferation, migration, angiogenesis, and wound healing.

Overall, these results demonstrate that before PEA, altered gene expression profile and signaling pathways together with changes in ECM and myocardium play an important role in the pathophysiology of CTEPH. In contrast, the reverse RV remodeling after PEA due to reverse ECM changes led to improved pulmonary hemodynamics and exercise capacity.

Zusammenfassung

Die chronische thromboembolische pulmonale Hypertonie (CTEPH) ist eine komplexe und multifaktorielle Erkrankung mit fortschreitendem Versagen des rechten Herzventrikel(RV). Die CTEPH mit ihrer hohen Morbidität und Mortalität wird nach WHO-Klassifikation zur Gruppe 4 der pulmonalen Hypertonie (PH) gezählt.

Die pulmonale Endarteriektomie (PEA) ist eine kurative Behandlung für operable CTEPH-Patienten, die zu einer Verringerung der RV-Nachlast und einer Verbesserung der Asynchronität des Interventrikelseptums (IVS) führt. Der Effekt von der Wirkung der PEA bei operablen CTEPH-Patienten auf den RV und der Übergang von einer chronischen Beeinträchtigung zur normalen Funktion des RV machen sie zu einem außergewöhnlichen und exzeptionellesn Modell für diese Studie. Der molekulare Mechanismus und das Momentum des RV wurden in verschiedenen Untergruppen von CTEPH-Patienten vor und nach der PEA untersucht.

Zusätzlich wurde Die RNA-Sequenzierung (RNA-seq) mit Gewebe des RV von zwei CTEPH-Patientenkohorten, der *exploratory*- (A-prePEA) und der *confirmatory*- (B-prePEA) Kohorte, durchgeführt. Darüber hinaus wurden die Patienten sowohl in der *exploratory*- als auch in der *confirmatory*-Kohorte anhand ihrer klinischen Parameter und der ESC/ERS-Leitlinien vor der PEA-Operation als Patienten mit moderatem Risiko (A-prePEAm n = 4; B-prePEAm n = 30) oder mit hohem Risiko (A-prePEAs n = 5; B-prePEAs n = 18) eingestuft. Des Weiteren gab eine Gruppe die in der *confirmatory*-Kohorte, als mittleres Risiko eingestuft wurde (B-prePEAi n = 23). Außerdem wurden die Genexpressionsmuster des Septums vor (B-pre-septal-PEA, n = 3) und nach PEA (B-postPEA, n = 21) mit denen RV (B-pre-septal-PEA, n = 3 und B-postPEA, n = 21) paarweise verglichen, um den reversiblen Wirkung der PEA-Operation zu ermitteln.

Es wurde Signalweganreicherungsanalyse durchgeführt, um die Unterschiede zwischen pre-PEA-Untergruppen zu bestimmen. Darüber hinaus wurden molekulare und biologische Ansätze verwendet, um die Rolle von differentiell regulierten Genen zu bestimmen. Die funktionelle Rolle von Ankyrin Repeat Domain 1 (ANKRD1), Activating Transcription Factor 3 (ATF3), Interleukin 7 Receptor (IL7R), Inhibin Subunit Beta B (INHBB) und Serpin Family E Member 1 (SERPINE1) in verschiedenen experimentellen Modellen, darunter *in vitro*, *ex vivo* und *in vivo*, bestimmt wurde. Die Befunde dieser Studie zeigen, dass sich erstens das RNA-Profil der pre-PEA-Untergruppen sowohl in der *exploratory* als auch in der *confirmatory*-Kohorte eindeutig zwischen pre-PEAm und pre-PEAs unterscheidet, was die Klassifizierung der Patienten auf der Grundlage ihrer klinischen Parameter und der ESC/ERS-Leitlinien bestätigt.

Zweitens können die Ergebnisse des RNA-Profils der *exploratory*-Kohorte in der *confirmatory*-Kohorte, die eine größere Anzahl an Patienten enthält, validiert werden.
Drittens zeigte sich, dass ECM-bezogene Signalwege in prePEAs im Vergleich zu pre-PEAm in beiden Kohorten wesentlich aktiviert sind. Adipogenese wird in allen Untergruppen von prePEA nachgewiesen, währenddessen die Oxidoreduktase-Aktivität in prePEAm im Vergleich zu prePEAi nicht beobachtet wurde. Der TGF-Beta-, der BMP- und der Hippo-Signalweg wurden in B-prePEAm im Vergleich zu B-prePEAs und B-prePEAm im Vergleich zu B-prePEAi ermittelt.
Viertens ergab die Signalweganreicherungsanalyse in B-prePEA und B-postPEA bei denselben Patienten die folgenden Signalwege: MAPK-, PI3K-Akt- und AGE-RAGE-Signalwege sind gemeinsam zwischen moderaten, mittleren und schweren Risikogruppen auftretend.
Fünftens zeigte die Bioinformatikanalyse, dass die hohe Expression von SERPINE1 in pre-PEAs im Vergleich zu pre-PEAm, eine wichtige Rolle bei Auslösung der Krankheit bei CTEPH spielt. Darüber hinaus bestätigte die Aktivierung des AGE-RAGE-Signalwegs in pre-PEAs im Vergleich zu pre-PEAm mit Beteiligung von SERPINE1 die Bedeutung von SERPINE1 für die Pathogenese von CTEPH.
Sechstens zeigte der Vergleich des Genexpressionsprofils des Septums (vor und nach PEA) mit dem RV vor der PEA, dass zusätzlich zu den ECM-Veränderungen, gleichzeitig Veränderungen im Myokard, einschließlich der Sarkomerorganisation und kontraktile Faser induziert werden und ANKRD1 an der Organisation der Aktinfilamente beteiligt ist. ATF3, INHBB und IL7R sind die Gene, die eine Rolle bei dem PI3K-Akt Signalweg spielen.
Siebtens die Untersuchung der funktionellen Rolle von ANKRD1, AFT3, IL7R, INHBB und SERPINE1 Molekülen in *in vitro* und *in vivo* Modellen, die mit diesen Signalwegen in Verbindung stehen, unterstreicht die entscheidende Rolle dieser Moleküle bei der Modulation der Herz-Zellproliferation, -Migration, -Angiogenese und -Wundheilung.
Insgesamt zeigen diese Ergebnisse, dass vor PEA-Operation ein verändertes Genexpressionsprofil und Signalwege zusammen mit Veränderungen der ECM und der Herzmuskulatur, spielen eine wichtige Rolle in der Pathophysiologie der CTEPH. Im Unterschied datz, dass „reverse RV-Remodeling“ nach einer PEA-Operation aufgrund umgekehrter ECM-Veränderungen zu einer Verbesserung der pulmonalen Hämodynamik und der körperlichen Leistungsfähigkeit führt.

References

Abe, K., Toba, M., Alzoubi, A., Ito, M., Fagan, K. A., Cool, C. D., Voelkel, N. F., McMurtry, I. F., & Oka, M. (2010). Formation of plexiform lesions in experimental severe pulmonary arterial hypertension. *Circulation*, *121*(25), 2747–2754. https://doi.org/10.1161/CIRCULATIONAHA.109.927681

Akazawa, Y., Okumura, K., Ishii, R., Slorach, C., Hui, W., Ide, H., Honjo, O., Sun, M., Kabir, G., Connelly, K., & Friedberg, M. K. (2020). Pulmonary artery banding is a relevant model to study the right ventricular remodeling and dysfunction that occurs in pulmonary arterial hypertension. *Journal of applied physiology (Bethesda, Md.: 1985)*, *129*(2), 238–246. https://doi.org/10.1152/japplphysiol.00148.2020

An, J., Nam, Y., Cho, H., Chang, J., Kim, D. K., & Lee, K. S. (2022). Acute Pulmonary Embolism and Chronic Thromboembolic Pulmonary Hypertension: Clinical and Serial CT Pulmonary Angiographic Features. *Journal of Korean medical science*, *37*(10), e76. https://doi.org/10.3346/jkms.2022.37.e76

Arias-Loza, P. A., Jung, P., Abeßer, M., Umbenhauer, S., Williams, T., Frantz, S., Schuh, K., & Pelzer, T. (2016). Development and Characterization of an Inducible Rat Model of Chronic Thromboembolic Pulmonary Hypertension. *Hypertension (Dallas, Tex. : 1979)*, *67*(5), 1000–1005. https://doi.org/10.1161/HYPERTENSIONAHA.116.07247

Asona, R., Ogo, T., Ohta-Ogo, K., Fukui, S., Tsuji, A., Ueda, J., Konagai, N., Fukuda, T., Morita, Y., Noguchi, T., Kusano, K., Anzai, T., Ishibashi-Ueda, H., & Yasuda, S. (2019). Prolonged QRS duration as a predictor of right ventricular dysfunction after balloon pulmonary angioplasty. *International journal of cardiology*, *280*, 176–181. https://doi.org/10.1016/j.ijcard.2018.11.026

Band, M., Joel, A., & Avivi, A. (2010). The muscle ankyrin repeat proteins are hypoxia-sensitive: in vivo mRNA expression in the hypoxia-tolerant blind subterranean mole rat, Spalax ehrenbergi. *Journal of molecular evolution*, *70*(1), 1–12. https://doi.org/10.1007/s00239-009-9306-6

Barata, J. T., Durum, S. K., & Seddon, B. (2019). Flip the coin: IL-7 and IL-7R in health and disease. *Nature immunology*, *20*(12), 1584–1593. https://doi.org/10.1038/s41590-019-0479-x

Beyer, S., Pontis, J., Schirwis, E., Battisti, V., Rudolf, A., Le Grand, F., & Ait-Si-Ali, S. (2016). Canonical Wnt signalling regulates nuclear export of Setdb1 during skeletal muscle terminal differentiation. *Cell discovery*, *2*, 16037. https://doi.org/10.1038/celldisc.2016.37

Bogomolovas, J., Brohm, K., Čelutkienė, J., Balčiūnaitė, G., Bironaitė, D., Bukelskienė, V., Daunoravičus, D., Witt, C. C., Fielitz, J., Grabauskienė, V., & Labeit, S. (2015). Induction of Ankrd1 in Dilated Cardiomyopathy Correlates with the Heart Failure Progression. *BioMed research international*, *2015*, 273936. https://doi.org/10.1155/2015/273936

Bolger, A. M., Lohse, M., & Usadel, B. (2014). Trimmomatic: a flexible trimmer for Illumina sequence data. *Bioinformatics (Oxford, England)*, *30*(15), 2114–2120. https://doi.org/10.1093/bioinformatics/btu170

Bonderman, D., Turecek, P. L., Jakowitsch, J., Weltermann, A., Adlbrecht, C., Schneider, B., Kneussl, M., Rubin, L. J., Kyrle, P. A., Klepetko, W., Maurer, G., & Lang, I. M. (2003). High prevalence of elevated clotting factor VIII in chronic thromboembolic pulmonary hypertension. *Thrombosis and haemostasis*, *90*(3), 372–376. https://doi.org/10.1160/TH03-02-0067

Boon, G., Ende-Verhaar, Y. M., Bavalia, R., El Bouazzaoui, L. H., Delcroix, M., Dzikowska-Diduch, O., Huisman, M. V., Kurnicka, K., Mairuhu, A., Middeldorp, S., Pruszczyk, P., Ruigrok, D., Verhamme, P., Vliegen, H. W., Vonk Noordegraaf, A., Vriend, J., Klok, F. A., & InShape II study group (2021). Non-invasive early exclusion of chronic thromboembolic pulmonary hypertension after acute

pulmonary embolism: the InShape II study. *Thorax*, *76*(10), 1002–1009. https://doi.org/10.1136/thoraxjnl-2020-216324

Boucherat, O., Yokokawa, T., Krishna, V., Martineau, S., Azhar, N., Bonilla, F., Gutstein, D., Potus, F., Lawrie, A., Jeyaseelan, J., Provencher, S., & Bonnet, S. (2022). Identification of LTBP-2 as a plasma biomarker for right ventricular dysfunction in human pulmonary arterial hypertension. *Nature Cardiovascular Research*, *1*(8), 748-760. https://doi.org/10.1038/s44161-022-00113-w

Baumeier, C., Escher, F., Aleshcheva, G., Pietsch, H., & Schultheiss, H. P. (2021). Plasminogen activator inhibitor-1 reduces cardiac fibrosis and promotes M2 macrophage polarization in inflammatory cardiomyopathy. *Basic research in cardiology*, *116*(1), 1. https://doi.org/10.1007/s00395-020-00840-w

Braams, N. J., van Leeuwen, J. W., Vonk Noordegraaf, A., Nossent, E. J., Ruigrok, D., Marcus, J. T., Bogaard, H. J., Meijboom, L. J., & de Man, F. S. (2021). Right ventricular adaptation to pressure-overload: Differences between chronic thromboembolic pulmonary hypertension and idiopathic pulmonary arterial hypertension. *The Journal of heart and lung transplantation : the official publication of the International Society for Heart Transplantation*, *40*(6), 458–466. https://doi.org/10.1016/j.healun.2021.02.018

Camelliti, P., Borg, T. K., & Kohl, P. (2005). Structural and functional characterisation of cardiac fibroblasts. *Cardiovascular research*, *65*(1), 40–51. https://doi.org/10.1016/j.cardiores.2004.08.020

Carlson M (2022). org.Hs.eg.db: Genome wide annotation for Human. R package version 3.16.0.

Castro, M. A., Piloto, B., Dos Santos Fernandes, C., Jardim, C., Filho, W. S., Oleas, F. G., Alves, J. L., Morinaga, L., Hoette, S., Filho, M. T., Filho, O. F., Jatene, F. B., & Souza, R. (2020). Use of medical therapies before pulmonary endarterectomy in chronic thromboembolic pulmonary hypertension patients with severe hemodynamic impairment. *PloS one*, *15*(5), e0233063. https://doi.org/10.1371/journal.pone.0233063

Chamarthy, M. R., Kandathil, A., & Kalva, S. P. (2018). Pulmonary vascular pathophysiology. *Cardiovascular diagnosis and therapy*, *8*(3), 208–213. https://doi.org/10.21037/cdt.2018.01.08

Chen, C., Shen, L., Cao, S., Li, X., Xuan, W., Zhang, J., Huang, X., Bin, J., Xu, D., Li, G., Kitakaze, M., & Liao, Y. (2014). Cytosolic CARP promotes angiotensin II- or pressure overload-induced cardiomyocyte hypertrophy through calcineurin accumulation. *PloS one*, *9*(8), e104040. https://doi.org/10.1371/journal.pone.0104040

Chen, C., Ge, C., Liu, Z., Li, L., Zhao, F., Tian, H., Chen, T., Li, H., Yao, M., & Li, J. (2018). ATF3 inhibits the tumorigenesis and progression of hepatocellular carcinoma cells via upregulation of CYR61 expression. *Journal of experimental & clinical cancer research : CR*, *37*(1), 263. https://doi.org/10.1186/s13046-018-0919-8

Chen, H., Sun, Y., Dong, R., Yang, S., Pan, C., Xiang, D., Miao, M., & Jiao, B. (2011). Mir-34a is upregulated during liver regeneration in rats and is associated with the suppression of hepatocyte proliferation. *PloS one*, *6*(5), e20238. https://doi.org/10.1371/journal.pone.0020238

Chen, S. C., Liu, Y. C., Shyu, K. G., & Wang, D. L. (2008). Acute hypoxia to endothelial cells induces activating transcription factor 3 (ATF3) expression that is mediated via nitric oxide. *Atherosclerosis*, *201*(2), 281–288. https://doi.org/10.1016/j.atherosclerosis.2008.02.014

Chen, T., Huang, J. B., Dai, J., Zhou, Q., Raj, J. U., & Zhou, G. (2018). PAI-1 is a novel component of the miR-17~92 signaling that regulates pulmonary artery smooth muscle cell phenotypes. *American journal of physiology. Lung cellular and molecular physiology*, *315*(2), L149–L161. https://doi.org/10.1152/ajplung.00137.2017

Chen, Z., Zhang, J., Wei, D., Chen, J., & Yang, J. (2021). GCN2 Regulates ATF3-p38 MAPK Signaling Transduction in Pulmonary Veno-Occlusive Disease. *Journal of cardiovascular pharmacology and therapeutics*, *26*(6), 677–689. https://doi.org/10.1177/10742484211015535

Chesne, J., Danger, R., Botturi, K., Reynaud-Gaubert, M., Mussot, S., Stern, M., Danner-Boucher, I., Mornex, J. F., Pison, C., Dromer, C., Kessler, R., Dahan, M., Brugière, O., Le Pavec, J., Perros, F., Humbert, M., Gomez, C., Brouard, S., Magnan, A., & COLT Consortium (2014). Systematic analysis of blood cell transcriptome in end-stage chronic respiratory diseases. *PloS one*, *9*(10), e109291. https://doi.org/10.1371/journal.pone.0109291

Clapham, K. R., Singh, I., Capuano, I. S., Rajagopal, S., & Chun, H. J. (2019). MEF2 and the Right Ventricle: From Development to Disease. *Frontiers in cardiovascular medicine*, *6*, 29. https://doi.org/10.3389/fcvm.2019.00029

Cramer, S. D., Aplan, P. D., & Durum, S. K. (2016). Therapeutic targeting of IL-7Rα signaling pathways in ALL treatment. *Blood*, *128*(4), 473–478. https://doi.org/10.1182/blood-2016-03-679209

Cufi, S., Vazquez-Martin, A., Oliveras-Ferraros, C., Martin-Castillo, B., Joven, J., & Menendez, J. A. (2010). Metformin against TGF-β-induced epithelial-to-mesenchymal transition (EMT): from cancer stem cells to aging-associated fibrosis. *Cell cycle (Georgetown, Tex.)*, *9*(22), 4461–4468. https://doi.org/10.4161/cc.9.22.14048

Czerner, C. P., Schoenfeld, C., Cebotari, S., Renne, J., Kaireit, T. F., Winther, H. B., Pöhler, G. H., Olsson, K. M., Hoeper, M. M., Wacker, F., & Vogel-Claussen, J. (2020). Perioperative CTEPH patient monitoring with 2D phase-contrast MRI reflects clinical, cardiac and pulmonary perfusion changes after pulmonary endarterectomy. *PloS one*, *15*(9), e0238171. https://doi.org/10.1371/journal.pone.0238171

Damas, J. K., Waehre, T., Yndestad, A., Otterdal, K., Hognestad, A., Solum, N. O., Gullestad, L., Frøland, S. S., & Aukrust, P. (2003). Interleukin-7-mediated inflammation in unstable angina: possible role of chemokines and platelets. *Circulation*, *107*(21), 2670–2676. https://doi.org/10.1161/01.CIR.0000070542.18001.87

Dang, I. Bae, Y. Brazzo, J. Assoian, R. (2022). Rac rather than Rho drives the early transcriptional response to extracellular matrix stiffness and mediates repression of ATF3. bioRxiv. https://doi.org/10.1101/2022.04.27.489717

Delcroix, M., Lang, I., Pepke-Zaba, J., Jansa, P., D'Armini, A. M., Snijder, R., Bresser, P., Torbicki, A., Mellemkjaer, S., Lewczuk, J., Simkova, I., Barberà, J. A., de Perrot, M., Hoeper, M. M., Gaine, S., Speich, R., Gomez-Sanchez, M. A., Kovacs, G., Jaïs, X., Ambroz, D., … Simonneau, G. (2016). Long-Term Outcome of Patients With Chronic Thromboembolic Pulmonary Hypertension: Results From an International Prospective Registry. *Circulation*, *133*(9), 859–871. https://doi.org/10.1161/CIRCULATIONAHA.115.016522

Delcroix, M., Vonk Noordegraaf, A., Fadel, E., Lang, I., Simonneau, G., & Naeije, R. (2013). Vascular and right ventricular remodelling in chronic thromboembolic pulmonary hypertension. *The European respiratory journal*, *41*(1), 224–232. https://doi.org/10.1183/09031936.00047712

Devy, L., Blacher, S., Grignet-Debrus, C., Bajou, K., Masson, V., Gerard, R. D., Gils, A., Carmeliet, G., Carmeliet, P., Declerck, P. J., Nöel, A., & Foidart, J. M. (2002). The pro- or antiangiogenic effect of plasminogen activator inhibitor 1 is dose dependent. *FASEB journal : official publication of the Federation of American Societies for Experimental Biology*, *16*(2), 147–154. https://doi.org/10.1096/fj.01-0552com

di Salvo, T. G., Yang, K. C., Brittain, E., Absi, T., Maltais, S., & Hemnes, A. (2015). Right ventricular myocardial biomarkers in human heart failure. *Journal of cardiac failure*, *21*(5), 398–411.https://doi.org/10.1016/j.cardfail.2015.02.005

Diekmann, F., Legchenko, E., Chouvarine, P., Lichtinghagen, R., Bertram, H., Happel, C. M., & Hansmann, G. (2021). Circulating Interleukin-7 in Human Pulmonary Arterial Hypertension. *Frontiers in cardiovascular medicine*, *8*, 794549. https://doi.org/10.3389/fcvm.2021.794549

Dobin, A., Davis, C. A., Schlesinger, F., Drenkow, J., Zaleski, C., Jha, S., Batut, P., Chaisson, M., & Gingeras, T. R. (2013). STAR: ultrafast universal RNA-seq aligner. *Bioinformatics (Oxford, England)*, *29*(1), 15–21. https://doi.org/10.1093/bioinformatics/bts635

Eisenberg, L. M., & Markwald, R. R. (1995). Molecular regulation of atrioventricular valvuloseptal morphogenesis. *Circulation research*, *77*(1), 1–6. https://doi.org/10.1161/01.res.77.1.1

Ende-Verhaar, Y. M., Huisman, M. V., & Klok, F. A. (2017). To screen or not to screen for chronic thromboembolic pulmonary hypertension after acute pulmonary embolism. *Thrombosis research*, *151*, 1–7. https://doi.org/10.1016/j.thromres.2016.12.026

Ervolino De Oliveira, C., Dourado, M. R., Sawazaki-Calone, Í., Costa De Medeiros, M., Rossa Júnior, C., De Karla Cervigne, N., Esquiche León, J., Lambert, D., Salo, T., Graner, E., & Coletta, R. D. (2020). Activin A triggers angiogenesis via regulation of VEGFA and its overexpression is associated with poor prognosis of oral squamous cell carcinoma. *International journal of oncology*, *57*(1), 364–376. https://doi.org/10.3892/ijo.2020.5058

Franco, D., Meilhac, S. M., Christoffels, V. M., Kispert, A., Buckingham, M., & Kelly, R. G. (2006). Left and right ventricular contributions to the formation of the interventricular septum in the mouse heart. *Developmental biology*, *294*(2), 366–375. https://doi.org/10.1016/j.ydbio.2006.02.045

Frangogiannis N. G. (2017). Fibroblasts and the extracellular matrix in right ventricular disease. *Cardiovascular research*, *113*(12), 1453–1464. https://doi.org/10.1093/cvr/cvx146

Fukumitsu, M., Westerhof, B. E., Ruigrok, D., Braams, N. J., Groeneveldt, J. A., Bayoumy, A. A., Marcus, J. T., Meijboom, L. J., de Man, F. S., Westerhof, N., Bogaard, H. J., & Vonk Noordegraaf, A. (2020). Early return of reflected waves increases right ventricular wall stress in chronic thromboembolic pulmonary hypertension. *American journal of physiology. Heart and circulatory physiology*, *319*(6), H1438–H1450. https://doi.org/10.1152/ajpheart.00442.2020

Gall, H., Hoeper, M. M., Richter, M. J., Cacheris, W., Hinzmann, B., & Mayer, E. (2017). An epidemiological analysis of the burden of chronic thromboembolic pulmonary hypertension in the USA, Europe and Japan. *European respiratory review : an official journal of the European Respiratory Society*, *26*(143), 160121. https://doi.org/10.1183/16000617.0121-2016

Gao H, Dong Y, Machado R, Chen J. An Il7 Monoclonal Antibody Rescues Hypoxia-Mediated Pulmonary Hypertension in Mice. *Journal of Investigative Medicine*. 2016;64(4):921-922. doi:10.1136/jim-2016-000120.22

Gerges, C., Gerges, M., Friewald, R., Fesler, P., Dorfmüller, P., Sharma, S., Karlocai, K., Skoro-Sajer, N., Jakowitsch, J., Moser, B., Taghavi, S., Klepetko, W., & Lang, I. M. (2020). Microvascular Disease in Chronic Thromboembolic Pulmonary Hypertension: Hemodynamic Phenotyping and Histomorphometric Assessment. *Circulation*, *141*(5), 376–386. https://doi.org/10.1161/CIRCULATIONAHA.119.041515

Geva, T., Powell, A. J., Crawford, E. C., Chung, T., & Colan, S. D. (1998). Evaluation of regional

differences in right ventricular systolic function by acoustic quantification echocardiography and cine magnetic resonance imaging. *Circulation*, *98*(4), 339–345. https://doi.org/10.1161/01.cir.98.4.339

Ghio, S., Crimi, G., Guida, S., Valentini, A., Celentano, A., Pin, M., Raineri, C., Turco, A., Scelsi, L., Oltrona Visconti, L., Naeije, R., & D'Armini, A. M. (2020). Magnetic resonance imaging of pulmonary

arterial compliance after pulmonary endarterectomy. *The European respiratory journal*, *55*(5), 1902171. https://doi.org/10.1183/13993003.02171-2019

Ghofrani, H. A., Simonneau, G., D'Armini, A. M., Fedullo, P., Howard, L. S., Jaïs, X., Jenkins, D. P., Jing, Z. C., Madani, M. M., Martin, N., Mayer, E., Papadakis, K., Richard, D., Kim, N. H., & MERIT study investigators (2017). Macitentan for the treatment of inoperable chronic thromboembolic pulmonary hypertension (MERIT-1): results from the multicentre, phase 2, randomised, double-blind, placebo-controlled study. *The Lancet. Respiratory medicine*, *5*(10), 785–794. https://doi.org/10.1016/S2213-2600(17)30305-3

Ghofrani, H. A., D'Armini, A. M., Grimminger, F., Hoeper, M. M., Jansa, P., Kim, N. H., Mayer, E., Simonneau, G., Wilkins, M. R., Fritsch, A., Neuser, D., Weimann, G., Wang, C., & CHEST-1 Study Group (2013). Riociguat for the treatment of chronic thromboembolic pulmonary hypertension. *The New England journal of medicine*, *369*(4), 319–329. https://doi.org/10.1056/NEJMoa1209657

Ghosh, A. K., & Vaughan, D. E. (2012). PAI-1 in tissue fibrosis. *Journal of cellular physiology*, *227*(2), 493–507. https://doi.org/10.1002/jcp.22783

Gu, Zuguang. 2022. " Complex Heatmap Visualization." *iMeta* 1, e43. https://doi.org/10.1002/imt2.43

Gu, Z., Eils, R., & Schlesner, M. (2016). Complex heatmaps reveal patterns and correlations in multidimensional genomic data. *Bioinformatics (Oxford, England)*, *32*(18), 2847–2849. https://doi.org/10.1093/bioinformatics/btw313

Guth, S., Mayer, E., Prüfer, D., & Wiedenroth, C. B. (2022). Pulmonary endarterectomy: technique and pitfalls. *Annals of cardiothoracic surgery*, *11*(2), 180–188. https://doi.org/10.21037/acs-2021-pte-185

Higashimoto, Y., Matsui, T., Nishino, Y., Taira, J., Inoue, H., Takeuchi, M., & Yamagishi, S. (2013). Blockade by phosphorothioate aptamers of advanced glycation end products-induced damage in cultured pericytes and endothelial cells. *Microvascular research*, *90*, 64–70. https://doi.org/10.1016/j.mvr.2013.08.010

Hai, T., Wolford, C. C., & Chang, Y. S. (2010). ATF3, a hub of the cellular adaptive-response network, in the pathogenesis of diseases: is modulation of inflammation a unifying component?. *Gene expression*, *15*(1), 1–11. https://doi.org/10.3727/105221610x12819686555015

Herrer, I., Roselló-Lletí, E., Rivera, M., Molina-Navarro, M. M., Tarazón, E., Ortega, A., Martínez-Dolz, L., Triviño, J. C., Lago, F., González-Juanatey, J. R., Bertomeu, V., Montero, J. A., & Portolés, M. (2014). RNA-sequencing analysis reveals new alterations in cardiomyocyte cytoskeletal genes in patients with heart failure. *Laboratory investigation; a journal of technical methods and pathology*, *94*(6), 645–653. https://doi.org/10.1038/labinvest.2014.54

Hong, J. H., & Zhang, H. G. (2022). Transcription Factors Involved in the Development and Prognosis of Cardiac Remodeling. *Frontiers in pharmacology*, *13*, 828549. https://doi.org/10.3389/fphar.2022.828549

Hooglugt, A., van der Stoel, M. M., Boon, R. A., & Huveneers, S. (2021). Endothelial YAP/TAZ Signaling in Angiogenesis and Tumor Vasculature. *Frontiers in oncology*, *10*, 612802. https://doi.org/10.3389/fonc.2020.612802

Horowitz, J. C., & Thannickal, V. J. (2006). Epithelial-mesenchymal interactions in pulmonary fibrosis. *Seminars in respiratory and critical care medicine*, *27*(6), 600–612. https://doi.org/10.1055/s-2006-957332

Horst, B., Pradhan, S., Chaudhary, R., Listik, E., Quintero-Macias, L., Choi, A. S., Southard, M., Liu, Y., Whitaker, R., Hempel, N., Berchuck, A., Nixon, A. B., Lee, N. Y., Henis, Y. I., & Mythreye, K.

(2022). Hypoxia-induced inhibin promotes tumor growth and vascular permeability in ovarian cancers. *Communications biology*, *5*(1), 536. https://doi.org/10.1038/s42003-022-03495-6

Ho, S. Y., & Nihoyannopoulos, P. (2006). Anatomy, echocardiography, and normal right ventricular dimensions. *Heart (British Cardiac Society)*, *92 Suppl 1*(Suppl 1), i2–i13. https://doi.org/10.1136/hrt.2005.077875

Hsieh, W. C., Jansa, P., Huang, W. C., Nižnanský, M., Omara, M., & Lindner, J. (2018). Residual pulmonary hypertension after pulmonary endarterectomy: A meta-analysis. *The Journal of thoracic and cardiovascular surgery*, *156*(3), 1275–1287. https://doi.org/10.1016/j.jtcvs.2018.04.110

Huang, J., Sabater-Lleal, M., Asselbergs, F. W., Tregouet, D., Shin, S. Y., Ding, J., Baumert, J., Oudot-Mellakh, T., Folkersen, L., Johnson, A. D., Smith, N. L., Williams, S. M., Ikram, M. A., Kleber, M. E., Becker, D. M., Truong, V., Mychaleckyj, J. C., Tang, W., Yang, Q., Sennblad, B., … Hamsten, A. (2012). Genome-wide association study for circulating levels of PAI-1 provides novel insights into its regulation. *Blood*, *120*(24), 4873–4881. https://doi.org/10.1182/blood-2012-06-436188

Humbert, M., Kovacs, G., Hoeper, M. M., Badagliacca, R., Berger, R., Brida, M., Carlsen, J., Coats, A., Escribano-Subias, P., Ferrari, P., Ferreira, D. S., Ghofrani, H. A., Giannakoulas, G., Kiely, D. G., Mayer, E., Meszaros, G., Nagavci, B., Olsson, K. M., Pepke-Zaba, J., Quint, J. K., … ESC/ERS Scientific Document Group (2022). 2022 ESC/ERS Guidelines for the diagnosis and treatment of pulmonary hypertension. European heart journal, 43(38), 3618–3731. https://doi.org/10.1093/eurheartj/ehac237

Inoue, K., Zama, T., Kamimoto, T., Aoki, R., Ikeda, Y., Kimura, H., & Hagiwara, M. (2004). TNFalpha-induced ATF3 expression is bidirectionally regulated by the JNK and ERK pathways in vascular endothelial cells. *Genes to cells : devoted to molecular & cellular mechanisms*, *9*(1), 59–70. https://doi.org/10.1111/j.1356-9597.2004.00707.x

Irving, J. A., Pike, R. N., Lesk, A. M., & Whisstock, J. C. (2000). Phylogeny of the serpin superfamily: implications of patterns of amino acid conservation for structure and function. *Genome research*, *10*(12), 1845–1864. https://doi.org/10.1101/gr.gr-1478r

Iwaki, T., Urano, T., & Umemura, K. (2012). PAI-1, progress in understanding the clinical problem and its aetiology. *British journal of haematology*, *157*(3), 291–298. https://doi.org/10.1111/j.1365-2141.2012.09074.x

Jaïs, X., D'Armini, A. M., Jansa, P., Torbicki, A., Delcroix, M., Ghofrani, H. A., Hoeper, M. M., Lang, I. M., Mayer, E., Pepke-Zaba, J., Perchenet, L., Morganti, A., Simonneau, G., Rubin, L. J., & Bosentan Effects in iNopErable Forms of chronIc Thromboembolic pulmonary hypertension Study Group (2008). Bosentan for treatment of inoperable chronic thromboembolic pulmonary hypertension: BENEFiT (Bosentan Effects in iNopErable Forms of chronIc Thromboembolic pulmonary hypertension), a randomized, placebo-controlled trial. *Journal of the American College of Cardiology*, *52*(25), 2127–2134. https://doi.org/10.1016/j.jacc.2008.08.059

Johnson, E. K., Matkovich, S. J., & Nerbonne, J. M. (2018). Regional Differences in mRNA and lncRNA Expression Profiles in Non-Failing Human Atria and Ventricles. *Scientific reports*, *8*(1), 13919. https://doi.org/10.1038/s41598-018-32154-2

Joshi, S. R., Liu, J., Bloom, T., Karaca Atabay, E., Kuo, T. H., Lee, M., Belcheva, E., Spaits, M., Grenha, R., Maguire, M. C., Frost, J. L., Wang, K., Briscoe, S. D., Alexander, M. J., Herrin, B. R., Castonguay, R., Pearsall, R. S., Andre, P., Yu, P. B., Kumar, R., … Li, G. (2022). Sotatercept analog suppresses inflammation to reverse experimental pulmonary arterial hypertension. *Scientific reports*, *12*(1), 7803. https://doi.org/10.1038/s41598-022-11435-x

Kalfon, R., Friedman, T., Eliachar, S., Shofti, R., Haas, T., Koren, L., Moskovitz, J. D., Hai, T., & Aronheim, A. (2019). JDP2 and ATF3 deficiencies dampen maladaptive cardiac remodeling and preserve cardiac function. *PloS one*, *14*(2), e0213081. https://doi.org/10.1371/journal.pone.0213081

Kanai, H., Tanaka, T., Aihara, Y., Takeda, S., Kawabata, M., Miyazono, K., Nagai, R., & Kurabayashi, M. (2001). Transforming growth factor-beta/Smads signaling induces transcription of the cell type-restricted ankyrin repeat protein CARP gene through CAGA motif in vascular smooth muscle cells. *Circulation research*, *88*(1), 30–36. https://doi.org/10.1161/01.res.88.1.30

Kaneda, H., Arao, T., Matsumoto, K., De Velasco, M. A., Tamura, D., Aomatsu, K., Kudo, K., Sakai, K., Nagai, T., Fujita, Y., Tanaka, K., Yanagihara, K., Yamada, Y., Okamoto, I., Nakagawa, K., & Nishio, K. (2011). Activin A inhibits vascular endothelial cell growth and suppresses tumour angiogenesis in gastric cancer. *British journal of cancer*, *105*(8), 1210–1217. https://doi.org/10.1038/bjc.2011.348

Karpov, A. A., Anikin, N. A., Mihailova, A. M., Smirnov, S. S., Vaulina, D. D., Shilenko, L. A., Ivkin, D. Y., Bagrov, A. Y., Moiseeva, O. M., & Galagudza, M. M. (2021). Model of Chronic Thromboembolic Pulmonary Hypertension in Rats Caused by Repeated Intravenous Administration of Partially Biodegradable Sodium Alginate Microspheres. *International journal of molecular sciences*, *22*(3), 1149. https://doi.org/10.3390/ijms22031149

Karpov, A. A., Vaulina, D. D., Smirnov, S. S., Moiseeva, O. M., & Galagudza, M. M. (2022). Rodent models of pulmonary embolism and chronic thromboembolic pulmonary hypertension. *Heliyon*, *8*(3), e09014. https://doi.org/10.1016/j.heliyon.2022.e09014

Keranov, S., Dörr, O., Jafari, L., Troidl, C., Liebetrau, C., Kriechbaum, S., Keller, T., Voss, S., Bauer, T., Lorenz, J., Richter, M. J., Tello, K., Gall, H., Ghofrani, H. A., Mayer, E., Wiedenroth, C. B., Guth, S., Lörchner, H., Pöling, J., Chelladurai, P., … Nef, H. (2021). CILP1 as a biomarker for right ventricular maladaptation in pulmonary hypertension. *The European respiratory journal*, *57*(4), 1901192. https://doi.org/10.1183/13993003.01192-2019

Keranov, S., Jafari, L., Haen, S., Vietheer, J., Kriechbaum, S., Dörr, O., Liebetrau, C., Troidl, C., Rutsatz, W., Rieth, A., Hamm, C. W., Nef, H., Rolf, A., & Keller, T. (2022). CILP1 as a biomarker for right ventricular dysfunction in patients with ischemic cardiomyopathy. *Pulmonary circulation*, *12*(1), e12062. https://doi.org/10.1002/pul2.12062

Kern, B., Li, W., Bono, C., Lee, L. F., & Kraynov, E. (2016). Receptor occupancy and blocking of STAT5 signaling by an anti-IL-7 receptor α antibody in cynomolgus monkeys. *Cytometry. Part B, Clinical cytometry*, *90*(2), 191–198. https://doi.org/10.1002/cyto.b.21247

Kiely, D. G., Levin, D., Hassoun, P., Ivy, D. D., Jone, P. N., Bwika, J., Kawut, S. M., Lordan, J., Lungu, A., Mazurek, J., Moledina, S., Olschewski, H., Peacock, A., Puri, G. D., Rahaghi, F., Schafer, M., Schiebler, M., Screaton, N., Tawhai, M., Van Beek, E. J., … Swift, A. J. (2019). EXPRESS: Statement on imaging and pulmonary hypertension from the Pulmonary Vascular Research Institute (PVRI). *Pulmonary circulation*, *9*(3), 2045894019841990. Advance online publication. https://doi.org/10.1177/2045894019841990

Kim, N. H., Delcroix, M., Jais, X., Madani, M. M., Matsubara, H., Mayer, E., Ogo, T., Tapson, V. F., Ghofrani, H. A., & Jenkins, D. P. (2019). Chronic thromboembolic pulmonary hypertension. *The European respiratory journal*, *53*(1), 1801915. https://doi.org/10.1183/13993003.01915-2018

Klinke, A., Schubert, T., Müller, M., Legchenko, E., Zelt, J., Shimauchi, T., Napp, L. C., Rothman, A., Bonnet, S., Stewart, D. J., Hansmann, G., & Rudolph, V. (2020). Emerging therapies for right ventricular dysfunction and failure. *Cardiovascular diagnosis and therapy*, *10*(5), 1735–1767. https://doi.org/10.21037/cdt-20-592

Knudsen, E. C., Seljeflot, I., Abdelnoor, M., Eritsland, J., Mangschau, A., Müller, C., Arnesen, H., & Andersen, G. Ø. (2011). Elevated levels of PAI-1 activity and t-PA antigen are associated with newly diagnosed abnormal glucose regulation in patients with ST-elevation myocardial infarction. *Journal of thrombosis and haemostasis : JTH*, *9*(8), 1468–1474. https://doi.org/10.1111/j.1538-7836.2011.04377.x

Koch, W., Schrempf, M., Erl, A., Mueller, J. C., Hoppmann, P., Schömig, A., & Kastrati, A. (2010). 4G/5G polymorphism and haplotypes of SERPINE1 in atherosclerotic diseases of coronary arteries. *Thrombosis and haemostasis*, *103*(6), 1170–1180. https://doi.org/10.1160/TH09-10-0702

Kojic, S. (2010). MARP Protein Family: A Possible Role in Molecular Mechanisms of Tumorigenesis. *J Med Biochem* 29: 157-164. https://doi.org/10.2478/v10011-010-0024-9

Koudstaal, T., van Uden, D., van Hulst, J., Heukels, P., Bergen, I. M., Geenen, L. W., Baggen, V., van den Bosch, A. E., van den Toorn, L. M., Chandoesing, P. P., Kool, M., Boersma, E., Hendriks, R. W., & Boomars, K. A. (2021). Plasma markers in pulmonary hypertension subgroups correlate with patient survival. *Respiratory research*, *22*(1), 137. https://doi.org/10.1186/s12931-021-01716-w

Krenning, G., Zeisberg, E. M., & Kalluri, R. (2010). The origin of fibroblasts and mechanism of cardiac fibrosis. *Journal of cellular physiology*, *225*(3), 631–637. https://doi.org/10.1002/jcp.22322

Krieg, V. J., Hobohm, L., Liebetrau, C., Guth, S., Kölmel, S., Troidl, C., Mayer, E., Konstantinides, S. V., Wiedenroth, C. B., & Lankeit, M. (2020). Risk factors for chronic thromboembolic pulmonary hypertension - Importance of thyroid disease and function. *Thrombosis research*, *185*, 20–26. https://doi.org/10.1016/j.thromres.2019.10.025

Kriechbaum, S. D., Rudolph, F., Wiedenroth, C. B., Mielzarek, L., Haas, M., Guth, S., Hamm, C. W., Mayer, E., Liebetrau, C., & Keller, T. (2020). Pregnancy-associated plasma protein A - a new indicator of pulmonary vascular remodeling in chronic thromboembolic pulmonary hypertension?. *Respiratory research*, *21*(1), 204. https://doi.org/10.1186/s12931-020-01472-3

Ku, H. C., & Cheng, C. F. (2020). Master Regulator Activating Transcription Factor 3 (ATF3) in Metabolic Homeostasis and Cancer. *Frontiers in endocrinology*, *11*, 556. https://doi.org/10.3389/fendo.2020.00556

Kuo, H., Chen, J., Ruiz-Lozano, P., Zou, Y., Nemer, M., & Chien, K. R. (1999). Control of segmental expression of the cardiac-restricted ankyrin repeat protein gene by distinct regulatory pathways in murine cardiogenesis. *Development (Cambridge, England)*, *126*(19), 4223–4234. https://doi.org/10.1242/dev.126.19.4223

Kumar, S., Liu, J., Pang, P., Krautzberger, A. M., Reginensi, A., Akiyama, H., Schedl, A., Humphreys, B. D., & McMahon, A. P. (2015). Sox9 Activation Highlights a Cellular Pathway of Renal Repair in the Acutely Injured Mammalian Kidney. *Cell reports*, *12*(8), 1325–1338. https://doi.org/10.1016/j.celrep.2015.07.034

Lamers, W. H., & Moorman, A. F. (2002). Cardiac septation: a late contribution of the embryonic primary myocardium to heart morphogenesis. *Circulation research*, *91*(2), 93–103. https://doi.org/10.1161/01.res.0000027135.63141.89

Lang, I. M., Dorfmüller, P., & Vonk Noordegraaf, A. (2016). The Pathobiology of Chronic Thromboembolic Pulmonary Hypertension. *Annals of the American Thoracic Society*, *13 Suppl 3*, S215–S221. https://doi.org/10.1513/AnnalsATS.201509-620AS

Lang, I., & Kerr, K. (2006). Risk factors for chronic thromboembolic pulmonary hypertension. *Proceedings of the American Thoracic Society*, *3*(7), 568–570. https://doi.org/10.1513/pats.200605-108LR

Lang, I. M., & Madani, M. (2014). Update on chronic thromboembolic pulmonary hypertension. *Circulation*, *130*(6), 508–518. https://doi.org/10.1161/CIRCULATIONAHA.114.009309

Leask A. (2015). Getting to the heart of the matter: new insights into cardiac fibrosis. *Circulation research*, *116*(7), 1269–1276. https://doi.org/10.1161/CIRCRESAHA.116.305381

Leek JT, Johnson WE, Parker HS, Fertig EJ, Jaffe AE, Zhang Y, Storey JD, Torres LC. sva: surrogate variable analysis. 2022. R package version 3.46.0.

LekanneDeprez, R. H., van den Hoff, M. J., de Boer, P. A., Ruijter, P. M., Maas, A. A., Chamuleau, R. A., Lamers, W. H., & Moorman, A. F. (1998). Changing patterns of gene expression in the pulmonary trunk-banded rat heart. *Journal of molecular and cellular cardiology*, *30*(9), 1877–1888. https://doi.org/10.1006/jmcc.1998.0753

Le, S., Josse, J., & Husson, F. (2008). FactoMineR: An R Package for Multivariate Analysis. *Journal of Statistical Software*, *25*(1), 1–18. https://doi.org/10.18637/jss.v025.i01

Liao, Y., Smyth, G. K., & Shi, W. (2014). featureCounts: an efficient general purpose program for assigning sequence reads to genomic features. *Bioinformatics (Oxford, England)*, *30*(7), 923–930. https://doi.org/10.1093/bioinformatics/btt656

Li, H., Cai, H., Deng, J., Tu, X., Sun, Y., Huang, Z., Ding, Z., Dong, L., Chen, J., Zang, Y., & Zhang, J. (2018). TGF-β-mediated upregulation of Sox9 in fibroblast promotes renal fibrosis. *Biochimica et biophysica acta. Molecular basis of disease*, *1864*(2), 520–532. https://doi.org/10.1016/j.bbadis.2017.11.011

Li, Y., Li, Z., Zhang, C., Li, P., Wu, Y., Wang, C., Bond Lau, W., Ma, X. L., & Du, J. (2017). Cardiac Fibroblast-Specific Activating Transcription Factor 3 Protects Against Heart Failure by Suppressing MAP2K3-p38 Signaling. *Circulation*, *135*(21), 2041–2057. https://doi.org/10.1161/CIRCULATIONAHA.116.024599

Lin, F. Y., Devereux, R. B., Roman, M. J., Meng, J., Jow, V. M., Jacobs, A., Weinsaft, J. W., Shaw, L. J., Berman, D. S., Callister, T. Q., & Min, J. K. (2008). Cardiac chamber volumes, function, and mass as determined by 64-multidetector row computed tomography: mean values among healthy adults free of hypertension and obesity. *JACC. Cardiovascular imaging*, *1*(6), 782–786. https://doi.org/10.1016/j.jcmg.2008.04.015

Litviňuková, M., Talavera-López, C., Maatz, H., Reichart, D., Worth, C. L., Lindberg, E. L., Kanda, M., Polanski, K., Heinig, M., Lee, M., Nadelmann, E. R., Roberts, K., Tuck, L., Fasouli, E. S., DeLaughter, D. M., McDonough, B., Wakimoto, H., Gorham, J. M., Samari, S., Mahbubani, K. T., … Teichmann, S. A. (2020). Cells of the adult human heart. *Nature*, *588*(7838), 466–472. https://doi.org/10.1038/s41586-020-2797-4

Liu, J., Yang, P., Tian, H., Zhen, K., McCabe, C., Zhao, L., & Zhai, Z. (2022). Right Ventricle Remodeling in Chronic Thromboembolic Pulmonary Hypertension. *Journal of translational internal medicine*, *10*(2), 125–133. https://doi.org/10.2478/jtim-2022-0027

Liu, M., Ma, Z. H., Guo, X. J., Wang, S. K., Chen, X. Y., Yang, Y. H., & Wang, C. (2012). A septal angle measured on computed tomographic pulmonary angiography can noninvasively estimate pulmonary vascular resistance in patients with chronic thromboembolic pulmonary hypertension. *Journal of thoracic imaging*, *27*(5), 325–330. https://doi.org/10.1097/RTI.0b013e3182541142

López, B., Ravassa, S., Moreno, M. U., José, G. S., Beaumont, J., González, A., & Díez, J. (2021). Diffuse myocardial fibrosis: mechanisms, diagnosis and therapeutic approaches. *Nature reviews. Cardiology*, *18*(7), 479–498. https://doi.org/10.1038/s41569-020-00504-1

Lorenz, G., Saeedan, M. B., Bullen, J., Klok, F. A., Kroft, L., Meijboom, L. J., Heresi, G. A., Sripariwuth, A., & Renapurkar, R. D. (2020). CT-Based Biomarkers for Prediction of Chronic Thromboembolic Pulmonary Hypertension After an Acute Pulmonary Embolic Event. *AJR. American journal of roentgenology*, *215*(4), 800–806. https://doi.org/10.2214/AJR.19.22541

Love, M. I., Huber, W., & Anders, S. (2014). Moderated estimation of fold change and dispersion for RNA-seq data with DESeq2. *Genome biology*, *15*(12), 550. https://doi.org/10.1186/s13059-014-0550-8

Lu, A., Clark, J. F., Ran, R., Pyne-Geithman, G., Wagner, K. R., Millhorn, D. E., & Sharp, F. R. (2009). Down-regulation of interleukin 7 mRNA by hypoxia is calcium dependent. *Neurological research*, *31*(5), 545–549. https://doi.org/10.1179/174313209X380928

Maarman, G., Lecour, S., Butrous, G., Thienemann, F., & Sliwa, K. (2013). A comprehensive review: the evolution of animal models in pulmonary hypertension research; are we there yet?. *Pulmonary circulation*, *3*(4), 739–756. https://doi.org/10.1086/674770

MacKenzie Ross, R. V., Toshner, M. R., Soon, E., Naeije, R., & Pepke-Zaba, J. (2013). Decreased time constant of the pulmonary circulation in chronic thromboembolic pulmonary hypertension. *American journal of physiology. Heart and circulatory physiology*, *305*(2), H259–H264. https://doi.org/10.1152/ajpheart.00128.2013

Madani, M. M., Auger, W. R., Pretorius, V., Sakakibara, N., Kerr, K. M., Kim, N. H., Fedullo, P. F., & Jamieson, S. W. (2012). Pulmonary endarterectomy: recent changes in a single institution's experience of more than 2,700 patients. *The Annals of thoracic surgery*, *94*(1), 97–103. https://doi.org/10.1016/j.athoracsur.2012.04.004

Mahmud, E., Madani, M. M., Kim, N. H., Poch, D., Ang, L., Behnamfar, O., Patel, M. P., & Auger, W. R. (2018). Chronic Thromboembolic Pulmonary Hypertension: Evolving Therapeutic Approaches for Operable and Inoperable Disease. *Journal of the American College of Cardiology*, *71*(21), 2468–2486. https://doi.org/10.1016/j.jacc.2018.04.009

Mandras, S. A., Mehta, H. S., & Vaidya, A. (2020). Pulmonary Hypertension: A Brief Guide for Clinicians. Mayo Clinic proceedings, 95(9), 1978–1988. https://doi.org/10.1016/j.mayocp.2020.04.039

Manz, X. D., Szulcek, R., Pan, X., Symersky, P., Dickhoff, C., Majolée, J., Kremer, V., Michielon, E., Jordanova, E. S., Radonic, T., Bijnsdorp, I. V., Piersma, S. R., Pham, T. V., Jimenez, C. R., Vonk Noordegraaf, A., de Man, F. S., Boon, R. A., Voorberg, J., Hordijk, P. L., Aman, J., … Bogaard, H. J. (2022). Epigenetic Modification of the von Willebrand Factor Promoter Drives Platelet Aggregation on the Pulmonary Endothelium in Chronic Thromboembolic Pulmonary Hypertension. *American journal of respiratory and critical care medicine*, *205*(7), 806–818. https://doi.org/10.1164/rccm.202109-2075OC

Martinez, C., Wallenhorst, C., Teal, S., Cohen, A. T., & Peacock, A. J. (2018). Incidence and risk factors of chronic thromboembolic pulmonary hypertension following venous thromboembolism, a population-based cohort study in England. *Pulmonary circulation*, *8*(3), 2045894018791358. https://doi.org/10.1177/2045894018791358

Masaki, T., Okazawa, M., Asano, R., Inagaki, T., Ishibashi, T., Yamagishi, A., Umeki-Mizushima, S., Nishimura, M., Manabe, Y., Ishibashi-Ueda, H., Shirai, M., Tsuchimochi, H., Pearson, J. T., Kumanogoh, A., Sakata, Y., Ogo, T., Kishimoto, T., & Nakaoka, Y. (2021). Aryl hydrocarbon receptor is essential for the pathogenesis of pulmonary arterial hypertension. *Proceedings of the National Academy of Sciences of the United States of America*, *118*(11), e2023899118. https://doi.org/10.1073/pnas.2023899118

Matsumura, A., Shigeta, A., Kasai, H., Yokota, H., Terada, J., Yamamoto, K., Sugiura, T., Matsumura, T., Sakao, S., Tanabe, N., & Tatsumi, K. (2021). Interventricular septal curvature as an additional echocardiographic parameter for evaluating chronic thromboembolic pulmonary hypertension: a single-center retrospective study. *BMC pulmonary medicine*, *21*(1), 328. https://doi.org/10.1186/s12890-021-01683-4

Matusov, Y., Singh, I., Yu, Y. R., Chun, H. J., Maron, B. A., Tapson, V. F., Lewis, M. I., & Rajagopal, S. (2021). Chronic Thromboembolic Pulmonary Hypertension: the Bedside. *Current cardiology reports*, *23*(10), 147. https://doi.org/10.1007/s11886-021-01573-5

McCabe, C., White, P. A., Hoole, S. P., Axell, R. G., Priest, A. N., Gopalan, D., Taboada, D., MacKenzie Ross, R., Morrell, N. W., Shapiro, L. M., & Pepke-Zaba, J. (2014). Right ventricular dysfunction in chronic thromboembolic obstruction of the pulmonary artery: a pressure-volume study using the conductance catheter. *Journal of applied physiology (Bethesda, Md.: 1985)*, *116*(4), 355–363. https://doi.org/10.1152/japplphysiol.01123.2013

Mihailovic, P. M., Lio, W. M., Yano, J., Zhou, J., Zhao, X., Chyu, K. Y., Shah, P. K., Cercek, B., & Dimayuga, P. C. (2019). IL-7R blockade reduces post-myocardial infarction-induced atherosclerotic plaque inflammation in $ApoE^{-/-}$ mice. *Biochemistry and biophysics reports*, *19*, 100647. https://doi.org/10.1016/j.bbrep.2019.100647

Molina, C. E., Heijman, J., & Dobrev, D. (2016). Differences in Left Versus Right Ventricular Electrophysiological Properties in Cardiac Dysfunction and Arrhythmogenesis. *Arrhythmia & electrophysiology review*, *5*(1), 14–19. https://doi.org/10.15420/aer.2016.8.2

Moulik, M., Vatta, M., Witt, S. H., Arola, A. M., Murphy, R. T., McKenna, W. J., Boriek, A. M., Oka, K., Labeit, S., Bowles, N. E., Arimura, T., Kimura, A., & Towbin, J. A. (2009). ANKRD1, the gene encoding cardiac ankyrin repeat protein, is a novel dilated cardiomyopathy gene. *Journal of the American College of Cardiology*, *54*(4), 325–333. https://doi.org/10.1016/j.jacc.2009.02.076

Mulchrone, A., Kellihan, H. B., Forouzan, O., Hacker, T. A., Bates, M. L., Francois, C. J., & Chesler, N. C. (2019). A Large Animal Model of Right Ventricular Failure due to Chronic Thromboembolic Pulmonary Hypertension: A Focus on Function. *Frontiers in cardiovascular medicine*, *5*, 189. https://doi.org/10.3389/fcvm.2018.00189

Mura, M., Anraku, M., Yun, Z., McRae, K., Liu, M., Waddell, T. K., Singer, L. G., Granton, J. T., Keshavjee, S., & de Perrot, M. (2012). Gene expression profiling in the lungs of patients with pulmonary hypertension associated with pulmonary fibrosis. *Chest*, *141*(3), 661–673. https://doi.org/10.1378/chest.11-0449

Murphy, N. P., Lubbers, E. R., & Mohler, P. J. (2020). Advancing our understanding of AnkRD1 in cardiac development and disease. *Cardiovascular research*, *116*(8), 1402–1404. https://doi.org/10.1093/cvr/cvaa063

Myllaerniemi, M., Tikkanen, J., Hulmi, J. J., Pasternack, A., Sutinen, E., Rönty, M., Leppäranta, O., Ma, H., Ritvos, O., & Koli, K. (2014). Upregulation of activin-B and follistatin in pulmonary fibrosis - a translational study using human biopsies and a specific inhibitor in mouse fibrosis models. *BMC pulmonary medicine*, *14*, 170. https://doi.org/10.1186/1471-2466-14-170

Namwanje, M., & Brown, C. W. (2016). Activins and Inhibins: Roles in Development, Physiology, and Disease. *Cold Spring Harbor perspectives in biology*, *8*(7), a021881. https://doi.org/10.1101/cshperspect.a021881

Newnham, M., South, K., Bleda, M., Auger, W. R., Barberà, J. A., Bogaard, H., Bunclark, K., Cannon, J. E., Delcroix, M., Hadinnapola, C., Howard, L. S., Jenkins, D., Mayer, E., Ng, C., Rhodes, C. J., Screaton, N., Sheares, K., Simpson, M. A., Southwood, M., Su, L., … Toshner, M. (2019). The

ADAMTS13-VWF axis is dysregulated in chronic thromboembolic pulmonary hypertension. *The European respiratory journal*, *53*(3), 1801805. https://doi.org/10.1183/13993003.01805-2018

Noly, P. E., Guihaire, J., Coblence, M., Dorfmüller, P., Fadel, E., & Mercier, O. (2015). Chronic Thromboembolic Pulmonary Hypertension and Assessment of Right Ventricular Function in the Piglet. *Journal of visualized experiments : JoVE*, (105), e53133. https://doi.org/10.3791/53133

Ogo T. (2015). Balloon pulmonary angioplasty for inoperable chronic thromboembolic pulmonary hypertension. *Current opinion in pulmonary medicine*, *21*(5), 425–431. https://doi.org/10.1097/MCP.0000000000000188

Okamoto, A., Iwamoto, Y., & Maru, Y. (2006). Oxidative stress-responsive transcription factor ATF3 potentially mediates diabetic angiopathy. *Molecular and cellular biology*, *26*(3), 1087–1097. https://doi.org/10.1128/MCB.26.3.1087-1097.2006

Park, J. F., Clark, V. R., Banerjee, S., Hong, J., Razee, A., Williams, T., Fishbein, G., Saddic, L., & Umar, S. (2021). Transcriptomic Analysis of Right Ventricular Remodeling in Two Rat Models of Pulmonary Hypertension: Identification and Validation of Epithelial-to-Mesenchymal Transition in Human Right Ventricular Failure. *Circulation. Heart failure*, *14*(2), e007058. https://doi.org/10.1161/CIRCHEARTFAILURE.120.007058

Pickens, S. R., Chamberlain, N. D., Volin, M. V., Pope, R. M., Talarico, N. E., Mandelin, A. M., 2nd, & Shahrara, S. (2011). Characterization of interleukin-7 and interleukin-7 receptor in the pathogenesis of rheumatoid arthritis. *Arthritis and rheumatism*, *63*(10), 2884–2893. https://doi.org/10.1002/art.30493

Pollmann, K., Raj Murthi, S., Kračun, D., Schwarzmayr, T., Petry, A., Cleuziou, J., Hörer, J., Klop, M., Ewert, P., Görlach, A., & Wolf, C. M. (2021). Molecular signaling pathways in right ventricular impairment of adult patients after tetralogy of Fallot repair. *Cardiovascular diagnosis and therapy*, *11*(6), 1295–1309. https://doi.org/10.21037/cdt-20-894

Pullamsetti, S. S., Perros, F., Chelladurai, P., Yuan, J., & Stenmark, K. (2016). Transcription factors, transcriptional coregulators, and epigenetic modulation in the control of pulmonary vascular cell phenotype: therapeutic implications for pulmonary hypertension (2015 Grover Conference series). *Pulmonary circulation*, *6*(4), 448–464. https://doi.org/10.1086/688908

Qi, Q., Yan, Y., Luo, C., Fang, C., Li, Y., Cai, X., Ling, G., Song, H., & Zheng, B. (2022). Bioinformatics Analysis Reveals Hub Genes That May Reduce Inflammation and Complications After Cardiopulmonary Bypass. *The heart surgery forum*, *25*(2), E243–E252. https://doi.org/10.1532/hsf.4487

Quarck, R., Nawrot, T., Meyns, B., & Delcroix, M. (2009). C-reactive protein: a new predictor of adverse outcome in pulmonary arterial hypertension. *Journal of the American College of Cardiology*, *53*(14), 1211–1218. https://doi.org/10.1016/j.jacc.2008.12.038

Quarck, R., Wynants, M., Ronisz, A., Sepulveda, M. R., Wuytack, F., Van Raemdonck, D., Meyns, B., & Delcroix, M. (2012). Characterization of proximal pulmonary arterial cells from chronic thromboembolic pulmonary hypertension patients. *Respiratory research*, *13*(1), 27. https://doi.org/10.1186/1465-9921-13-27

Qu, H., Zou, Z., Pan, Z., Zhang, T., Deng, N., Chen, G., & Wang, Z. (2016). IL-7/IL-7 receptor axis stimulates prostate cancer cell invasion and migration via AKT/NF-κB pathway. *International immunopharmacology*, *40*, 203–210. https://doi.org/10.1016/j.intimp.2016.08.017

Rahman, F. A., & Krause, M. P. (2020). PAI-1, the Plasminogen System, and Skeletal Muscle. *International journal of molecular sciences*, *21*(19), 7066. https://doi.org/10.3390/ijms21197066

Ricci, M., Mohapatra, B., Urbiztondo, A., Birusingh, R. J., Morgado, M., Rodriguez, M. M., Lincoln, J., & Vatta, M. (2010). Differential changes in TGF-β/BMP signaling pathway in the right ventricular myocardium of newborns with hypoplastic left heart syndrome. *Journal of cardiac failure*, *16*(8), 628–634. https://doi.org/10.1016/j.cardfail.2010.03.007

Risbridger, G. P., Schmitt, J. F., & Robertson, D. M. (2001). Activins and inhibins in endocrine and other tumors. *Endocrine reviews*, *22*(6), 836–858. https://doi.org/10.1210/edrv.22.6.0450

Robertson, D. M., Hayward, S., Irby, D., Jacobsen, J., Clarke, L., McLachlan, R. I., & de Kretser, D. M. (1988). Radioimmunoassay of rat serum inhibin: changes after PMSG stimulation and gonadectomy. *Molecular and cellular endocrinology*, *58*(1), 1–8. https://doi.org/10.1016/0303-7207(88)90047-0

Rohini, M., Haritha Menon, A., & Selvamurugan, N. (2018). Role of activating transcription factor 3 and its interacting proteins under physiological and pathological conditions. *International journal of biological macromolecules*, *120*(Pt A), 310–317. https://doi.org/10.1016/j.ijbiomac.2018.08.107

Rosen, K., Raanani, E., Kogan, A., Kenet, G., Misgav, M., Lubetsky, A., Niznik, S., Schäfers, H. J., Segel, M. J., & Agmon-Levin, N. (2022). Chronic thromboembolic pulmonary hypertension in patients with antiphospholipid syndrome: Risk factors and management. *The Journal of heart and lung transplantation : the official publication of the International Society for Heart Transplantation*, *41*(2), 208–216. https://doi.org/10.1016/j.healun.2021.10.016

Ryan, J. J., Huston, J., Kutty, S., Hatton, N. D., Bowman, L., Tian, L., Herr, J. E., Johri, A. M., & Archer, S. L. (2015). Right ventricular adaptation and failure in pulmonary arterial hypertension. *The Canadian journal of cardiology*, *31*(4), 391–406. https://doi.org/10.1016/j.cjca.2015.01.023

Ryanto, G., Ikeda, K., Miyagawa, K., Tu, L., Guignabert, C., Humbert, M., Fujiyama, T., Yanagisawa, M., Hirata, K. I., & Emoto, N. (2021). An endothelial activin A-bone morphogenetic protein receptor type 2 link is overdriven in pulmonary hypertension. *Nature communications*, *12*(1), 1720. https://doi.org/10.1038/s41467-021-21961-3

Sadushi-Kolici, R., Jansa, P., Kopec, G., Torbicki, A., Skoro-Sajer, N., Campean, I. A., Halank, M., Simkova, I., Karlocai, K., Steringer-Mascherbauer, R., Samarzija, M., Salobir, B., Klepetko, W., Lindner, J., & Lang, I. M. (2019). Subcutaneous treprostinil for the treatment of severe non-operable chronic thromboembolic pulmonary hypertension (CTREPH): a double-blind, phase 3, randomised controlled trial. *The Lancet. Respiratory medicine*, *7*(3), 239–248. https://doi.org/10.1016/S2213-2600(18)30367-9

Sakao, S., Miyauchi, H., Voelkel, N. F., Sugiura, T., Tanabe, N., Kobayashi, Y., & Tatsumi, K. (2015). Increased Right Ventricular Fatty Acid Accumulation in Chronic Thromboembolic Pulmonary Hypertension. *Annals of the American Thoracic Society*, *12*(10), 1465–1472. https://doi.org/10.1513/AnnalsATS.201504-236LE

Senavirathna, L. K., Huang, C., Pushparaj, S., Xu, D., & Liu, L. (2020). Hypoxia and transforming growth factor β1 regulation of long non-coding RNA transcriptomes in human pulmonary fibroblasts. *Physiological reports*, *8*(1), e14343. https://doi.org/10.14814/phy2.14343

Senoo, T., Hattori, N., Tanimoto, T., Furonaka, M., Ishikawa, N., Fujitaka, K., Haruta, Y., Murai, H., Yokoyama, A., & Kohno, N. (2010). Suppression of plasminogen activator inhibitor-1 by RNA interference attenuates pulmonary fibrosis. *Thorax*, *65*(4), 334–340. https://doi.org/10.1136/thx.2009.119974

Sharma, S., Hofbauer, T. M., Ondracek, A. S., Chausheva, S., Alimohammadi, A., Artner, T., Panzenboeck, A., Rinderer, J., Shafran, I., Mangold, A., Winker, R., Wohlschläger-Krenn, E., Moser, B., Taghavi, S., Klepetko, W., Preissner, K. T., & Lang, I. M. (2021). Neutrophil extracellular traps

promote fibrous vascular occlusions in chronic thrombosis. *Blood*, *137*(8), 1104–1116. https://doi.org/10.1182/blood.2020005861

Samaras, S. E., Almodóvar-García, K., Wu, N., Yu, F., & Davidson, J. M. (2015). Global deletion of Ankrd1 results in a wound-healing phenotype associated with dermal fibroblast dysfunction. *The American journal of pathology*, *185*(1), 96–109. https://doi.org/10.1016/j.ajpath.2014.09.018

Shikhare, S., Balki, I., Shi, Y., Kavanagh, J., Donahoe, L., Xu, W., Rozenberg, D., de Perrot, M., & McInnis, M. (2022). Right-to-left ventricle ratio determined by machine learning algorithms on CT pulmonary angiography images predicts prolonged ICU length of stay in operated chronic thromboembolic pulmonary hypertension. *The British journal of radiology*, *95*(1139), 20210722. https://doi.org/10.1259/bjr.20210722

Shinjo, S. K., Oba-Shinjo, S. M., Uno, M., & Marie, S. K. N. (2017). The expression of gene *ANKRD1* correlates with hypoxia status in muscle biopsies of treatment-näive adult dermatomyositis. *Medicalexpress*, *4*(MedicalExpress (São Paulo, online), 2017 4(4)). https://doi.org/10.5935/MedicalExpress.2017.04.02

Shimizu, I., & Minamino, T. (2016). Physiological and pathological cardiac hypertrophy. *Journal of molecular and cellular cardiology*, *97*, 245–262. https://doi.org/10.1016/j.yjmcc.2016.06.001

Shimizu, T., Uematsu, M., Yoshizaki, T., Obata, J. E., Nakamura, T., Fujioka, D., Watanabe, K., Watanabe, Y., & Kugiyama, K. (2016). Myocardial Production of Plasminogen Activator Inhibitor-1 is Associated with Coronary Endothelial and Ventricular Dysfunction after Acute Myocardial Infarction. *Journal of atherosclerosis and thrombosis*, *23*(5), 557–566. https://doi.org/10.5551/jat.32300

Shi, Y., Reitmaier, B., Regenbogen, J., Slowey, R. M., Opalenik, S. R., Wolf, E., Goppelt, A., & Davidson, J. M. (2005). CARP, a cardiac ankyrin repeat protein, is up-regulated during wound healing and induces angiogenesis in experimental granulation tissue. *The American journal of pathology*, *166*(1), 303–312. https://doi.org/10.1016/S0002-9440(10)62254-7

Silva, A., Almeida, A. R. M., Cachucho, A., Neto, J. L., Demeyer, S., de Matos, M., Hogan, T., Li, Y., Meijerink, J., Cools, J., Grosso, A. R., Seddon, B., & Barata, J. T. (2021). Overexpression of wild-type IL-7Rα promotes T-cell acute lymphoblastic leukemia/lymphoma. *Blood*, *138*(12), 1040–1052. https://doi.org/10.1182/blood.2019000553

Simone, Tessa M., and Paul J. Higgins. 2015. "Inhibition of SERPINE1 Function Attenuates Wound Closure in Response to Tissue Injury: A Role for PAI-1 in Re-Epithelialization and Granulation Tissue Formation" *Journal of Developmental Biology* 3, no. 1: 11-24. https://doi.org/10.3390/jdb3010011

Simonneau, G., Dorfmüller, P., Guignabert, C., Mercier, O., & Humbert, M. (2022). Chronic thromboembolic pulmonary hypertension: the magic of pathophysiology. *Annals of cardiothoracic surgery*, *11*(2), 106–119. https://doi.org/10.21037/acs-2021-pte-10

Simonneau, G., Montani, D., Celermajer, D. S., Denton, C. P., Gatzoulis, M. A., Krowka, M., Williams, P. G., & Souza, R. (2019). Haemodynamic definitions and updated clinical classification of pulmonary hypertension. *The European respiratory journal*, *53*(1), 1801913. https://doi.org/10.1183/13993003.01913-2018

Simonneau, G., Torbicki, A., Dorfmüller, P., & Kim, N. (2017). The pathophysiology of chronic thromboembolic pulmonary hypertension. *European respiratory review: an official journal of the European Respiratory Society*, *26*(143), 160112. https://doi.org/10.1183/16000617.0112-2016

Smolders, V., Lodder, K., Rodríguez, C., Tura-Ceide, O., Barberà, J. A., Jukema, J. W., Quax, P., Goumans, M. J., & Kurakula, K. (2021). The Inflammatory Profile of CTEPH-Derived Endothelial Cells Is a Possible Driver of Disease Progression. *Cells*, *10*(4), 737. https://doi.org/10.3390/cells10040737

Song, C., Burgess, S., Eicher, J. D., O'Donnell, C. J., & Johnson, A. D. (2017). Causal Effect of Plasminogen Activator Inhibitor Type 1 on Coronary Heart Disease. *Journal of the American Heart Association*, *6*(6), e004918. https://doi.org/10.1161/JAHA.116.004918

Soraya, A. S., Tali, H., Rona, S., Tom, F., Roy, K., & Ami, A. (2020). ATF3 expression in cardiomyocytes and myofibroblasts following transverse aortic constriction displays distinct phenotypes. *International journal of cardiology. Heart & vasculature*, *32*, 100706. https://doi.org/10.1016/j.ijcha.2020.100706

Spurney, C. F., Knoblach, S., Pistilli, E. E., Nagaraju, K., Martin, G. R., & Hoffman, E. P. (2008). Dystrophin-deficient cardiomyopathy in mouse: expression of Nox4 and Lox are associated with fibrosis and altered functional parameters in the heart. *Neuromuscular disorders: NMD*, *18*(5), 371–381. https://doi.org/10.1016/j.nmd.2008.03.008

Stam, K., Cai, Z., van der Velde, N., van Duin, R., Lam, E., van der Velden, J., Hirsch, A., Duncker, D. J., & Merkus, D. (2019). Cardiac remodelling in a swine model of chronic thromboembolic pulmonary hypertension: comparison of right vs. left ventricle. *The Journal of physiology*, *597*(17), 4465–4480. https://doi.org/10.1113/JP277896

Strippoli, R., Sandoval, P., Moreno-Vicente, R., Rossi, L., Battistelli, C., Terri, M., Pascual-Antón, L., Loureiro, M., Matteini, F., Calvo, E., Jiménez-Heffernan, J. A., Gómez, M. J., Jiménez-Jiménez, V., Sánchez-Cabo, F., Vázquez, J., Tripodi, M., López-Cabrera, M., & Del Pozo, M. Á. (2020). Caveolin1 and YAP drive mechanically induced mesothelial to mesenchymal transition and fibrosis. *Cell death & disease*, *11*(8), 647. https://doi.org/10.1038/s41419-020-02822-1

Sun, Y., Cai, H., Ge, J., Shao, F., Huang, Z., Ding, Z., Dong, L., Chen, J., Zhang, J., & Zang, Y. (2022). Tubule-derived INHBB promotes interstitial fibroblast activation and renal fibrosis. *The Journal of pathology*, *256*(1), 25–37. https://doi.org/10.1002/path.5798

Sun, Y., Yan, J., Zhang, J., Wang, A., Zou, J., & Gao, C. (2020). Contribution of IL-7/7R genetic polymorphisms in coronary heart disease in Chinese Han population. *International immunopharmacology*, *79*, 106084. https://doi.org/10.1016/j.intimp.2019.106084

Suresh, K., & Shimoda, L. A. (2016). Lung Circulation. *Comprehensive Physiology*, *6*(2), 897–943. https://doi.org/10.1002/cphy.c140049

Sutendra, G., Dromparis, P., Paulin, R., Zervopoulos, S., Haromy, A., Nagendran, J., & Michelakis, E. D. (2013). A metabolic remodeling in right ventricular hypertrophy is associated with decreased angiogenesis and a transition from a compensated to a decompensated state in pulmonary hypertension. *Journal of molecular medicine (Berlin, Germany)*, *91*(11), 1315–1327. https://doi.org/10.1007/s00109-013-1059-4

Suntharalingam, J., Treacy, C. M., Doughty, N. J., Goldsmith, K., Soon, E., Toshner, M. R., Sheares, K. K., Hughes, R., Morrell, N. W., & Pepke-Zaba, J. (2008). Long-term use of sildenafil in inoperable chronic thromboembolic pulmonary hypertension. *Chest*, *134*(2), 229–236. https://doi.org/10.1378/chest.07-2681

Tabibiazar, R., Wagner, R. A., Liao, A., & Quertermous, T. (2003). Transcriptional profiling of the heart reveals chamber-specific gene expression patterns. *Circulation research*, *93*(12), 1193–1201. https://doi.org/10.1161/01.RES.0000103171.42654.DD

Tabima, D. M., Philip, J. L., & Chesler, N. C. (2017). Right Ventricular-Pulmonary Vascular Interactions. *Physiology (Bethesda, Md.)*, *32*(5), 346–356. https://doi.org/10.1152/physiol.00040.2016

Talman, V., & Kivelä, R. (2018). Cardiomyocyte-Endothelial Cell Interactions in Cardiac Remodeling and Regeneration. *Frontiers in cardiovascular medicine*, *5*, 101. https://doi.org/10.3389/fcvm.2018.00101

Tamura, K., Hua, B., Adachi, S., Guney, I., Kawauchi, J., Morioka, M., Tamamori-Adachi, M., Tanaka, Y., Nakabeppu, Y., Sunamori, M., Sedivy, J. M., & Kitajima, S. (2005). Stress response gene ATF3 is a target of c-myc in serum-induced cell proliferation. *The EMBO journal*, *24*(14), 2590–2601. https://doi.org/10.1038/sj.emboj.7600742

Tang, S., Liu, Y., & Liu, B. (2022). Integrated bioinformatics analysis reveals marker genes and immune infiltration for pulmonary arterial hypertension. *Scientific reports*, *12*(1), 10154. https://doi.org/10.1038/s41598-022-14307-6

Tang, W., Li, M., Yangzhong, X., Zhang, X., Zu, A., Hou, Y., Li, L., & Sun, S. (2022). Hippo signaling pathway and respiratory diseases. *Cell death discovery*, *8*(1), 213. https://doi.org/10.1038/s41420-022-01020-6

Teng, B., Xie, C., Zhao, Y., Zeng, Q., Zhan, F., Feng, Y., & Wang, Z. (2022). Identification of MEDAG and SERPINE1 Related to Hypoxia in Abdominal Aortic Aneurysm Based on Weighted Gene Coexpression Network Analysis. *Frontiers in physiology*, *13*, 926508. https://doi.org/10.3389/fphys.2022.926508

Triposkiadis, F., Xanthopoulos, A., Boudoulas, K. D., Giamouzis, G., Boudoulas, H., & Skoularigis, J. (2022). The Interventricular Septum: Structure, Function, Dysfunction, and Diseases. *Journal of clinical medicine*, *11*(11), 3227. https://doi.org/10.3390/jcm11113227

Tsigkou, A., Luisi, S., De Leo, V., Patton, L., Gambineri, A., Reis, F. M., Pasquali, R., & Petraglia, F. (2008). High serum concentration of total inhibin in polycystic ovary syndrome. *Fertility and sterility*, *90*(5), 1859–1863. https://doi.org/10.1016/j.fertnstert.2007.08.082

Tunariu, N., Gibbs, S. J., Win, Z., Gin-Sing, W., Graham, A., Gishen, P., & Al-Nahhas, A. (2007). Ventilation-perfusion scintigraphy is more sensitive than multidetector CTPA in detecting chronic thromboembolic pulmonary disease as a treatable cause of pulmonary hypertension. *Journal of nuclear medicine : official publication, Society of Nuclear Medicine*, *48*(5), 680–684. https://doi.org/10.2967/jnumed.106.039438

UniProt Consortium (2014). Activities at the Universal Protein Resource (UniProt). *Nucleic acids research*, *42*(Database issue), D191–D198. https://doi.org/10.1093/nar/gkt1140

van Albada, M. E., Bartelds, B., Wijnberg, H., Mohaupt, S., Dickinson, M. G., Schoemaker, R. G., Kooi, K., Gerbens, F., & Berger, R. M. (2010). Gene expression profile in flow-associated pulmonary arterial hypertension with neointimal lesions. *American journal of physiology. Lung cellular and molecular physiology*, *298*(4), L483–L491. https://doi.org/10.1152/ajplung.00106.2009

van de Veerdonk, M. C., Bogaard, H. J., & Voelkel, N. F. (2016). The right ventricle and pulmonary hypertension. *Heart failure reviews*, *21*(3), 259–271. https://doi.org/10.1007/s10741-016-9526-y

Verhoeven, M. O., van der Mooren, M. J., Teerlink, T., Verheijen, R. H., Scheffer, P. G., & Kenemans, P. (2009). The influence of physiological and surgical menopause on coronary heart disease risk markers. *Menopause (New York, N.Y.)*, *16*(1), 37–49. https://doi.org/10.1097/gme.0b013e31817c42d6

Verbelen, T., Godinas, L., Maleux, G., Coolen, J., Claessen, G., Belge, C., Meyns, B., & Delcroix, M. (2022). Chronic thromboembolic pulmonary hypertension: diagnosis, operability assessment and patient

selection for pulmonary endarterectomy. *Annals of cardiothoracic surgery*, *11*(2), 82–97. https://doi.org/10.21037/acs-2021-pte-12

Wickham, J., Jr, & Walsh, S. T. (2007). Crystallization and preliminary X-ray diffraction of human interleukin-7 bound to unglycosylated and glycosylated forms of its alpha-receptor. *Acta crystallographica. Section F, Structural biology and crystallization communications*, *63*(Pt 10), 865–869. https://doi.org/10.1107/S1744309107042807

Woodruff, T. K., Besecke, L. M., Groome, N., Draper, L. B., Schwartz, N. B., & Weiss, J. (1996). Inhibin A and inhibin B are inversely correlated to follicle-stimulating hormone, yet are discordant during the follicular phase of the rat estrous cycle, and inhibin A is expressed in a sexually dimorphic manner. *Endocrinology*, *137*(12), 5463–5467. https://doi.org/10.1210/endo.137.12.8940372

Wu, T., Hu, E., Xu, S., Chen, M., Guo, P., Dai, Z., Feng, T., Zhou, L., Tang, W., Zhan, L., Fu, X., Liu, S., Bo, X., & Yu, G. (2021). clusterProfiler 4.0: A universal enrichment tool for interpreting omics data. *Innovation (Cambridge (Mass.))*, *2*(3), 100141. https://doi.org/10.1016/j.xinn.2021.100141

Wu, X., Qiu, F., Jin, X., Zhou, J., & Zang, W. (2021). ATF3: a novel biomarker for the diagnosis of acute kidney injury after cardiac surgery. *Annals of translational medicine*, *9*(22), 1655. https://doi.org/10.21037/atm-21-5231

Yang, K. C., Yamada, K. A., Patel, A. Y., Topkara, V. K., George, I., Cheema, F. H., Ewald, G. A., Mann, D. L., & Nerbonne, J. M. (2014). Deep RNA sequencing reveals dynamic regulation of myocardial noncoding RNAs in failing human heart and remodeling with mechanical circulatory support. *Circulation*, *129*(9), 1009–1021. https://doi.org/10.1161/CIRCULATIONAHA.113.003863

Yano, T., Miura, T., Ikeda, Y., Matsuda, E., Saito, K., Miki, T., Kobayashi, H., Nishino, Y., Ohtani, S., & Shimamoto, K. (2005). Intracardiac fibroblasts, but not bone marrow derived cells, are the origin of myofibroblasts in myocardial infarct repair. *Cardiovascular pathology : the official journal of the Society for Cardiovascular Pathology*, *14*(5), 241–246. https://doi.org/10.1016/j.carpath.2005.05.004

Yaoita, N., Satoh, K., Satoh, T., Sugimura, K., Tatebe, S., Yamamoto, S., Aoki, T., Miura, M., Miyata, S., Kawamura, T., Horiuchi, H., Fukumoto, Y., & Shimokawa, H. (2016). Thrombin-Activatable Fibrinolysis Inhibitor in Chronic Thromboembolic Pulmonary Hypertension. *Arteriosclerosis, thrombosis, and vascular biology*, *36*(6), 1293–1301. https://doi.org/10.1161/ATVBAHA.115.306845

You, Z., Xu, J., Li, B., Ye, H., Chen, L., Liu, Y., & Xiong, X. (2019). The mechanism of ATF3 repression of epithelial-mesenchymal transition and suppression of cell viability in cholangiocarcinoma via p53 signal pathway. *Journal of cellular and molecular medicine*, *23*(3), 2184–2193. https://doi.org/10.1111/jcmm.14132

Yu, G., Wang, L. G., Han, Y., & He, Q. Y. (2012). clusterProfiler: an R package for comparing biological themes among gene clusters. *Omics: a journal of integrative biology*, *16*(5), 284–287. https://doi.org/10.1089/omi.2011.0118

Zagorski, J., Sanapareddy, N., Gellar, M. A., Kline, J. A., & Watts, J. A. (2008). Transcriptional profile of right ventricular tissue during acute pulmonary embolism in rats. *Physiological genomics*, *34*(1), 101–111. https://doi.org/10.1152/physiolgenomics.00261.2007

Zhang, M., Zhang, Y., Pang, W., Zhai, Z., & Wang, C. (2019). Circulating biomarkers in chronic thromboembolic pulmonary hypertension. *Pulmonary circulation*, *9*(2), 2045894019844480. https://doi.org/10.1177/204589401984448

Zhang, L., Yan, P., Yang, K., Wu, S., Bai, Y., Zhu, X., Chen, X., Li, L., Cao, Y., & Zhang, M. (2021). Association between splenectomy and chronic thromboembolic pulmonary hypertension: a systematic review and meta-analysis. *BMJ open*, *11*(2), e038385. https://doi.org/10.1136/bmjopen-2020-038385

Zhong, L., Chiusa, M., Cadar, A. G., Lin, A., Samaras, S., Davidson, J. M., & Lim, C. C. (2015). Targeted inhibition of ANKRD1 disrupts sarcomeric ERK-GATA4 signal transduction and abrogates phenylephrine-induced cardiomyocyte hypertrophy. *Cardiovascular research*, *106*(2), 261–271. https://doi.org/10.1093/cvr/cvv108

Zhou, Y., Zhou, B., Pache, L., Chang, M., Khodabakhshi, A. H., Tanaseichuk, O., Benner, C., & Chanda, S. K. (2019). Metascape provides a biologist-oriented resource for the analysis of systems-level datasets. *Nature communications*, *10*(1), 1523. https://doi.org/10.1038/s41467-019-09234-6

Zhu, H., Liu, M., Zhang, N., Pan, H., Lin, G., Li, N., Wang, L., Yang, H., Yan, K., & Gong, F. (2018). Serum and Adipose Tissue mRNA Levels of ATF3 and FNDC5/Irisin in Colorectal Cancer Patients With or Without Obesity. *Frontiers in physiology*, *9*, 1125. https://doi.org/10.3389/fphys.2018.01125

Zou, G., Ren, B., Liu, Y., Fu, Y., Chen, P., Li, X., Luo, S., He, J., Gao, G., Zeng, Z., Xiong, W., Li, G., Huang, Y., Xu, K., & Zhang, W. (2018). Inhibin B suppresses anoikis resistance and migration through the transforming growth factor-β signaling pathway in nasopharyngeal carcinoma. *Cancer science*, *109*(11), 3416–3427. https://doi.org/10.1111/cas.13780

A-1. List of the sequence of human primers for qRT-PCR

Gene Name	Sequence (5'-3')	Anneling (°C)
HPRT1	F: TGACACTGGCAAAACAAT R: GGTCCTTTTCACCAGCAA	60
ANKRD1	F: TACGGAACCTGTGGATGTGC R: CACGGAATTCGATCTGGGCT	60
SERPINE1	F: GAAGACTCCCTTCCCCGACT R: TGGGCACTCAGAATGTTGGT	60
IL7R	F: GCCCTCGTGGAGGTAAAGTG R: TTGGCTCCTTCCCGATAGAC	60
ATF3	F: CCGAGCGGAGCCTGG R: GTGGCAGAGGTGCTTGTTCT	60
CILP1	F: AATTACACCGTACGCTTCCTC R: CATCTCTGCCAAGCAAATGC	60
INHBB	F: AAATCATCAGCTTCGCCGAGA R: ACAGGTTCTGGTTGCCTTCG	60

A-2. List of the sequence of rat primers

Gene name	Sequence (5'-3')	Anneling (°C)
Ankrd1	F: ACTTCCAGCCAACAGTGTGAA R: TCAGAAACCTTGGCACATCCA	60
Serpine1	F: GGCCACCAACTTCGGAGTAA R: TGTTCCATGACCCCATGAGC	60
Il7r	F: AAGCATGATGTGGCCTACCG R: CTCCACTCACTCCAGAAGCC	60
Atf3	F: CCTCTAGCCGCTCTCTGGA R: GGCAAAGGTGCTTGTTCTGG	60
Inhbb	F: GAGCGCGTCTCTGAGATCAT R: GTCCACCTTCTTCTCCACC	60
Gapdh	F:AGATGGTGAAGGTCGGTGTG R: GACTGTGCCGTTGAACTTGC	60

A-3. Sequence of siRNA

Gene	Product	Target sequence
CONTROL	ON-TARGET plus Non-targeting Pool D-001810-01-05	UGGUUUACAUGUCGACUAA
	ON-TARGET plus Non-targeting Pool D-001810-02-05	UGGUUUACAUGUUGUGUGA
	ON-TARGET plus Non-targeting Pool D-001810-03-05	UGGUUUACAUGUUUUCUGA
	ON-TARGET plus Non-targeting Pool D-001810-04-05	UGGUUUACAUGUUUUCCUA
ANKRD1	ON- TARGETplus SMARTpool siRNA J-012515-05	CUACAAGACCUCUCGCAUA
	ON- TARGETplus SMARTpool siRNA J-012515-06	GAACCAAAGCAAUAUUCGA
	ON- TARGETplus SMARTpool siRNA J-012515-07	CGAAUUCCGUGAUAUGCUU
	ON- TARGETplus SMARTpool siRNA J-012515-08	GCUAUAAGAUGAUCCGACU
ATF3	ON- TARGETplus SMARTpool siRNA J-008663-05	GAGCUAAGCAGUCGUGGUA
	ON- TARGETplus SMARTpool siRNA J-008663-06	GCAAAGUGCCGAAACAAGA
	ON- TARGETplus SMARTpool siRNA J-008663-07	AGAAGCAGCAUUUGAUAUA
	ON- TARGETplus SMARTpool siRNA J-008663-08	CGAGAAAGAAAUAAGAUUG
IL7R	ON- TARGETplus SMARTpool siRNA J-007996-06	CAAAUGGACGCAUGUGAAU
	ON- TARGETplus SMARTpool siRNA J-007996-07	GGAUUAAGCCUAUCGUAUG
	ON- TARGETplus SMARTpool siRNA J-007996-08	GAAUGGGCCUCAUGUGUAC
	ON- TARGETplus SMARTpool siRNA J-007996-09	CAGGGUCAGCCCAUUCUUA
INHBB	ON- TARGETplus SMARTpool siRNA J-011702-06	GGUGAACUCCUGCUGCAUU
	ON- TARGETplus SMARTpool siRNA J-011702-07	GGCAACAGUUCUUCAUUGA
	ON- TARGETplus SMARTpool siRNA J-011702-08	GGUGGAACAUGGUGGAGAA
	ON- TARGETplus SMARTpool siRNA J-011702-09	GGACGUGCCCAACAUGAUU
SERPINE1	ON- TARGETplus SMARTpool siRNA J-019376-09	GGACAUCCAGCGUGACGGA
	ON- TARGETplus SMARTpool siRNA J-019376-10	UGCAGAAAGUGAAGAUCGA
	ON- TARGETplus SMARTpool siRNA J-019376-11	UCUCCAAACCAGACGGUGA
	ON- TARGETplus SMARTpool siRNA J-019376-12	GAGACAGGCAGCUCGGAUU

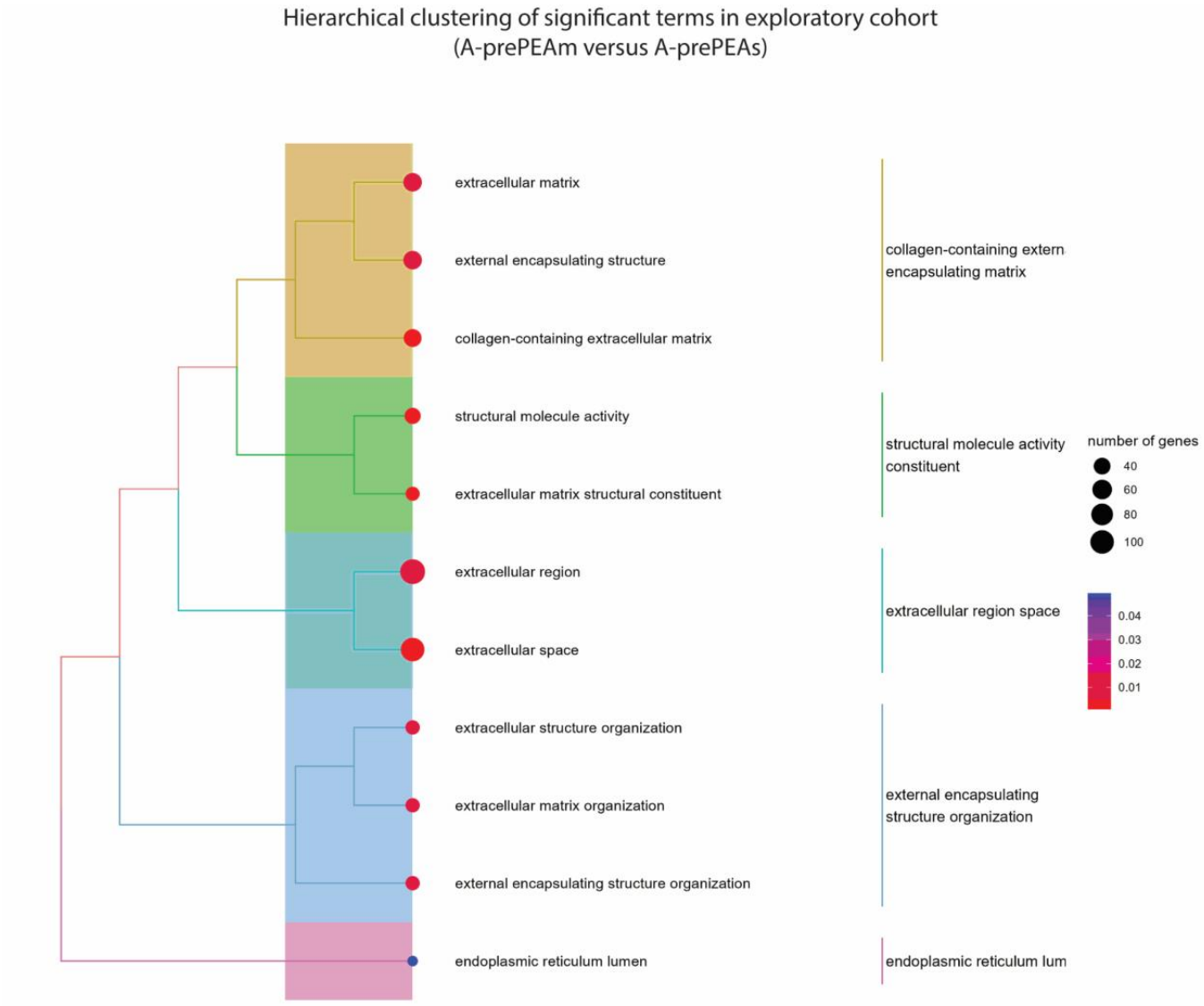

A-4. Hierarchical clustering of highly expressed genes. Hierarchical clustering of enriched terms for the significant genes in the exploratory cohort of A-prePEAm (n = 4) versus A-prePEAs (n = 5). The enriched gene ontology was identified by each cluster based on the adjusted P value (< 0.05).

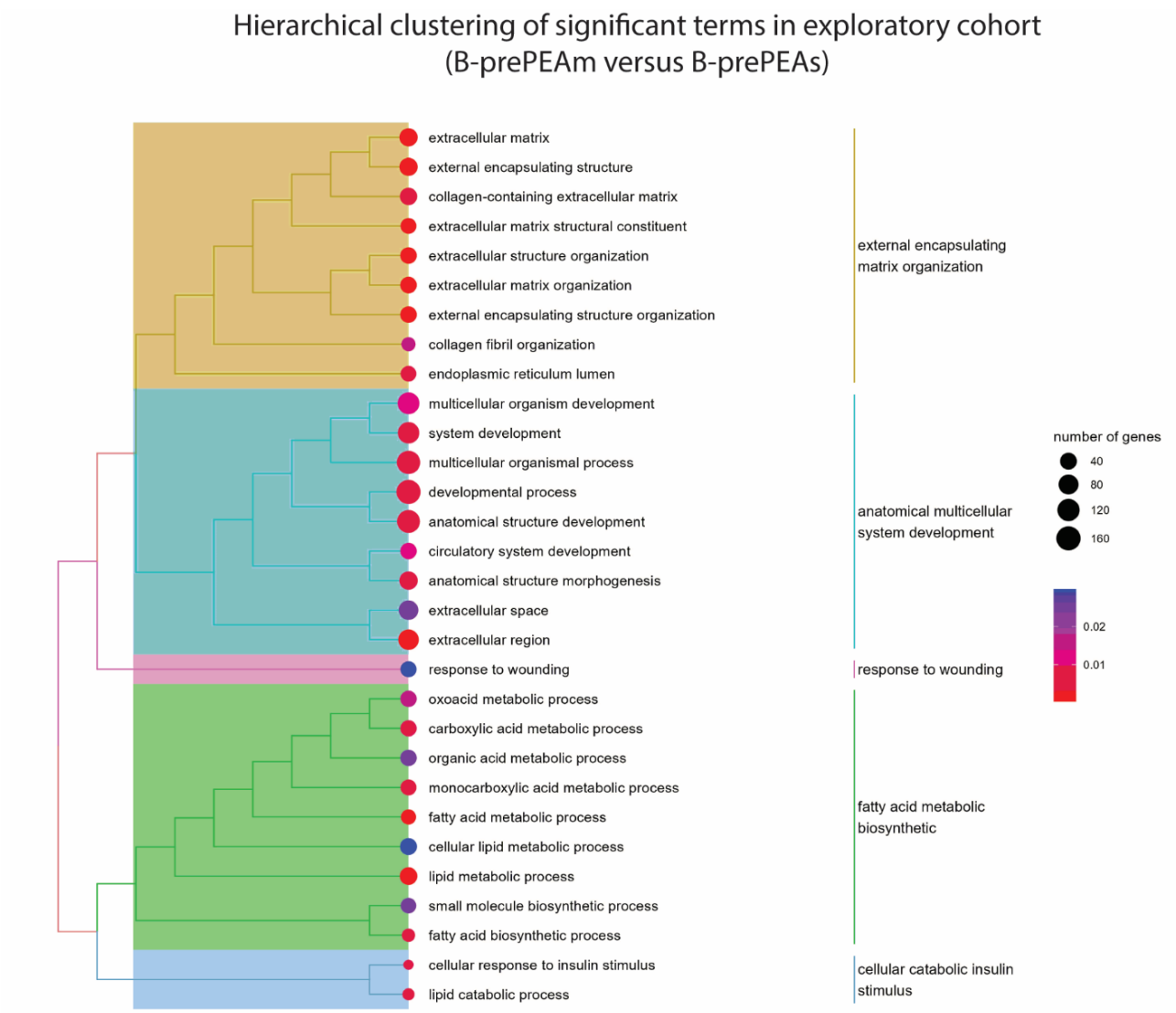

A-5. Hierarchical clustering of highly expressed genes. Hierarchical clustering of enriched terms for the significant genes in the confirmatory cohort of B-prePEAm (*n*= 30) versus B-prePEAs (*n*= 18). The enriched gene ontology was identified by each cluster based on the adjusted *P* value (< 0.05).

Acknowledgments

The completion of this thesis depends largely on the encouragement and guidelines of many others. I take this opportunity to express my gratitude to the people who have been instrumental in the successful completion of this thesis. I hardly know where to start expressing my gratitude, but for sure the gratitude goes to all those who have assisted me in the process of completing this thesis.

first and foremost, I would like to thank the **patients** who with their consent allowed us to use their samples as the pillar of this huge research, as without them we would not have been able to conclude this research, and without them, we would not have made it through to this place and spot where we stand right now!

I had the privilege to work with thousands of human samples among which blood and heart tissue were the most important ones. I remember when I was isolating RNA from the heart tissue, I was so careful, as I was isolating it from my own heart. To all our patients who donated their samples, I wish I could hold your hands and say thank you, for being so generous! I am short of words to express how much I learned from your generosity and I hope everybody who is working with these data in the future, could bring lots of discoveries and new therapy for you. I was deeply touched and amazed by the beauty and the harmony of nature and the colorful path to the unknown world where we have to try to find and connect the dots.

I would like to express my sincere gratitude to **Prof. Dr. Holger Nef** who gave me this opportunity to do my PhD in his group and gave me the chance to work on different projects. By the way, I never forget your Christmas present ever!

My special thanks to the principal investigators (PIs) of project B07/SFB 1213 especially **Prof. Dr. med. Christian W. Hamm** and **Prof. Dr. med. Oliver Dörr** for their great support and opportunities especially in the field of biomarker research and discovery.

I am immensely indebted to all the PIs of Project CP01/ SFB 1213 **Prof. Dr. med Eckhard Mayer**, **Prof. Dr. med. Christoph Liebetrau**, **PD. Dr. Dr. Peter Dorfmüller**, as well as **Prof. Dr. Norbert Weissmann** (Spokesperson of CRC 1213) for giving me the opportunity to work on this project during my PhD.

I would like to thank especially **Prof. Dr. med. Christoph Liebetrau** for his time to classify the patients as well as for the long discussion and his endless support throughout this path even on the weekends. His insightful comments and reviews on my PhD dissertation were invaluable. He helped draft it with a professional touch, incorporating both critiques and positive feedback, and his unwavering support has been instrumental throughout my journey.

I want to express my deep appreciation to **Prof. Dr. med. Christoph B. Wiedenroth** for his invaluable support and guidance for CTEPH patients. His constant help and advice have been crucial on this journey, and his expertise and willingness to answer my questions have been greatly appreciated.

I would like to show my greatest appreciation to **Prof. Dr. Soni Savai Pullamsetti** for not only giving me the opportunity to work in her lab at Max Plank Institute but for her endless support and scientific discussion and for disposing me to anything that I needed to perform the experiments throughout these years. Without her encouragement and guidance, this thesis would not have materialized, especially her comments and corrections to this dissertation.

Further, I would like to thank **Prof. Dr. med. Werner Seeger** who granted me the opportunity to pursue my PhD at Max Plank Institute for Heart and Lung Research. I am always stunned by his vast knowledge and how he connects basic research to the clinic. Special thanks to the guidance and comments on my PhD dissertation and the manuscript.

I would like to thank **PD. Dr. Christian Troidl** for his endless support throughout my PhD. I appreciate all his support, arrangements, and how he cared especially whenever I faced any problem he was the only hope that I had. Thank you for your comments on my thesis.

I should say thank you to **Dr. Stefan Günther** who gave me this opportunity to perform the RNA isolation of the heart of the CTEPH cohort in his lab at Deep Sequencing Platform in Max plank- Institute for Heart and Lung Research. It was not an easy process and I remember how many times it failed but finally, we made it! Thanks for the time and long discussion during these years. I also would like to take the opportunity to thank **Dr. Carsten Kuenne** for his assistance in RNA-Seq analysis. And also, thanks to **Samina Mahmood** for her technical assistance.

My special thanks to **Prof. Dr. Mario Looso** for his great help and the support that I always received from his group during my PhD.

My special thanks to **Prof. Dr. med. Till Keller** for his help and great support during my PhD. I would like to thank **Dr. med. Steffen Kriechbaum** for his great help and support regarding the CTEPH patients cohort. I would like to thank **Dr. med. Stefan Guth** for his support and comments.

My special thanks to **Dimitri Grün**, the best bioinformatician ever! For his great help in the analysis of RNA-seq data, almost everyday discussion, and of course his patience.

I should say thank you to **Prof. Dr. Rajkumar Savai** for his help and the support that I always received from his lab.

My special thanks to **Dr. Stanislav Keranov** for all the great collaboration and work that we did together during my PhD. Special thanks to **Dr. Jakob Lorenz** we worked together at the beginning of my PhD a lot together.

I should say thank you to **Dr. Baktybek Kojonazarov**, Project CP02/SFB 1213 for his great support provide the animal models for my thesis.

My sincere gratitude to the international Giessen Graduate Centre for Life Sciences (GGL) for its great graduate program. Especially **Prof. Dr. Eveline Baumgart-Vogt**, **Dr. Lorna Lück**, and the GGL team.

My enormous appreciation goes to the molecular biology and medicine of lung (MBML) in Giessen for its unique international graduate program. Especially **Prof. Dr. med. Werner Seeger** and the MBML team.

My special thanks to all the Technicians with whom I have had the privilege to work together with, especially The technician in Kerckhoff Herzforschungsinstitut (KHFI) **Monika Rieschel** (for her great help in preparing the biopsy of the CTEPH cohort after surgery), **Sigrun Sass**, and **Nora Staubach** (for great help for biomarker discovery research) and of course **Anett Kirchhof**, our study nurse. My special thanks to all the technicians in Prof. Dr Soni Savai Pullamsetti's lab for their great help especially **Uta Eule**, **Natascha Wilker**, **Jana Rostkovius**, and **Daniel Grella** for their great technical support.

My special thanks to **Julia Paul**, **Monika Hauselbauer**, **Nina Riekes**, and **Carina Römer** for their great cooperation and assistance.

A heartfelt thanks to my colleagues and friends at the Max Plank Institute Bad Nauheim, particularly those in Pullamsetti's lab, the Experimental Cardiology Giessen, and the Kerckhoff Herzforschungsinstitut (KHFI). I am particularly thankful to **Dr. Christoph Lipps**, **Dr. Neslihan Sevinc**, and **Dr. Anoop Cherian** for their valuable scientific discussions.

My special gratitude goes to **Dr. Prakash Chelladurai**, for the enriching scientific discussions and his invaluable support at the start of my PhD journey. Also, my special thank goes to **Dr. Elizabeth Martinson** for providing me with editorial support during my PhD.

Special thanks to all the colleagues in the **IT department** in Max Planck for their great round-the-clock support particularly taking care of our data during my PhD. Thanks for all thediscussion that we had even on the train we commute together daily. They were always available with their unconditional assistance.

Finally, I should say thank you to my best friends ever **mami**, **dadi**, **my sister**, and **brothers** and of course **my husband** for all their support, caring, and unconditional love. I'm so lucky and grateful to have you all.